Infrared Laser Spectroscopy of Isolated Biomolecules in Superfluid Helium Nanodroplets

Myong Yong Choi

A dissertation submitted to the faculty of the University of North Carolina at Chapel Hill in partial fulfillment of the requirements for the degree of Doctor of Philosophy in the Department of Chemistry.

Chapel Hill
2006

Approved by,

Advisor: Tomas Baer

Reader: John M. Papanikolas

Reader: Lee G. Pedersen

In memory of Professor Roger Ervin Miller, F.R.S.
and
to my family

ABSTRACT
MYONG YONG CHOI: Infrared Laser Spectroscopy of Isolated
Biomolecules in Superfluid Helium Nanodroplets.
(Under the direction of Roger E. Miller)

The focus of this thesis is the identification and structural characterization of isolated biomolecules in superfluid helium nanodroplets. We have recently developed structural tools for studying isolated biomolecules, including nucleic acid bases (NABs) (cytosine, guanine, uracil, thymine, and adenine), their mono-hydrated complexes and other biologically important molecules, using high resolution infrared laser spectroscopy. The structural tool called vibrational transition moment angle (VTMA) has been developed for measuring the angle between the permanent dipole moment and transition dipole directions in these species and provides unambiguous structural determinations for many systems. This is a very powerful technique, especially for larger systems, because relatively low level ab initio calculations are able to predict the correct VTMA, when the calculated and experimental vibrational frequencies do not agree. Another powerful tool for structural determination is used to determine the dipole moments of various isomers by measuring the intensity of a particular band as a function of direct current electric field. We have applied these new techniques to the study of the isolated biomolecules, such as tautomerism of NABs, their nonplanarities, energetics, and the intermolecular interactions in the hydrated NABs. These results provide benchmarks for the evaluation of ab initio calculations being carried out on these systems.

ACKNOWLEDGMENTS

There are so many people who have supported me in various ways that I would like to recognize them in this acknowledgment.

Foremost, I am deeply grateful to my late advisor, forever mentor, and friend, Professor Roger E. Miller, F.R.S. for his enthusiasm and support during my graduate school period. He graciously took me on and introduced me to many exciting new ideas. It was his consistently innovative vision that led to the completion of this thesis. I only wish that I had more time to work with and learn from Roger. I am extremely proud to be his student. I also thank Roger's family for their kind hospitality in Chapel Hill.

I wish to express my sincere gratitude to Professor Tomas Baer who has guided me in Roger's absence. Even though it was a short time, his clear advice and patience, especially in writing papers and this thesis, have proven invaluable. I also wish to thank Professor John Papanikolas, who is special to me at UNC–CH, for his bright comments and friendly advice. I also thank Professor Lee Pedersen for his comments, discussion, and support as a dissertation committee member.

I also thank past and present Miller Group members for their work and enthusiasm, especially Feng Dong, Jeremy Merritt, Paul Stiles, William Lewis, Gary Douberly, Travis Falconer, Michael Lindsay, and Michael Barrett. Even though the Miller Group is now no longer at UNC–CH, I believe that the time and memories that we shared will connect us forever.

I thank my immediate family for being extremely supportive and patient throughout my life. Special thanks are due to my sisters and their families for taking care of my grandmother in my absence. I am also very grateful to Kyeong Soon's immediate family for generous support and patience throughout my education.

Finally, none of this work would have taken place without my lovely wife's full support and devotion. She never complains about my staying late in the lab and always teaches me to be a better person with her heart. I also want to express my love for my daughter, Sophia Minji, who has missed so many of the things that a young girl should share with her father only because I was studying. I am sorry Minji and I love you very much.

Lastly, there are so many others to whom I am grateful. I regret that I could not list all of them here. Instead I would like to end this by saying "Thank you all."

Myong Yong Choi
Chapel Hill, North Carolina
Summer, 2006

TABLE OF CONTENTS

LIST OF TABLES

LIST OF FIGURES

xxiii

Chapter 1

Introduction

The two helium isotopes, ^{4}He and ^{3}He, have some remarkable chemical properties, which are essential for the work described in this thesis. They remain a liquid without solidifying under their saturated vapor pressure, and even at the lowest temperature, approaching absolute zero Kelvin. In addition, they are superfluids below 2.17 K and 2.6 mK, respectively [1]. Specifically, the reluctance to solidify is a direct result of both the extremely weak He–He interaction and the small mass of the helium atoms, which leads to a high zero-point energy. As a result, the solidification of the helium is only possible at external pressures in excess of 25 Bar. The weak He–He interaction also causes helium to have the lowest boiling point of all elements, namely 4.21 K and 3.19 K for ^{4}He and ^{3}He, respectively [2].

This weak He–He interaction is useful in the study of the solutes immersed into the bulk helium because helium binds more strongly to the foreign species than to itself, which makes it a good solvent. However, the solvation power is sufficiently weak that in bulk helium, the solutes tend to bind more strongly to the container walls than to the helium solvent [3]. This problem can be overcome through the use of the finite size helium clusters, called liquid helium droplets in this thesis, which act as a wall-less solvent. The helium droplet experiments are based on the molecular beam techniques and some of essentials of this technique are explained in Chapter 2. Because almost

any atoms or molecules can be easily trapped inside or on the surface of the helium droplets, we can study isolated biomolecules, such as nucleic acid bases (NABs), their hydrated complexes and other biologically important molecules. This thesis describes the results of several such investigations.

1.1   Helium Nanodroplet Spectroscopy

The high resolution associated with gas-phase spectroscopy results from the fact that a vacuum is a uniform and non-dissipative medium. In contrast, liquids and solids tend to be rather inhomogeneous on the microscopic scale and provide ways in which the molecules can relax, resulting in significant spectral broadening. As a result, much of the information contained in a frequency domain spectrum is lost in the broad bands that are typical in condensed phases. The homogeneity of liquid helium, combined with its superfluidity (non-dissipative), make an ideal spectroscopic medium [4]. Nevertheless, the isolation of the molecules in bulk liquid helium has proven difficult [5–8], owing to rapid diffusion of the solute to the container walls. However, nanoscale helium droplets, first produced by Becker *et al.*, [7] can provide the needed isolation and the species of interest can easily be introduced by pick-up [8] from the gas-phase. It is important to point out here that the helium nanodroplet method requires very little vapor pressure in order to fill the droplets with the molecules of interest. In a typical pick-up cell the pressure need only be $10^{-6} - 10^{-5}$ Torr to optimize for the capture of a single molecule by the droplets. This is an important feature when studying biomolecules of moderate size, where the thermal stability becomes a real issue, a point emphasized in Chapter 4.

A brief summary of the experimental investigations of helium droplets is given to show the range of the ongoing research in both the physical and chemical helium droplet community. The first liquidfication of helium dates back to 1908 by H. K. Onnes [9,10].

Subsequent research revealed the properties of superfluidity of helium in 1938 by Allen, Misener, and Kapitza [11,12]. Almost two decades later, in 1961, Becker and co-workers succeeded in producing the first ^{4}He beam [7]. However, no convincing evidence of superfluidity of ^{4}He droplets was discovered from the study. Later in 1980, Gspann and co-workers studied the electron-impact excitation of larger clusters of helium and discovered that both helium isotopes were electronically metastable [13]. The first demonstration of helium droplet pick-up was reported in 1990 by Scheideman *et al.*, [14, 15] while the first infrared spectra of helium solvated molecules were reported by Goyal *et al.* [16] for SF_6 in 1992. In those studies, a depletion spectroscopy, the attenuation of the droplet beam on laser induced absorption, was employed using mass-spectrometric or bolometric detectors. A few years later, the Toennies group used a continuously tunable diode laser to obtain a high resolution spectrum of SF_6 in pure ^{4}He and mixed ^{4}He/^{3}He droplets [17–19]. In pure ^{4}He droplets, a rotational structure of the solvated molecule was observed. In the mixed ^{4}He/^{3}He droplets, ^{4}He clusters form inside of the ^{3}He droplets, due to its lower zero point energy. The SF_6 was found to be in the interior of the helium droplet, in agreement with theoretical calculations [20, 21]. Most remarkably, the direct measurement of the droplet temperature, 0.37 K for ^{4}He and 0.15 K for ^{3}He droplets, was obtained from these studies, which is in excellent agreement with the calculations of Brink and Stringari [22]. In 1996, the first direct experimental evidence of superfluidity in ^{4}He droplets was revealed by Hartmann *et al.* [23]. A few years later, the free rotation of OCS molecule in ^{4}He droplets was demonstrated, showing its sharp rotationally resolved structure, by the same group [24]. They also demonstrated the reappearance of the sharp rotational structure of OCS by gradually adding an average of 60 ^{4}He atoms to the ^{3}He droplets [24]. Similar to the study of SF_6, the rotational constants extracted from the this study were about a factor of three smaller than that in the gas-phase [24,25]. In 2000, Even *et al.* produced up to 20 ^{4}He

atoms in a pulsed jet expansion [26,27], which can bridge the gap to the studies of larger ^{4}He droplets. Interestingly, the study showed that even the first solvation shell helium density is decoupled from the rotational motion of the molecule. There is now a rapidly growing literature on the spectroscopy of both atoms [5,28–32] and molecules [24,33–41] in helium droplets, along with studies of the cross sections for total scattering [42], capture and coagulation [43]. Positively [44–48] and negatively [49–51] charged droplets have also been studied in helium, providing information on such processes as resonant charge hopping and electron solvation, respectively.

1.2 Motivation: Studying Isolated Biomolecules

Although an important goal in biochemistry is the understanding of molecular function under physiological conditions, much of our fundamental knowledge of biomolecules comes form experiments carried out far from these conditions. This is perhaps best illustrated by the importance that crystal diffraction and mass spectrometry techniques have played in biochemistry. The premise upon which all of this work is built is that the things we learn about biomolecules under these non-physiological conditions can be transferred to functional systems. Recently, nucleic acid bases (NABs) (Figure 1.1) have been the subject of numerous experimental and theoretical studies. The conformational variability of NABs plays a very important role in transferring the information through biomolecular recognition processes and hydrogen-bondings in base pairs and hydrated molecules. Although the understanding of these mechanisms in local interactions of the biologically important molecules is in great demand, the experimental approach for such mechanisms in the condensed phase can not be applied because of their interactions with the local environment. However, this problem can be avoided by using the gas-phase experiments, in which the determination and characterization of the structure and properties of clusters is done without the interaction of a solvent, i.e. an "isolated"
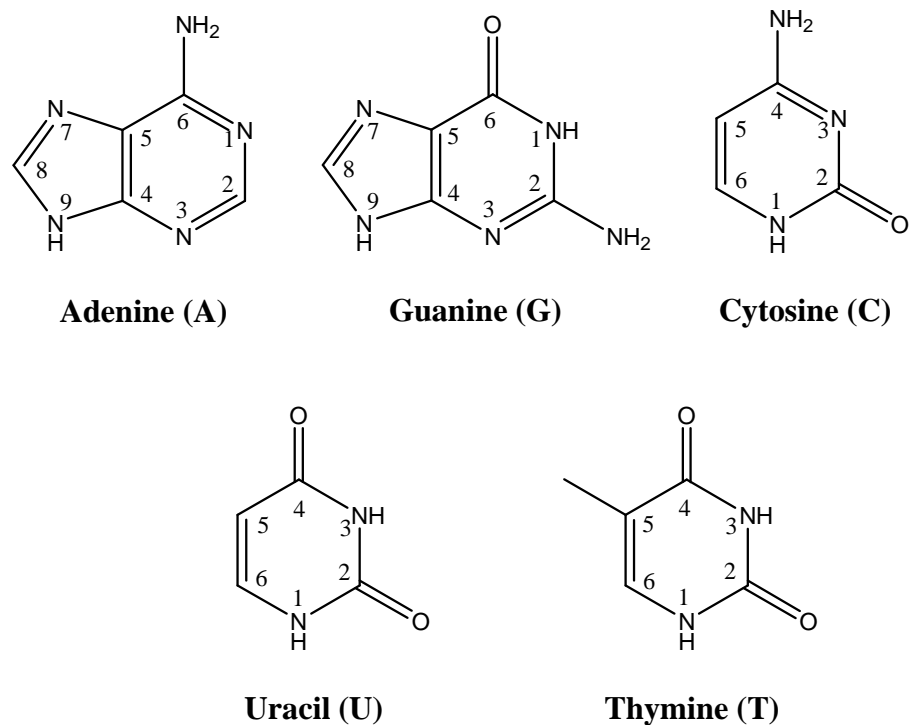
Figure 1.1: Structures of isolated nucleic acid bases (NABs).

system. This is a considerable advantage for the study of local interactions in the NABs and their complexes. As a result, there has been an increasing effort devoted to the spectroscopic study of biomolecules in the gas-phase [38,52–76], motivated by the fact that these can be compared directly with results of high level *ab initio* calculations on isolated systems, thus providing us with benchmarks that can be used to test the accuracy of such calculations. In addition, important structural information is provided by these gas-phase studies, often at a level that would be impossible under physiological conditions.

Previous studies showed that the tautomeric equilibrium strongly depends on the chemical environment so that the NAB structures may depend on the environment (crystalline, aqueous or other solution and gas-phase) [59,77,78]. Different tautomers of NABs are formed by the formal migration of a hydrogen atom accompanied by a switch

of adjacent conjugated double bonds, a chemical reaction called tautomerization. The amino groups of NABs can form several isomers as shown in Figure 1.2. The enol forms are structural isomers of keto forms and both forms have cis and trans stereoisomers.
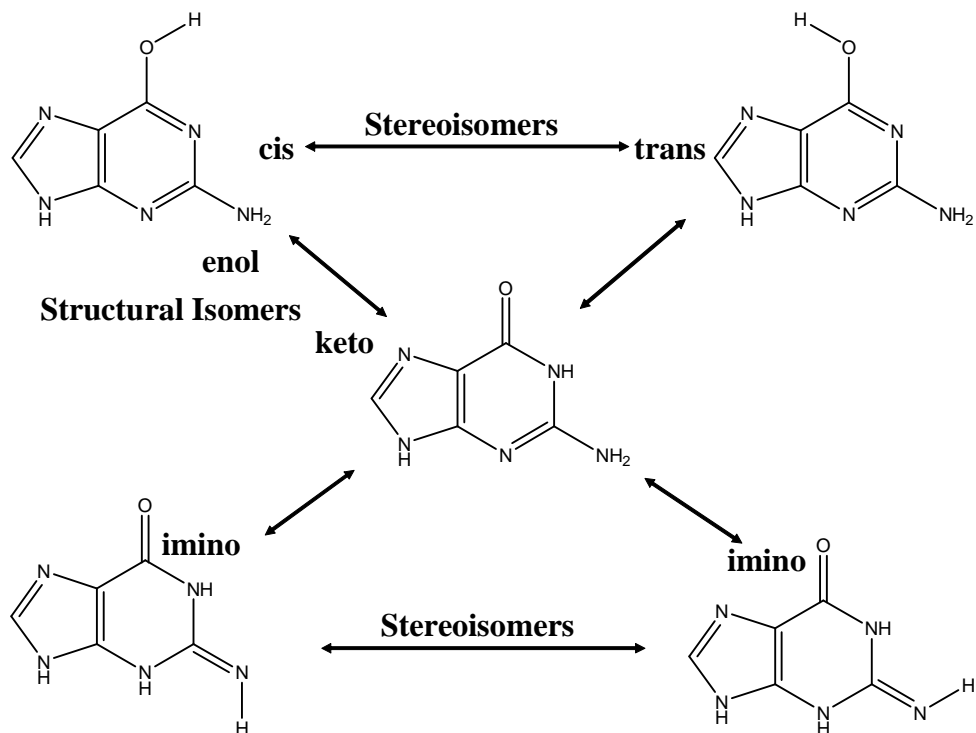
Figure 1.2: Schematic example of structural isomers (keto–enol) and stereoisomers (cis–trans) of guanine.

High resolution spectroscopy is now routinely used to identify different tautomers of these biomolecules [79–82], providing insights into how these systems undergo structural rearrangements of importance in understanding processes as diverse as mutation, solvent interactions, and protein folding. For example, mutation can result from the fact that these tautomers form nonstandard base pairs [83], such as the imino tautomer of adenine (A) pairing with cytosine (C). The fact that C is now corporated into the DNA strand, where thymine (T) was expected, means that cytosine (C) will pair with guanine (G) in the next generation, the net results being the formation of a G–C pair in place of an A–T pair, as shown in Figure 1.3.
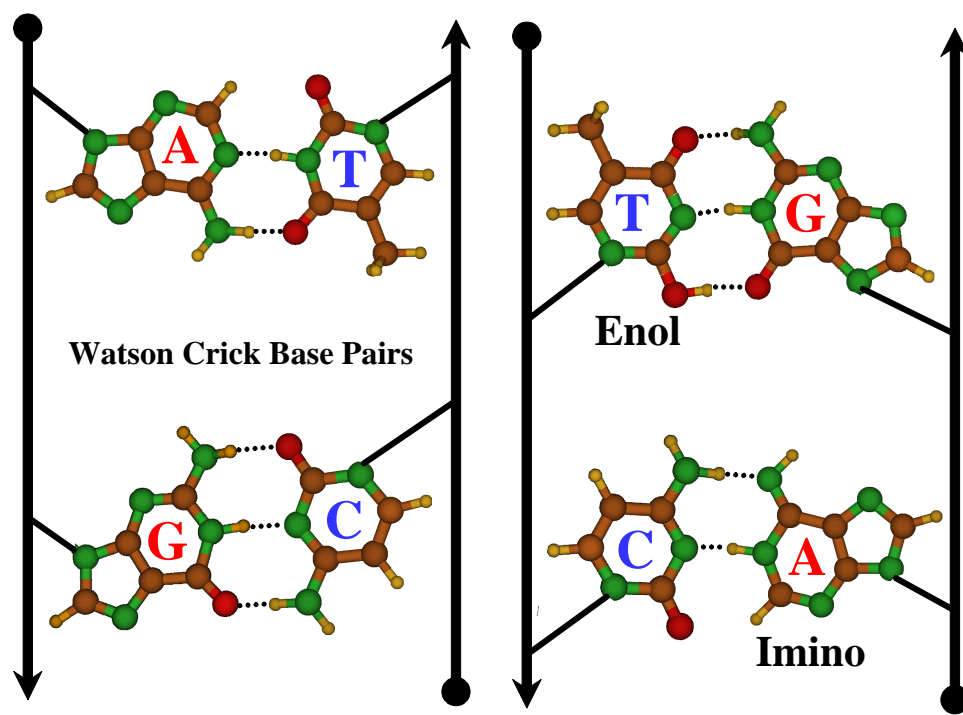
Figure 1.3: Watson–Crick base pairs and base pairs with tautomer forms of nucleic acid bases. An enol form of thymine is hydrogen bonding with guanine and the canonical form of cytosine is base pairing with an imino form of adenine.

The fact that nature searches for the lowest energy design and arrangement to relax into the potential energy surfaces is of great consequences in science. In particular, the minor tautomers have a higher energy relative to those of the canonical (major) form observed in the building block, so that they are rarely observed in most biological processes. This could be partially explained on the basis of the energetic and structural properties of the NAB system. For example, the energy gap between the canonical form and the next lowest energy tautomers of uracil and thymine is very large, but for the other NABs (cytosine and guanine) they have several energetically similar tautomers which can be detectable in the gas-phase study. However, the N7H tautomers of guanine and adenine can not be employed in the building blocks of life due to the fact that sugar is attached to the position of N9, as shown in Figure 1.3. The same is true for the tautomers of cytosine, uracil, and thymine where the hydrogen in the N1 position must be substituted by a sugar moiety. Although the canonical forms make the dominant contribution for the building blocks, knowledge of the energetics, and structures of the rare tautomers can provide useful information about the intrinsic stability of various tautomers of NABs and give an insight into mutations.

One of the challenges in this field is related to the increasing difficulty of volatilizing these species as the molecular size increases. Helium nanodroplet methods have an advantage here, given that relatively low pressures ($10^{-6} - 10^{-5}$ Torr) are needed to dope the droplets. The correspondingly lower temperatures therefore reduce the likelihood that the molecules will thermally decompose [70, 72, 80, 84]. In addition, solvation in helium ensures that the molecules are cooled to the ground vibrational state, a condition that is not always met using free jet expansions [85]. In fact, the cooling rate experienced by a molecule captured by a droplet is so fast (as high as 10^{16} K/sec. [15]) that the isomer distribution characteristic of the oven temperature is likely quenched into the droplets. Thus it is possible to observe multiple isomers and tautomers of

biomolecules, even when they have significantly different energies [79, 86–89]. Once again, the high resolution of the method provides us with the means for characterizing these systems.

1.3   Outline

In Chapter 2, a brief review of the experimental setup is introduced. Particularly, a thorough explanation of the vibrational transition moment angle (VTMA), which is a key technique in this thesis, is provided. The main focus of this thesis is on the identification and structural determination of the various tautomers of nucleic acid bases (NABs), namely, cytosine (C), guanine (G), uracil (U), thymine (T), and adenine (A), and their mono–hydrated complexes formed in helium nanodroplets. In Chapter 3, six different tautomers of cytosine were assigned using the measured VTMAs. The data presented therein clears up some puzzles arising from the previously published experimental results in both the gas-phase and in matrices. Specifically, a "missing" tautomer of cytosine in the gas-phase has been in dispute since the first gas-phase study of cytosine with microwave spectroscopy almost two decades ago. The work described in this chapter has finally solved this puzzle. In Chapter 4, the first successful infrared laser spectroscopic study of guanine by thermal evaporation is presented. Along with the measurement of VTMAs, an electric field dependent approach for the vibrational bands for each tautomer conclusively assign the four lowest energy tautomers. As a result, a tautomer that was missing in the gas-phase was observed and also the discrepancies in the assignment of the guanine tautomers between the previous gas-phase studies were reviewed and discussed.

Chapter 5 provides the structural information on the uracil and thymine monomer, which reveals that only the global minimum structure of uracil and thymine was observed in this work. Chapter 6 discusses a nonplanarity of adenine, which is supported

by using the VTMA analysis. This work shows the first direct experimental evidence for the nonplanarity of the NABs, which was proposed theoretically many years ago. In Chapter 7, four theoretically predicted uracil–water binary complexes were observed and characterized and the importance of finding a distribution of conformations in the helium droplets is highlighted in this work. In the case of the HCN study, the dipole-oriented structure was the only form in the helium droplets, however, in this study a water molecule simply falls into the potential energy well that is closest to the point where it encounters the uracil molecule. Furthermore, relative intensities of these bands are related to the relative widths of the potential energy entrance channels that funnel into a given minimum. Chapter 8 focuses on the intermolecular interactions of hydrated imidazole complexes, which is very relevant to the study of the mechanism of the ammonia channel, whose neutral condition in the channel shed light on the study of isolated biomolecules in the gas-phase. Finally, a brief summary and outlook of the research direction is provided in Chapter 9.

Chapter 2

Experimental Method

Since the discovery of the formation of liquid helium droplets, many theoretical and experimental investigation of the droplets have been conducted in order to understand their physical and chemical properties. Now, the understanding of the helium droplet properties permits us to choose the appropriate experimental conditions that permit our spectroscopic investigation. The important concepts and techniques of helium droplets experiments are discussed in this chapter. This includes the formation of the helium droplets, the doping the molecules of interest, the pick-up cell, multipass and Stark cells, detectors and finally the laser system. Discussed also is the measurement technique, in particular the vibrational transition moment angles (VTMAs) and the dipole moment curvature, whose techniques are all based on pendular-state spectroscopy.

2.1 Formation of Helium Droplets

Helium droplet beams are produced by supersonic expansion and generated with essentially any size, $10^2 - 10^6$ atom range [90–93], depending on the following critical parameters, nozzle orifice size, nozzle temperature, stagnation pressure of helium gas and the pumping speed of the source chamber pump. In this experimental set up a constant pressure of $50 - 60$ bar was applied behind a 5 μm nozzle at $20 - 21$ K to

produce helium beams with average size droplets of 3000 helium atoms.

The droplets are formed in the early and high pressure portion of the expansion. As the pressure falls below the equilibrium vapor pressure of the droplets, they cool by evaporation. This evaporative cooling of the helium droplets reduces the total energy of the droplets. In the case of ^{4}He the evaporation rate becomes negligible at 0.37 K [22], on the time scale of the flight time through the apparatus. The weaker interaction, characteristic of ^{3}He, makes the corresponding droplets evaporatively cool to 0.15 K [22,94]. The cooling rate of these systems, first reported by Brink *et al.* [22], showed almost no change with the droplet size after 10^{-7} s. During the flight time of the droplets throughout the apparatus helium droplets remain almost at a constant internal temperature of 0.37 K.

Due to the lack of a technique for measuring the droplet size directly, a scaling law for measuring the droplet size was introduced by the Toennies group [43,93] using a mass-spectrometric analysis of the scattered droplets. The size distributions of the droplets are given by a log-normal distribution function, $P_N(N)$ [43]

$$P_N(N) = \frac{1}{N\sigma\sqrt{2\pi}} \exp\left[-\frac{(\ln N - \mu)^2}{2\sigma^2}\right] . \tag{2.1}$$

where μ and σ are the mean and standard deviation of the distribution of the size.

The log-normal distribution function can be normalized, i.e. $\int_0^\infty P_N(N)\ dN = 1$. The distribution has one maximum at:

$$N_{\text{max}} = \exp(\mu - \sigma^2) , \tag{2.2}$$

with

$$P_N(N_{\text{max}}) = \frac{1}{\sigma\sqrt{2\pi}} \exp\left(\frac{\sigma^2}{2} - \mu\right) . \tag{2.3}$$

The qth log-normal distribution can be calculated analytically:

$$\overline{N^q} = \int_0^\infty N^q P_N(N) \; dN = \exp\left(q\mu + \frac{q^2\sigma^2}{2}\right) . \qquad (2.4)$$

The mean droplet size, $\overline{N}$, and the standard deviation, S, of the log-normal distribution function $P_N(N)$ are given by:

$$\overline{N} = \int_0^\infty N P_N(N) \; dN = \exp\left(\mu + \frac{\sigma^2}{2}\right) , \qquad (2.5)$$

and

$$S = \left[\int_0^\infty \left(N - \overline{N}\right)^2 P_N(N) \; dN\right]^{\frac{1}{2}} = \overline{N}\sqrt{\exp(\sigma^2) - 1} . \qquad (2.6)$$

The qth log-normal distribution function can be obtained from equations 2.3 and 2.4:

$$\overline{N^q} = \overline{N}^q \cdot \exp\left(\frac{q(q-1)}{2}\sigma^2\right) . \qquad (2.7)$$

σ and μ are easily obtained as a function of $\overline{N}$ and S by inverting equation 2.5 and 2.6 to yield:

$$\mu = \ln\left(\frac{\overline{N}^2}{\sqrt{\overline{N}^2 + S^2}}\right) , \qquad (2.8)$$

and

$$\sigma^2 = \ln\left(\frac{S^2}{\overline{N}^2 + 1}\right) . \qquad (2.9)$$

The full width at half maximum, $\Delta N_{1/2}$, of the log-normal distribution is determined for a range of nozzle conditions:

$$\Delta N_{1/2} = \exp\left(\mu - \sigma^2 + \sigma\sqrt{2\ln 2}\right) - \exp\left(\mu - \sigma^2 - \sigma\sqrt{2\ln 2}\right) \qquad (2.10)$$

$$= 2\exp(\mu - \sigma^2)\sinh\left(\sigma\sqrt{\ln 4}\right) , \qquad (2.11)$$

and the relative width can be expressed as:

$$\frac{\Delta N_{1/2}}{\overline{N}} = 2\left(\frac{S^2}{\overline{N}^2} + 1\right)^{-\frac{3}{2}} \sinh\left[\sqrt{\ln 4 \cdot \ln\left(\frac{S^2}{\overline{N}^2} + 1\right)}\right] . \qquad (2.12)$$

The empirical scaling law for the mean droplet size, $\overline{N}$, as a function of the scaling parameter, Γ, was developed by Knuth *et al.* [93]:

$$\ln(\overline{N}) = 2.44 + 2.55\ln(\Gamma) , \qquad (2.13)$$

where the scaling parameter Γ was empirically established as

$$\Gamma = K_1^{0.6} K_2^{0.4} , \qquad (2.14)$$

$$K_1 = n_0 v \frac{d}{a_0}\sqrt{\frac{2\gamma}{\pi m}}\left(\frac{T_{ref}}{T_0}\right)^{\frac{3}{4}} , \qquad (2.15)$$

$$K_2 = \frac{p_0}{A}\left(\frac{T_{ref}}{T_0}\right)^{\frac{5}{2}} , \qquad (2.16)$$

where, v, γ, A, and T_{ref} are the atomic volume of helium (27.34 cm^3/mol), the surface tension (0.35 dyne/cm), a vapor pressure constant (7.8 bar) and T_{ref} is given as 3.23 K [93]. The scaling parameters Γ in equation 2.14 are the stagnation temperature, T_0, pressure, p_0. The nozzle size, d, is 5 μm in this experimental setup; the density, n_0; speed of sound, a_0, at stagnation conditions are provided by McCarthy [95]. The standard deviation, S, and the mean droplet size, $\overline{N}$, are found to be approximately

linearly related to each other [96]:

$$S \approx 0.65\overline{N} \ , \tag{2.17}$$

which translates equation 2.6 to:

$$\sigma \approx 0.55 \ . \tag{2.18}$$

Therefore, the full width at half maximum (FWHM) is also derived from equation 2.12, which is also linearly related to the mean droplet size, $\overline{N}$:

$$\Delta_{1/2} \approx 0.87\overline{N} \ . \tag{2.19}$$

If the density of the helium droplets is known and the droplets are assumed to have a spherical shape, the droplet radius can be calculated from the mean droplet size of the droplets, $\overline{N}$.

$$R = r_0 \cdot N^{\frac{1}{3}} \ , \tag{2.20}$$

where, the unit radius, r_0, equals 2.22 Å for ^{4}He and 2.44 Å for ^{3}He [97] if the bulk helium density, 0.0218 Å^{-3}, is used ($V = \frac{4}{3}\pi R^3 = \frac{N}{0.0218}$). For example, the radius of a 3000 helium atom droplet is estimated to be $\sim$32 Å.

The mean droplet size, $\overline{N}$, is calculated from equation 2.13 for the most common source conditions, stagnation pressure (50 – 60 bar) and nozzle temperature (16 – 28 K), and tabulated in Table 2.1. The droplet size distribution, $P_N(N)$, can be calculated using the standard deviation, S, and the predicted mean droplet sizes, $\overline{N}$. Figure 2.1 shows the log-normal distributions for a fixed stagnation pressure of 60 bar and several nozzle temperatures. As shown in Figure 2.1, the droplet size distribution is rather

15

Table 2.1: Mean droplet sizes produced for a stagnation pressure of 50 and 60 bar with 5 micron nozzle and various nozzle temperatures, 16 – 28 K.

T	$\overline{N}$		T	$\overline{N}$	
(K)	50 bar	60 bar	(K)	50 bar	60 bar
16	9700	11600	22	2400	3000
17	7500	9100	23	1900	2500
18	5900	7200	24	1600	2100
19	4600	5700	25	1300	1700
20	3700	4600	26	1100	1400
21	2900	3700	28	750	1000

broad, so that a wide range of sizes are present in the beam for a given mean droplet size. The ability to vary the droplet size is extremely important for studying larger solutes, given that the droplet must have a sufficient heat capacity to accommodate the thermal energy of these species, without the loss of all the helium atoms by evaporation. For spectroscopic studies it is generally best to work with the smallest possible droplets, since by simple conservation of helium, there are fewer droplets when the mean size is large. Fewer droplets means fewer dopant molecules, which translates into low spectroscopic signals, assuming the sensitivity is linearly dependent upon the number of absorbers. Depending upon the nozzle temperature, the droplet velocities [43, 98] typically fall in the range 200 – 400 m/sec (although droplets as slow as 50 m/s have been produced [91]), meaning that in a typical apparatus, with a beam path length of 1 meter, the flight time of the droplets is approximately 2 – 5 msec.

2.2   Doping the Droplets

Although doping foreign atoms and molecules into the helium droplets has already been reviewed in a number of previous papers on helium nanodroplet spectroscopy [5, 32, 99–101], further review is conducted in order to put this thesis in the context
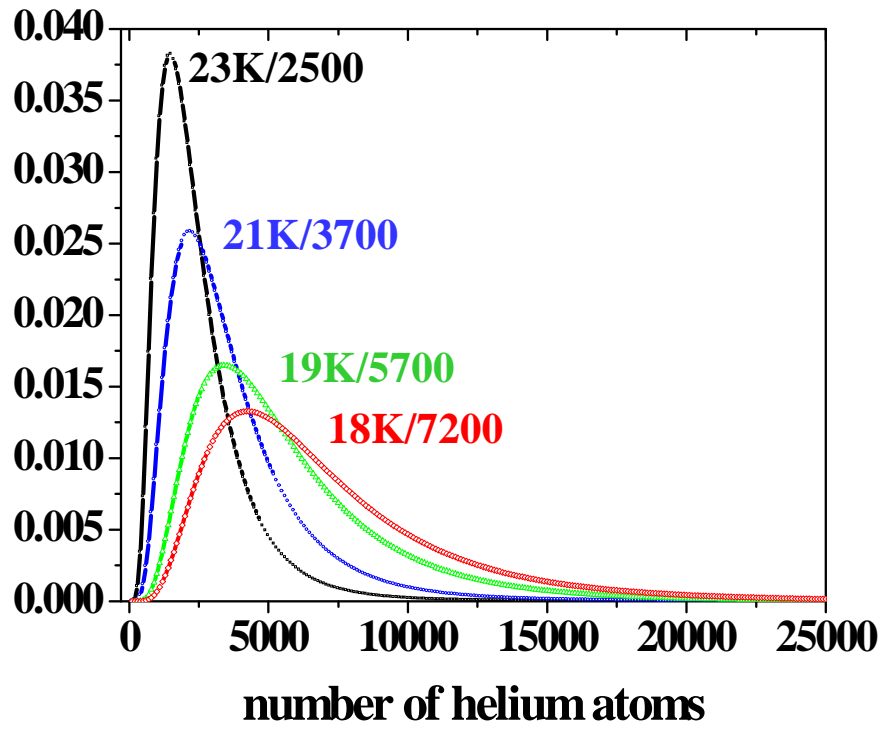
Figure 2.1: Predicted log-normal droplet size distributions for various nozzle temperatures (18, 19, 21, and 23 K) and at a 60 bar stagnation pressure. The corresponding mean droplet sizes are given in Table 2.1.

of focusing on doping biomolecules in the helium droplets. Basically, any molecules can be easily doped into the helium droplets by collisions while they fly through the apparatus because the solubility of the droplets is better than that of vacuum. Since the droplets pick up virtually all gas-phase molecules in their beam path, it is essential to maintain a vacuum of 10^{-7} Torr or less, where the pick-up region is located, to avoid unwanted pick-up of any residual background gases. A detailed explanation of the pick-up methods that has been used for biomolecules and water molecules can be found in Subsection 2.3.1. Upon picking up the foreign molecules, the droplets undergo evaporation of surface helium atoms due to thermal energy transfer from the vibrationally and rotationally hot dopant molecules to the droplets. The number of evaporated helium atoms can be estimated from the binding energy ($E_{bind} \simeq 5$ cm^{-1} = 7.2 K) of a helium atom to the droplet [22]. If the vapor pressure of molecules in the pick-up region is sufficiently high, multiple collisions occur and eventually the successive doping of several foreign molecules can arise, which leads to the formation of van der Waals complexes within 10^{-10} to 10^{-8} s [42].

The cross section of a spherical droplet, σ, is obtained from the classical droplet radius, R, and the bulk unit radius, r_0, given in equation 2.20. We find

$$\sigma = \pi R^2 = \pi r_0^2 N^{2/3} = 15.5 N^{2/3} \ . \tag{2.21}$$

The probability of N number of helium atom droplet that dopes k molecules at given density, η, is obeyed by the Poisson distribution:

$$P_{N,k}(p) = \frac{\beta_N^k}{k!} \exp(-\beta_N) \ , \tag{2.22}$$

where, $\beta_N = \sigma \eta L = 15.5 \eta L N^{2/3}$ from equation 2.21, and L is the length of the pick-up cell. The evaporative loss of helium atoms due to the pick-up process is generally is on

the order of a few hundred helium atoms.

2.3 The Experimental Apparatus

The apparatus used in the present study of biomolecule systems has been discussed in detail elsewhere [102] and is shown in Figure 2.2. A closed cycle helium refrigerator (CTI–Cryogenics, Coldhead model 22 and Compressor 8200) is used to cool a 5 μm diameter nozzle, sealed to the end of a copper tube, to approximately 20 K, measured from a LakeShore Si diode thermal sensor (LakeShore model 321 autotuning temperature controller). The nozzle temperature is controlled with a PID setting of the temperature controller using a Kaptan heater. The nozzle is a platinum disc crimped to a 2" × 1/4" diameter copper tube (Lenox Laser). By expanding ultra-pure helium gas from 50 – 60 bar, droplets with a mean size of several thousand helium atoms, a radius of 3 – 4 nm, are generated [43, 93]. Once formed, the helium droplets pass through a 0.4 mm diameter skimmer into the second pumping station, maintained below 1 × 10^{-6} Torr. This main chamber contains pick-up cells, shown in the Figure 2.2, used to introduce target molecules into the droplets. By maintaining this region at a pressure of 10^{-6} to 10^{-5} Torr of the species of interest, the droplets can be loaded with one or more molecules.

2.3.1 Pick-up Cell and Oven

As shown in Figure 2.2, right after the skimmer, the droplets pass through an oven and a pick-up cell, which is pumped independently from the main chamber by a turbo-molecular pump (Varian, Turbo-V 250). The turbo pump helps unwanted background gas molecules in the pick-up region. In addition to the fixed pick-up cell, a load-lock was implemented to allow for the possibility of inserting an oven without venting the
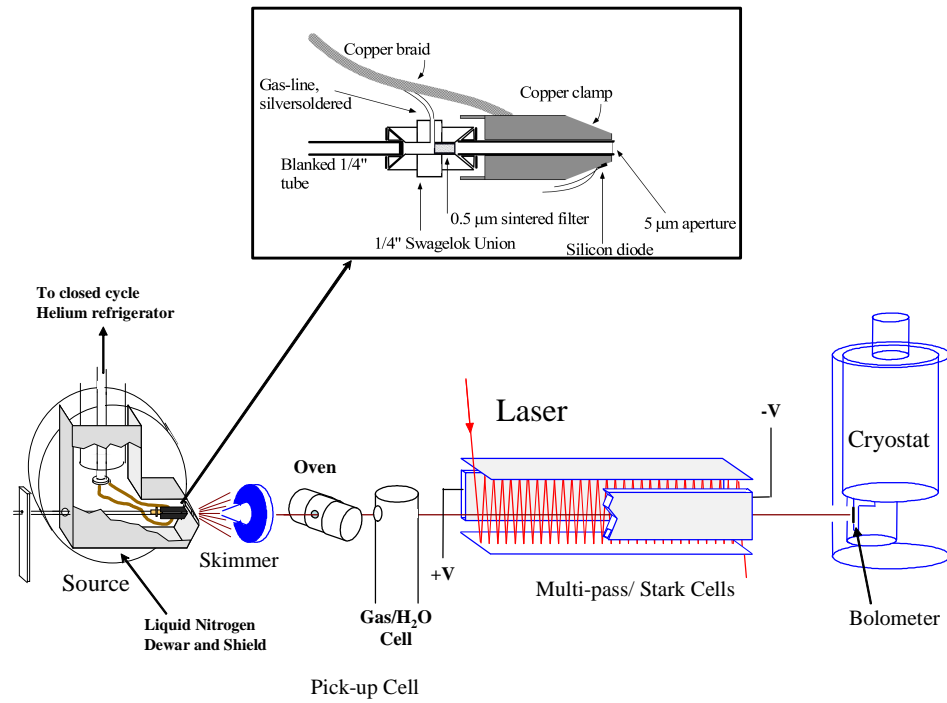
Figure 2.2: A schematic diagram of the helium nanodroplet apparatus [102]. The enlarged view of the nozzle assembly used in the helium droplet experiment is shown in inset. The nozzle is connected to a closed cycle helium refrigerator by copper braids, so that it can be coolded to approximately 20 K.

apparatus for changing samples. Two types of oven, shown in Figure 2.3, have been used for specific experiments in this thesis. In order to maximize the probability of picking up target molecules, the scattering-box oven, shown in Figure 2.3(a), is used most of this work, from Chapter 3 to Chapter 7. However, for molecules which have high vapor pressures, the scattering-box oven resulted in the pick-up of too many molecules, therefore, an effusive oven, shown in Figure 2.3(b), was used in Chapter 8. Both ovens consist of a 3/4" stainless steel tube and the parts shown in Figure 2.3 are all made of copper for a good thermal conductivity with the cartridge heater. The tip of the scattering-box oven is blanked and two holes (2 mm) are clear for the droplet beam to pass through. For the effusive oven, the tip of the effusive oven, 1 mm diameter hole, faces along the droplet beam axis and the end of the oven is positioned just down the helium nanodroplet beams so that the droplets pass by and pick up the target molecules at the exit of the effusive oven.

A second pick-up cell is positioned downstream of the oven in order to add water to the droplets. Because of the high mobility of molecules in the helium droplets, all molecules added to the droplets end up in a complex, located close to the middle of the droplet.

2.3.2   Multipass and Stark Cell

After doping the target molecules, the droplets pass through the laser interaction region, where two highly reflective gold-coated mirrors and two Stark electrodes are positioned. The multipass cell enhances excitation efficiency by multiple interactions $(20-50 \text{ times})$ of the IR laser beam with the doped helium droplets. In this work, a two meter telescope was used to improve the focusing of the spreading laser beam which helped the signal-to-noise significantly.

As shown in Figure 2.2, the laser interaction region is positioned between two Stark
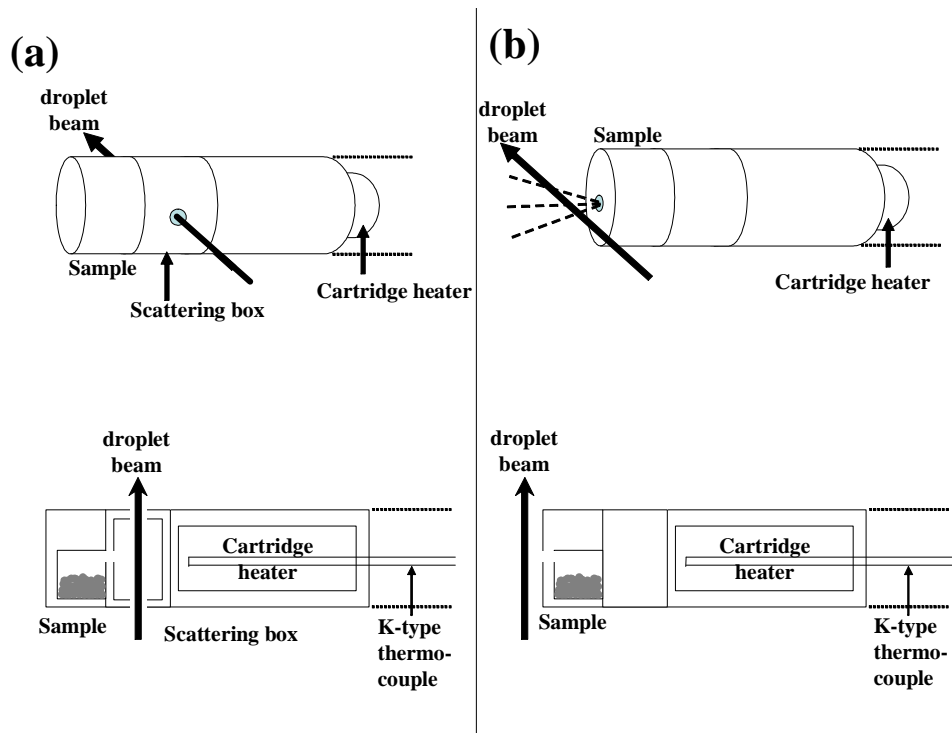
Figure 2.3: Two different types of oven, (a) scattering-box oven and (b) effusive oven, used in conjunction with a load-lock.

electrodes, used to apply a large electric field. Applying a high electric field to the two steel electrodes produces a homogeneous direct current (DC) electric field perpendicular to the droplet beam axis. The distance between the two electrodes can be adjusted from outside of the chamber to align the machine while maximizing the signal. At the high electric fields (80 – 100 kV/cm) and a low temperature typical of our experiments (0.37 K), the interaction energy with the electric field for polar molecules is much larger than kT, such that the molecules between the electrodes become highly oriented. The combination of multipass and Stark cell is essential in the measurement of vibrational transition moment directions [79, 86–89] and dipole moment of several different tautomers [89], in Chapter 4, which contain considerable structural information and provide unambiguous assignments of vibrational spectra.

2.3.3   Detector: Bolometer

A Si/diamond composite bolometer (Infrared Laboratories) is used to detect the total energy in the helium beam. The bolometer element is a semiconductor so that it has a large resistance at cryogenic temperatures due to the removal of thermal energy from the material and the corresponding depletion of electrons in the conduction band. When used as a variable resistor in a simple DC current, changes in the bolometer temperature will be seen as changes in current. These changes in the current are the basis for the use of the bolometer as a detector for optothermal spectroscopy. Detection of the infrared spectrum of a molecule is based upon the fact that the vibrationally excited molecule quickly relaxes back to the ground state as energy flows into the helium. The result is the evaporation of approximately 600 helium atoms, depleting the flux of helium in the droplet beam. This laser induced attenuation of the beam is detected by the bolometer detector.

A small mechanical pump evacuates the helium reservoir in the cryostat, shown in

Figure 2.4, which cools the liquid helium by evaporation to a temperature below the lamda point (2.17 K). The operating temperature of the bolometer (1.6 K) is achieved by further cooling of the superfluid helium.
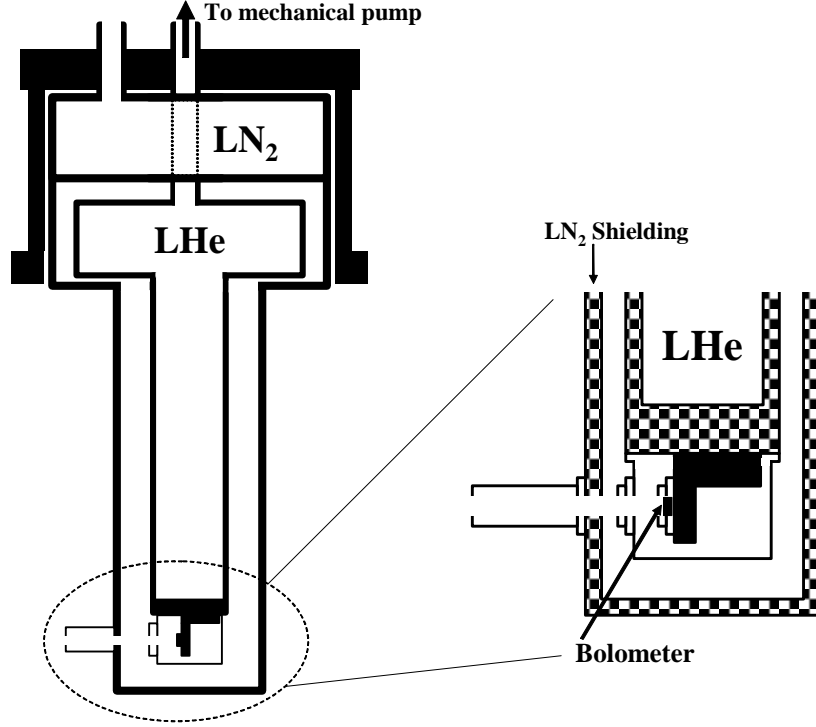
Figure 2.4: Schematic diagram of the bolometer. The enlarged view of the bottom part where the bolometer is attached onto the surface of 1.6 K helium temperature is shown in inset.

A schematic of the bolometer circuit is given in Figure 2.5. The electric circuit is a voltage divider biased with a stable 15 V mercury battery, and a 20 MΩ load resistor. The microphonic and excess input capacitance are greatly reduced by placing the preamplifier (LN-6C JFET), a low-noise voltage amplifier, near the bolometer so that the Johnson noise is minimized. The JFET and bolometer specifications are listed in Table 2.2.

Table 2.2: Specifications of the bolometer and JFET, a preamplifier.

Bolometer	
Type	Si/diamond composite
Operating temperature	1.6 K
Collector	2×5 mm diamond
Thermal Conductivity	11.02 μW/K
Resistance (1.6K)	62.6 MΩ
Load resistor	20 MΩ
Sensitivity	7.60×10^5 V/W
NEP	3.96×10^{-14} W/$\sqrt{Hz}$
Noise	42.6 nV/$\sqrt{Hz}$ at 20 Hz
	29.8 nV/$\sqrt{Hz}$ at 200 Hz

LN-6C JFET	
First Stage	Remote at cold surface
Voltage Gain	200 and 1000 $\pm$ 5 %
Input Impedance	$> 1 \times 10^{13}$ Ω
Output Impedance	< 500 Ω
Frequency Response	0.75 Hz to 30 KHz
Maximum Output	$\pm$ 7V
Power Requirements	$\pm$ 9V
Shorted Input Noise	5 nV/$\sqrt{Hz}$
Size	6.5" $\times$ 3" $\times$ 4" wide
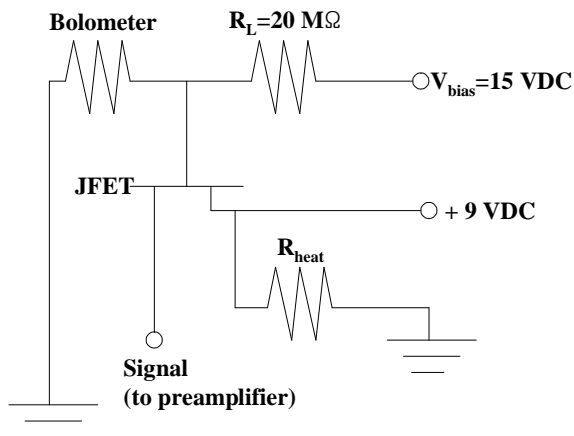
Figure 2.5: Schematic of bolometer electric circuit.

2.3.4 Laser System

The laser system used in this thesis is a periodically poled lithium niobate (PPLN) optical parametric oscillator (OPO) from Linos Photonics (OS 4000). The OPO generates three laser beams, one signal and two idler beams. The signal has a power of up to 40 mW and is tunable in the wavelength range of 1.45 – 2.0 μm. Each idler beam provides tunable infrared light form 2.3 to 4.0 μm and has a power up to 60 – 80 mW and can be used to vibrationally excite a wide range of molecules containing C–H, N–H and O–H stretches.

The OPO (Linos Photonics – OS 4000) is shown in Figure 2.6. An OPO consists of a nonlinear crystal, PPLN, inside an optical linear cavity pumped longitudinally by a diode-pumped continuous wave (cw) Nd:YAG laser. The PPLN crystal splits the pump beam into a signal and idler beams so that the optical cavity has to be resonant

for one or both of the OPO beams. The sum of the frequencies of the signal and the idler frequencies is equal to the pump frequency due to the energy conservation law: $\omega_p = \omega_s + \omega_i$. The OPO frequencies are obtained from the phase matching condition inside the PPLN crystal by changing the temperature of the crystal. The overall tunability range of wavelengths of 2.3 to 4.0 μm for the OPO beams can be obtained from several different ways, as detailed below.
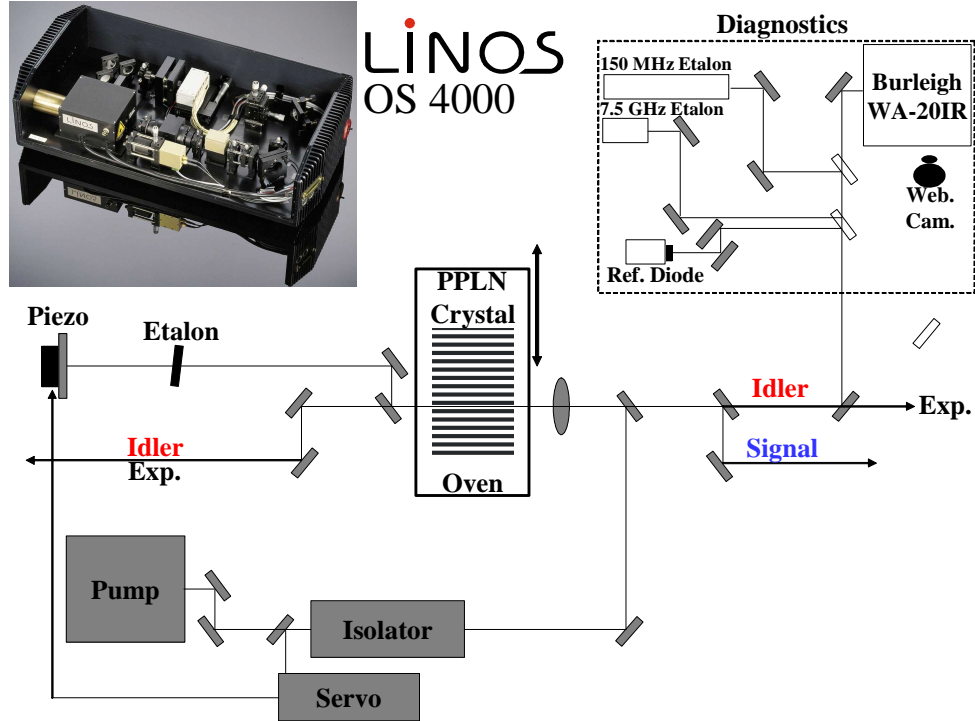
Figure 2.6: Schematic of Linos PPLN–OPO and diagnostic etalons and wavemeter used for spectral calibration purposes. The idler laser beam is used for experiment with the apparatus in Figure 2.2. The web camera is for reading out the numbers from the wavemeter.

A rough tuning is performed by changing the poling period of the PPLN crystal, which has 33 different poling periods. The frequency range of each poling period, about 100 cm^{-1}, covers about 20 % of those of the neighboring poling periods. The frequency ranges of the every poling periods are listed in Table 2.3.

Fine tuning is obtained by varying the PPLN crystal temperature and/or tilting the

Table 2.3: The frequency range for each poling period of a PPLN temperature range from 155 to 180 Celsius

Poling Period	Signal frequency (cm^{-1})		Idler frequency (cm^{-1})	
	T = 155 °C	T=180 °C	T = 155 °C	T=180 °C
1	5455.54	5146.68	3941.66	4251.70
2	5580.36	5361.93	3816.79	4035.51
3	5659.31	5485.46	3738.32	3912.36
4	5753.74	5605.38	3646.97	3792.19
5	5824.11	5698.01	3573.98	3699.59
6	5892.75	5770.34	3505.08	3628.45
7	5955.93	5844.54	3442.34	3553.66
8	6013.23	5913.66	3384.09	3484.32
9	6066.12	5973.72	3331.67	3424.07
10	6112.47	6029.54	3285.15	3368.14
11	6163.33	6082.73	3234.15	3315.10
12	6203.47	6131.21	3194.38	3266.37
13	6250.00	6176.65	3147.62	3222.17
14	6284.96	6222.78	3112.65	3174.91
15	6327.91	6266.06	3069.74	3131.56
16	6360.11	6301.20	3037.48	3096.45
17	6395.09	6341.56	3002.55	3056.05
18	6430.45	6376.33	2967.18	3021.33
19	6459.95	6409.02	2937.63	2988.55
20	6492.24	6443.71	2905.37	2953.86
21	6521.88	6476.26	2875.79	2921.33
22	6548.79	6505.76	2848.84	2891.84
23	6575.49	6535.52	2822.15	2862.54
24	6602.40	6562.54	2795.40	2853.03
25	6626.91	6589.35	2770.70	2808.28
26	6653.80	6616.38	2743.86	2781.25
27	6678.24	6643.19	2719.39	2754.44
28	6702.41	6667.56	2695.20	2730.08
29	6724.05	6691.65	2673.58	2705.92
30	6745.36	6713.21	2652.24	2684.42
31	6769.56	6737.64	2628.05	2659.93
32	6791.17	6759.04	2606.47	2638.59
33	6810.13	6780.58	2587.46	2617.05

Table 2.4: Free spectral range (FSR) of the etalons

Etalon thickness (mm)	Free spectral range (FSR) (cm^{-1})
0.5	5.46
0.4[a]	6.83
0.3	9.10
0.21	13.00
0.19[b]	14.37

[a] used in this work.
[b] used in free O–H stretch region $(3700 – 3750 \text{ cm}^{-1})$.

intracavity etalon. Each poling period of the PPLN crystal has a specific temperature tuning range, 155 – 180 °C, so that during the temperature scan the amplification profile of the optical parametric process shifts slowly in frequency. Decreasing the temperature results in an increasing signal frequency and a decreasing idler frequency. During the temperature scan the idler frequency mode hops to the mode distance of the OPO cavity (0.5 – 0.6 GHz) or to the free spectral range (FSR) of the intracavity etalons, which is listed in Table 2.4. In this thesis, most of scans were done using a 0.40 mm etalon, except for the free O–H region where a 0.19 mm etalon was used. The etalon is used because the amplification bandwidth of the parametric process is very broad so that a lot of OPO cavity modes have almost the same amplification. It is possible to select a specific mode of the OPO cavity with the etalon, so that a mode hop scan is accomplished by tilting simultaneously the etalon while changing the PPLN crystal temperature.

A continuous tuning is also possible by varying the temperature (frequency) of the pump laser. The continuous tuning range of the pump laser without mode hops is about 8 – 10 GHz at maximum. The continuous scan is not necessary for the work

described in this thesis because of the broad band characteristics of the biomolecules, for which the mode hop scan (~ 500 MHz) gives sufficient spectral resolutions.

A series of diagnostic etalons and wavemeter was used to calibrate the spectra. A 7.5 GHz free spectral range confocal etalon is used to monitor the mode structure of the laser and to aid in high resolution scanning. Laser frequencies are measured by a wavemeter (Burleigh WA-20IR), a device that measures transmission fringes from the OPO and a He–Ne laser standard and uses the standard to calibrate the frequency of the infrared laser. The frequency resolution of the wavemeter is 0.01 cm^{-1}, sufficient for the modes of the biomolecules studied in this thesis.

2.4   Pendular-state Spectroscopy

The high resolution and low temperatures characteristic of helium nanodroplet spectroscopy makes it ideal for the application of pendular-state spectroscopy [103–106]. This term comes from the fact that polar molecules behave as the quantum equivalent of a pendulum when placed in a DC electric field, given that the dipole tends to become oriented with the field. The higher the electric field and lower the rotational temperature, the better oriented the molecules become. In the gas-phase, this approach has been used to orient molecules in the laboratory frame for both photodissociation [107–109] and cross molecular beam experiments [110–119]. At high temperatures, the fields required to achieve significant orientation are often impractically high. However, at the low temperatures associated with helium nanodroplets, strong orientation can be achieved with even modest electric fields (< 50 kV/cm). Indeed, for most polar molecules in helium, the interaction between the dipole moment and the DC electric field (μE) is much larger than the rotational energy. A detailed examination of the corresponding states and selection rules [103, 120] reveals that, for a parallel band (transition moment parallel to the permanent electric dipole moment)

the entire ro-vibrational spectrum collapses into a single transition when the laser polarization direction is aligned parallel to the DC electric field. The corresponding signal enhancement is even more dramatic if one considers that in this polarization geometry the transition dipole moment is also better aligned (on average) with the laser electric field, in comparison with the isotropic, zero-field case. This field induced pendular transition appears near the vibrational origin of a given vibrational band and so is often referred to as a field induced Q branch. Figure 2.7 shows the corresponding configuration, namely with the two Stark electrodes straddling the laser excitation region, along with a series of spectra for cyanoacetylene (a linear polar molecule) [121]. The spectrum starts out at zero-field as a relatively weak band, showing P and R branches. The field induced Q branch quickly dominates the spectrum as the field is increased. As discussed in detail elsewhere [120] the pendular Q branch transition is actually composed of a number of transitions that, in the pendular limit, have approximately the same frequency (assuming that the vibrational dependence of the dipole moment and the rotational constant are small [120, 122]). In this case, the entire population can be pumped with a single frequency, accounting in part for the high intensity of this transition.

At more moderate fields, Stark spectra can also be recorded for helium solvated molecules and complexes, from which the magnitude of the permanent dipole moment can be determined [37]. As discussed in detail elsewhere [123], the dipole moment determined from such studies is slightly different from that of the gas-phase molecule, owing to the fact that the solvent cage is in general not exactly spherical. As a result, the polarization of the solvent surrounding the molecule results in a net dipole moment that can either enhance (oblate symmetric top) or diminish (prolate symmetric top) the dipole from that of the isolated molecule [123]. However, given that this effect is generally quite weak ($< 10\%$ of the molecular dipole), a simple correction factor can
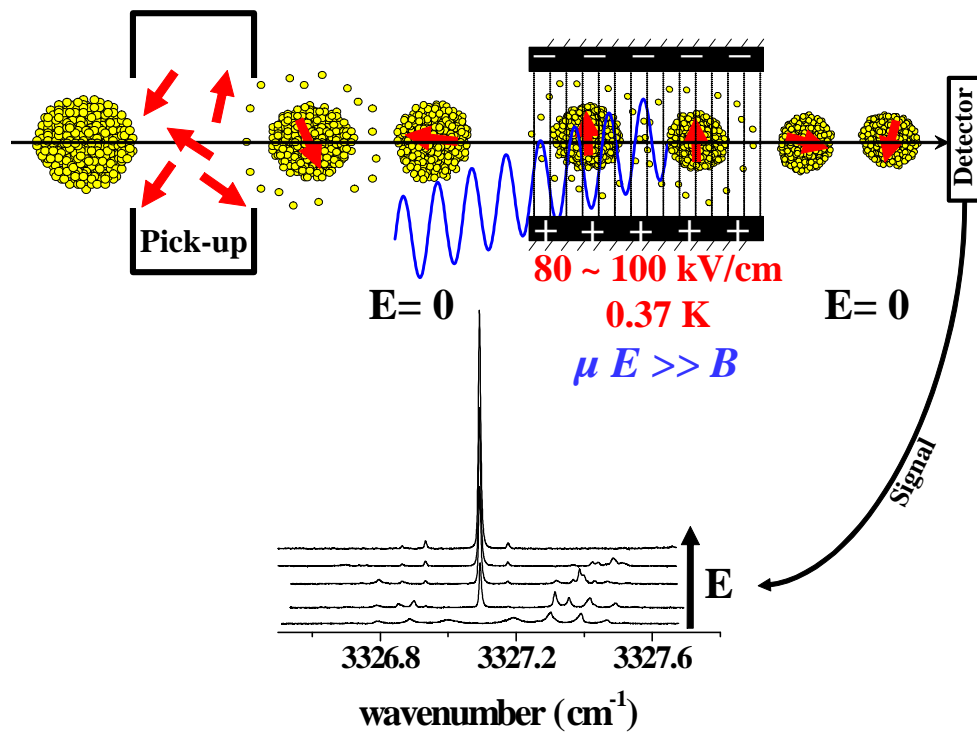
Figure 2.7: A schematic diagram showing the geometry used for pendular-state spectroscopy. The laser electric field is aligned parallel to the DC electric field, the latter being used to orient the electric dipole moment of the helium solvated molecules in the laboratory frame. The lower set of spectra shows the evolution of the IR spectrum of cyanoacetylene from the field free (P and R branches) to the pendular (Q branch only) regimes.

be applied to quite accurately determine the dipole moment of the isolated system. This correction is applied for many of the systems we have studied in helium [124–127], given that the analogous gas-phase species have not been previously observed, so that comparisons can be made with *ab initio* theory.

2.5   Vibrational Transition Moment Angle (VTMA)

The orientation of polar molecules in the laboratory fixed frame has a number of important advantages, discussed in Section 2.4. In addition, however, we have found that this approach can be used as a structural tool for molecules. In particular, we are interested in the application of this method to the study of isolated or water solvated biomolecules [79, 86, 87, 89]. The approach is based upon the fact that the vibrational transition moment associated with a given vibrational mode is a vector quantity that points in a well-defined direction in the molecule fixed frame. Likewise, the permanent dipole moment has a well-defined direction, defining a unique angle between the two, for each molecular vibration. In the case of high frequency H–X stretches, where the modes are quite local in character, the transition moments are often (approximately) along the associated bonds. This is illustrated along the top of Figure 2.8 for N–H stretching vibrations for three of the tautomers of guanine, for example, having transition moments (dashed arrows) that are approximately parallel to the N–H bonds (red double arrows). As a result, the measurement of a set of such angles for a number of different vibrational modes of a molecule can provide detailed structural information that can be compared directly with *ab initio* calculations of the same quantities. Since these vibrational transition moment angles (VTMAs) are defined in the molecule fixed frame, their experimental measurement requires orientation of the molecule in the laboratory frame. In the limit of pendular behavior, the polarization dependence of the vibrational band intensities can be used to measure these VTMAs [79, 86, 87, 89].
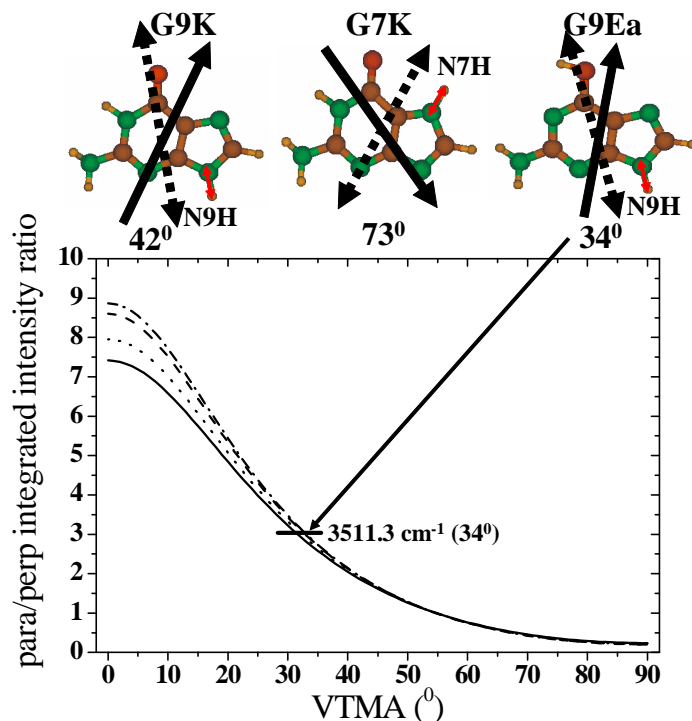
Figure 2.8: The polarization ratio, $\rho(\alpha)$, obtained from equation 2.27 (see text) for the G9Ea tautomer of guanine (top right). The *ab initio* constants, $\mu_p = 3.11$ debye, $A = 0.063668$, $B = 0.037634$, and $C = 0.023668$ cm^{-1}, were used to determine the dipole distribution function, $P(\cos\theta)$ (equation 2.23), resulting in the solid curve for $\rho(\alpha)$. In comparison, the dotted, dashed and dot-dashed lines were obtained by reducing the rotational constants by factor of 1.5, 3.0, and 6.0, respectively. The experimental VTMAs are determined for the heavy rotors by comparison to $\rho(\alpha)$ with A, B, and C as the *ab initio* values divided by a factor of three, accounting for the solvent induced increase in the rotor's effective moment of inertia. Even if the rotational constant correction factor is changed by a factor of two (reduced by factor of six), only a small change in the VTMA, α, is observed, with the error increasing for more parallel bands. Also shown are the permanent dipole moment (solid arrows), and transition dipole moment (dashed double arrows) directions for three of the guanine tautomers. The transition dipole moment vectors shown are all approximately parallel to the N–H bonds involved in the vibrations (red solid arrows).

The directions of the permanent dipole, μ_p, and the transition dipole, μ_t, are shown in Figure 2.9. The direction of the permanent dipole is set to be the z axis in the molecular frame and their transition dipole moment is set to be within the x and z plane so that the the angle, VTMA (α), is formed with the permanent dipole moment. The φ and χ are azimuthal angles in the laboratory and the molecular frame. The transition dipole can be represented by the vector that spins on the corn formation with z axis, which is on the other hand spinning on the corn with θ angle in the laboratory frame, shown in Figure 2.9 [128].
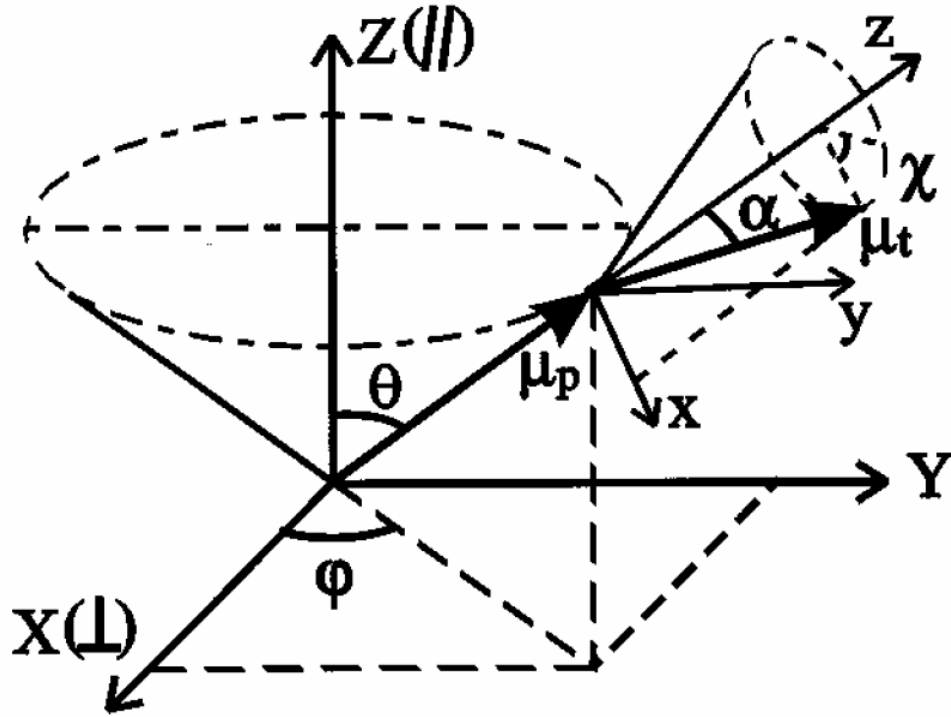
Figure 2.9: Coordinate system of a molecule with a permanent dipole and transition dipole moment in the laboratory frame and the moleuclar frame. In the molecular frame, the permanent dipole is set to be the z axis, and the azimuthal angle of the transition dipole is set to $0\,^\circ$. In the laboratory frame, the orientation electric field is chosen to be the Z axis, and the two laser polarizations are defined on the XZ plane. This figure is taken from ref. [128].

The quantitative analysis of the experimental data requires that the degree of dipole

orientation in the electric field be accurately determined. At finite electric fields, this distribution of orientations can be calculated using the approach discussed by Kong *et al.* [128–131] and is dependent upon the rotational states that are populated in the droplets, which is determined by the rotational constants and the droplet temperature. However, since the present experimental spectra are broadened beyond the rotational contour, the sensitivity of the orientation distribution to the rotational constants is rather muted. As a result, we find that the *ab initio* rotational constants, divided by a factor of three to account for the effects of the helium [99], can be used to determine accurate VTMAs. This is largely the result of the fact that the rotational temperature is well determined in these experiments (namely, the droplet temperature of 0.37 K [18,22]). In detail, the normalized orientation distribution is then given by:

$$P(\cos\theta) = \int_0^{2\pi} P\left(\cos\left(\theta,\varphi\right)\right) d\varphi = \frac{1}{2}\left(1 + \sum_{n=1}^{\infty} a_n P_n\left(\cos\theta\right)\right) , \qquad (2.23)$$

where:

$$\begin{aligned}
a_n &= \left(n+\frac{1}{2}\right)\sum_M N_M \sum_\tau e^{-E_{\tau M}/k_B T} \sum_{J_1,J_2,K,s_1,s_2} C^{\tau M}_{J_1 K s_1} C^{\tau M}_{J_2 K s_2} \\
&\times \left[1+(-1)^{s_1+s_2+J_1+J_2+n}\right](-1)^{M-K} N_k \\
&\times \frac{\left[(2J_1+1)(2J_2+1)\right]^{\frac{1}{2}}}{2}\begin{pmatrix} J_2 & J_1 & n \\ M & -M & 0 \end{pmatrix}\begin{pmatrix} J_2 & J_1 & n \\ K & -K & 0 \end{pmatrix} , \qquad (2.24)
\end{aligned}$$

and $\begin{pmatrix} J_2 & J_1 & n \\ M & -M & 0 \end{pmatrix}$ is a 3-J symbol, N_M is the degeneracy for each M value, and N_k is the nuclear statistical weighting factor.

The absorption efficiency for a linearly polarized laser depends upon the angle α between the permanent dipole and the transition moment (a molecular fixed property),

referred to here as vibrational transition moment angles (VTMAs), as well as the angle between the laser electric field and the DC electric field.

The parallel and perpendicular intensities, as a function of α, can be calculated using:

$$A_\parallel(\alpha) = \int_0^{2\pi} d\varphi \int_0^{2\pi} d\chi \int_0^\pi P(\cos\theta) \left[\sin\theta\cos\chi\sin\alpha - \cos\theta\cos\alpha\right]^2 \sin\theta d\theta \ , \qquad (2.25)$$

$$
\begin{aligned}
A_\perp(\alpha) \ &= \ \int_0^{2\pi} d\varphi \int_0^{2\pi} d\chi \int_0^\pi P(\cos\theta)[\cos\varphi\cos\theta\cos\chi\sin\alpha - \sin\varphi\sin\chi\sin\alpha \\
&\quad - \cos\varphi\sin\theta\cos\alpha]^2 \sin\theta d\theta \ .
\end{aligned}
\qquad (2.26)
$$

The polarization ratios are therefore given by:

$$\rho(\alpha) = \frac{A_\parallel(\alpha)}{A_\perp(\alpha)} = \frac{2\int_0^\pi P(\cos\theta)\left[2\cos^2\theta + \sin^2\alpha - 3\cos^2\theta\sin^2\alpha\right]\sin\theta d\theta}{\int_0^\pi P(\cos\theta)\left[2 - \sin^2\alpha - 2\cos^2\theta + 3\cos^2\theta\sin^2\alpha\right]\sin\theta d\theta} \ , \qquad (2.27)$$

or in the limit of infinite electric field

$$\rho(\alpha) = 2\left(\frac{1}{\sin^2\alpha} - 1\right), \text{where } P(\cos\theta) = 2\pi\delta(\cos\theta - 1) \ . \qquad (2.28)$$

The experimental VTMAs (α) are determined from equation 2.27 by measuring the ratio of the integrated band intensities for parallel and perpendicular polarization, normalized using the corresponding field free spectra. The polarization ratio as a function of the VTMA (equation 2.27) is shown in Figure 2.8 for the G9Ea tautomer of guanine along with the experimentally measured VTMA for the N9H vibration ($32 \pm 4°$).

These angles can also be extracted from *ab initio* calculations for direct comparison with the experimental values [79]. Given that a non-linear molecule has 3N–6 vibrational modes, the corresponding VTMAs can provide a great deal of information on both the molecular structure and the assignment of the spectrum. [79, 86, 87, 89].

It is interesting to note that for teracene [132] there was some degree of zero-field alignment in the laboratory frame, resulting in a 10 – 20 % increase in the band intensity with the laser polarization aligned parallel to the droplet beam direction as compared to the perpendicular alignment. It was proposed, and later confirmed [133], that this spontaneous alignment was a result of a fraction of the droplet angular momentum (deposited to the droplet upon pick-up of the droplet) being transferred to the embedded rotor. Clearly this effect would bias the measurement of the experimental VTMAs, since the comparison of the experimental polarization ratio to $\rho(\alpha)$ (see Figure 2.8) relies on the assumption that the zero-field intensity is isotropic without the field. Assuming the solvated molecule was oriented in the laboratory frame to the same degree as was measured for teracene [132], a 10 – 20 % error in the measured $\rho(\alpha)$ would occur, which, depending on the associated constants of the solvated molecule, would lead to an error of about $\pm$ 5°. However, for all the systems reported thus far [79, 86, 87, 89], the zero-field intensities were the same within the experimental error for both polarization alignments, and the error due to any zero-field laboratory frame alignment is likely within the error associated with the measurement of the polarization ratios.

The polarization ratios, $\rho(\alpha)$, are obtained from the "gen_f" program in Professor Wei Kong's Lab at Oregon State University. The program needs some variables for the calculation, such as rotational constants and dipole moment components which are obtained from ab inito calculations and the temperature of the molecule of interest, 0.37 K in our experimental condition. The rotational constants and the dipole moment

components of all molecules studied in this thesis are listed in Table 2.5. As mentioned above, the rotational constants used in this thesis were reduced by a factor of three upon solvation in helium [99]. The variational calculations were converged for all the molecules studied in this thesis by including states up to $J = 15$. The values in Table 2.5 were obtained from ab inito methods (MP2/6-311++G(d,p)) except for uracil and thymine, where MP2/aug-cc-pVDZ calculations were used.

The *ab initio* VTMAs are directly obtained using "Law of Cosines", since the two points (in x, y and z coordinates), permanent dipole moment and transition dipole components, are easily obtained from the ab inito calculations. The *ab initio* VTMAs (shown on top of Figure 2.8 for guanine) for all the molecules in this thesis are shown in each chapter and compared with the experimental VTMAs obtained using the integrated area ratios ($A_{para.}/A_{perp.}$) for the various vibrational bands from three different polarization scans of parallel and perpendicular polarizations to the DC electric field. The zero-field spectrum of each polarization is needed to correct for power differences (normalization) of each laser direction.

2.6 Measurement of Dipole Moment: Field Dependence Experiment

We recently developed a technique that takes advantage of the fact that the dipole moment for the various tautomers of NABs are different. As a result, the dependence of the band intensities on the magnitude of the electric field should be quite different for the various tautomers. In particular, a molecule with a small dipole moment will require a large electric field for complete orientation between the two Stark electrodes, while much lower fields are needed to reach this saturation condition if the dipole moment is large. Figure 2.10 shows the theoretical changes in the band intensity ratios with

Table 2.5: A summary of information for the VTMA analysis of the molecules in this thesis. The rotational constants and dipole moment components were performed at the MP2 level with a 6-311++G(d,p) basis set.

	Rotational Constant $(\text{cm}^{-1})^a$			Dipole Moment		
	A	B	C	x	y	z
Cytosine^b						
C1	0.0428779876	0.0223736090	0.0147141173	-3.8012	5.0603	0.7813
C31	0.0437509384	0.0222283139	0.0147531110	-2.7948	1.7081	0.8730
C32	0.0431043101	0.0224020821	0.0147548089	4.4077	-0.7946	0.8751
C21	0.0424747669	0.0224487534	0.0147213535	0.6259	4.7416	-0.2289
C22	0.0427415052	0.0222348895	0.0146597063	0.8430	2.1936	-0.1221
C4	0.0431353427	0.0220419113	0.0146090823	-7.6318	-0.5041	0.8871
Guanine^c						
G9K	0.0212340434	0.0123810420	0.0078298776	-2.7025	-5.5839	0.8187
G7K	0.0212253151	0.0124434708	0.0078565227	-0.8683	1.3360	1.0007
G9Ea	0.0212225329	0.0125446732	0.0078892543	-0.5658	-2.9033	0.9478
G9Eb	0.0212987549	0.0125861975	0.0079162353	-2.1167	-3.3365	0.9392
G7Ea	0.0210897355	0.0125742960	0.0078838962	1.0455	4.0925	0.8202
G7Eb	0.0209412304	0.0125793117	0.0078701967	-3.6544	3.4087	0.8709
Uracil^{d,e}						
UK	0.0426907111	0.0221086887	0.0145655021	-1.1975	4.2113	-0.0010
UE12	0.0428393831	0.0221269069	0.0145906907	-4.7060	4.4277	0.0014
UE14	0.0427926307	0.0222565545	0.0146414825	1.7834	4.4960	0.0000
UE32	0.0432227500	0.0220057751	0.0145818123	2.8950	0.8710	-0.0003
Thymine^{d,e}						
TK	0.0351630453	0.0153944991	0.0107718807	-1.0488	-4.2134	0.0000
TE12	0.0355987474	0.0154069711	0.0108183096	2.4845	-5.5578	0.0003
TE14	0.0350356214	0.0155784866	0.0108497191	4.0214	-3.4037	0.0000
TE32	0.0353237400	0.0154053722	0.0107921959	-1.8714	-1.7152	0.0000
	(Continued)					

(Continued)	Rotational Constant $(\text{cm}^{-1})^a$			Dipole Moment		
	A	B	C	x	y	z
Adenine^f						
A9	0.0262076606	0.0174539581	0.0104823255	-2.5886	-0.7880	0.8034
A7	0.0263881347	0.0171565630	0.0104119134	0.1300	-6.6097	0.7201
A3	0.0260977289	0.0175517781	0.0104991728	-3.3891	2.1905	0.6796
A1	0.0256203301	0.0177476183	0.0104984934	-8.2989	-1.9473	0.9452
A9Ia	0.0262085613	0.0172838146	0.0104194719	1.8955	-3.3549	-0.0676
A9Ib	0.0260183816	0.0173106198	0.0104017964	0.5749	4.5400	-0.0667
A7Ia	0.0263563515	0.0171411212	0.0103940243	-0.1814	3.3651	0.1995
A7Ib	0.0259924881	0.0174612209	0.0104505268	-2.9796	2.3679	0.0497
Uracil-Water^g						
UW1	0.0405463455	0.0108418137	0.0085830409	-2.9263	2.4600	-0.9537
UW2	0.0242616069	0.0150643146	0.0093143202	-1.8373	-4.1384	0.7757
UW3	0.0246288093	0.0149213488	0.0093118462	-3.0592	-2.2147	0.7899
UW4	0.0242616069	0.0150643146	0.0093143202	-0.8286	2.6111	0.7523
Imidazole^h						
IM	0.0541409777	0.0517371333	0.0264558900	1.8963	3.4862	0.0041
IMD	0.0537505426	0.0050346941	0.0050220853	9.4266	-0.5059	1.7333
IMD1	0.0531957346	0.0051969232	0.0047388434	0.0064	-0.0004	-0.0661
IMD2	0.0523693516	0.0053636021	0.0048774183	2.2806	-2.1487	-0.3051
IMD3	0.0520097901	0.0055150226	0.0049965654	0.0016	0.0001	-0.0198
IMW1	0.1053157834	0.0187299328	0.0160073684	-6.6330	0.7183	0.0001
IMW2	0.1029859547	0.0195745484	0.0166504321	-5.5203	-0.8795	1.1937

^{a} The rotational constants are reduced by factor of three (see context).

^{b} For a naming scheme, see Chapter 3.

^{c} For a naming scheme, see Chapter 4.

^{d} For a naming scheme, see Chapter 5.

^{e} The values of uracil and thymine are obtained from the MP2/aug-cc-pVDZ calculations.

^{f} For a naming scheme, see Chapter 6.

^{g} For a naming scheme, see Chapter 7.

^{h} For a naming scheme, see Chapter 8.

different electric fields between the two Stark electrodes for 19 different bands obtained from the "gen_f" program for the G9K (red) and G7K (black) tautomers of guanine. In this calculations, however, the polarization ratios of parallel polarization to zero-field ($A_{para.}/A_{zero}$) are used instead of parallel to perpendicular polarization ($A_{para.}/A_{perp.}$) used in the VTMA analysis. Since most of vibrational bands of biomolecules studied in this thesis are broad and their $\Delta\mu$ is very small, we can park the laser on top of the broad bands and start measuring the intensities with different electric fields. However, for the rotationally resolved molecules, the application of this technique would be difficult unless the calculations account for all of rotational states. Furthermore, experimental difficulties accompanied with the rotational bands would be obstructive.

In Figure 2.10, the calculated curvature of the polarization ratios of the two tautomers are quite different, due to their quite different dipole moments, G9K (6.26 D) and G7K (1.88 D). The comparisons with experimental results will be given in Chapter 4. The combination of these dipole curve measurements and the VTMA assignments is very useful in characterizing and assigning structures of various tautomers and very complex bands associated with large biomolecules.
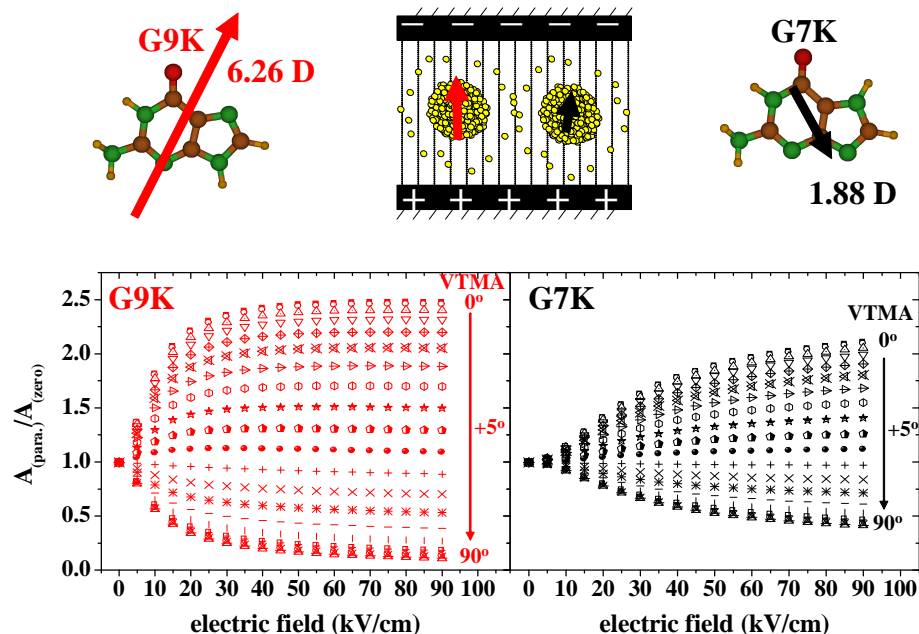
Figure 2.10: Calculated polarization ratios, $A_{(para.)}/A_{(zero)}$, of the G9K (red) and G7K (black) tautomers of guanine with increasing the electric field between the two Stark electrodes (shown on top center) for 19 different ($0-90°$ with a $5°$ gap) bands obtained from the "gen_f" program. The *ab initio* constants for each tautomer, dipole moments and rotational constants, listed in Table 2.5, were used to in the calculations. The graphs clearly show that the curvature of the polarization ratio, $A_{(para.)}/A_{(zero)}$, with different dipole moments are very different, which will be tested with experimetnal results for the various guanine tautomers in Chapter 4.

Chapter 3

Multiple Tautomers of Cytosine Identified and Characterized by Infrared Laser Spectroscopy in Helium Nanodroplets: Probing Structure and Energetics Using Vibrational Transition Moment Angles

Infrared laser spectroscopy in helium nanodroplets is used to identify and characterize several distinct tautomers of cytosine. The experimentally observed species correspond to the lowest energy structures obtained from *ab initio* calculations, also reported here. The assignment of the infrared vibrational bands in the spectra is aided by the measurement of the corresponding vibrational transition moment angles (VTMAs), which

are also calculated using *ab initio* methods. In the present study we confirm the existence of three primary tautomers, as well as provide tentative assignments for even higher energy forms of cytosine in helium nanodroplets.

3.1 Introduction

Isolated nucleic acid bases (NABs) continue to be the subjects of intensive experimental [59, 61, 76, 134–136] and theoretical [74, 137–143] study. In part this is the result of the role that the rare tautomers play in causing alterations in the normal base pairing (mutation), as first noted in the landmark paper by Watson and Crick [144]. It was hypothesized that mutagenesis is correlated with the frequency of occurrence of these rare tautomers. A detailed understanding of the structures, relative stabilities and rate constants associated with the equilibrium between the various tautomers is clearly important for understanding the mechanisms for mutation [74].

Theoretical studies of the tautomers of the NABs far outnumber the corresponding experimental studies. Indeed, in recent years the *ab initio* studies of these systems have converged and there is general agreement concerning the energy ordering of the various tautomers [145, 146]. Interest in benchmarking these calculations against experiment has driven the study of these systems in "isolation", namely in the absence of a solvent. True isolation requires experiments done in the gas-phase, under collision free conditions. Considerable progress has been made in this direction using molecular beam techniques, often based upon laser spectroscopic approaches [59, 61, 80, 147]. For thermally stable species a simple oven can be used to vaporize the molecules of interest, while for less stable species laser vaporization methods can be used in conjunction with a free jet expansion [80], the latter being used to cool the molecules so that the resulting spectra are sufficiently well resolved to permit detailed analysis. Microwave [59], infrared [80, 147], and visible/UV [61, 148] spectroscopies have been used to study NABs

in the gas-phase, providing a wealth of data on these systems. Nevertheless, for systems which show significant population of more than one tautomeric form, there is still a lack of agreement on which are being observed experimentally.

Low temperature matrix isolation spectroscopy has been used in the study of these systems [149–153]. This approach has he advantage that high concentrations can be built up by long, slow depositions. Although the interactions with the matrix can be quite weak, particularly when using argon or even neon to provide the isolation, there is some evidence that the associated intermolecular interactions are sufficient to change the tautomer distribution [134] from that observed in the gas-phase. Such effects are even stronger for NABs in the crystalline solid [77, 134], or in aqueous solutions [136]. The other difficulty with traditional matrix isolation spectroscopy is that the resolution is often limited, preventing the observation of closely spaced bands, making the assignment of some of the bands questionable.

In recent years there have been considerable advances in the use of helium nanodroplets as an ideal matrix for infrared spectroscopy [4, 18, 36, 154, 155]. The weak interactions between the helium and the molecule of interest result in small vibrational frequency shifts and high spectral resolution. Indeed, the infrared spectra obtained in helium are essentially unperturbed from that of the gas-phase molecule, the solvent shifts typically being fractions of a wavenumber [18, 36, 156–158]. The fact that these shifts are small compared to the accuracy of *ab initio* vibrational frequency calculations, helium nanodroplets spectroscopy is an ideal isolation method [4]. The temperature of the droplets is also very low (0.37 K [18, 22]), thus providing the necessary cooling for such spectroscopic studies.

In a recent paper [79] we reported helium nanodroplets studies of a number of NABs, using infrared laser spectroscopy. The high resolution obtained in the associated spectra enabled us to identify three distinct tautomers of cytosine. This preliminary study also

discussed a method for measuring vibrational transition moment angles (VTMAs) (the angles between the vibrational transition moment vectors and the permanent dipole moment of the molecule), which provide unambiguous assignments of the vibrational bands to specific tautomers. We also showed that these VTMAs are highly sensitive to the molecular structure, providing the first conclusive experimental evidence for the non-planarity of adenine [79]. In this chapter we report a more complete study of the tautomers of cytosine using the helium nanodroplet approach. The assignment of the observed spectra is based upon both the vibrational frequencies of the N–H, O–H, and NH_2 stretches and their associated VTMAs [79]. Improved signal levels have been realized using a periodically poled lithium niobate optical parametric oscillator (PPLN–OPO) [159, 160], which allows us to detect even higher energy tautomers.

As noted above, the recent theoretical work on cytosine provides us with detailed information on the ordering of the various tautomers. Figure 3.1 shows the lowest energy tautomers, calculated herein at the MP2/6-311++G** level of theory (see below). There are only a few of the fourteen that have been identified by *ab initio* calculations [138, 139, 161]. As noted above, the previous experimental studies are not in complete agreement, some indicating the existence of two tautomers [61, 134, 162, 163], while others have observed three [59, 79]. It is not entirely clear whether these differences arise from the methods used to prepare the samples or if the effects of the local environment (vacuum, matrix, solid, solution etc.) significantly change the tautomer distributions. Even in the gas-phase studies, the effects of the free jet expansion are not fully understood.

Microwave studies of gas-phase cytosine have revealed three different tautomers of cytosine, yielding three sets of rotational constants [59]. This study did not include results for multiple isotopomers, so that an independent determination of the molecular structures could not be obtained. As a result, the structures were obtained by
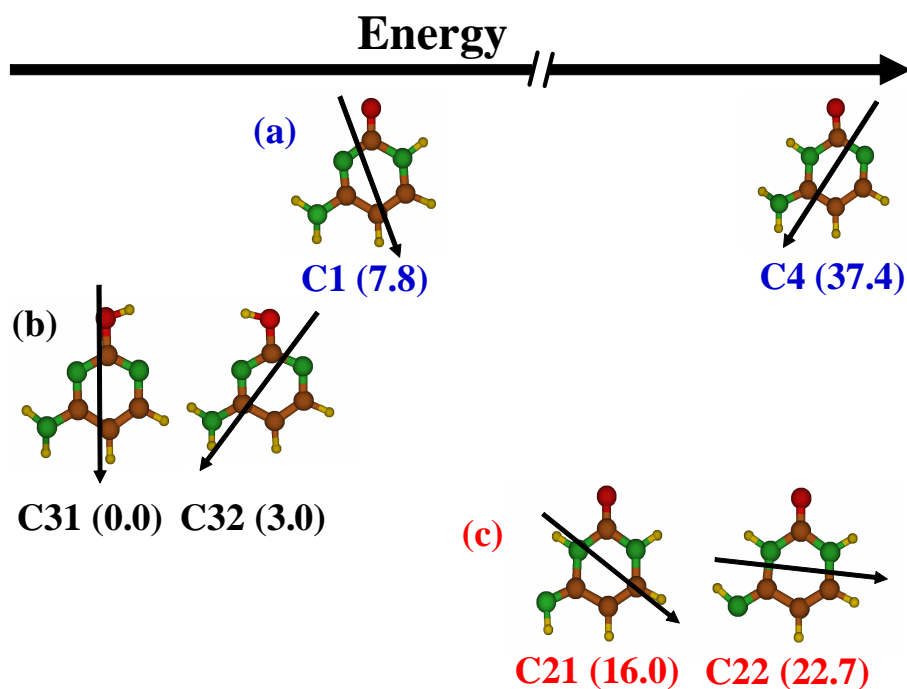
Figure 3.1: The *ab initio* structures and relative (to the C31 tautomer) energies in kJ/mol. The numbers in parentheses are for the six lowest-energy tautomers of isolated cytosine. The *ab initio* calculations were performed at the MP2/6-311++G** level. The solid arrows show the calculated directions of the permanent electric dipole moments. (a) Amino-oxo; (b) amino-hydroxy; (c) imino-oxo.

comparing the experimental rotational constants with those obtained from quite low level *ab initio* calculations (based upon today's standards). These comparisons lead the authors to conclude that they had observed the amino-oxo (C1), amino–hydroxy (C31), and imino-oxo (C21) forms [59] (see Figure 3.1). Two amino-oxo tautomers (C1 and C4) have been observed in aqueous solution [136], while the amino-oxo (C1) and amino–hydroxy (C31) forms have been identified in conventional solid matrices [134]. In this case, the overlap of the vibrational bands from the different tautomers makes the assignment of the spectra somewhat inconclusive, requiring that comparisons be made with the spectra of simpler pyrimidines, as well as with *ab initio* calculations. This assignment was further supported by experiments on the UV processing of the matrix, which helps to separate the contributions to the spectrum from the two tautomers [134, 162]. As shown below, the helium nanodroplet studies provide definitive structural assignments that help to unify the results from these other experiments.

3.2   Experimental

Infrared spectra of cytosine, isolated in helium nanodroplets, have been obtained using the apparatus described in detail previously [102]. Helium nanodroplets represent a nearly ideal spectroscopic matrix [4], providing high-resolution spectra that are completely devoid of hot bands. In addition, the vibrational frequencies are essentially unshifted from those in the gas-phase. Nanodroplets with a mean size of 3,000 helium atoms were formed by expanding ultrahigh pure helium (99.9999%) from a 5 μm diameter orifice, operated at 50 atm pressure and a temperature of 20.5 K. Cytosine molecules were added to the droplets by pick-up [164] in an oven, the temperature of which was optimized for the capture of a single molecule ($\sim$210 °C). Upon being captured by the droplets, the cytosine molecules are quickly cooled to the temperature of the droplets, namely 0.37 K [18, 22].

The infrared laser used in the present study is a commercially available Periodically Poled Lithium Niobate Optical Parametric Oscillator (PPLN–OPO) from Linos Photonics. The laser is directed into a multipass cell [102], used to improve the excitation efficiency by having many laser-droplet beam crossings. Vibrational excitation of the solvated molecules results in the evaporation of several hundred helium atoms. The resulting laser induced decrease in the energy of the droplet beam is detected by a bolometer detector [165], positioned downstream of the laser interaction region. The laser beam is amplitude modulated and phase sensitive detection of the bolometer signal is used to make the spectra essentially background free. However, the high power (60 mW) associated with the PPLN–OPO resulted in some scattered infrared light being detected by the bolometer, which is at the same modulation frequency as the droplet beam depletion signal. Several steps were taken to minimize the effects of the scattered light. First, the diamond collector on the bolometer was partially covered by a gold coating, used to reflect the infrared radiation away from the active element of the bolometer, resulting in a reduction in the scattered light signal by a factor of approximately five. The remainder was removed using a modulation scheme mentioned in a paper by Lehmann and co-workers [166]. In particular, we take advantage of the fact that the velocity of the droplet beam is rather low, such that there is a significant difference between the arrival times at the detector for the light and the droplets, originating from the laser interaction region. At a modulation frequency of 350 Hz (for our experimental configuration) the scattered infrared signal is $90°$ out-of-phase with the droplet depletion signal, so that optimizing the phase for the latter permits the rejections of the scattered infrared signal.

In a number of previous helium nanodroplet experiments [37, 108, 155, 167] we have shown that the dipole moment of a solvated polar molecule can be strongly oriented by a large DC electric field. For this purpose, we positioned electrodes on either side

of the laser interaction region. The laser electric field direction was then aligned either parallel or perpendicular to the DC electric field. When the applied field orients the dipole moment of a molecule, the excitation efficiency depends upon the direction and magnitude of both the vibrational transition moment and the laser electric field. As a result, the angle between the vibrational transition moment and the permanent electric dipole moment could be obtained by measuring the polarization angle that maximizes the band intensity. Alternatively, the signal levels can be measured with the laser polarized parallel and perpendicular to the electric field, compared with that in the absence of the field. A quantitative analysis of this data requires an accurate characterization of the orientation distribution of the permanent dipole moment at the relevant electric field strength, which can be done using the methods discussed in detailed by Kong and co-workers [128–130]. Given that the spectra presented here are not rotationally resolved [79], a thermal population of the pendular states of the molecule [128], corresponding to the rotational temperature of the droplets (0.37 K [18]) was used to calculate the normalized permanent dipole moment orientation distribution $P(cos\theta)$, in equation 2.23 on page 36.

The absorption efficiency for a linearly polarized laser depends upon the angle α between the permanent dipole and the transition moment (a molecular fixed property), referred to here as Vibrational Transition Moment Angles (VTMAs), as well as the angle between the laser electric field and the DC field. This is illustrated in Figure 3.2(a), where the effects of the applied electric field are shown for a vibrational band that has a VTMA near zero degrees. For the laser electric field polarized parallel/perpendicular to the DC field, the integrated intensity of the associated vibrational mode is increased/decreased upon application of the field. In contrast, Figure 3.2(b) shows the case where the VTMA is near $90°$, where the behavior is reversed. At intermediate angles the effects of the electric field are more muted and at the magic angle,

namely 54.7°, the band intensity is independent of the field [168].

The parallel and perpendicular intensities, as a function of α, can be calculated using equation 2.24 and 2.25. The polarization ratios are therefore given by equation 2.27.
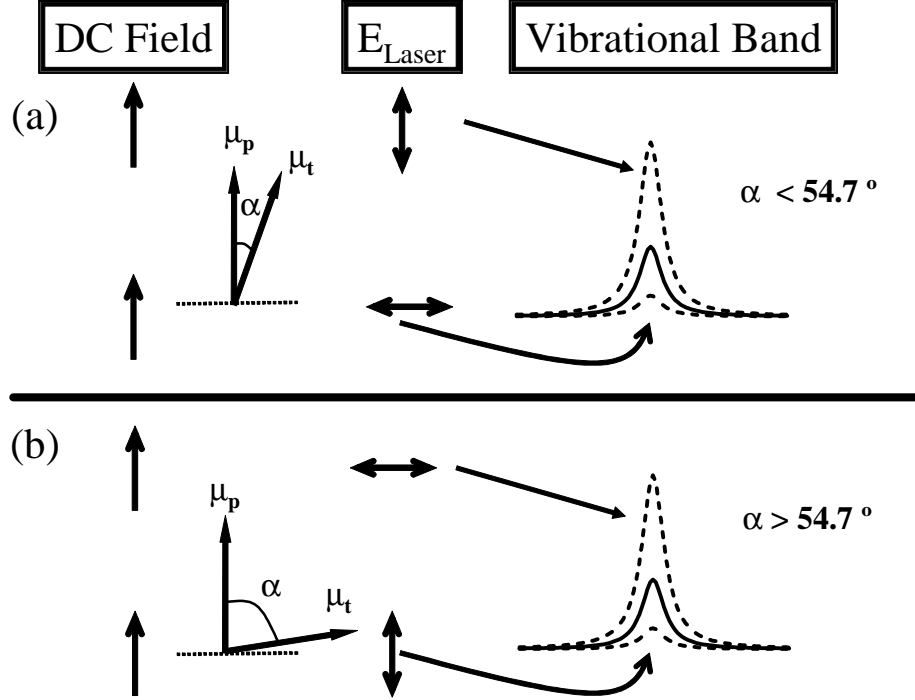
Figure 3.2: A schematic showing the effect of a DC electric field on the vibrational band intensity, for different VTMAs (α) and as a function of the laser polarization direction (parallel or perpendicular), relative to the DC electric field. The DC field orients the permanent dipole moment (μ_p), modifying the interaction between the laser field and the vibrational transition moment (μ_t). The spectra represented by the solid lines represent those obtained at zero field. In all cases, the bands are represented by Lorentzian line shapes.

The experimental polarization ratio can be obtained by integrating the area under the corresponding vibrational bands, for both parallel and perpendicular configurations, normalized using the corresponding field free spectra. The experimental VTMAs reported here were determined by comparing these ratios with those obtained from equation 2.27. Given that a non-linear molecule has 3N-6 vibrational modes, the cor-

responding VTMAs can provide a great deal of information on both the molecular structure and the assignment of the spectrum [79].

3.2.1   *Ab initio* Calculations

Although a number of previous *ab initio* calculations have been reported for cytosine, VTMAs were not quoted in any of them. As a result, we carried out extensive calculations to determine the VTMAs using *ab initio* methods, based upon full geometry optimizations and harmonic vibrational analysis using Gaussian 03 [169]. Unless otherwise specified, the calculations reported here were carried out at the MP2 level using the 6-311++G(d,p) basis set. The six lowest-energy tautomers obtained at this level of theory are shown in Figure 3.1, in order of increasing energy. The solid arrows drawn on each of these structures represent the calculated directions of the permanent electric dipole moments. The magnitudes and directions of these dipole moments are important, as they are used in the determination of the orientation distribution at a given applied electric field, as discussed above. The calculated VTMAs for the various vibrational bands of interest here (N–H stretches, NH_2 symmetric stretches (SS), asymmetric stretches (AS) and O–H stretches) are summarized in Table 3.1, along with the magnitudes of the permanent electric dipole moments and scaled harmonic frequencies (see table caption).

3.3   Results

As noted above, there are at least 14 tautomers of cytosine that have been identified by *ab initio* calculations [138, 139], most of which have not been experimentally observed. These tautomers are grouped into three main types, namely the keto (A), enol (B), and imine (C) forms. The goal of the present study is to expand on the experimental

Table 3.1: A summary of the experimental and calculated vibrational frequencies and VTMAs for the various isomers of cytosine.

	Harm.[a] freq. (cm^{-1})	Scaled[a] freq. (cm^{-1})	Exp. freq. (cm^{-1})	IR intensity (km/mol)	Assignment	ab initio VTMA $(°)$	Exp. VTMA $(°)$	μ (Debye)
C1								6.38
	3737.1	3568.9	3572.7	43.2	NH_2 (AS)	6	12	
	3644.2	3480.2	3471.7	93.0	N1H	78	71	
	3604.8	3442.5	3451.7	70.5	NH_2 (SS)	88	74	
C31								3.39
	3832.1	3659.6	3609.7	107.6	OH (COH)	47	43	
	3732.2	3564.3	3572.3	41.1	NH_2 (AS)	26	22	
	3605.0	3442.8	3455.9	59.5	NH_2 (SS)	70	66	
C32								4.56
	3838.5	3665.8	3617.9	96.1	OH (COH)	88	81	
	3730.8	3562.9	3570.9	38.9	NH_2 (AS)	64	61	
	3605.8	3443.5	3457.2	53.8	NH_2 (SS)	29	29	
C21								4.79
	3670.4	3505.2	3550.0	117.0	N1H	68	61[b]	
	3617.8	3455.0	-	64.0	N3H	12	-	
	3542.3	3382.9	-	12.8	N8H	72	-	
C22								2.35
	3670.7	3505.5	3550.0	113.0	N1H	38	61[b]	
	3619.7	3456.8	-	41.9	N3H	25	-	
	3496.1	3338.8	-	9.3	N8H	64	-	
C4								7.70
	3709.5	3542.6	-	35.8	NH_2 (AS)	59	-	
	3608.5	3446.1	-	56.7	N3H	84	-	
	3596.2	3434.4	-	51.8	NH_2 (SS)	23	-	

[a]The *ab initio* calculations were performed at the MP2/6-311++G** level and the scaled frequencies are obtained from the harmonic frequencies, by multiplying them by a factor of 0.955, to qualitatively account for the effects of anharmonicity.

[b]The N1H bands that are tentatively assigned to the experimental peak at 3550 cm^{-1} are not resolved,so that the experimental VTMA is likely a weighted average of the two values

database, in hopes of reconciling the existing experimental studies with those of *ab initio* theory and to provide new insights into these systems.

In our preliminary study of cytosine [79], the focus was on the NH_2 symmetric stretching vibration, where we observed three bands that were assigned to the C31, C32 and C1 tautomers (see Figure 3.1). The assignment was based upon the measurement of the VTMAs for these three bands, which were in excellent agreement with the results of *ab initio* calculations [79]. Figure 3.3a shows a new scan of this spectral region, obtained using the PPLN–OPO, at a sufficiently low oven temperature (196 °C) to ensure that the contribution from cytosine complexes is negligible. For comparison, the spectrum of cytosine in an argon matrix (b) is also shown [134, 162]. The three bands on the low frequency side of the spectrum are those previously assigned to the NH_2 symmetric stretching vibrations of the C31, C32 and C1 tautomers, while the highest frequency band is assigned to the N–H stretch in the C1 tautomer. It is immediately apparent that the resolution in the helium droplet spectrum is significantly better than that of the argon matrix and that the argon matrix shift is significant for the symmetric NH_2 stretch and negligible for the N–H stretch. This differential matrix shift can obviously be problematic in congested spectra, making it difficult to compare the results with *ab initio* calculations. Although there may be (in retrospect) a shoulder in the matrix spectrum indicative of the third band in the helium nanodroplet spectrum, no such assignment was made based upon the matrix data alone.

Figure 3.4 shows three spectra of the NH_2 symmetric stretch and N–H stretch regions, recorded with (a) an applied DC electric field directed perpendicular to the laser polarization direction, (b) no applied field, and (c) an applied DC electric field directed parallel to the laser polarization direction. These spectra were recorded at a somewhat higher oven temperature ($\sim$210 °C) than the one shown in Figure 3.3. The two peaks marked with an * only appear at high oven temperatures, which favors
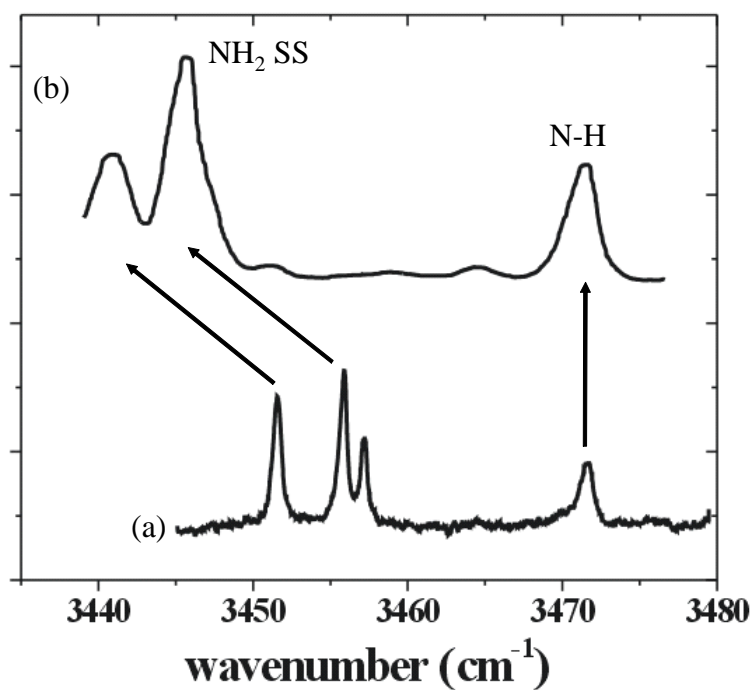
Figure 3.3: A comparison between (a) the helium nanodroplet spectrum and (b) the argon matrix isolation spectrum [134, 162] of the NH_2 symmetric stretch and N–H stretch of cytosine. The three bands in the helium nanodroplet spectrum in the NH_2 (SS) region correspond to the three lowest energy tautomers.

their assignment to the cytosine dimer. Namely, higher oven temperatures result in higher cytosine pressures in the pick-up cell and thus a greater probability for picking up more than one molecule. However, as discussed below, higher energy tautomers are also favored at higher temperatures, so that a definitive assignment of these bands will have to await a more detailed investigation in which the vapor pressure of the sample in the pick-up cell can be varied independently of the temperature, which is beyond the scope of the present study study. The four bands indicated by the arrows all have a temperature dependence that is consistent with the pick-up of a single molecule by the droplets.

The NH_2 symmetric stretching region clearly provides conclusive evidence for the existence of three tautomers, given that each one has only a single band in this region. Nevertheless, we must consider the possibility that a single tautomer could give rise to more than one band in this region due to strong vibrational coupling (such as a Fermi resonance). Fortunately, the experimental and calculated VTMAs discussed below provide additional support for the assignment of these three vibrational modes to three separate tautomers. This is important given that a conclusive assignment cannot be obtained from comparing the experimental and *ab initio* frequencies, owing to the fact that the bands are much closer together than the typical accuracy of the calculations.

It is apparent from Figure 3.4 that the VTMAs for the three NH_2 symmetric stretching vibrations are quite different. Indeed, by carrying out the analysis presented above for these bands, we obtained the experimental VTMAs listed in Table 3.1, namely 78°, 66°, and 29°, in order of increasing frequency. For comparison, the *ab initio* VTMAs for the C1, C31, and C32 tautomers are 88°, 70°, and 29°, respectively. As noted in our preliminary study [79], the *ab initio* VTMAs for these high frequency H–X stretches are rather insensitive to basis set, given that they are mainly determined by the structure of the molecule. For example, an N–H stretch has its transition moment directed
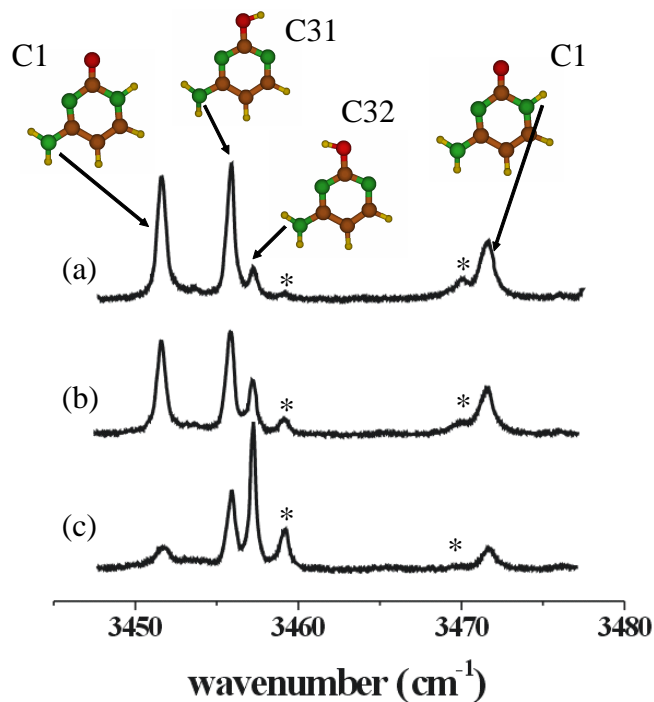
Figure 3.4: Cytosine spectra recorded with an applied DC electric field oriented (a) parallel or (c) perpendicular to the laser polarization direction. Spectrum (b) was obtained in the absence of an electric field. The field and polarization dependences for the various bands in the spectra are clearly have quite different and are used to determine the corresponding VTMAs, which aid in the assignment of the bands to specific tautomers. The bands marked with an * are due to clusters (dimers) of cytosine

approximately along the corresponding bond axis. Actually, Figure 3.5 shows a summary of the *ab initio* transition moment vectors (dashed double ended arrows) and permanent electric dipole moments (solid arrows) for the three tautomers in question. Although there are some deviations from a simple bond axis model for the transition moment directions, the correlations are clearly evident.
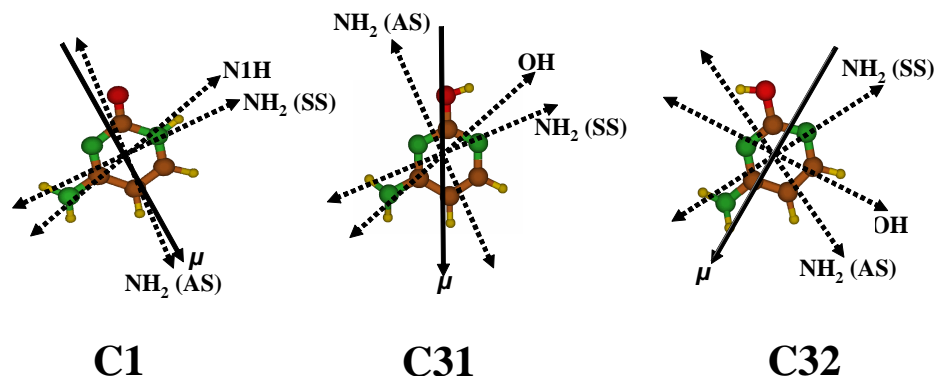
Figure 3.5: The three lowest energy tautomers of cytosine, showing the directions of the permanent electric dipole moments (solid, single headed arrows) and the transition moments (dashed, double headed arrows) for the various vibrational modes of each.

Of the three tautomers presently under consideration, only the C1 structure has an N–H stretching vibration. We can therefore tentatively assign the band at 3472 cm^{-1} to this tautomer. Analysis of the field and polarization dependence of the band intensities in Figure 4 yields an experimental VTMA of 71 °, compared with an *ab initio* value of 78 °, providing further support for this assignment.

We now turn our attention to the region of the spectrum corresponding to the O–H

stretching vibrations. In agreement with our expectations we find two bands in this region, as indicated by the vertical arrows in Figure 3.6. The other two bands, labeled α and β in the figure, are assigned from their oven temperature dependence (see Figure 3.7) to cytosine complexes and tend to disappear at lower oven temperatures. Here again, we find that the field and polarization dependence of the two bands assigned to the cytosine monomer are quite different, one being somewhat parallel and the other being nearly perpendicular. A detailed analysis of these two bands yields the VTMAs listed in Table 3.1, namely $43°$ and $81°$ for the low and high frequency bands, respectively. For comparison, the *ab initio* VTMAs for the O–H stretches of the C31 and C32 tautomers are $47°$ and $88°$, respectively. The agreement is again very good, providing us with a convincing assignment of these two bands. The VTMAs are particularly important here given that the *ab initio* vibrational frequencies for these two bands are quite poor (see Table 3.1), even when scaled to account for anharmonicity. Indeed, the experimental frequencies for the C31 and C32 tautomers are 3609.7 cm^{-1} and 3617.9 cm^{-1}, respectively, while the corresponding scaled *ab initio* values are 3659.6 cm^{-1} and 3665.8 cm^{-1}. Clearly the anharmonic effects for the O–H stretches are quite different from those of the N–H and NH_2 stretches, as noted previously in the literature [170,171].

The final band to be considered is the asymmetric NH_2 stretch, shown in Figure 3.8 as a function of electric field and laser polarization direction. Once again, the band marked with an * is assigned by the oven temperature dependence to be associated with the cytosine dimer, the discussion of which is beyond the scope of the present study. The three tautomers all have an asymmetric NH_2 vibrational mode, so we expect to see three other bands in this region. These three bands are most clearly discerned in the spectrum recorded under parallel polarization conditions (a), with two of the bands being only partially resolved. The vertical solid line shows that the higher frequency band almost completely disappears with perpendicular polarization, suggesting that it is the more
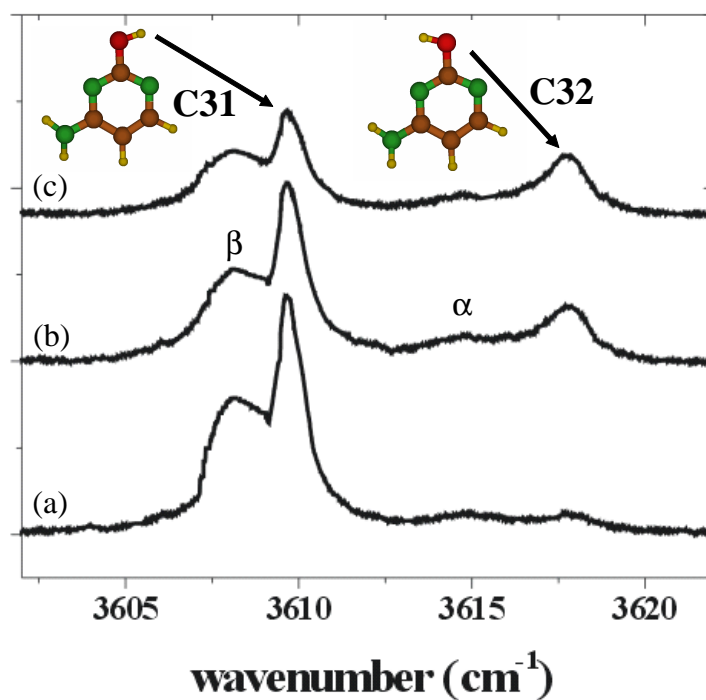
Figure 3.6: Spectra of the O–H stretches of cytosine, assigned to the C31 and C32 tautomers. Spectra (a), (b), and (c) were recorded with parallel polarization, zero-field, and perpendicular polarization conditions, respectively. The two bands marked with a α and β are due to the cytosine dimer.
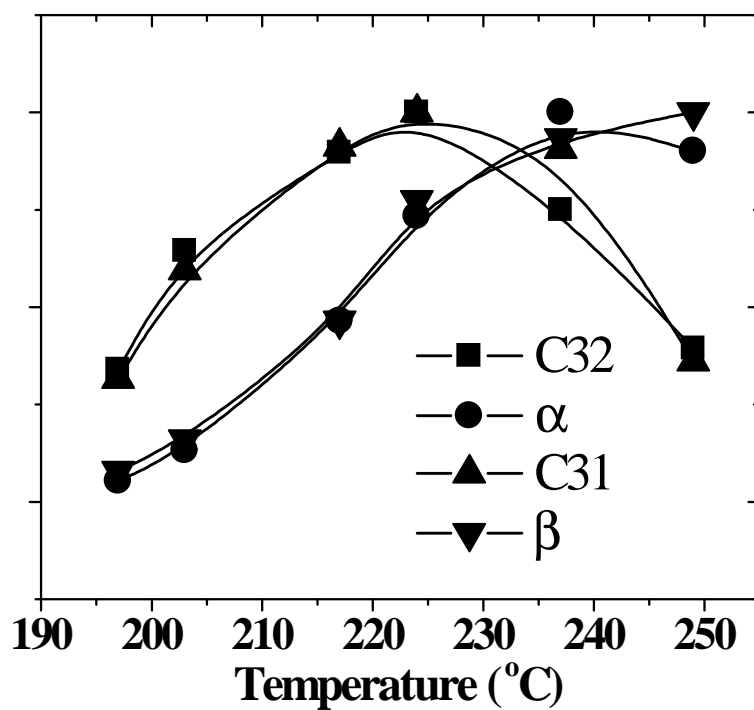
Figure 3.7: The oven temperature dependence of the intensities of the four bands shown in Figure 3.6. The two bands assigned to the C31 and C32 tautomers clearly optimize at lower temperatures, consistent with the fact that lower vapor pressures are required for the pick-up of a single molecule. The other two bands are assigned to the dimer and require higher vapor pressures for optimum signals.

parallel of the two vibrational modes (although both are clearly on the parallel side of the magic angle ($54.7°$)). In contrast, the lower frequency band, which is well separated from the other two, is clearly on the perpendicular side of the magic angle. Analysis of these band, based upon fitting to three Lorentzian line shapes, yielded VTMAs for these three bands of $61°$, $22°$, and $12°$, in order of increasing frequency. The *ab initio* VTMAs for the three tautomers are $64°$, $26°$, and $6°$ for C32, C31, and C1, respectively. The assignment based upon the VTMAs is again unambiguous. It is interesting to note that the assignment based upon the vibrational frequencies is even less obvious in this case. In fact, the *ab initio* calculations suggest that the C31 and C32 tautomers lie very close together and that it is the C1 tautomer that is more separated (actually to the high frequency side of the other two). Here again, the VTMAs are essential for obtaining an unambiguous assignment of the experimental spectrum through comparisons with the *ab initio* calculations. Figure 3.9 shows an overall comparison between experiment and theory for all of the vibrational modes of the three tautomers considered here, along with estimates of the experimental errors. In all cases the agreement is within the experimental uncertainties, giving unambiguous confirmation of these assignments.

Figure 3.10 shows a survey scan of the entire spectral region of interest here, recorded under conditions where the contribution from clusters is quite small, with labels given for the four regions discussed above. It is important to note that we have accounted for all of the high frequency bands of the three tautomers discussed above, which leads us to consider the origin of the weaker bands in the spectrum, emphasized by the oval in Figure 3.10. The two likely assignments for these bands are to either higher order clusters or tautomers with even higher free energies (thus lower abundances). In accordance with the results presented above, it seems straightforward to differentiate between these two possibilities by simply recording the oven temperature dependence of the band intensities and comparing them with the results for the three tautomers
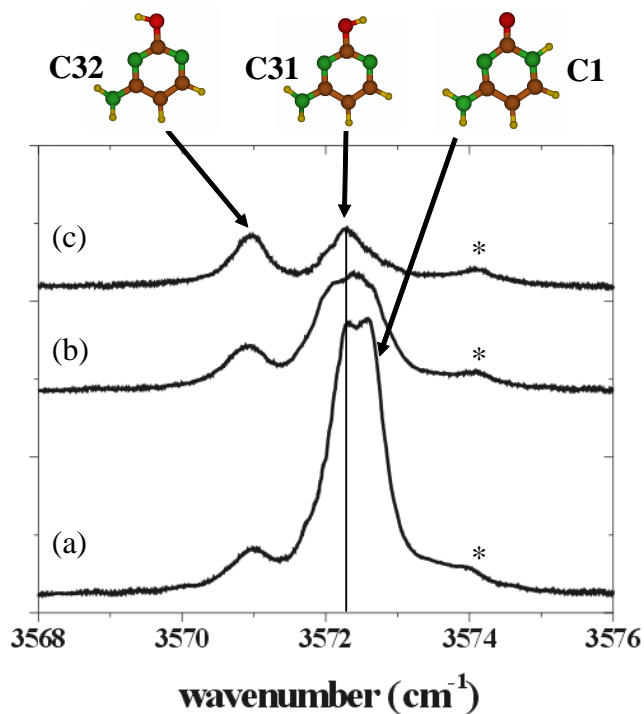
Figure 3.8: Spectra of the NH_2 asymmetric stretches of cytosine, showing the corresponding bands assigned to the C31, C32, and C1 tautomers. Spectra (a), (b), and (c) were recorded with parallel polarization, zero-field, and perpendicular polarization conditions, respectively. The band marked with an * is due to the cytosine dimer. The vertical line is provided as an aid to show that the left component of the closely spaced doublet is the one that disappears more slowly in perpendicular polarization, indicating that the corresponding VTMA is somewhat larger than that for the other component.
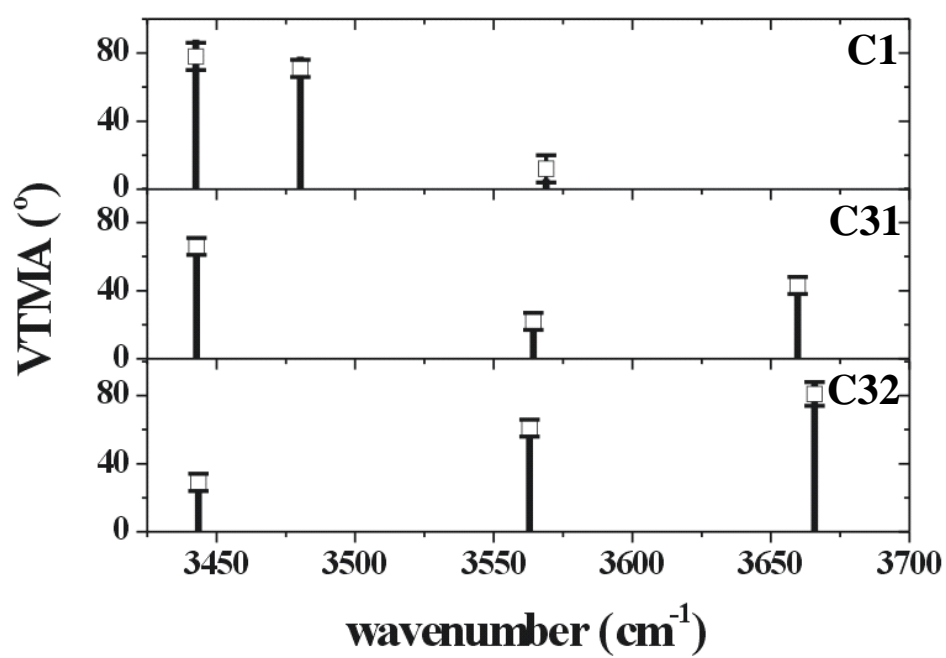
Figure 3.9: A summary of the experimental (open squares and error bars) and *ab initio* (vertical lines) VTMAs for the three tautomers of cytosine, showing the excellent agreement.

discussed above. Unfortunately, since the pressure of cytosine also changes with temperatures, these two variables are not independent in our current oven design. A two stage oven is currently under construction and should help in making the differentiation between higher energy tautomers and clusters. Nevertheless, we can make use of the VTMAs for some of these smaller bands to make some tentative assignments.
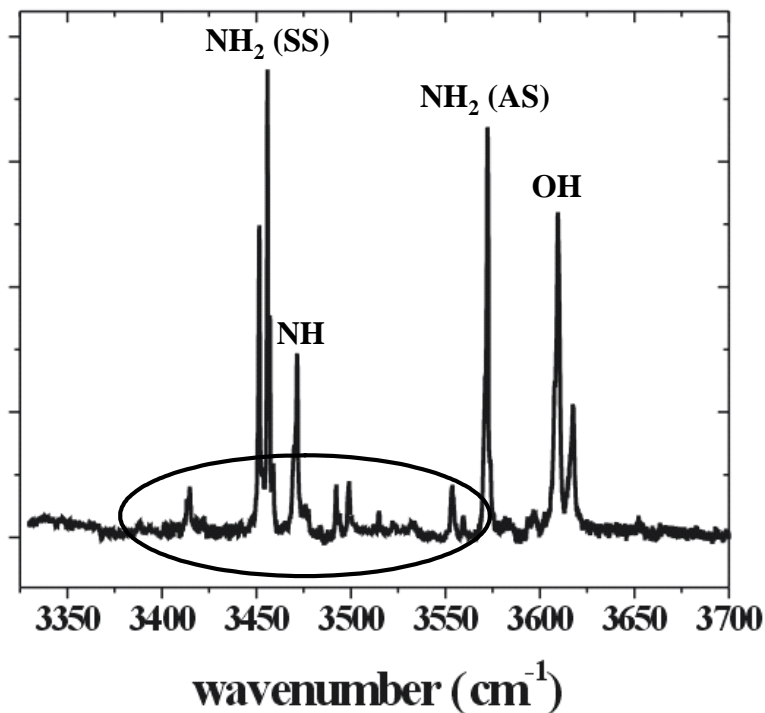
Figure 3.10: An overview of the cytosine spectrum in helium nanodroplets. The oval emphasizes the bands associated with the higher energy tautomers (C21 and C22).

Figure 3.11(b) shows an expanded view of these bands, along with *ab initio* calculations for the next two lowest energy tautomers (Figure 3.11(a)), namely C21 and C22. The *ab initio* frequencies have been scaled by a factor of 0.955 (the same scale factor as used for the other tautomers). The *ab initio* calculations for the C21 and C22 tautomers place the corresponding N1H and N3H vibrations at approximately the same frequency, while the N8H stretches of the two tautomers are well separated. Unfortunately, the latter bands are an order of magnitude weaker than the other two, making

them below our present detection sensitivity. In addition, the N3H bands are predicted to lie very close to the intense bands from the other tautomers. Although there are some weak bands in this region (see expanded spectrum in Figure 3.11(c)), a definitive assignment is currently not possible. The most promising bands for observation in the experimental spectrum are associated with the N1H vibrations of the C21 and C22 tautomers, which have calculated VTMAs of $68°$ and $38°$, respectively. Since the C22 tautomer lies higher in energy than C21, we would expect an overlapped band to be dominated by the latter. Indeed, we find that the band near 3500 cm^{-1}, which is the closest to the *ab initio* calculated frequencies for N1H, has an experimental VTMA of $61°$. This is consistent with the band being composed of mainly the C21 isomer, with a smaller contribution from C22. More convincing evidence for the existence of the C22 and C21 tautomers will require the observation of the two lower frequency N8H bands. We now have new PPLN lasers that have much higher powers that should provide the sensitivity needed to observe these bands. A more thorough study of these higher energy tautomers, including measurements of the corresponding VTMAs and more careful oven temperature dependent studies, is underway and will be discussed in a future paper.

3.4   Discussion

We begin this discussion by pointing out that the previous gas-phase study (microwave spectroscopy) of cytosine characterized three tautomers that survived the free jet expansion [59]. Given the weak interactions involved in the helium nanodroplet experiments, it seems reasonable to expect that the most abundant tautomers would be the same in the two experiments. Although the rotational constants reported in this study are certainly determined to very high accuracy, their assignment to specific tautomers structures is problematic, given that isotopic variants were not studied. As mentioned
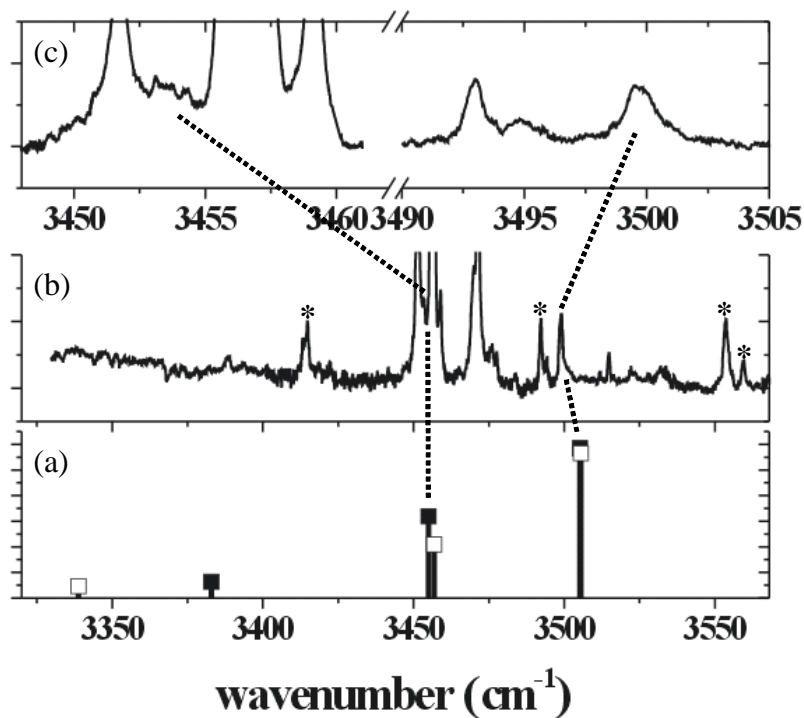
Figure 3.11: A vertically expanded experimental spectrum (b) emphasizing the weaker bands in the spectrum shown in Figure 3.10. The *ab initio* frequencies in (a) have been scaled by a factor of 0.955 (the same scale factor as used for the other tautomers). The filled and open squares correspond to the C21 and C22 tautomer, respectively. The bands marked with an * are as of yet unassigned, but are likely due to either the cytosine dimer or to higher energy tautomers. The spectrum in (c) is a further expansion of the N1H and N3H stretch regions of the experimental spectrum.

above, the authors were forced to determine the corresponding structures through comparisons with the *ab initio* rotational constants, calculated using modest basis sets. The authors of this study assigned the three sets of rotational constants, labeled α, β, and γ to the C1, C31, and C21 tautomers (using the present naming scheme). In light of the present study, which was also based upon the thermal evaporation of cytosine, this assignment is surprising, given that we observe the most abundant tautomers to be C1, C31, and C32, with only minor abundances of C21 and C22.

One possibility is that the cooling experienced by a molecule in liquid helium is sufficiently different from that in a free jet expansion to give rise to quite different tautomers population distributions. However, since the cooling rates are fast in both cases, the most likely outcome is that the tautomers distribution present at high temperatures is simply frozen in by both the helium nanodroplet and free jet expansion cooling. Thus it would take a considerably non-thermal process to give rise to different tautomers distributions in the two cases. More likely is that the assignment of the tautomers based upon the *ab initio* rotational constants obtained in the previous study is not secure. Indeed, the earlier *ab initio* calculations were only carried out at the 3-21G SCF level, with scaling factors for the rotational constants obtained from the study of other systems [59]. Much higher level calculations are now available, making it interesting to revisit these assignments. We have carried out an extensive study of the dependence of the root mean square (RMS) deviations, between the experimental rotational constants and the *ab initio* values, on the basis set size, at the MP2 level. As shown in Figure 3.12, for basis sets which include polarization functions, the C32, C31, and C1 tautomers have the lowest RMS deviations for the α, β, and γ sets of experimental rotational constants, respectively, which is in agreement with the present study. Thus we ascribe the differences between the previous microwave study and the present one to the quality of the *ab initio* calculations in the early work. It is interesting

to note the significant decrease in RMS error as soon as the polarization functions are added to the basis sets. We find that these polarization functions are needed in order to obtain the non-planar geometries for the cytosine tautomers.
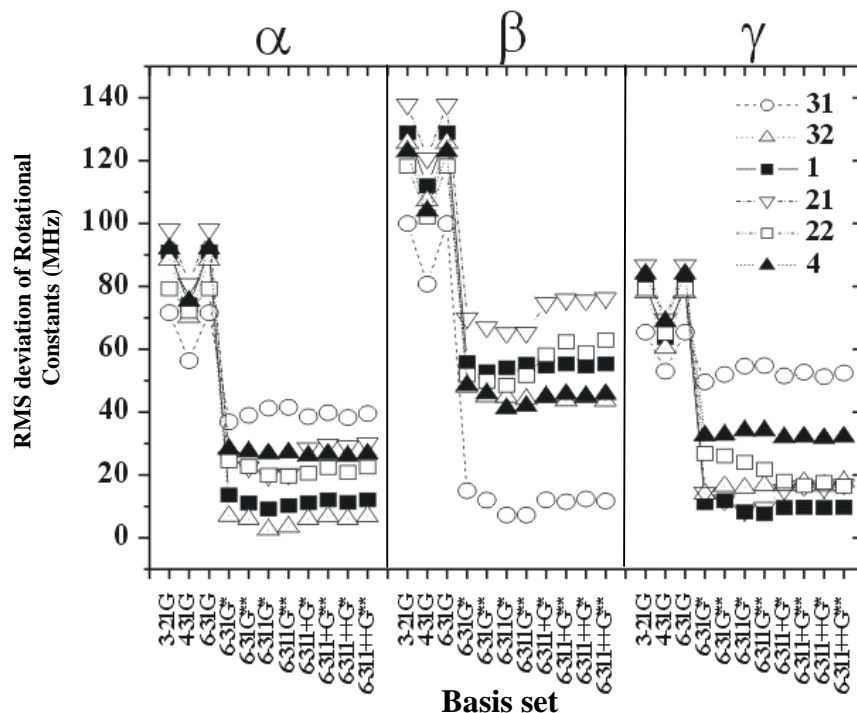
Figure 3.12: A plot of the RMS deviation between the three sets of experimental rotational constants (α, β, and γ) obtained in a previous microwave study [59] and those obtained *ab initio* using various basis sets. From this we conclude that the α, β, and γ data sets are best assigned to the C32, C31, and C1 tautomers, respectively.

The RMS deviations were also calculated using the scaled *ab initio* data given in the earlier study by Brown *et al.* [59] (the scaling of the *ab initio* rotational constants was based upon comparisons with experiment for other molecules, where the assignment was more definitive). Even though they originally assigned the α, β, and γ data sets to the C1, C31 and C21 tautomers, respectively, we found that this unbiased criterion actually gave the best agreement for the C1, C31 and C32 tautomers, in agreement with the present study. In particular, the RMS deviation for the C32 tautomer is slightly less than that of C21. It is also interesting to consider the other *ab initio*

calculations of the rotational constants that have been reported in the literature, using a Dunning correlation-consistent basis set (MP2/cc-pVTZ(-f)) [146] and a Karslruhe basis set (RIMP2/TZVPP) [145]. It is important to note that Hobza and co-workers [145] have also carried out *ab initio* calculations on cytosine using even larger bases sets, extrapolating to the complete basis set limit, but did not report the corresponding rotational constants. We find that the lowest RMS deviation from the α, β, and γ data sets for the MP2/cc-pVTZ(-f) and RIMP2/TZVPP calculates correspond to the C21, C31, and C21 tautomers, respectively. The fact that two different experimental sets of rotational constants correspond best to the same tautomers is clear evidence that these calculations are less reliable. It is interesting to note that Abrams *et al.* [172] also found that for full configuration interaction calculations that the 6-31G** basis set gives better rotational constants for simple diatomic molecules than does the cc-pVDZ basis set. It is our conclusion that the tautomers observed in the microwave study are the same three major tautomers observed in the present helium nanodroplets experiment, namely C32, C31 and C1.

In our first report on the measurement of VTMAs [79] we showed for the case of adenine that these angles are quite sensitive to the detailed geometry of the molecule, in particular to the non-planarity corresponding to the out-of-plane tilting of the NH_2 group, the latter having been predicted previously by theory [173]. We now consider the sensitivity of these VTMAs to the non-planarity of the cytosine tautomers. Figure 3.13 shows the dependence of the *ab initio* VTMAs on the dihedral angles of $H^{13}N^8C^4N^3$ for tautomers C1 (a), C31 (b), and C32 (c), calculated at the MP2 6-311G(d,p) level. The squares, dots, and triangles represent the NH_2 (AS), O–H/N–H, and NH_2 (SS) stretches, respectively. The open symbols are the results from full geometry optimizations and the solid symbols are the results for the various non-planar constraint angles. It is apparent that the VTMAs are again able to distinguish between the planar and non-

planar geometries and that the best overall agreement between theory and experiment occurs very near the optimized geometry, which is to say that the agreement becomes worse for both larger and smaller dihedral angles than that of the optimized structure. It is interesting to note that for all three tautomers, the out-of-plane angles are slightly smaller than that obtained previously for adenine [79], in agreement with the theoretical predictions from Hobza and coworker [173].
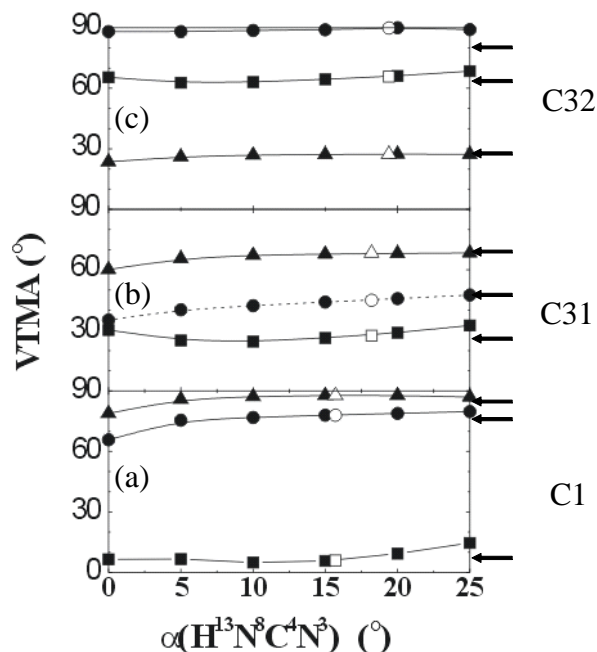
Figure 3.13: *Ab initio* calculations (solid data points) of the VTMAs as a function of the out-of-plane angle of the NH_2 group. The open data points represent the results from full geometry optimizations. The vertical lines emphasize these geometries. The horizontal arrows indicate the experimental values for the corresponding VTMAs.

3.5 Summary

In this study we report high-resolution infrared laser spectra of cytosine monomers isolated in helium nanodroplets. By making use of a DC electric field to orient the

molecules in the laboratory frame of reference, the VTMAs were measured for many of the observed vibrational bands. This has lead to the definitive assignment of three tautomers, namely the C32, C31, and C1 structures shown in Figure 3.1. Preliminary results are also reported for two minor tautomers of cytosine, namely the C21 and C22 structures. A definitive assignment for the latter two will require more careful studies of the temperature dependence of the observed intensities and the detection of two weak bands that were not observed in the present study. In addition, future studies will include the experimental measurement of the permanent electric dipole moments of the various tautomers. The *ab initio* dipole moments summarized in Table 3.1 indicate just how different these values can be for the various tautomers. Re-analysis of the microwave experiments, using better *ab initio* calculations, confirms that the three primary tautomers observed in these earlier experiments are the same three observed here in highest abundance. In future studies we also plan to carry out studies at even higher oven temperatures with the goal of observing more tautomers at even higher energies. Now that we have a method for unambiguously identifying the various tautomers of a given system, the challenge for the future is the development of experimental methods that are compatible with the helium nanodroplet experiment and will enable us to measure their relative energies.

Chapter 4

Four Tautomers of Isolated Guanine from Infrared Laser Spectroscopy in Helium Nanodroplets

Infrared laser spectroscopy is used to study the four lowest energy tautomers of guanine, isolated in helium nanodroplets. The large number of vibrational bands observed in the infrared spectrum are assigned by comparing the corresponding experimental vibrational transition moment angles with those obtained from *ab initio* theory. The result is the conclusive assignment of the spectrum to the N9H–Keto, N7H–Keto, N9Ha–Enol(trans), and N9Hb–Enol(cis) tautomers. The dipole moments of these tautomers are also experimentally determined and compared with *ab initio* theory.

4.1   Introduction

Nucleic acid bases (NABs) are of fundamental importance in biology, forming the building blocks for the genetic code for life [174]. Their various tautomers have been shown to play a central role in mutation [74]. In recent years there has been growing interest in characterizing the isolated systems so that detailed comparisons can be made between

theory and experiment. To date, however, the theoretical studies of these systems have far outpaced the experiments. Nevertheless, there are a growing number of experimental methods that provide at least some information on these important systems, in particular using microwave [59,175–178] and IR–UV laser [80,179] spectroscopic methods. An interesting aspect of many NABs, including guanine, is the existence of various conformers, and a number of gas-phase studies have been directed at identifying these structures and determining their relative energies [69,179–181].

Studies of this type require that the molecule be vaporized, so that gas-phase spectroscopy can be used. Although many of these systems are thermally stable, making vaporization by simple thermal evaporation possible, guanine has proven to be somewhat more challenging. Indeed, Nir *et al.* [182] have recently stated that "Especially guanine cannot be vaporized intactly by simple thermal heating." For this reason, considerable effort has been expended by several groups to make use of laser desorption methods [70,182,183], which suffer less from thermal decomposition [84,184,185].

Because of its thermal instability, guanine is the only NAB for which microwave spectra have not been reported [71]. As a result, the experimental identification of the tautomers of guanine has been attempted exclusively by infrared laser spectroscopy [70,80,182,186–188]. It is interesting to note that even microwave spectroscopy, often considered the most definitive gas-phase structural probe, can have difficulties in distinguishing between the various tautomers for NABs, as we previously demonstrated for cytosine [86]. The gas-phase infrared studies from a number of different laboratories have also produced conflicting structural assignments. Specifically, Mons *et al.* [70] and Nir *et al.* [80,182] have both used IR–UV depletion spectroscopy to study the tautomers of guanine, with conflicting results. Figure 4.1 shows the various tautomers of guanine, which differ in the location of the hydrogen atom attached to the nitrogen atom in position 7 or 9, in their keto and enol forms. In addition, the enol forms have two

rotational orientations of the OH group, which are designated as a and b. Because the naming schemes are not the same, we have introduced a third nomenclature, which is somewhat more systematic than the other two. Nir *et al.* [80, 182] observed spectral features, which they assigned to the G9K, G7K, and G9Ea tautomers, whose structures are shown in Figure 4.1. In contrast, Mons *et al.* [70] reported the observation of four isomers, corresponding to structures of G9K, G7K, G9E(a or b), and G7Ea in Figure 4.1. The disagreement with regard to the assignments of the observed tautomers has not been resolved to date.
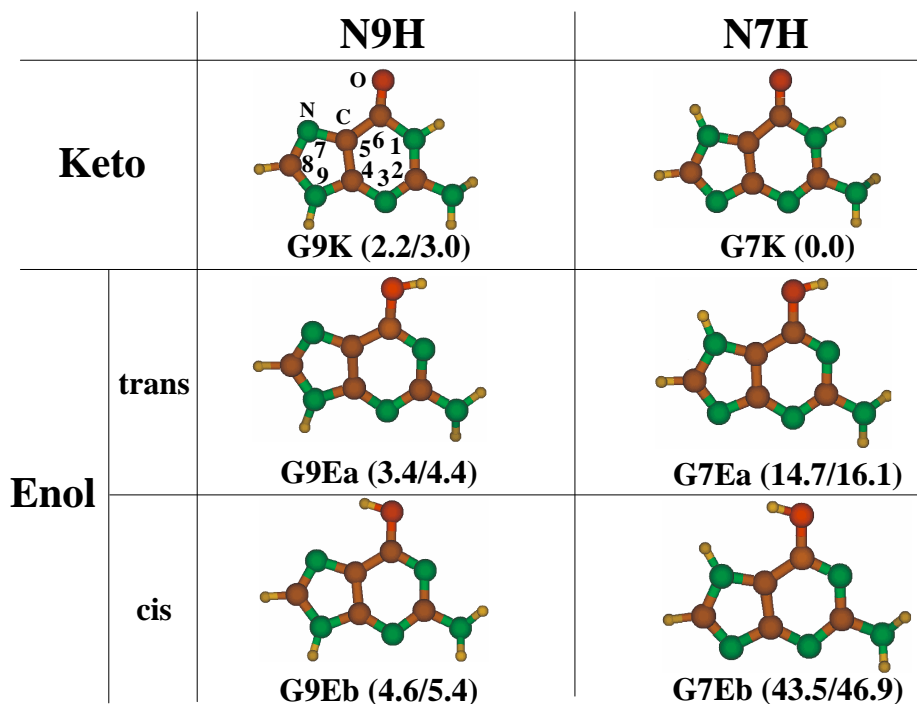
Figure 4.1: *Ab initio* structures and relative energies (MP2/aug-cc-pVDZ level) of the various tautomers of guanine. Amino-oxo (keto) and amino-hydroxy (enol) are classified by certain functional groups in the positions 2 and 6 of the purine base, namely NH_2 (amino-), C=O (-oxo) and O–H (-hydroxy). In addition, the enol forms have two rotational orientation of the O–H group: trans (a–form) and cis (b–form) to the five-membered ring. The values in parentheses give the energies relative to G7K in kJ/mol with/without a harmonic zero point energy correction. Only the four lowest energy tautomers are experimentally observed in the present study.

The primary reason for the discrepancy between the various assignments is that the vibrational frequencies of the various tautomers are rather similar, making it difficult to unambiguously assign the structures simply by comparison between the experimental and *ab initio* vibrational frequencies. We have recently introduced a new approach for assigning such vibrational spectra, based upon comparisons between the vibrational transition moment angles (VTMAs) [79] determined from theory and experiment. These VTMAs are defined as the angle between the transition moment for a particular vibrational mode and the permanent electric dipole moment. The experimental measurement of these angles requires that the molecule be oriented in the laboratory frame of reference, which is done using a large direct current (DC) electric field. This pendular state spectroscopy has been discussed in detail in the literature [103–106].

We have found that, for high-frequency H–X stretching vibrational modes, the VTMAs are quantitatively determined by modest *ab initio* calculations [79]. Unlike the vibrational frequency calculations, no scaling factor is required for the comparison between experiment and theory. In this chapter we apply this method to the study of the various tautomers of guanine. We obtain conclusive assignment of the infrared spectra (3400 – 3650 cm^{-1} region) of the guanine tautomers as a result of comparisons of the experimental vibrational frequencies, VTMAs, and dipole moments with those obtained from high level *ab initio* calculations.

4.2 Experimental Method

The infrared spectra of isolated guanine were obtained using a helium nanodroplet apparatus that has been described in detail previously [102]. Helium nanodroplets were formed by expanding ultrahigh purity helium (99.9999%) in vacuum through a 5 μm diameter orifice. The spectra were recorded using a source pressure of 55 atm, the nozzle being maintained at 21 K by use of a closed-cycle helium refrigerator. Under

these conditions droplets are produced with a mean size of approximately 3000 helium atoms. The droplets were doped with guanine from the gas-phase, using a heated oven. Although there have been a number of failed attempts at evaporating guanine [70, 80, 182], due to thermal decomposition of the sample, we observed no such effects at the oven temperature of 350 °C used here. The present success is most likely the result of the fact that helium nanodroplet experiments require much lower vapor pressures than those typically used in free jet experiments [38]. For all of the experiments discussed here the oven temperature was adjusted so that the only significant features in the corresponding spectra are attributable to the guanine monomer.

The seeded droplets pass between the two parallel gold coated mirrors [102], where they are irradiated by multiple passes of a continuous-wave tunable infrared laser (a PPLN–OPO laser [159, 160]). Upon vibrational excitation of the solvated molecules, vibrational relaxation to the helium results in the evaporation of several hundred helium atoms from each droplet. Detection is then based on the depletion of the helium beam flux in the forward direction, using a bolometer detector [165]. In practice, the laser was amplitude modulated, and the signals were recorded using phase-sensitive detection.

A large DC electric field was applied to the laser interaction region using two electrodes positioned at right angles to the multipass cell. The laser electric field was aligned either parallel or perpendicular to the DC electric field. The signal levels associated with a given vibrational band could then be recorded as a function of the electric field strength and polarization direction. This was necessary in order to measure the associated VTMAs. At the low temperatures characteristic of both free jet expansions [104, 120, 189–191] and helium nanodroplets [37, 108, 155, 167] a polar molecule can be strongly oriented along the DC electric field direction. For such an oriented molecule, the infrared transition intensity depends on the direction (relative to the permanent dipole direction) and magnitude of both the vibrational transition moment and

the laser electric field. In the present study the vibrational bands were recorded at zero electric field and at high fields (80 kV/cm) corresponding to parallel and perpendicular laser polarization directions (relative to the DC electric field). The approach is quite analogous to that of linear dichroism in bulk phases [192].

4.2.1   Vibrational Transition Moment Angles (VTMAs)

The permanent dipole orientation distribution for a polar molecule in a DC electric field can be calculated accurately using the methods discussed most thoroughly by Kong and co-workers [128–130]. Given that the present vibrational spectra are not rotationally resolved, the dipole orientation distributions, $P(cos\theta)$, represent a thermal average over the Stark levels at the rotational temperature of the molecules in the droplets (0.37 K [18]). This distribution is given by equation 2.23.

It is important to note that the Stark energies in this equation depend on both the dipole moment of the molecule and its rotational constants. However, the thermal average is only weakly dependent upon these quantities, so that we can use the *ab initio* values (the rotational constants being reduced by a factor of three to account for the effects of the helium [99]) in this analysis.

With the molecule oriented in the laboratory frame of reference, the vibrational band intensity depends on the angle α, defined as the angle between the permanent electric dipole and the transition moment (the VTMA). For a vibrational mode with its transition moment parallel to the permanent moment, and therefore also the DC electric field, the intensity of the associated band is enhanced by the application of a DC electric field when the laser electric field is aligned parallel to the DC electric field. Rotation of the laser polarization by 90° will result in a field induced decrease in the corresponding band intensity, because in this case the laser is polarized perpendicular to the transition moment. At the magic angle (54.7°), the intensity of the band will not depend on the

electric field [168]. Throughout this chapter, parallel and perpendicular polarization configurations correspond to the laser being polarized parallel and perpendicular to the DC electric field, respectively. The parallel and perpendicular band intensities can now be written in terms of both α and the permanent dipole distribution as equation 2.25 and 2.26. As a result, the ratio of the intensities corresponding to parallel and perpendicular polarization is given by equation 2.27.

The experimental intensity ratios are obtained by integrating the area under the vibrational bands (with parallel and perpendicular polarization configurations), using the corresponding field free spectra to normalize. The latter is necessary given that a different laser alignment was needed for the two measurements and one could not rely on the optimizations alone to ensure that the overall pumping efficiency was the same for both. The VTMAs for the various vibrational modes of the molecule were then determined by comparing the calculated intensity ratios with those obtained from equation 2.27.

4.2.2   *Ab initio* Calculations

The *ab initio* VTMAs, obtained by full geometry optimization and harmonic vibrational analysis using Gaussian 03 [169], were carried out using Møller-Plesset perturbation theory at the second-order level (MP2) with a 6-311++G(d,p) basis set and an aug-cc-pVDZ basis set. Figure 4.1 shows the lowest six tautomers of guanine with relative energies listed in kJ/mol with and without zero point energy corrections. In both cases, the amino-oxo G7K tautomer has the lowest energy. In general, the free energy is more useful for comparison with experiment, particularly given that guanine is produced at a temperature of 350 °C in the oven. Rapid quenching of the guanine upon capture by a helium droplet is likely to freeze in the corresponding tautomer population distribution [69,70,80,147,193], making the free energy at the oven temperature

the most relevant quantity. Figure 4.2 shows a plot of the calculated free energies for the lowest four tautomers of guanine. The vertical dashed line corresponds to the experimental conditions used here. According to this measure, the G7K tautomer is the most stable tautomer, which agrees generally with the energy ordering of the various tautomers [194]. Nevertheless, all four of these have sufficiently low free energies in comparison to the temperature of the oven that we would expect to see them all. In contrast, the next lowest form lies approximately 15 kJ/mol higher in free energy and therefore is unlikely to be present in our samples. The relative intensities of these four tautomers will be discussed below.
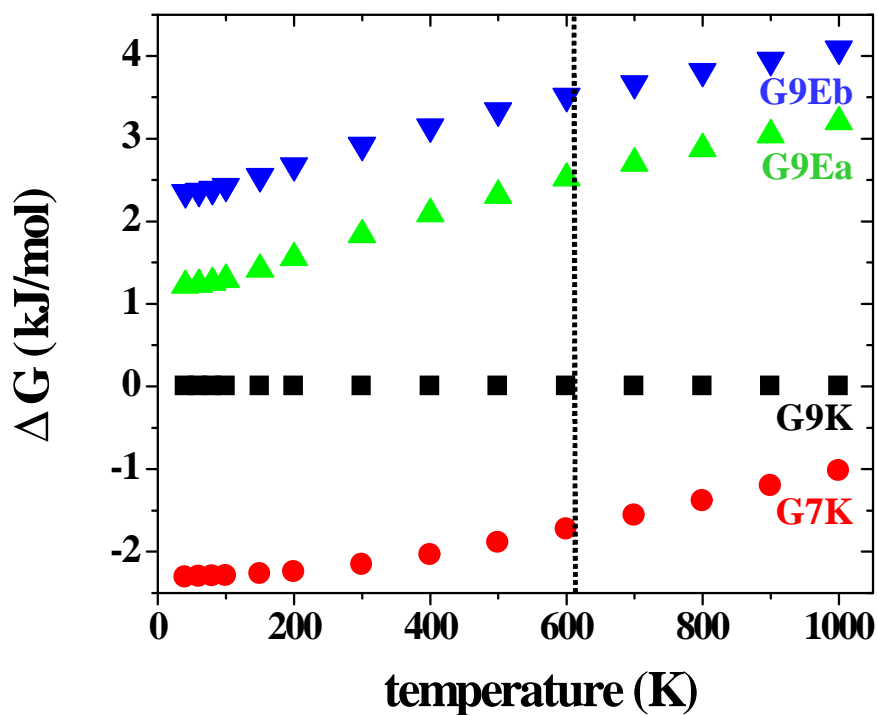
Figure 4.2: *Ab initio* free energies for the four lowest energy tautomers of guanine as a function of temperature. The vertical dashed line corresponds to the experimental conditions used here at 620 K.

Figure 4.3 shows the four lowest energy tautomers of guanine, onto which are superimposed vectors representing the directions of the permanent electric dipole moments

(solid arrows) and the vibrational transition moments (dashed arrows). The magnitudes of the various moments are given in Table 4.1. It is clear from the figure that the patterns of VTMAs for the various tautomers are quite different, making them a useful tool for assigning the associated vibrational spectra.

It is interesting to note that the permanent electric dipole moments are quite different for the four tautomers shown in Figure 4.3, namely 6.26 D, 1.88 D, 3.11 D, and 4.06 D for tautomers G9K, G7K, G9Ea, and G9Eb, respectively. Given that the experimentally measured dipole moments for molecules solvated in helium are only slightly different from the corresponding gas-phase values [123], these can also be used to help in the spectral assignments, as discussed below.
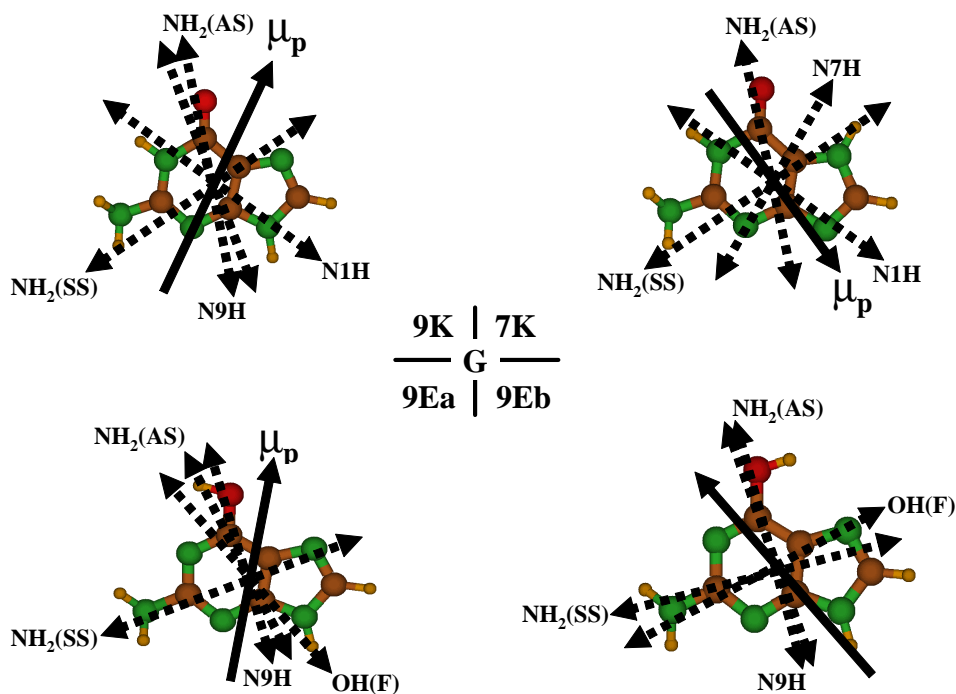
Figure 4.3: The four lowest energy tautomers of guanine, showing the corresponding directions of the permanent electric dipole moments (the length of the solid arrows is proportional to the dipole magnitudes) and the vibrational transition moments (dashed arrows) for the various vibrational modes. The magnitudes of these moments are given in Table 4.1.

Table 4.1: The experimental and ab initio vibrational data for the guanine tautomers.

	Harm.[a] freq. (cm^{-1})	Scaled[a] freq. (cm^{-1})	Exp. freq. (cm^{-1})	IR intensity (km/mol)	Assignment	ab[b] initio VTMA $(°)$	Exp. VTMA $(°)$	μ (debye)
G9K								6.26
	3701.3	3542.2	3544.5	38.7	NH_2 (AS)	44	50	
	3664.8	3507.2	3506.9	100.4	N9H	42	44	
	3606.6	3451.5	3437.9	58.8	N1H	80[77]	68	
	3587.7	3433.4	3444.5	44.7	NH_2 (SS)	31	40	
G7K								1.88
	3687.1	3528.6	3526.6	36.7	NH_2 (AS)	29	29	
	3660.6	3503.2	3504.8	120.2	N7H	73	73	
	3607.4	3452.3	3441.1	64.3	N1H	47[41]	20	
	3576.2	3422.4	3430.5	38.1	NH_2 (SS)	83	80	
G9Ea								3.11
	3801.1	3637.6	3584.4	109.6	OH (F)	57	65	
	3737.9	3577.2	3580.9	41.5	NH_2 (AS)	37	38	
	3669.6	3511.8	3511.3	104.0	N9H	34	33	
	3610.6	3455.3	3465.2	58.1	NH_2 (SS)	60	55	
G9Eb								4.06
	3807.9	3644.2	3590.6	100.3	OH (F)	83	85	
	3741.7	3580.8	3583.2	45.3	NH_2 (AS)	20	22	
	3667.4	3509.7	3509.6	105.1	N9H	21	19	
	3612.3	3457.0	3466.1	66.2	NH_2 (SS)	73	73	

[a] The *ab initio* calculations were performed at the MP2/6-311++G(d,p) level, and the scaled frequencies were obtained by multiplying the harmonic frequencies by a factor of 0.957.

[b] The *ab initio* VTMAs for the N1H bands presented in square brackets were obtained at the MP2 theory with an aug-cc-pVDZ basis set.

4.3   Results

The upper panel in Figure 4.4 shows an experimental spectrum of guanine in helium that spans the regions corresponding to the N–H, NH_2, and O–H stretching vibrations. The other four panels show the *ab initio* spectra (all scaled by a factor of 0.957 with a 6-311++G(d,p) basis set) for the four lowest energy tautomers of guanine. Unlike the IR-REMPI method used by a large number of groups [69, 70, 80, 147, 193], the present method does not separate out the contributions to the spectrum associated with the different tautomers. Rather, this linear spectroscopy shows all of the bands in a single spectrum. The apparent difficulty with this is that there are many bands that are closely spaced, making an assignment based purely on the vibrational frequencies impossible. This problem is compounded by the fact that the accuracy of scaled *ab initio* calculations is less than the spacing between the various bands. Note, for example, that there is a large discrepancy between the experimental and scaled *ab initio* frequencies for the two free O–H stretching bands of the G9Ea and G9Eb isomers. As we will see below, the group of bands in the experimental spectrum, near 3575 cm^{-1} includes these O–H stretches. Even if a pump-probe method were used to separate out the spectra for the different tautomers, a unique assignment could not be made, given that some of the vibrational frequencies do not depend very strongly on the tautomer geometry. We believe that this is in part the reason for the assignment differences in the assignments for the various experimental studies.

In an effort to overcome the problem discussed above, we now turn to the measurement of the VTMAs for the various bands in the experimental spectrum. Figure 4.5 shows an expanded view of the highest frequency cluster of bands near 3585 cm^{-1} measured with (a) parallel polarization, (b) zero electric field, and (c) perpendicular polarization (the corresponding electric field being 80 kV/cm). Given that these bands do not correspond at all to the scaled *ab initio* calculations, an assignment based upon
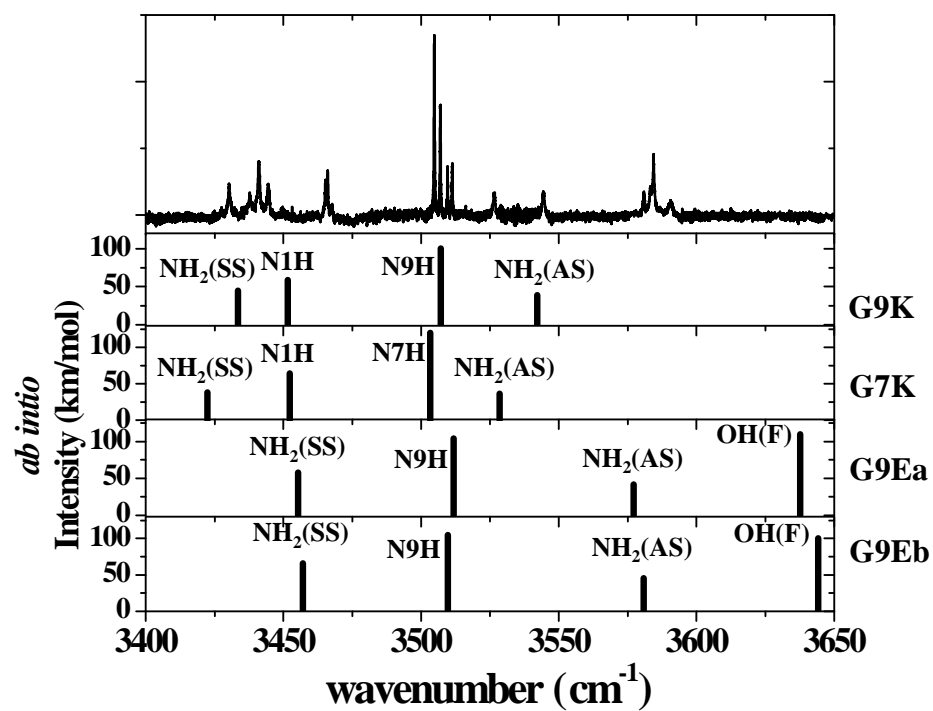
Figure 4.4: Survey spectrum of guanine isolated in helium droplets. The corresponding *ab initio* vibrational spectra for the four lowest energy tautomers of guanine are shown in separate panels below the experimental spectrum.

frequencies would be pure guesswork. However, qualitatively it seems reasonable that these four bands correspond to the O–H and NH_2 asymmetric stretches of the G9Ea and G9Eb tautomers, which are the only ones that are anywhere close to this region. This would imply that the O–H stretches are much lower in frequency than predicted by the scaled *ab initio* results, a fact that has been noted in previous studies [86,87], while the asymmetric NH_2 stretches are higher than those from theory. Stated differently, the empirical scaling factors for the various vibrational modes are different, making the *ab initio* frequencies of limited use.

It is clear from Figure 4.5 that two of the bands are enhanced in intensity by application of an electric field with parallel polarization, while the other two are enhanced with perpendicular polarization, one more strongly (iii) than the other (iv). Quantitative analysis of the data reveals that these two bands have experimental VTMAs of (iii) 85° and (iv) 65°. This is to be compared with the *ab initio* VTMAs for the O–H stretches of the G9Ea and G9Eb tautomers of 83° and 57°, respectively. Bands (i) and (ii) were similarly analyzed to give experimental VTMAs of 38° and 22°, respectively. Here again the agreement with *ab initio* theory is excellent, the corresponding values for the G9Ea and G9Eb tautomers being 37° and 20° for the asymmetric NH_2 bands. The ability to uniquely assign the spectra of these rotamers has a great deal of potential for obtaining a more quantitative understanding of the intramolecular interactions between various functional groups in such systems. Indeed, it is interesting to note that the experimental O–H stretch (3584.4 cm^{-1}) for the G9Ea tautomer is lower in frequency than the corresponding vibration for the G9Eb tautomer (3590.6 cm^{-1}). This ordering and frequency difference (6.2 cm^{-1}) is in excellent agreement with the *ab initio* calculations (6.6 cm^{-1}), even though the absolute scaled frequencies are not as well reproduced. Such differences are most likely reflective of the difference in the intramolecular interactions in the cis and trans configurations. The same is true

for the asymmetric NH_2 stretches, where again the ordering and frequency differences for the cis and trans tautomers are consistent between theory and experiment. It is worth pointing out here that the ability to resolve the spectra associated with these cis and trans amino-hydroxy tautomers (G9Ea and G9Eb) is afforded by the extremely low temperature and homogeneous environment provided by the helium nanodroplets. Indeed, the line widths typically observed in conventional matrices (argon, for example [134, 162, 186, 187]) would be too broad for these four bands to be resolved.
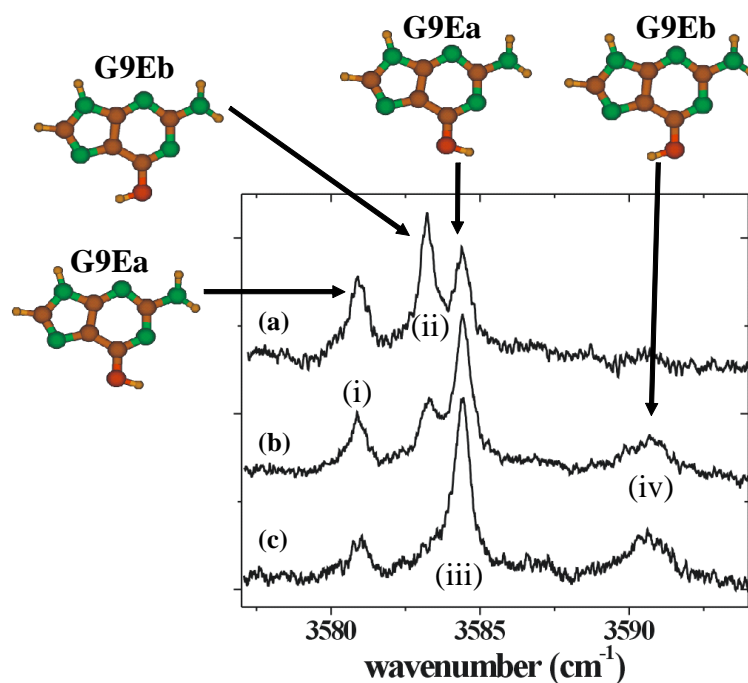
Figure 4.5: Expanded view of the high frequency section (O–H and NH_2 (AS)) of the guanine spectrum. Spectra (a), (b), and (c) correspond to parallel polarization, zero-field, and perpendicular polarization, respectively. The assignments shown in the figure are based upon comparisons between the experimental and *ab initio* VTMAs and are consistent with the dipole curves presented in Figure 4.12 and 4.13.

We now shift our attention to the region corresponding to the NH_2 asymmetric stretches of the G9K and G7K isomers, which according to the scaled *ab initio* calculations are at 3542.2 cm^{-1} and 3528.6 cm^{-1}, respectively. Careful inspection of the

spectrum shown in Figure 4.4 reveals that there are two bands that are in good correspondence with these *ab initio* frequencies. Indeed, the expanded view of this region shown in Figure 4.6 shows the level of agreement between the *ab initio* calculations (vertical arrows) and the experimental spectra. Although, the calculations for both the G9K and G7K tautomers do not match quantitatively well with the NH_2 asymmetric stretches, the differences, which are within 2 cm^{-1}, are certainly less than the uncertainty associated with the calculations. Once again the three spectra correspond to (a) parallel polarization, (b) field free, and (c) perpendicular polarization conditions. The results for the higher frequency band suggest that the associated VTMA is near the magic angle, since the band intensity does not depend upon the field, while for the lower frequency band the VTMA is clearly somewhat parallel. Quantitative analysis of this data gives experimental VTMAs of $50°$ and $29°$ for the high and low frequency band, respectively. As expected, the higher frequency band has a VTMA which is very close to the magic angle. The *ab initio* VTMAs for these two modes of the G9K and G7K tautomers are $44°$ and $29°$, respectively, in good agreement with the experimental results. From this, the assignment of the two bands in Figure 4.6 is obvious, as shown. It is interesting to note that these weak bands have not been observed in previous experimental studies of guanine [70, 80, 182].

Figure 4.7 shows another expanded section of the guanine spectrum, in this case corresponding to the most intense bands in the spectrum near 3505 cm^{-1}. Once again the three spectra correspond to (a) parallel polarization, (b) zero-field, and (c) perpendicular polarization conditions. It is encouraging that both theory and experiment show four bands in this spectral region. Consider first the lowest frequency band (i), for which the experiments show strongly perpendicular behavior. According to the *ab initio* calculations, the lowest frequency band should be the N7H stretch of the G7K tautomer, as indicated by the vertical arrow at 3503.2 cm^{-1}. As can be seen in Table
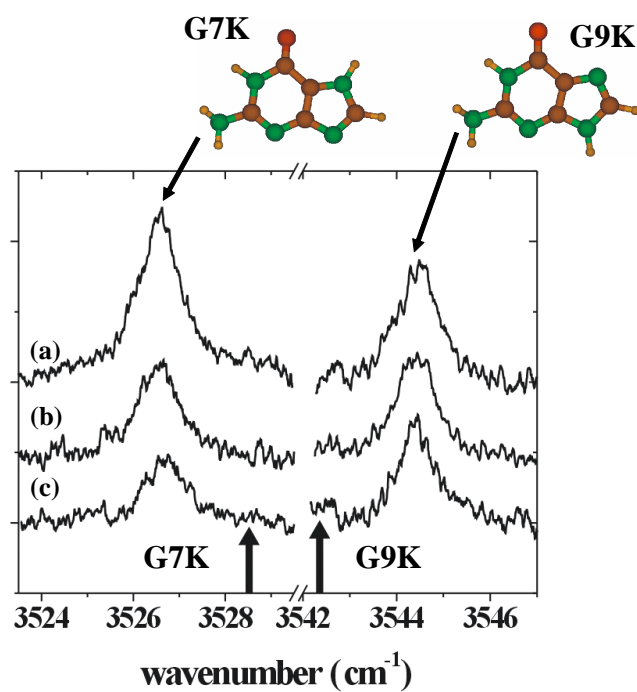
Figure 4.6: A set of expanded spectra corresponding to (a) parallel polarization, (b) zero-field, and (c) perpendicular polarization. The vertical arrows show the corresponding *ab initio* frequencies (NH_2 (AS)) and the assignments are based upon the VTMAs. In this case the scaled *ab initio* frequencies are in reasonable agreement with experiment.

4.1, the *ab initio* VTMA for this vibrational mode is 73°, in perfect agreement with the experimental value for the lowest frequency band in Figure 4.6, namely 73°. Although the experimental and calculated frequencies do not match as well as for the other three bands, the assignment is clear.
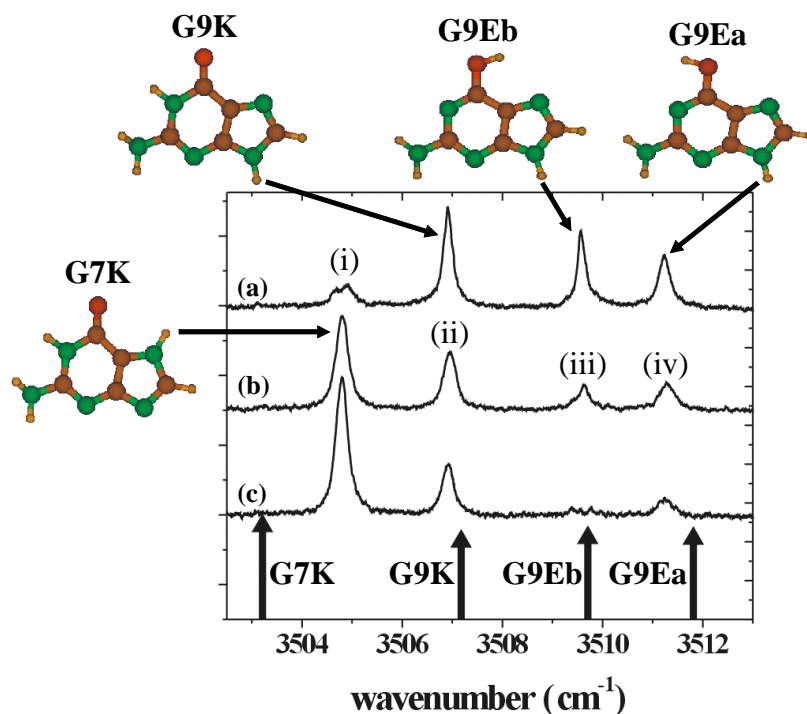
Figure 4.7: Assignments of the most intense bands in the guanine spectrum, based upon the VTMAs. The three spectra correspond to (a) parallel polarization, (b) zero-field, and (c) perpendicular polarization. The three higher frequency bands correspond to the N9H vibrational modes of the tautomers shown, while the lowest frequency band is associated with the N7H vibrational mode of the G7K tautomer.

Band (ii) in Figure 4.7 clearly has parallel character. The scaled *ab initio* frequency for the G9K tautomer is in excellent agreement with experiment, and the *ab initio* VTMA (42°) for this N9H vibration is also in excellent agreement with the experimental value of 44°. It is evident that band (iii) is more strongly parallel in character, given that the band is strongly reduced in perpendicular polarization. The *ab initio* vibrational frequency suggests that this is the N9H vibration of the G9Eb tautomer.

Indeed, the *ab initio* VTMA for this vibrational mode is 21°, in excellent agreement with the experimental value of 18°. Finally, band (iv) appears to have an intermediate VTMA between those of bands (ii) and (iii), based upon the polarization dependence of the band intensities. Assigning this band to the N9H vibration of the G9Ea tautomer, as shown in the figure, is straightforward based on both the experimental and *ab initio* vibrational frequencies and the VTMAs. This is confirmed by the *ab initio* VTMA for this vibrational mode of 37°, in excellent agreement with the experimental value of 38°. This spectral region appears to be ideal for probing all four of the tautomers of guanine, with excellent signal-to-noise ratio.

The electric field and polarization dependence of the next two vibrational bands near 3465 cm^{-1} are shown in Figure 4.8. Once again, the VTMAs for these two bands are clearly quite different, which aids in their assignment. This is particularly important in these cases given that the *ab initio* vibrational frequencies for the candidate vibrational modes are in rather poor agreement with the experimental values. The higher frequency band has strong perpendicular character, suggesting its assignment to the NH$_2$ (SS) vibration of the G9Eb tautomer, which has an *ab initio* VTMA of 73°. A quantitative analysis of the experimental results yields a VTMA for this band of 73°. The polarization dependence of the lower frequency band is much weaker, suggesting a VTMA near the magic angle. Quantitative analysis yields an experimental VTMA of 55°, compared to the *ab initio* value for the NH$_2$ (SS) of the G9Ea tautomer of 60°. Once again, the assignment is clear. It is interesting to note that while the scaled vibrational frequencies for these two modes are off by approximately 10 cm^{-1}, the ordering of the two bands is correct. The experimental and *ab initio* differences between the two vibrational bands are 0.9 cm^{-1} and 1.7 cm^{-1}, respectively. Here again, these differences are likely due to the different intramolecular interactions associated with the two rotamers.
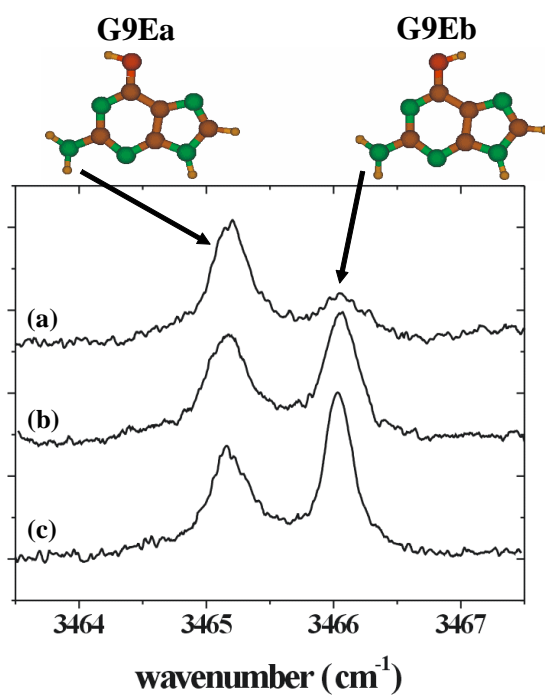
Figure 4.8: Expanded view of a doublet appearing near 3465 cm^{-1}, where (a), (b), and (c) correspond to parallel polarization, zero-field, and perpendicular polarization, respectively. These two bands are assigned to the NH$_2$ (SS) vibrations of the G9Ea and G9Eb tautomers of guanine, as shown.

The final expanded spectra are shown in Figure 4.9, where we observe four vibrational bands. A quick tally of the modes already assigned (12) suggests that we still have four vibrational modes to identify, given that there are a total of 16, namely four vibrational modes for each of the four tautomers. Based purely on the frequency ordering of the four bands, comparisons with the *ab initio* frequencies would suggest that from low to high frequency these bands should be assigned as NH_2 (SS) of G7K, NH_2 (SS) of G9K, N1H of G9K, and N1H of the G7K tautomer. However, anticipating the assignment based on the VTMAs and dipole moment experiments (to be discussed below), we note that this assignment is good only for the NH_2 (SS) of the G7K tautomer. The observed N1H bands of the G9K and G7K tautomers are shifted further to the red (compared to the others), so they lie between the NH_2 (SS) bands of G9K and G7K.
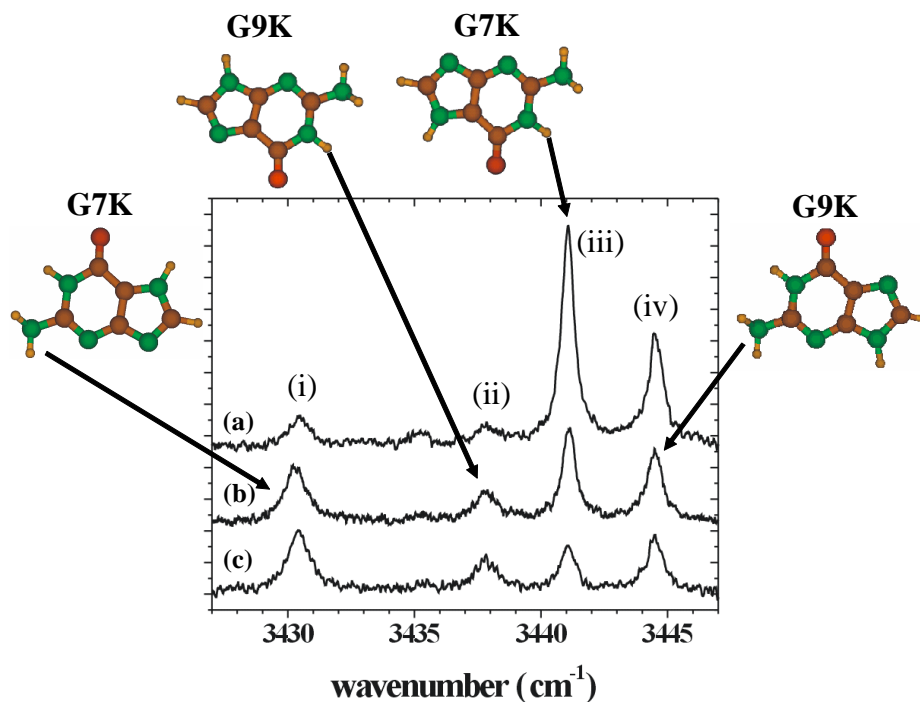
Figure 4.9: A low frequency section of the experimental spectrum, recorded under (a) parallel polarization, (b) zero-field, and (c) perpendicular polarization conditions. The assignments of the various vibrational bands are based upon comparisons between the experimental and calculated VTMAs.

Band (i) is clearly perpendicular in character (experimental VTMA of 80°), consistent with the *ab initio* VTMA for the NH_2 (SS) of the G7K tautomer of 83^0. For band (ii) the experimental VTMA is 68°, compared with the *ab initio* VTMA for the N1H vibration of the G9K tautomer of 80°. The difference here is a bit larger than what we have seen for the other bands, but this band is also quite weak, making the associated experimental error larger (normal experimental error being within $\pm\, 5° \sim 7°$) [86, 87]. Bands (iii) and (iv) are both clearly parallel in character with experimental VTMAs of 20° and 40°, respectively. While the N1H stretches of the G7K and NH_2 (SS) of the G9K tautomers are both parallel bands, a comparison of the VTMAs alone does not allow us to distinguish which band belongs to which tautomer. Therefore, at this point, we will only tentatively assign bands (iii) and (iv) to G9K/NH_2 (SS) (*ab initio* VTMA, 31°), and G7K/N1H (*ab initio* VTMA, 47°), respectively. As shown below, the dipole moment measurements for these bands will confirm this assignment.

In view of the fact that some of the comparisons between the experimental and *ab initio* VTMAs are outside the typical differences we have come to expect from the other bands of this system, as well as from previous studies [86, 87], we were interested in developing another approach that could give an independent test of the above assignments. We discuss here an approach that takes advantage of the fact that the dipole moments for the four tautomers of guanine (see Table 4.1) are all quite different. As a result, the dependence of the band intensities on the magnitude of the electric field should be quite different for these tautomers. In particular, a molecule with a small dipole moment will require a large electric field for complete orientation, while much lower fields are needed to reach this saturation condition if the dipole moment is large.

Figure 4.10 shows a plot of the ratio of the integrated areas ($A_{para.polarization}/A_{zerofield}$) for the various vibrational bands assigned to the G9K tautomer. As indicated in Table 4.1, this is the tautomer with the largest *ab initio* dipole moment. The solid lines

represent the experimental data, while the various symbols show the results calculated using the methods discussed above, using the *ab initio* dipole moment. The agreement for all four vibrational bands is clearly excellent. To contrast this data, we present in Figure 4.11 the corresponding results from the G7K tautomer, namely the one with the smallest dipole moment. In this case the curves are much slower to reach the saturation levels, in agreement with our expectation. Here again, the agreement between theory and experiment is quantitative for all four vibrational modes. Now, the ambiguity in the assignments of bands (iii) and (iv) in Figure 4.9 based on *ab initio* frequencies and the VTMAs is obviously resolved. Notice that, in order to get the best agreement between experiment and theory the bands (iii) and (iv) in Figure 4.9 must be attributed to the N1H G7K and NH_2 (SS) G9K, respectively, confirming our previous assignments, as indicated at the two of Figure 4.9. Figure 4.12 and 4.13 show the corresponding data for the G9Ea and G9Eb tautomers, respectively, which are clearly intermediate cases, consistent with the corresponding *ab initio* dipoles moments. The combination of the VTMAs and these dipole curves gives us a redundancy in the assignment that is not often available. The NH_2 symmetric and N1H stretching region clearly show that a conclusive assignment based purely on the vibrational frequency ordering cannot be obtained, given that the two bands are much closer together than the typical accuracy of *ab initio* calculations. Here, we show that the dipole moment curves provide unambiguous assignment of these four vibrational modes to two separate tautomers. As a result, we feel that the vibrational assignments presented here are firm. This is important given that we now have a complete set of data that can be used to make detailed comparisons with more sophisticated theories, including those which include the effects of anharmonicity [183, 195, 196].
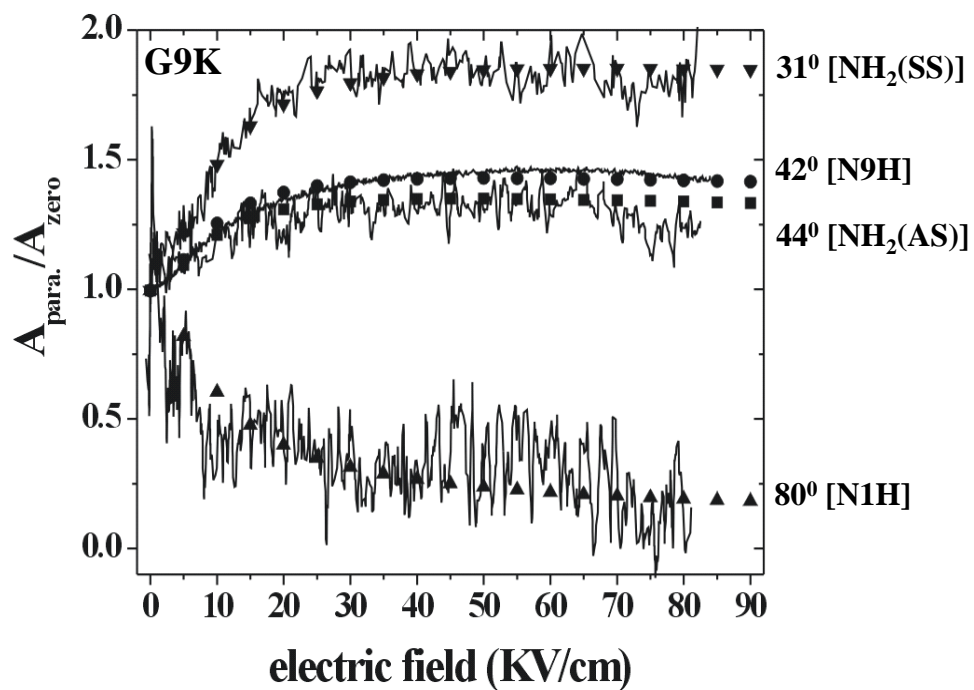
Figure 4.10: A plot of the electric field dependence of the ratio of the vibrational band intensities for the four vibrational modes of the G9K tautomer, with and without the electric field and with parallel polarization. The solid lines show the experimental results, while the symbols correspond to the calculations based upon the *ab initio* dipole moment of 6.26 D.
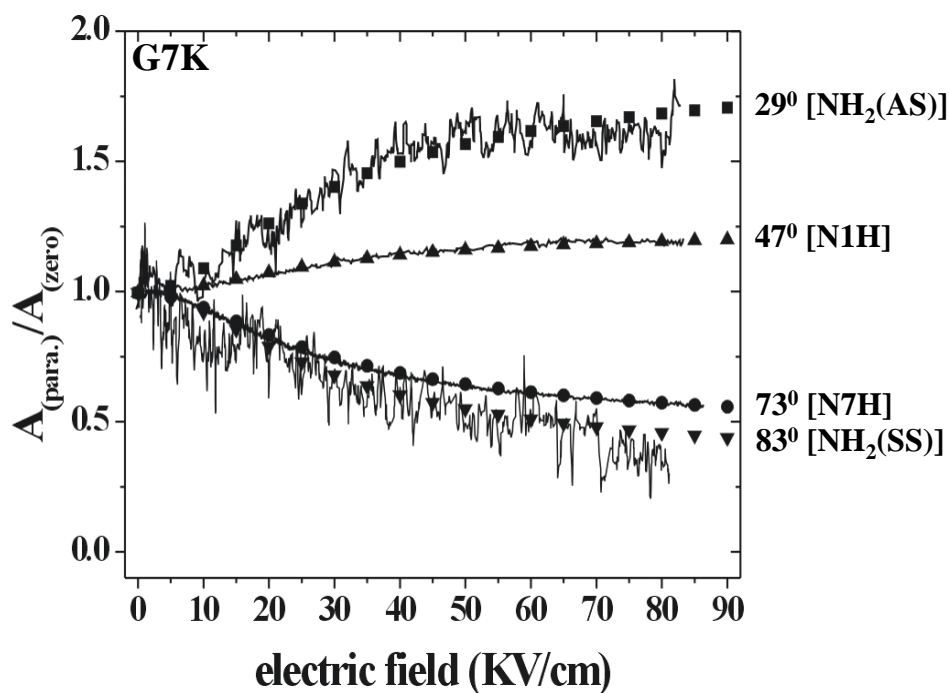
Figure 4.11: A plot of the electric field dependence of the ratio of the vibrational band intensities for the four vibrational modes of the G7K tautomer, with and without the electric field and with parallel polarization. The solid lines show the experimental results, while the symbols correspond to the calculations based upon the *ab initio* dipole moment of 1.88 D.
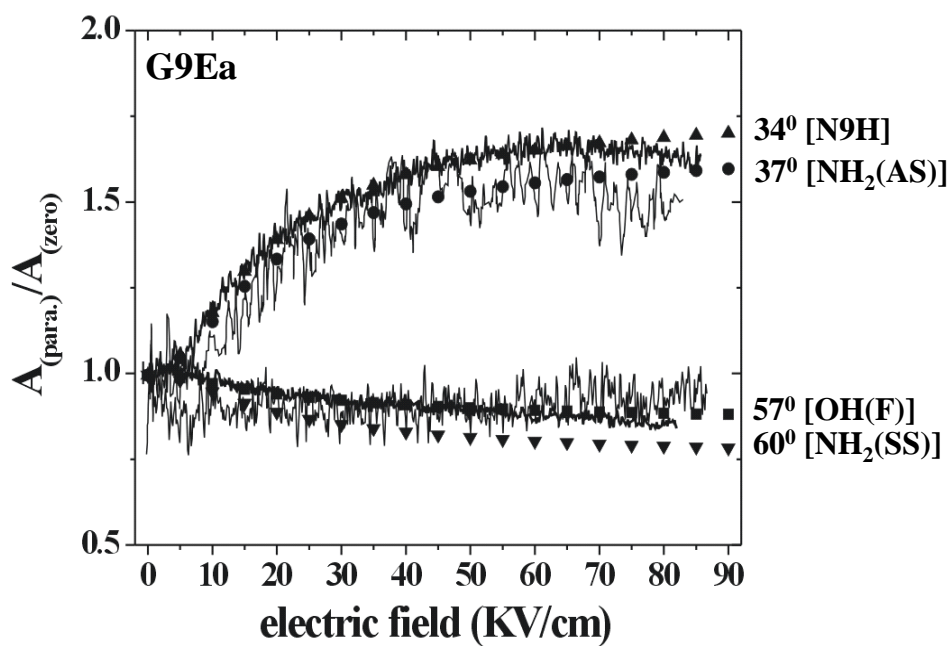
Figure 4.12: A plot of the electric field dependence of the ratio of the vibrational band intensities for the four vibrational modes of the G9Ea tautomer, with and without the electric field and with parallel polarization. The solid lines show the experimental results, while the symbols correspond to the calculations based upon the *ab initio* dipole moment of 3.11 D.
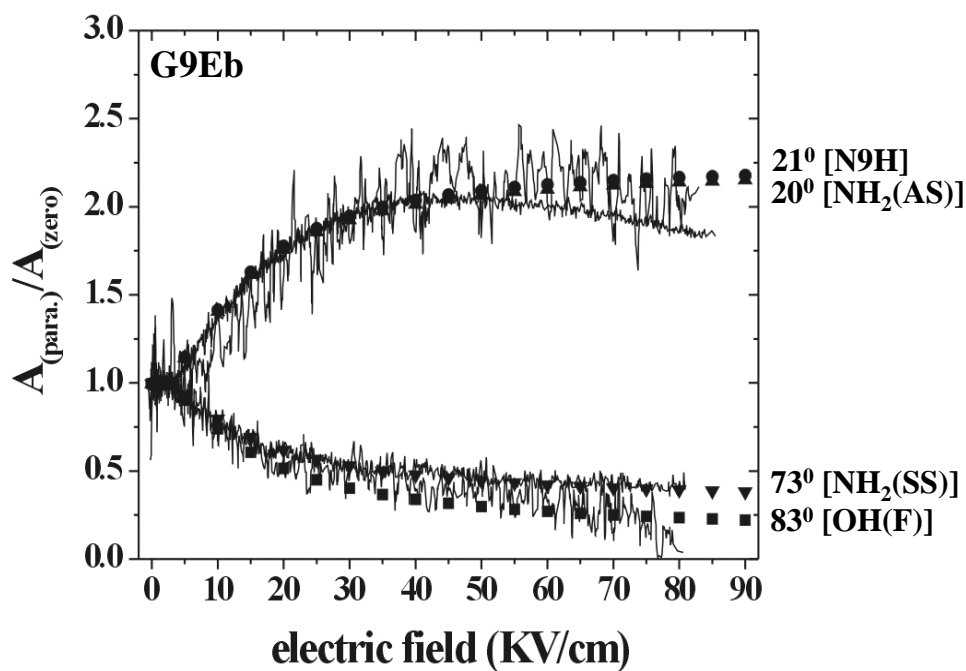
Figure 4.13: A plot of the electric field dependence of the ratio of the vibrational band intensities for the four vibrational modes of the G9Eb tautomer, with and without the electric field and with parallel polarization. The solid lines show the experimental results, while the symbols correspond to the calculations based upon the *ab initio* dipole moment of 4.06 D.

4.4 Discussion

We begin this discussion by considering the discrepancy in the assignment of the N1H bands with *ab initio* calculations and the VTMAs. Although the separation between NH_2 (AS) and NH_2 (SS) vibrational bands of the G9K and G7K tautomers is well predicted by *ab initio* calculations, the calculations fail to correctly predict the ordering of the N1H and NH_2 (SS) bands of the G9K tautomer (see Table 4.1). This discrepancy may have several different sources, and the understanding of these could provide further insight into this system. For example, the large red shift in frequency of the N1H band of the amino-oxo tautomers (G9K and G7K) is due to a strong intramolecular hydrogen bond. Since this interaction is sensitive to the relative orientations of the C=O, N1H, NH_2 groups and the ring, the discrepancy with *ab initio* calculations may be a measure of the quality of the local geometry of these functional groups. Indeed, for this band we also observe an unusual sensitivity of the VTMAs on the basis set reflecting changes in the geometry, however, for the other bands the theoretical VTMAs show no dependence on the basis set (the typical dependence of the VTMAs on different basis sets is only $\pm$ $1° \sim 2°$) [79]. This supports the above assumption that the VTMA discrepancy in the N1H assignment results from the failure of the 6-311++G(d,p) basis set to accurately describe the dihedral angles of the N1H groups for the G9K and G7K tautomers. In contrast, the dihedral angles of the adjacent and more remote H atoms of the NH_2 group show no change with the basis sets and are in good agreement with experiment. The dihedral angles of the N1H group in the G9K and G7K tautomers, obtained with an aug-cc-pVDZ / 6-311++G(d,p) basis set, are $5°$ / $9°$ and $6°$/ $10°$ from the plane of the ring system, respectively. Better agreement for the N1H VTMA assignments with the aug-cc-pVDZ basis set is observed when compared to the calculations using the 6-311++G(d,p) basis set (see values in brackets in Table 4.1). This is likely due to the fact that the intramolecular interactions of the N1H group between the C=O and NH_2

groups are better described by the aug-cc-pVDZ basis set than by the 6-311++G(d,p) basis set. However, more theoretical work to account for the effect of anharmonicity would definitely be needed in this system. It would also be interesting to compare the *ab initio* vibrational frequencies, including the effects of anharmonicity, to see if the agreement with experiment is improved.

We now consider the relative integrated intensities of the various vibrational bands in the spectrum, with the goal of determining the relative populations for the four tautomers of guanine. It is helpful that we have four bands for each tautomer, giving us some redundancy in this determination. This is important given that we have to depend upon the *ab initio* vibrational transition moment amplitudes (see the IR intensities in Table 4.1) to normalize the bands relative to one another.

Considerable theoretical effort has already been devoted to the study of tautomers of neutral guanine [186,194,197–200]. It has been generally known that the G7K tautomer is most stable. Recently, Hobza and co-workers predicted that the G7K tautomer is the global minimum in both energy and Gibbs free energy, while the canonical form (G9K) is the next lowest local minimum using the RI-MP2 method, MP2 and CCSD(T) theory with the aug-cc-pVDZ basis set [194]. They found the ordering of the relative Gibbs free energies for the four tautomers to be G7K < G9K < G9Ea < G9Eb, -1.8, 0.0, 0.5, and 1.8 kJ/mol, respectively. Although, the calculations were done at 298 K, the ordering is consistent with our experimental observation at approximately 620 K.

On the basis of the *ab initio* infrared intensities and the experimental integrated intensities for all of the vibrational modes, we estimate that the experimental relative abundances of the four tautomers are 1 : 0.8 : 0.4 : 0.3 for G7K, G9K, G9Ea, and G9Eb tautomers, respectively. Table 4.2 gives a summary of the integrated experimental intensities and *ab initio* intensities for the four vibrational bands, normalized to the most stable G7K tautomer (except for the free OH bands, which were normalized to

Table 4.2: Integrated experimental areas and ab initio relative populations of the guanine tautomers

Tautomer	OH[a] (F)	NH$_2$ (AS)	N9/7H	N1H	NH$_2$ (SS)	Average of N9/7H & NH2(SS)	ab initio[b] relative populations
G9K	–	0.95	0.7	0.62	0.83	0.76	0.72
G7K	–	1	1[c]	1	1	1	1
G9Ea	1	0.77	0.34	–	0.36	0.35	0.44
G9Eb	0.86	0.65	0.25	–	0.31	0.28	0.36

[a] The free OH bands are normalized to the G9Ea tautomer.
[b] Exp(-ΔG/kT). MP2/aug-cc-pVDZ basis set was used for the free energy calculation at 620K.
[c] The intensity was compared with that of the N9H bands of the other tautomers.

the G9Ea tautomer). For the N7H band of the G7K tautomer, indicated by an asterisk, the intensity was compared with N9H bands of the other tautomers. Since the NH$_2$ (AS) bands for G9Ea and G9Eb are slightly overlapped, we averaged only the N9/7H and NH$_2$ (SS) bands to have a more reliable value for the relative abundances. The experimental relative abundances of the four tautomers in helium nanodroplets are in excellent agreement with those of relative free energy calculations conducted at the same temperature as used in the capture of a single molecule (ca. 620 K), as shown in Figure 4.2. Taking all of the data presented above together, there is no doubt that the lowest four tautomers, G7K, G9K, G9Ea, and G9Eb, are observed in helium nanodroplets.

The close correspondence between the vibrational frequencies of molecules obtained in helium droplets and those isolated in the gas-phase molecule is well known [18, 36, 156–158] and is attributed to the very weak forces between solute and solvent. However, we observe large discrepancies in the vibrational frequencies, which results in the different assignments for the guanine tautomers in our helium droplet environment relative to those obtained by de Vries and Mons using their IR–UV double resonance approach [70, 80]. A detailed comparison of the data reported by the groups of de

Vries and Mons and in our work is shown in Figure 4.14. The vertical dotted lines are meant as a guide to compare the bands observed in the IR–UV experiments reported by (a) de Vries and (b) Mons to the IR spectrum (c) obtained from this study. A close examination shows that most of the observed bands in the IR–UV experiments do not overlap with those in this study. Figure 4.14 clearly shows the disagreement in the assignments of the N9H and NH_2 (AS) bands of the G9K and G7K tautomers between the two groups, (a) and (b), mentioned in the previous papers [70, 182]. Note that a direct comparison of the G7E tautomer observed in (b) cannot be made because of the absence of G7E in (a) and (c). However, the frequency patterns of G9Ea from (a) and G7E from (b) are very similar, which clearly suggests that these belong to the same molecular structure but are assigned differently. It is also interesting to note that the observation of the higher energy tautomer, G7E (see Figure 4.1), is questionable, because the higher energy tautomer was observed with the highest signal-to-noise ratio in the Mons experiment, but it was not observed at all in the de Vries experiments, even though the both groups used similar techniques.

The discrepancies in the assignments of specific bands for each tautomers among three groups are discussed below. First, the frequencies of the NH_2 (AS) stretch for the G9K / G7K tautomer are separated by about 50 cm^{-1} / 25 cm^{-1} between the IR–UV (a and b) and this study (c). Similarly, the frequencies of the N9/7H stretch for the G9K/G7K tautomer, which was not observed by Mons due to the lack of the IR laser power in this region, are also red shifted by about 20 cm^{-1} / 10 cm^{-1} between the IR–UV (c and d) and this study. Even if we reassigned the de Vries G9K/G7K tautomer spectra, where the NH_2 (AS) bands are assigned to the N9/7H bands, the origin of the bands at around 3490 cm^{-1} cannot be explained. Furthermore, not all the expected bands were observed in IR–UV experiments and the specific assignments for G9K, G7K and G9E were determined by the three (or two) observed bands out
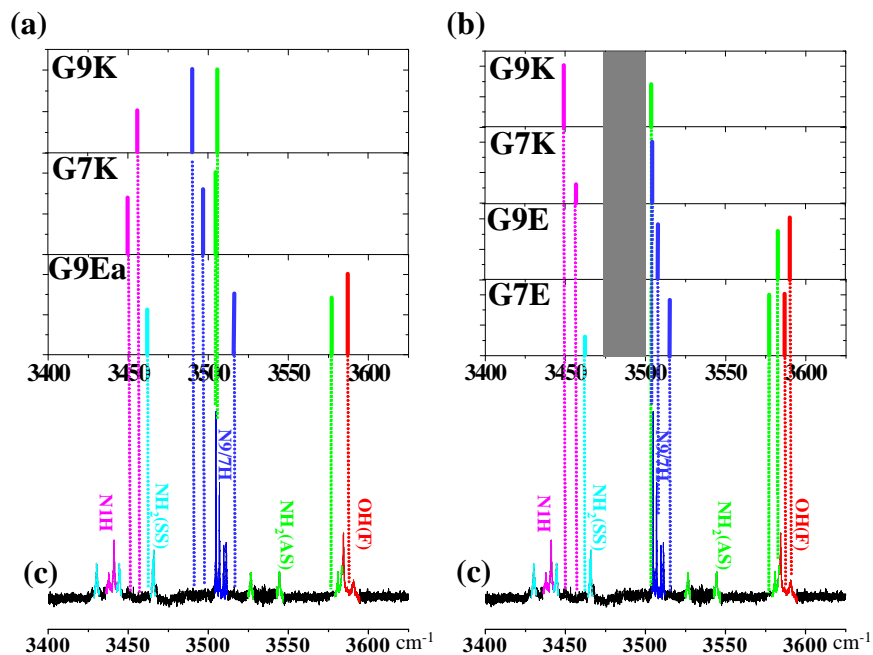
Figure 4.14: Direct comparisons of the guanine spectra from the three groups: (a) de Vries [182], (b) Mons [70], and (c) this work. The naming of each tautomer of the two different groups followed the present naming scheme. Each vibrational band is classified in different colors. The gray box in (b) is the frequency region $(3470 - 3500 \text{ cm}^{-1})$ where no spectrum was taken due to the lack of IR laser power [70]. The frequencies of G7E (b) are not compared to those of (c) due to the absence of the G7E in (c)

104

of four expected bands. Specifically, the NH_2 (SS) band for G9K and G7K in both of the IR–UV experiments is missing, even though it is observed for the G9Ea tautomer with high intensity in G9Ea (a) and moderate intensity in G7E (b). Further comparisons related to this issue can be found in Figure 4.15. As shown in Figure 4.14, it is clear that the discrepancy in the assignment of the infrared spectra for guanine occurs not only between the IR–UV experiments and this work, but even between the two IR–UV experiments, in which the experimental conditions are very similar. This disagreement is perhaps surprising because there has been good agreement between the gas-phase experiments and our work for the other NABs, such as adenine [54, 79, 182], cytosine [79, 86, 182, 201], uracil [54, 202], and thymine [54, 202]. The major difference between the two approaches is the method of sample preparation. While thermal evaporation methods have been used successfully for other NABs, guanine was observed to undergo decomposition before sufficient pressure was obtained [70, 182]. To generate the needed vapor pressure, laser desorption methods were used in the IR–UV experiments. However, as mentioned previously, much lower vapor pressures are needed in the helium droplet experiments. Based on the definitive assignments presented in this work, thermal decomposition is apparently negligible at our oven temperatures. Since we are not performing a double resonance (selective excitation), we might also see a spectral signature of the decomposition products, which are clearly absent. It is thus possible that the discrepancy between the experiments is the result of decomposition or the presence of species other than the three and/or four lowest energy guanine tautomers in the laser desorption experiments.

4.5 Conclusions

This work represents the first successful IR spectroscopic study of guanine by thermal evaporation, a task made difficult by guanine's low vapor pressure. Helium nanodroplet
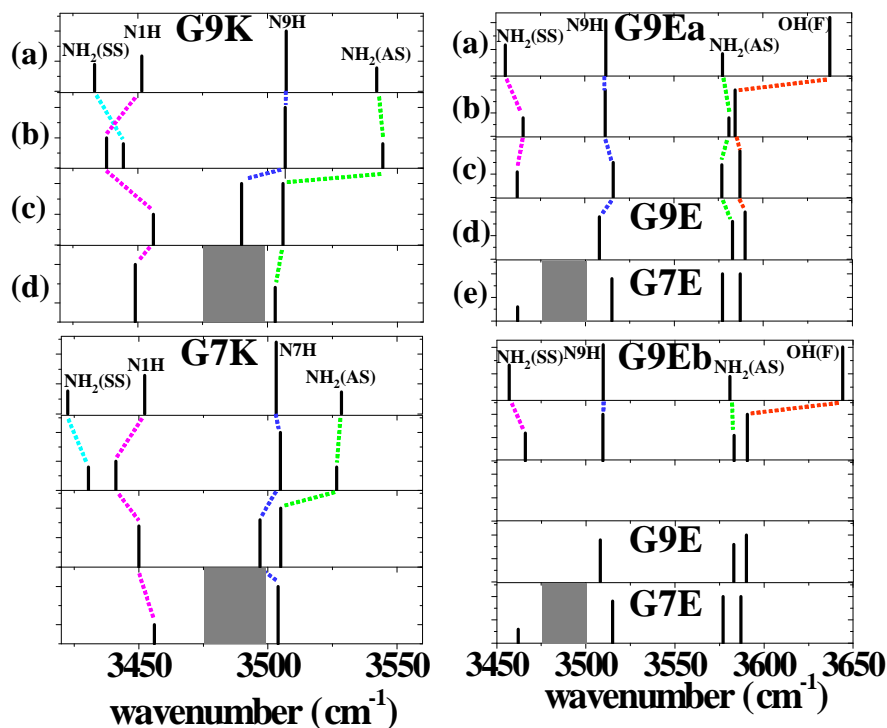
Figure 4.15: Assignments of all vibrational bands of the four (or three) different tautomers from (a) *ab initio* frequency calculations and the observed frequencies of the three groups, (b) this work, (c) de Vries, (d) and (e) Mons. The MP2/6-311++G(d,p) basis set was used for the frequency calculations. Note that the observed frequencies of the G9E and G7E tautomer, to which the Mons group assigned, were repeatedly plotted in the G9Ea and G9Eb panel, since their spectral resolution prohibited a firm assignment of the Ea and Eb tautomer. The gray boxes represent the no laser power frequency region ($3470 - 3500$ cm^{-1}) where no spectrum has been obtained. The best agreement in the frequency comparison would be the G9Eb and G9E of this study and Mons, respectively, however, the NH$_2$ (SS) band of the G9E is not observed in (d). The enol tautomer, G9E, of the IR–UV experiments has a relatively similar frequency pattern with this work, not like the keto tautomers, however, a close examination shows that the frequencies for the N9H and NH$_2$ (SS) bands are still not in good agreement with those observed in this study (see Figure 4.14 for clarity). However, a direct comparison of the G7E tautomer observed in (b) cannot be accomplished because of the absence of the G7E in this work. The similar frequency pattern of not only the G9Ea and G7E tautomer, but also the G9K and G7K tautomers, from de Vries and Mons, respectively, leaves more questions in the tautomer assignments.

experiments have the advantage of requiring much lower vapor pressures (10^{-6} Torr or less) than those typically used in free-jet experiments. This is important because the lower temperatures reduce the likelihood that guanine will thermally decompose. In fact no evidence of thermal decomposition of guanine is observed at the operating temperature of our pick-up cell.

In this chapter we have presented a comprehensive study of guanine tautomers isolated in helium nanodroplets. When these data are combined with results from *ab initio* calculations, we obtain definitive assignments of all 16 observed vibrational bands for the guanine tautomers in the $3400 - 3650$ cm^{-1} region of the spectrum. By orienting the molecules in the laboratory frame of reference, the vibrational transition moment angles (VTMAs) are measured for many of the observed vibrational bands to aid in the assignment of the specific tautomer vibrational bands. Further conclusive assignment is supported by an electric field dependent approach for each tautomer, taking advantage of the fact that the dipole moments for the four tautomers of guanine are all quite different. The firm assignment leads us to determine the relative populations for the four structures of guanine as 1 : 0.8 : 0.4 : 0.3 for the G7K, G9K, G9Ea, and G9Eb tautomers, respectively, which are in excellent agreement with those obtained from *ab initio* relative free energy calculations. These provide conclusive evidence that all four of the lowest energy tautomers, G7K, G9K, G9Ea, and G9Eb, are present in the helium droplets.

In this study, we have observed and identified the G9Eb tautomer that was missing in the gas-phase experiments discussed above [70, 182]. The difficulty in determining the structure in several experiments could be due to its almost identical relative energy difference and the similar vibrational frequencies between the two N9H enol rotamers, G9Ea and G9Eb. We also have discussed the discrepancies in the assignments of the guanine tautomers with the previous studies.

The *ab initio* frequency calculations, the electric field dependence experiments (for dipole moments), and the VTMAs were used throughout this study to confirm the assignments of the various modes for the four tautomers of guanine. However, more theoretical work is needed to understand the nonplanarity of the N1H groups of the keto forms (G9K and G7K), where the VTMAs of experiment and theory show unusually large differences depending on the basis set. Nevertheless, the present study clearly shows the power of using VTMAs and dipole moments in assigning vibrational spectra and determining molecular structure, particularly when more than one isomer is present in the sample.

Chapter 5

Infrared Laser Spectroscopy of Uracil and Thymine in Helium Nanodroplets

Vibrational spectra are reported in the N–H stretching region for uracil and thymine monomers in helium nanodroplets. Each monomer shows only a single isomer, the global minimum, in agreement with previous experimental and theoretical studies. The assignment of the infrared vibrational bands in the spectra is aided by the measurement of the corresponding vibrational transition moment angles (VTMAs) and *ab initio* frequency calculations.

5.1   Introduction

Uracil and its methylated molecule, thymine (5-methyluracil), are the simplest of the naturally occurring nucleic acid bases (NABs) of RNA and DNA, respectively, and as such represent benchmark systems for both experimental and theoretical studies. In the present study we focus our attention on isolated molecules, such that direct comparisons can be made between theory and experiment. The theoretical literature on uracil and

thymine monomers is in agreement that the lowest energy tautomer of each are the diketo forms shown in Figure 5.1, and that they are well separated from the higher energy structures [203–207]. The next lowest energy enol tautomer, U(T)E32, lies approximately 40 kJ/mol above the global minimum on the potential energy surface. As a result, experiments carried out at the moderate temperatures needed to evaporate uracil and thymine are expected to show only the diketo tautomers, UK and TK, respectively. This is confirmed by rotationally resolved microwave [175, 176, 208] and infrared laser [209] studies of jet cooled uracil and/or thymine, which show only the diketo form.

Nucleic acid bases (NABs) are known to be difficult to investigate by electronic spectroscopy owing to the rapid non-radiative deactivation of the S_1 state, which makes the associated spectra broad with low quantum yields for fluorescence [210–215]. In the present study we make use of infrared laser spectroscopy to obtain vibrational spectra of the diketo tautomers of uracil and thymine, in the N–H stretching region of the spectrum. The molecules are solvated in helium nanodroplets, which provide the cooling necessary to obtain high-resolution spectra. Pendular-state spectroscopy [103–106] is used to orient the molecules in a strong electric field, allowing for the measurement of vibrational transition moment angles (VTMAs), explained in detail below.

5.2   Experimental Methods

The apparatus used in the present study has been described in detail elsewhere [102]. Helium nanodroplets are formed by expanding helium gas (99.9999%) through a 5 μm diameter nozzle cooled to approximately 20 K by a closed cycle helium refrigerator. Uracil and thymine are added to the droplets as they pass through an oven maintained at approximately 160 °C and 175 °C, respectively, corresponding to vapor pressures between 10^{-6} and 10^{-5} Torr (Aldrich, 98% purity). The pick-up process is governed
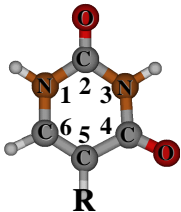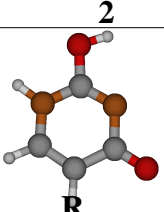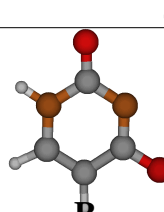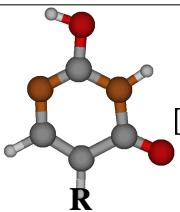
Figure 5.1: The *ab initio* structures and relative energies (MP2/aug-cc-pVDZ level) of the various tautomers of uracil (U) and thymine (T). Keto and enol forms are classified by certain functional groups, namely C=O (keto) and O–H (enol), in the pyrimidine base. In addition, the naming scheme is followed by U or T for uracil or thymine and the K or E for keto or enol forms. Next, the following numbers identify the nitrogen position (1 or 3) to which hydrogen is attached, and very similarly the certain carbon position (2 or 4) to which the O–H is attached. The values in the brackets give the energies relative to U(T)K in kJ/mol with a harmonic zero point energy correction. Uracil and thymine is classified by the substituent, R = H and CH_3, respectively.

by Poisson statistics, allowing us to control the average number of molecules captured by the droplets [42]. In order to remove water from the solid uracil/thymine samples, they were held in the oven overnight at 110 °C.

The N–H stretching vibrations of uracil/thymine were excited using a Periodically Poled Lithium Niobate Optical Parametric Oscillator (PPLN–OPO) (LINOS Photonics). Several external etalons and a wavemeter were used to calibrate the spectra. A multi-pass cell [102] was used to reflect the laser across the droplet beam approximately 20 times in order to increase the excitation efficiency [88, 101]. Two electrodes were positioned on either side of the laser interaction region so that an 80 kV/cm DC electric field could be applied. The IR excited molecules undergo rapid vibrational relaxation to the helium, resulting in the evaporation of several hundred helium atoms. A bolometer detector [165] was used to monitor the resulting depletion of the droplet beam. The spectra reported here were recorded by amplitude modulating the laser and using phase sensitive detection methods.

Previous studies [37, 108, 120, 155, 167] have shown that the electric dipole moment of a polar molecule can be oriented in a large DC electric field. In the present study we make use of this method to measure vibrational transition moment angles (VTMAs) [79, 86–89] for both uracil and thymine. VTMAs are defined as the angles between the permanent dipole moment and the transition moment vectors for the various vibrational modes of the molecule. The VTMAs are experimentally determined by measuring the band intensities for the various vibrational modes, as a function of the laser polarization direction relative to the DC electric field. For a vibrational mode with its transition moment parallel to the permanent dipole moment, parallel polarization of the laser will result in a significant increase in the band intensity compared to the zero-field case, and perpendicular laser polarization will result in a decrease in intensity. A quantitative description of this effect requires that the orientation distribution for the

permanent dipole moment be known. This distribution depends upon the magnitude of the dipole moment, the applied electric field, the rotational constants and temperature of the molecule in question. The methods for calculating these distribution have been discussed in detail previously by Kong *et al.* [128–131]. For the systems discussed herein, the experimental spectra are broadened to a Lorentzian line shape. Although this means that the rotational constants cannot be directly determined from the experimental spectra, it also means that the overall orientation distribution is less sensitive to the rotational constants. In this case we use the *ab initio* rotational constants, divided by a factor of three to account for the effects of the helium [88, 99], to determine the orientation distribution needed to calculate the VTMAs. This approach works rather well given that the rotational temperature of the droplets, and hence the rotational temperature of the molecules, are well known, namely 0.37 K [18, 22]. A detailed discussion of how the experimental VTMAs are extracted from the integrated areas of the zero-field, parallel and perpendicular polarization spectra is given elsewhere [79, 86, 87, 89, 216].

5.2.1 *Ab initio* Calculations

Although both the uracil and thymine have been the subjects of numerous previous *ab initio* calculations, none of these have reported permanent dipole or transition dipole directions needed for comparison with the experimental VTMAs. For this reason, we carried out extensive *ab initio* calculations for the various tautomers of uracil and thymine, using Gaussian 03 [169]. Unless otherwise specified, the calculations were performed using second order Møller-Plesset perturbation theory (MP2) with an aug-cc-pVDZ basis set. Figure 5.1 shows the four lowest tautomers of uracil and thymine, whose relative energies are listed in kJ/mol for the equilibrium geometries, with a harmonic zero point energy correction.

Figure 5.2 shows the lowest energy diketo form of uracil and thymine monomer, onto which are superimposed vectors representing the directions of the permanent electric dipole moments (solid arrow) and the vibrational transition moments (empty double ended arrows).
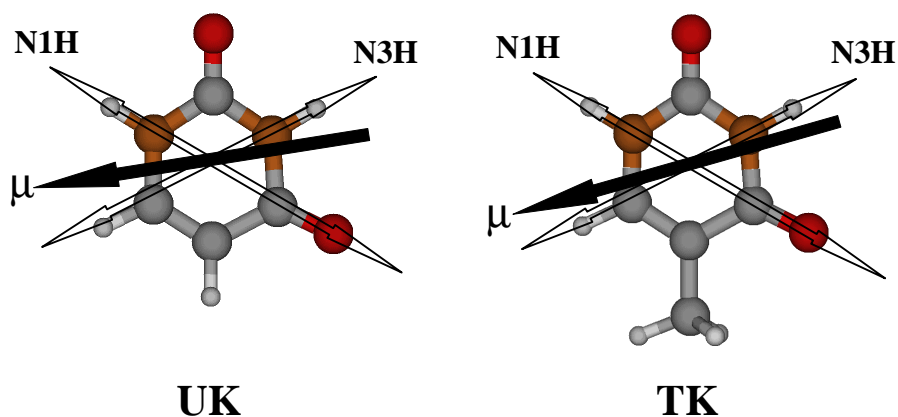
Figure 5.2: The lowest energy tautomer of uracil (UK) and thymine (TK), showing the corresponding directions of the permanent electric dipole moments (solid arrow) and the vibrational transition moments (empty double ended arrows) for the various vibrational modes. The magnitudes of these moments are given in Table 5.1.

5.3   Results

We begin this discussion by considering the spectra, Figure 5.3, of the uracil monomer in the region of the N–H stretching vibrations. In light of the published experimental [175,176,208,209] and theoretical [203–207] work on this system, we expect to see only a single tautomer, namely the diketo form. As shown in Figure 5.1, the diketo tautomers

of uracil/thymine possess two N–H vibrational modes, referred to hereafter as N1H and N3H. The upper panel in Figure 5.3 shows an experimental spectrum of uracil monomer in helium droplets that spans both the N1H and N3H stretching vibration region. The other four panels show the *ab initio* spectra (all scaled by a factor of 0.958458 with an aug-cc-pVDZ basis set) for the four lowest energy tautomers of uracil. Figure 5.4 shows the corresponding data for the thymine tautomers, which are clearly similar to the spectrum of uracil, both experimentally and theoretically. The two main peaks in the both spectra, Figure 5.3 and 5.4, are easily assigned by comparison with the scaled *ab initio* calculations to be the N1H and N3H vibrations of the monomer. The vertical bars in Figure 5.4 are the calculated intensities of these two vibrational modes of each thymine tautomer, scaled by a factor of 0.95877 to obtain the best overall agreement between theory and experiment, particularly for the free N1H stretch. The weaker bands in the spectrum are assigned to the uracil dimer, given that they grow in at higher oven temperatures, indicating that they require the pick-up of more than one uracil/thymine molecule. A detailed discussion of these peaks is given below.

Figure 5.5 shows the three different laser polarization spectra of uracil in the N1H region corresponding to (a) a pendular spectrum with parallel polarization, (b) a zero-field spectrum, and (c) a pendular spectrum with perpendicular polarization (electric field strength being 80 kV/cm), all plotted on the same absolute intensity scale. Using the methods discussed elsewhere [79,86–89], we made use of the integrated areas under the peaks to determine experimental VTMAs for the monomer, yielding 43° and 17° for the N1H and N3H modes, respectively. These results are in excellent agreement with the result of *ab initio* calculations (MP2/aug-cc-pVDZ) for the diketo tautomer, which gave 43° and 15°, respectively (see Table 5.1). Although there are no real surprises here since the calculated frequency of N1H of the diketo form is also in very good agreement with the experimental value, these results do provide another example in
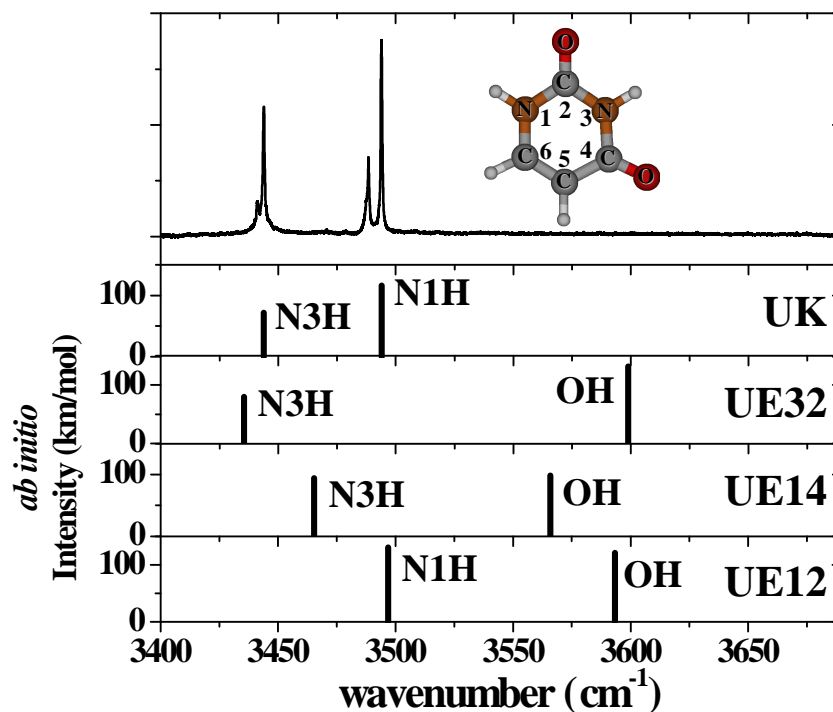
Figure 5.3: A survey spectrum of uracil isolated in helium droplets. The *ab initio* vibrational spectra for the four lowest energy tautomers of uracil are shown in separate panels below the experimental spectrum. The vertical bars in the bottom panels summarize the *ab initio* frequencies and intensities for the N1H and N3H modes of the various tautomers. The harmonic ab initio calculations were all scaled by a factor of 0.958458 to obtain the best overall agreement between theory and experiment, particularly for the free N1H stretch of the UK tautomer.
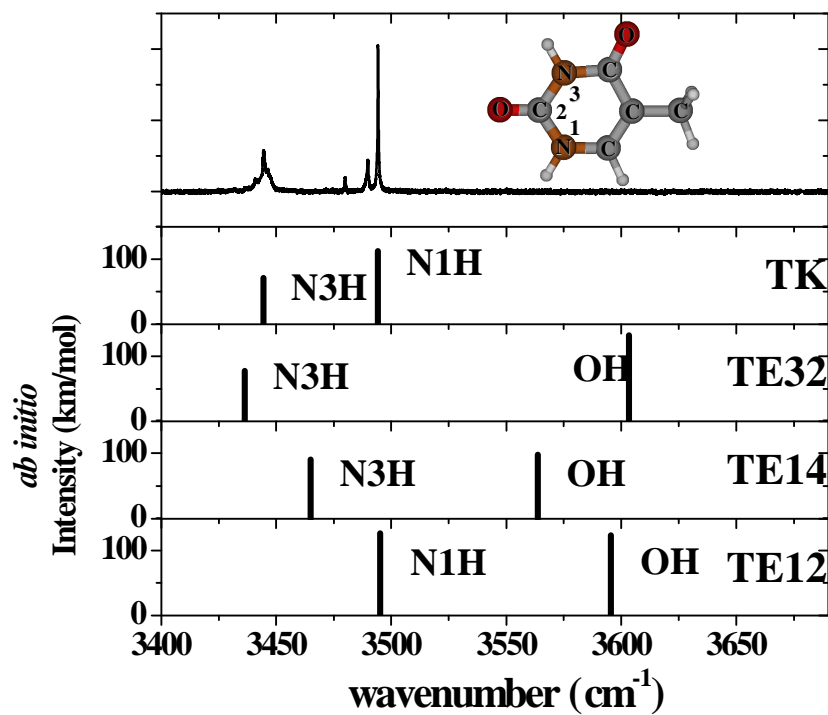
Figure 5.4: A survey spectrum of thymine isolated in helium droplets. The *ab initio* vibrational spectra for the four lowest energy tautomers of thymine are shown in separate panels below the experimental spectrum. The vertical bars in the bottom panels summarize the ab initio frequencies and intensities for the N1H and N3H modes of the various tautomers. The harmonic *ab initio* calculations were all scaled by a factor of 0.95877 to obtain the best overall agreement between theory and experiment, particularly for the free N1H stretch of the TK tautomer.

which the experimental and *ab initio* VTMAs are in quantitative agreement, generating more confidence that this is a general method that can be used as an aid in assigning the spectra of unknown species, which we have already shown with the uracil–water complexes [87] (see Chapter 7).
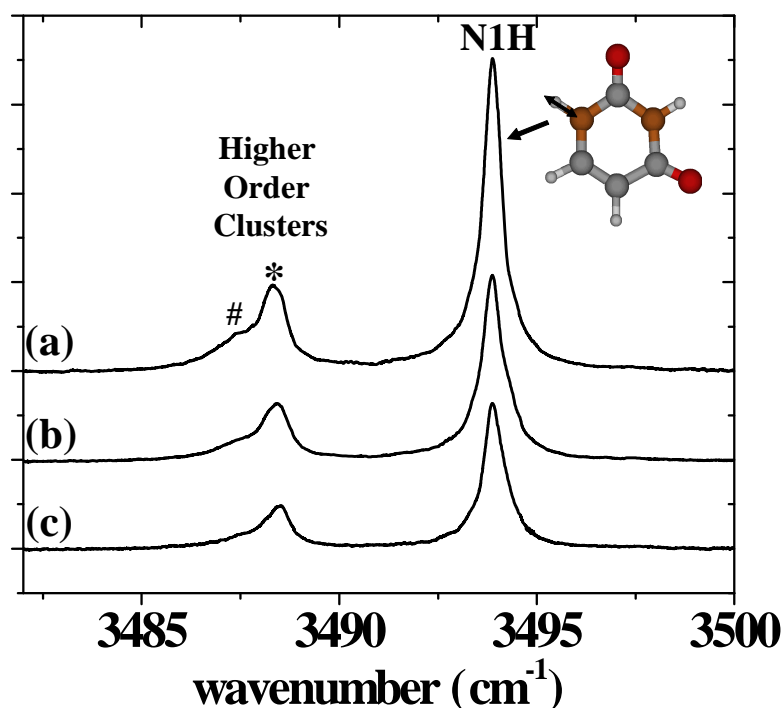
Figure 5.5: An expanded view of the N1H stretching region of the uracil (UK) spectrum. Spectra (a), (b), and (c) correspond to parallel polarization, zero-field, and perpendicular polarization, respectively. The two bands marked with an "*" and a "#" are due to the uracil dimer and trimer, respectively.

The oven temperature dependence of the intensities of the three bands in Figure 5.5 is shown in Figure 5.6. The band assigned to the N1H stretch mode clearly optimizes at lower temperatures, consistent with the fact that lower vapor pressures are required for the pick-up of a single molecule. The other two bands are assigned to the higher order self associated complexes of uracil and require higher vapor pressures for optimum signals. The other two bands, labeled with an "*" and a "#", are assigned to dimer and trimer, respectively. The vapor pressure in the pick up region of the oven (scattering

box, see Figure 2.3) can be varied to pick up the desired number of uracil molecules, according to the associated Poisson statistics [42]. The disappearance of both bands at lower oven temperatures indicates that the bands are associated with higher order uracil complexes. Indeed, the oven temperature dependence of the N–H stretching spectrum of uracil revealed the presence of the band marked with an "*" clearly arises from the dimer. A shoulder on the peak marked with a "#" optimizes at an even higher temperatures, which we presume is associated with the uracil trimer. The small frequency shifts associated with these two bands suggest that these N1H modes are associated with non–hydrogen bonded vibrations, which is also very similar to the case of the N3H stretching modes (see Figure 5.7).
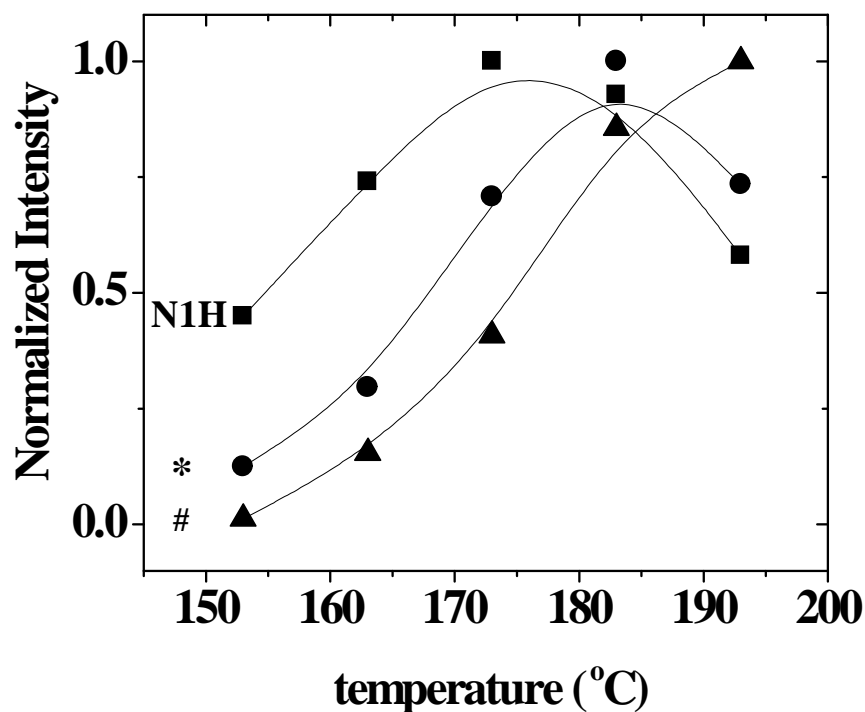
Figure 5.6: The oven temperature dependence of the intensities of the three bands shown in Figure 5.5. The N1H band clearly optimizes at lower temperatures, consistent with the fact that lower vapor pressures are required for the pick-up of a single molecule. The other two bands, "*" and "#", are assigned to the dimer and trimer, respectively, which require higher vapor pressures for optimum signals.
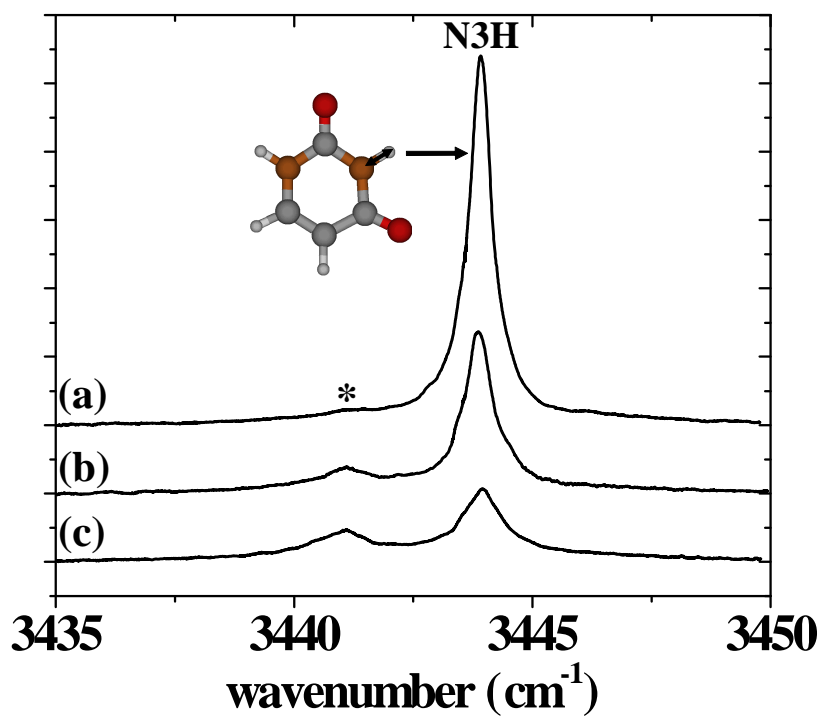
Figure 5.7: An expanded view of the N3H stretching region of the uracil (UK) spectrum. Spectra (a), (b), and (c) correspond to parallel polarization, zero-field, and perpendicular polarization, respectively. The band marked with an "*" is due to the uracil dimer.

Figure 5.8 shows the three different laser polarization spectra of thymine in the N1H region recorded with (a) an applied 80 kV/cm DC electric field directed parallel to the laser polarization direction, (b) zero electric field, and (c) an applied 80 kV/cm DC electric field directed perpendicular to the laser polarization direction. The peak marked with an "*" only appears at high oven temperatures, which indicates that the peak should be assigned to be the thymine dimer, as shown in the case of uracil (see Figure 5.5 and 5.6). We also made use of the integrated areas under the peaks to determine experimental VTMAs for the monomer, yielding 52° and 8° for the N1H (Figure 5.8) and N3H (Figure 5.9) modes, respectively. These results are in excellent agreement with the result of *ab initio* calculations (MP2/aug-cc-pVDZ) for the diketo tautomer, which gave 52° and 13°, respectively (see Table 5.1).
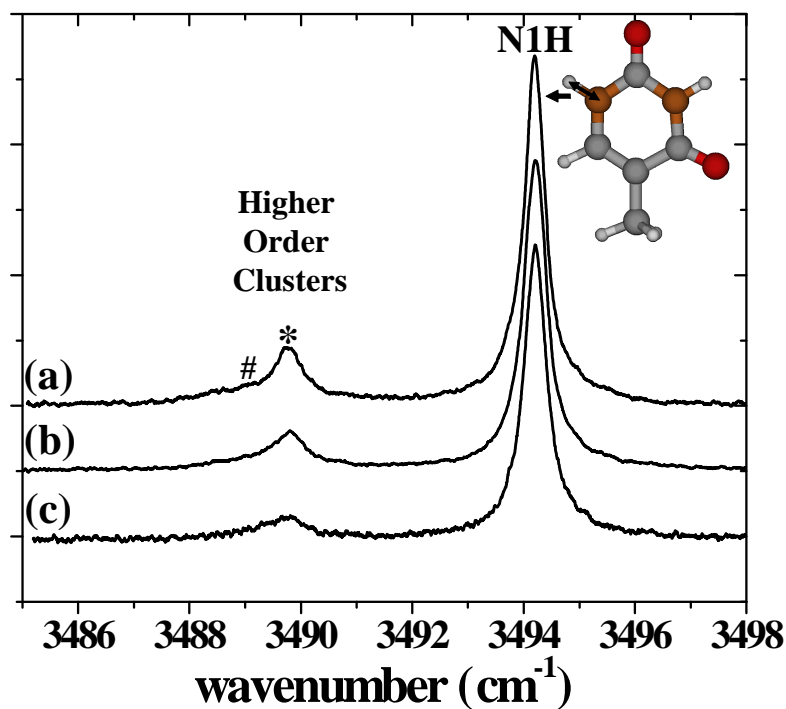
Figure 5.8: An expanded view of the N1H stretching region of the thymine (TK) spectrum. Spectra (a), (b), and (c) correspond to parallel polarization, zero-field, and perpendicular polarization, respectively. The two bands marked with an "*" and a "#" are due to the thymine dimer and trimer, respectively.
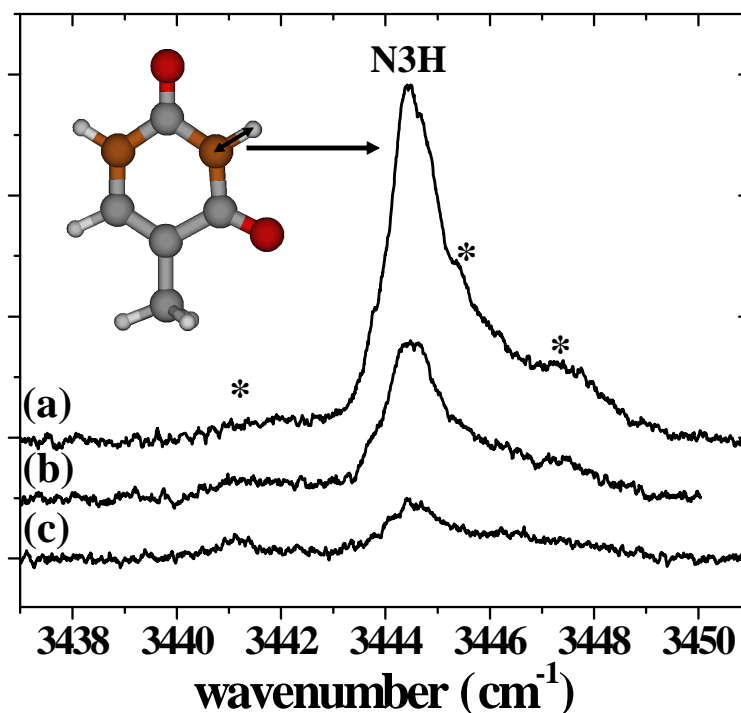
Figure 5.9: An expanded view of the N3H stretching region of the thymine (TK) spectrum. Spectra (a), (b), and (c) correspond to parallel polarization, zero-field, and perpendicular polarization, respectively. The bands marked with an "*" are due to the thymine dimers.

5.4   Summary

In this study we report high-resolution infrared laser spectra of isolated uracil and thymine monomers in helium nanodroplets. By orienting the target molecules in the laboratory frame of reference with a strong DC electric field, we measured the VTMAs of the uracil and thymine monomers. The calculated frequencies are very well matched with the observed frequencies, and the VTMA assignments provide additional and unambiguous assignment for the uracil and thymine molecules. The survey scans shown in Figure 5.3 and 5.4 of both uracil and thymine show that only the global minimum tautomer (diketo form) of the uracil and thymine is present in the helium nanodroplets.

Table 5.1: A summary of the experimental and calculated vibrational frequencies and VTMAs for the various isomers of uracil and thymine

	Scaled[a] freq. (cm^{-1})	Exp. freq. (cm^{-1})	IR intensity (km/mol)	Assignment	ab initio VTMA (°)	Exp. VTMAs (°)	μ (D)	Relative energy (kJ/mol)
UK							4.38	0
	3493.9	3493.9	116.5	N1H	43	43		
	3443.8	3443.9	72.2	N3H	15	17		
UE32							3.02	40.8
	3599.0	–	131.9	OH	3	–		
	3435.4	–	80.0	N3H	79	–		
UE14							4.84	44.8
	3565.8	–	98.1	OH	41	–		
	3465.3	–	94.2	N1H	85	–		
UE12							6.46	72.2
	3593.3	–	121.0	OH	66	–		
	3496.8	–	130.3	N1H	11	–		
TK	[b]						4.34	0
	3494.3	3494.2	112.3	N1H	51	52		
	3444.5	3444.5	70.9	N3H	8	13		
TE32							2.54	38.9
	3603.3	–	132.8	OH	10	–		
	3436.3	–	78.1	N3H	74	–		
TE14							5.27	48.1
	3563.7	–	97.8	OH	45	–		
	3464.9	–	90.3	N1H	90	–		
TE12							6.09	69.3
	3595.4	–	123.6	OH	63	–		
	3495.2	–	126.4	N1H	14	–		

[a] The *ab initio* calculations were performed at the MP2/aug-cc-pVDZ level and the scaled frequencies were obtained by multiplying the harmonic frequencies by a factor of 0.958458.

[b] The *ab initio* calculations were performed at the MP2/aug-cc-pVDZ level and the scaled frequencies were obtained by multiplying the harmonic frequencies by a factor of 0.95877.

Now that we have well characterized spectra of uracil and thymine monomer, the challenge for the future is the study of the dimers of the given systems, which would be more biologically important systems. The formation of hydrogen bonds between pairs of NABs is fundamental to the structure and dynamics of DNA and RNA and is the subject of continued intensive study. Although the Watson-Crick base pairs are justifiably often the center of such attention, NAB dimers can also provide important information concerning such hydrogen-bonding. For example, N–H $\cdots$ O–C hydrogen bonds are of fundamental importance and are amenable to study in the simplest of these systems, namely the uracil and thymine dimers.

Chapter 6

Nonplanarity of Adenine from Infrared Laser Spectroscopy in Helium Nanodroplets

Infrared laser spectroscopy of adenine in helium nanodroplets is described in this chapter. We show that there is only one tautomer of adenine, the global minimum structure, observed and characterized by using *ab initio* calculations and the measurement of vibrational transition moment angles (VTMAs) for the various vibrational modes of the adenine monomer. In this work, we also studied the nonplanarity of adenine with the aid of the VTMA analysis on the amide group of adenine. The experimental VTMAs of NH_2 asymmetric stretch (AS) match with *ab initio* calculated values under Møller-Plesset perturbation theory at the 2nd order level (MP2) with a non-planar structure, but mismatch with those calculated under the density functional theory at Becke's three parameters hybrid functional method (B3LYP), which predicts adenine a perfectly planar structure. Nonplanarity has been further confirmed by studying the evolution of VTMAs with the dihedral angle $N^1C^6N^{10}H^{14}$, and by the comparisons between MP2 and B3LYP calculations under planar and non-planar constraints.

6.1 Introduction

Although nucleic acid bases (NABs) are well known as the building blocks of life [144, 174], the detailed structure of isolated NABs still remains to be solved. NABs were believed to be perfectly planar for many years, until the predictions of nonplanarity of the amino group on the NABs in the early 1990's [135, 137, 138, 152, 173, 217–221]. Hobza and co-workers [137, 138, 173] conducted a series of *ab initio* studies on the non-rigidity of NABs, and showed that the non-planar structure was indeed more stable than the planar structure. Although a large inertial defect of adenine was observed in a microwave study [177], its cause was not directly related to the nonplanarity of adenine. Other evidence also supports nonplanarity [135, 221–224] which is caused by the partial sp^3 hybridization of the aminogroup nitrogen atom [137, 217]. Unfortunately, due to the experimental difficulties associated with the isolation of single molecules as well as in sufficient experimental spectral resolutions, no direct experimental evidence for the nonplanarity of isolated NABs has been provided. The existence of the nonplanarity of amino groups has only been proved by the spectroscopic studies on similar compounds, such as the inversion-torsion frequencies of aniline and 2-aminopyrimidine [225, 226].

We have recently discussed a method for determining vibrational transition moment angles (VTMAs) for isolated molecules [79, 86–89] and showed that these VTMAs are highly dependent on the molecular structure and are rather insensitive to the basis sets used in the *ab initio* calculations. Furthermore, no scaling factor is needed to account of the anharmonicity [79, 86–89]. In this work, improved signal levels have been obtained by using a periodically poled lithium niobate optical parametric oscillator (PPLN–OPO) which provides he first direct experimental evidence of the nonplanarity of the amino group in isolated adenine.

Although the recent systematic theoretical studies [227–230] on the tautomers of adenine provide a detailed information on the energetic ordering of the various tau-

tomers, the information about the permanent dipole and transition dipole directions needed for the comparison with the experimental VTMAs has never been reported. Therefore, we conducted extensive *ab initio* calculations for the 8 amino and imino tautomers of adenine, using Gaussian 03 [169]. Figure 6.1 shows these tautomers of adenine with their relative equilibrium energies listed in brackets (kJ/mol), with harmonic zero point energy corrections at the MP2/6-311G++(d,p) basis set. Detailed information about the *ab initio* VTMAs, obtained from MP2/6-311++G(d,p) basis set of the tautomers in Figure 6.1 is listed in Table 6.1.

6.2   Experimental and Computations

The infrared spectrum of isolated adenine was carried out by solvating adenine in the liquid helium nanodroplets. The experimental apparatus has been described elsewhere in detail [102]. Superfluid helium droplets have been shown to be an ideal spectroscopic matrix [4], resulting in high-resolution spectra completely devoid of hot bands and vibrational frequencies unperturbed from those in the gas-phase. Nanodroplets with a mean size of 3,000 helium atoms were formed by expanding ultrahigh purity helium (99.9999%) from a 5 μm diameter orifice, operated at 50 atm pressure and a temperature of 20.5 K. Adenine was doped to the droplets by pick-up [164] in a scattering-box oven (Figure 2.3), the temperature of which was optimized for the capture of a single molecule ($\sim$175 °C). Upon being captured by the droplets, adenine is quickly cooled to the 0.37 K temperature of the droplets [18, 22].

A periodically poled lithium niobate (PPLN) cw–OPO [159, 160] IR laser with a 70 mW power from Linos Photonics was used for the most of the measurements. The signal is enhanced by the use of a multipass cell [102]. Vibrational excitation of the solvated molecules results in the evaporation of several hundred helium atoms. The resulting laser induced decrease in the energy of the droplet beam is detected by a

		N9H	N7H	N3H	N1H
AMINO		A9 (0.0)	A7 (34.0)	A3 (35.0)	A1 (75.6)
IMINO	**cis (a)**	A9Ia (54.7)	A7Ia (83.5)		
	trans (b)	A9Ib (77.8)	A7Ib (73.7)		

MP2/6-311++G**
$\triangle$E (kJ/mol)

Figure 6.1: The *ab initio* structures and relative energies (MP2/6-311++G(d,p)) of the various tautomers of adenine (A). Amino and imino tautomers are classified by the functional groups attached to the carbon at position 6 of the purine base, namely NH_2 (Amino) and N–H (Imino). In addition, the naming scheme is followed by "A" for adenine and the particular nitrogen position (9, 7, 3, or 1) to which a hydrogen is attached. Next, "I" stands for imino form. The imino forms have two rotational orientation of the NH group, which are cis (a form) and trans (b from) to the five-membered ring. The values in the brackets give the energies relative to A9 in kJ/mol with a harmonic zero point energy correction at the MP2/6-311++G(d,p) level of theory. The atom numbering for A9 is shown at the right lower corner as an example.

Table 6.1: A summary of ab initio vibrational data for the adenine tautomers. All calculations were performed at the MP2/6-311++G(d,p) level of theory.

	Harmonic frequency (cm^{-1})	IR intensity (km/mol)	Assignment	*ab initio* VTMA $(^{\circ})$	Dipole moment μ, (Debye)
A9					2.8
	3733.7	52.7	NH$_2$ (AS)	21	
	3666.4	112.8	N9H	59	
	3602.3	73.7	NH$_2$ (SS)	76	
A7					6.7
	3686.5	32.5	NH$_2$ (AS)	61	
	3667.7	85.3	N7H	15	
	3570.9	37.0	NH$_2$ (SS)	54	
A3					4.1
	3740.9	67.3	NH$_2$ (AS)	10	
	3608.3	45.3	N3H	79	
	3603.0	178.5	NH$_2$ (SS)	88	
A1					8.6
	3686.6	45.5	NH$_2$ (AS)	39	
	3619.6	84.3	N1H	21	
	3569.0	66.6	NH$_2$ (SS)	62	
A9Ia					3.9
	3660.6	108.9	N9H	14	
	3611.7	76.0	N1H	57	
	3533.7	25.1	N10H	19	
A9Ib					4.6
	3664.0	108.3	N9H	52	
	3619.4	46.0	N1H	78	
	3493.2	7.9	N10H	7	
A7Ia					3.4
	3662.1	84.0	N7H	12	
	3612.7	74.4	N1H	88	
	3545.8	13.6	N10H	41	
A7Ib					3.8
	3653.8	110.0	N7H	57	
	3623.3	49.0	N1H	48	
	3512.1	10.4	N10H	36	

bolometer [165], which is positioned downstream of the laser interaction region (see Figure 2.2). The laser beam is amplitude modulated and a phase sensitive detection of the bolometer signal is used to make the spectra essentially background free. A series of external etalons and a wavemeter were used to calibrate the resulting infrared spectra.

The pendular-state spectroscopic method has been applied previously to both gas-phase [104, 120, 190, 191, 231] and helium nanodroplet [37, 108, 120, 155, 167] studies. A large DC electric field applied between the Stark electrodes results in the orientation of the permanent dipole moment of the molecule parallel to the electric field, in the limit where μE is large compared to the rotational temperature of 0.37 K [18, 22]. For a linearly polarized laser the result will be a change in the excitation efficiency, given that the molecular transition moments will also be oriented in the laboratory frame of reference. If the laser electric field is aligned parallel (perpendicular) to the DC electric field (referred to here as parallel and perpendicular polarization alignments) the corresponding change in the vibrational band intensity will depend upon the angle between the permanent dipole axis and the corresponding transition moment direction. This angle is referred to here as the vibrational transition moment angle or VTMA. For a vibrational mode which has its angle between the transition moment and the permanent dipole moment is less than the magic angle (54.7 °), a parallel polarization scan will result in an increase in the band intensity, and vice versa for the perpendicular polarization scan, compared to the corresponding band in the zero-field scan. A quantitative description of this effect requires that the orientation distribution for the permanent dipole moment be known. This distribution depends upon the magnitude of the dipole moment, the applied electric field, the rotational constants, and temperature of the molecule in question. The methods for calculating these distribution have been discussed in detail previously [128–131] (also refer to Section 2.5).

The *ab initio* VTMAs were obtained by a harmonic vibrational analysis of the

molecules with fully optimized geometries using Gaussian 03 [169]. As noted in our preliminary studies [79, 86–89], the *ab initio* VTMAs for these high frequency X–H stretches are rather insensitive to basis set, given that they are mainly determined by the structure of the molecule. For example, an N–H stretch has its transition moment directed approximately along the corresponding bond axis. Figure 6.2 shows that the *ab initio* transition moment vectors (empty double ended arrows) and permanent electric dipole moments (solid arrows) for the two tautomers (A9 and A7) are superimposed on the molecules. The density functional theory calculations (DFT) at Becke's three parameters hybrid functional method (B3LYP) has also been applied for the comparison which will be discussed below.
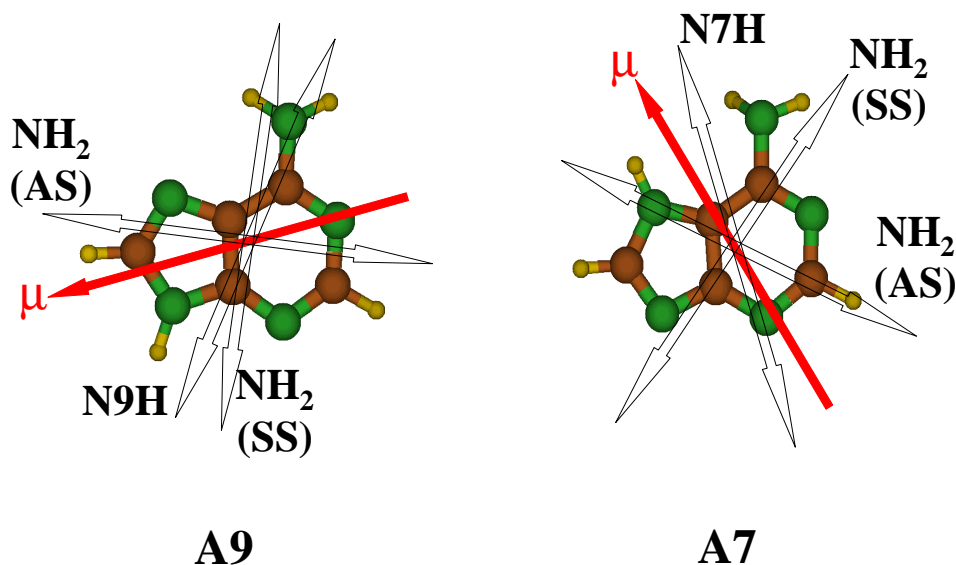
Figure 6.2: The two lowest energy tautomers of adenine (A9 and A7), showing the corresponding directions of the permanent electric dipole moments (solid arrows) and the vibrational transition moments (empty double ended arrows) for the various vibrational modes. The magnitudes of these moments are listed in Table 6.1.

6.3 Results and Discussions

The upper panel in Figure 6.3 shows an experimental spectrum of adenine in helium nanodroplets that spans the regions corresponding to the NH_2 (AS), N–H, and NH_2 (SS) modes. The middle panel shows the *ab initio* predicted spectrum and the bottom panel shows the predicted spectrum of the next lowest energy tautomer, A7. The frequencies for the scaled spectra were scaled by a factor of 0.95713 with a 6-311++G(d,p) basis set determined by scaling the calculated harmonic frequency for the N–H stretch of adenine to the corresponding experimental frequency to account for anharmonicity. The assignment of this spectrum is quite straightforward, given that the vibrational bands are widely separated. Indeed, *ab initio* frequencies calculated at MP2/6-311++G(d,p) with Gaussian 03 [169], give a convincing assignment, as guided by the dotted lines in Figure 6.3. However, even here, some frequency differences between the experimental and scaled calculations still exist, illustrating the difficulties that can arise in assigning vibrational spectra of more complicated molecules, where the spacing between vibrational levels can be smaller than the typical accuracy of the calculations [86, 87, 89]. Given that the assignments of the vibrational bands in adenine are well established, it serves as an excellent test case for illustrating the use of the present method for measuring VTMAs [79].

Figure 6.4 shows three spectra of the NH_2 asymmetric stretch (AS) region, recorded with (a) an applied DC electric field directed parallel, (b) no applied field, and (c) an applied DC electric field directed perpendicular to the laser polarization direction for the NH_2 (AS) band at 3568.2 cm^{-1}. Quantitative analysis of this band gives experimental VTMAs of $24°$ which is in excellent agreement with the *ab initio* value, $21°$.

Figure 6.5 shows another expanded region of the adenine spectrum, in this case corresponding to the most intense band, N9H, at 3509.2 cm^{-1}. Once again the three spectra correspond to (a) parallel polarization, (b) zero-field, and (c) perpendicular
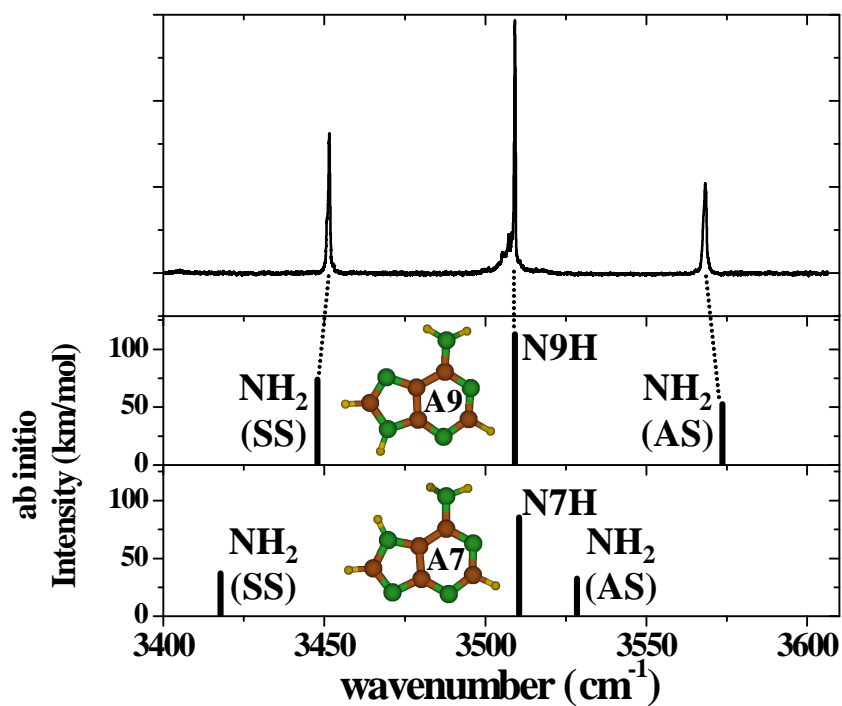
Figure 6.3: A survey spectrum of isolated adenine in helium droplets. The corresponding *ab initio* vibrational spectra for A9 and A7 (both scaled by a factor of 0.95713 with 6-311++G(d,p) basis set) are shown below the experimental spectrum. It clearly shows that the tautomer in the helium droplets is the A9 tautomer.
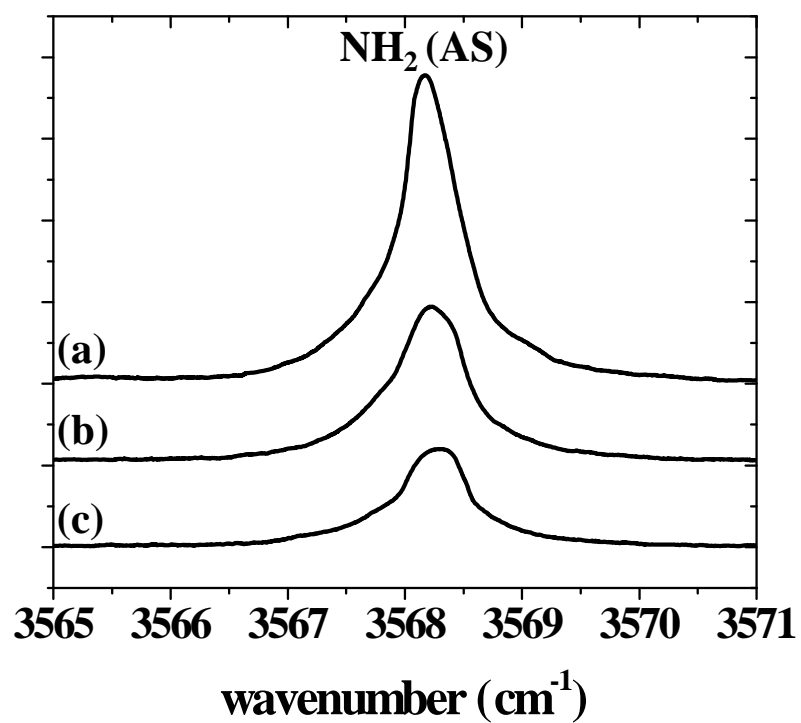
Figure 6.4: Expanded spectra of the NH_2 (AS) stretch mode of the A9 tautomer. Spectra (a), (b), and (c) were recorded parallel polarization, zero-field, and perpendicular polarization conditions, respectively.

polarization conditions. As listed in Table 6.2, the *ab initio* VTMA for this vibrational mode is $59°$, in good agreement with the experimental value, namely $63°$. The bands in the region of $3504 - 3508$ cm^{-1} are assigned to the adenine dimers or high energy tautomers. Because, higher oven temperatures result in higher adenine pressures in the scattering-box oven and thus a greater probability for picking up more than one molecule. However, as discussed in Chapter 3, higher energy tautomers are also favored at higher temperatures, so that a definitive assignment of these bands will have to await a more detailed investigation in which the vapor pressure of the sample in the pick-up cell can be varied independently of the temperature, which will be discussed in Section 9.2.1. The band at 3509.2 cm^{-1} has a temperature dependence that is consistent with the pick-up of a single molecule by the droplets, shown in Figure 6.6.
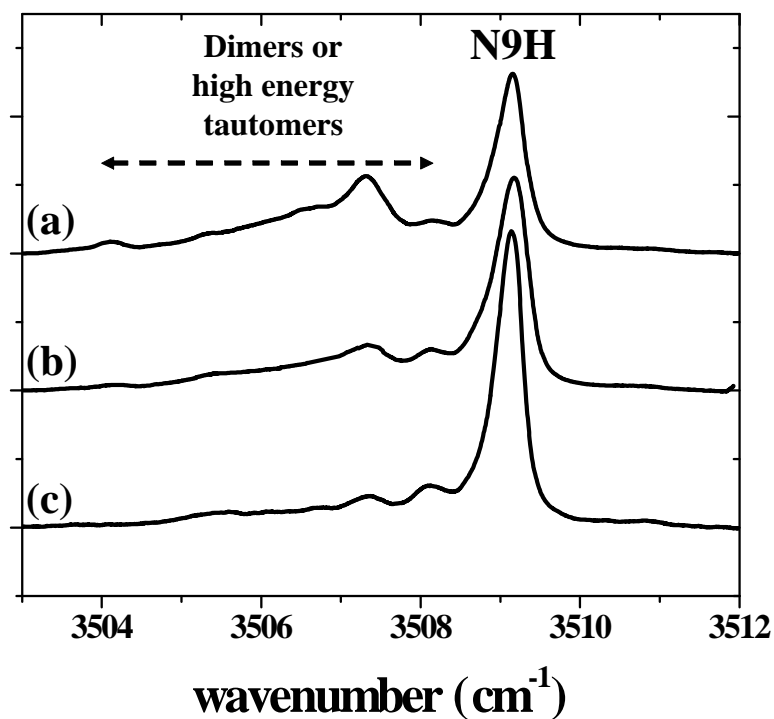
Figure 6.5: An expanded view of the N9H stretching region of the adenine (A9) spectrum. Spectra (a), (b), and (c) correspond to parallel polarization, zero-field, and perpendicular polarization, respectively. The bands in the region of $3504 - 3508$ cm^{-1} are due to the adenine dimer or higher energy tautomers.
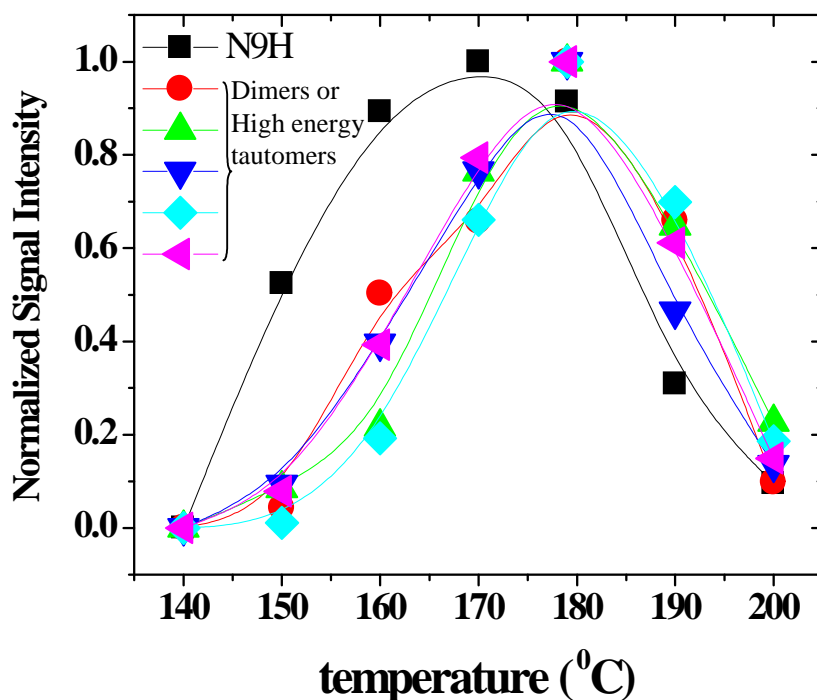
Figure 6.6: The oven temperature dependence of the intensities of the N9H band region shown in Figure 6.5. The N9H band (square) clearly optimizes at lower temperatures, consistent with the fact that lower vapor pressures are required for the pick-up of a single molecule. The other five bands are assigned to the dimer or higher energy tautomers and require higher vapor pressures for optimum signals.

We now turn our attention to the region of the spectrum corresponding to the NH_2 (SS) vibration. Figure 6.7 shows the three different laser polarization spectra of adenine in 3450 cm^{-1} region corresponding to (a) a pendular spectrum with parallel polarization, (b) a zero-field spectrum, and (c) a pendular spectrum with perpendicular polarization (electric field being 80 kV/cm). The other two bands, labeled α and β in Figure 6.7, which disappear at lower oven temperature, are assigned (see Figure 6.8) to adenine dimer or to high energy tautomers. Using the methods discussed elsewhere [79, 86–89], we made use of the integrated areas under the corresponding peaks to determine experimental VTMAs for the monomer, namely 77°, which is in excellent agreement with the result of *ab initio* value of 76°.

Table 6.2: A summary of the experimental and calculated vibrational frequencies and VTMAs for the lowest energy tautomer of adenine

	Harm.[a] freq. (cm^{-1})	Scaled[a] freq. (cm^{-1})	Exp. freq. (cm^{-1})	IR Intensity (km/mol)	Assignment	ab initio VTMA (°)	Exp. VTMA (°)	Dipole moment μ (D)
A9								2.8
	3733.7	3573.6	3568.2	52.7	NH_2 (AS)	21	24	
	3666.4	3509.2	3509.2	112.8	N9H	59	63	
	3602.3	3447.9	3451.6	73.7	NH_2 (SS)	76	77	

[a] The *ab initio* calculations were performed at the MP2/6-311++G(d,p) level and the scaled frequencies were obtained by multiplying the harmonic frequencies by a factor of 0.95713.

The oven temperature dependence of the intensities of the three bands in Figure 6.7 is shown in Figure 6.8. The band assigned to the NH_2 (SS) mode clearly optimize at lower temperatures. The other two bands, labeled α and β, which require higher vapor pressures for optimum signals, are assigned to the higher order self associated complexes or higher energy tautomers of adenine.

Up to now, we have shown that the combination of the *ab initio* frequencies and the VTMA assignment of each vibrational band of the global minimum structure of adenine (A9) gives a conclusive assignment of the adenine monomer. Now we begin discussing the issue of adenine nonplanarity. The dependency of the calculated vibrational frequencies and VTMAs of three vibrational modes [NH_2 (AS), N9H, and NH_2 (SS)] on the basis sets is shown in Figure 6.9. It is interesting to note that the smallest basis set (STO–3G) in Figure 6.9 shows an unreasonable prediction of both the VTMAs and the frequencies of the three modes, but were included here simply to show how stable the VTMAs are to basis set size. As shown in Figure 6.9(b), the calculated frequencies of the three bands fluctuate considerably at lower basis sets, but stabilize at higher basis sets, showing basis set dependence on frequency. Furthermore, the calculated
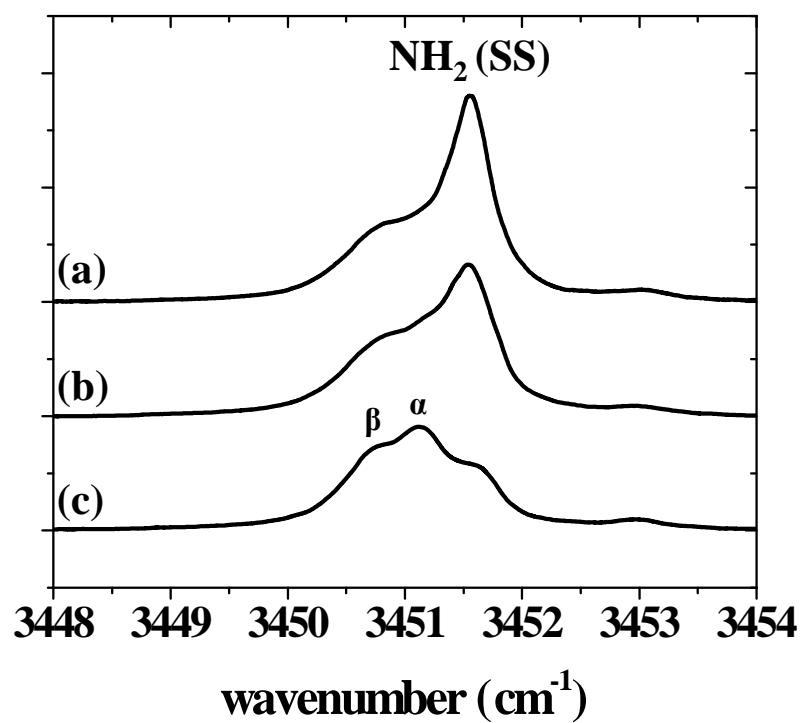
Figure 6.7: An expanded view of the NH_2 (SS) stretching region of the adenine spectrum. Spectra (a), (b), and (c) correspond to parallel polarization, zero-field, and perpendicular polarization, respectively. The bands marked with an α and β are due to the adenine dimer or higher energy tautomers.
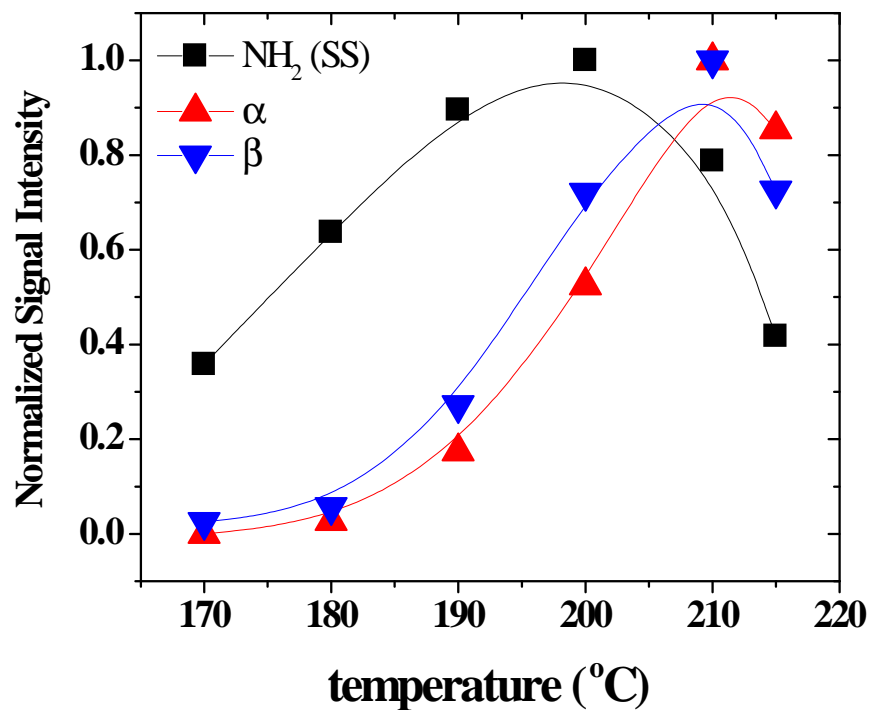
Figure 6.8: The oven temperature dependence of the intensities of the NH_2 (SS) stretch band region shown in Figure 6.7. The NH_2 (SS) (square) band clearly optimizes at lower temperatures, consistent with the fact that lower vapor pressures are required for the pick-up of a single molecule. The bands marked with an α and β are assigned to the dimer or higher energy tautomers and require higher vapor pressures for optimum signals.

harmonic frequencies have to be scaled to correct for the anharmonicity. In contrast, the calculated VTMAs are essentially independent of a basis set size, suggesting that quantitative comparisons can be made with experiment even using very modest *ab initio* calculations. This is important when applying these techniques to much larger systems, where large basis sets may be prohibitively expensive. The reason for the insensitivity of the VTMAs to basis set size can be appreciated by noting that, for the localized vibrations considered here, the transition moment directions are primarily determined by bond directionality, rather than by the detailed force fields between the atoms. Therefore, as long as the calculated structure is good, the directions of the permanent and transition moments will be rather well determined. Note that no scale factors are required in making the comparison between the experimental (horizontal colored lines in the figure) and calculated values.

It is very interesting to note that the *ab initio* VTMAs, listed in Table 6.3, show a large dependence on the type of theory used, namely MP2 and B3LYP method. The adenine tautomer, A9, showed a planar structure at the B3LYP level of theory, however, a non-planar structure was obtained with a full optimization at the MP2 level of theory. This is, while the MP2 and DFT calculations may disagree about the planarity of adenine, they both agree about the values of the VTMAs at their non-planar geometry of adenine. As shown in Table 6.3, the experimental VTMAs match much better with the non-planar structure as proposed by many theoretical studies [135, 137, 138, 152, 173, 217–221].

The nonplanarity of the A9 tautomer is reflected in the dihedral angles of $N^1C^6N^{10}H^{14}$, $N^1C^6N^{10}H^{15}$ and $C^2N^1C^6N^{10}$ (see Figure 6.1). The dihedral angles of $N^1C^6N^{10}H^{14}$ is $0°$ and $20°$ with a B3LYP and MP2 level of theory, respectively. Figure 6.10(a) and (b) show the evolution of the other two dihedral angles, namely $N^1C^6N^{10}H^{15}$ and $C^2N^1C^6N^{10}$, and the VTMAs for the corresponding vibrational bands, respectively, as
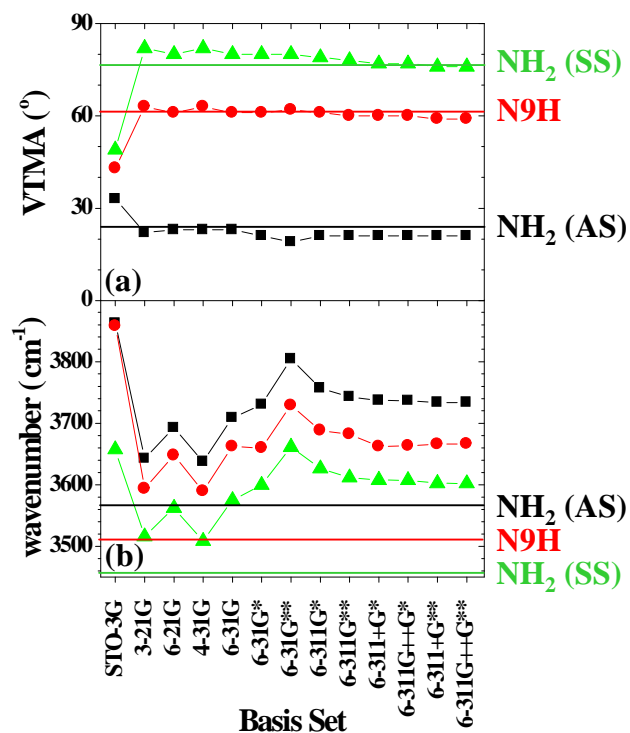
Figure 6.9: Basis set dependence of the VMTAs (a) and the vibrational frequencies (b) for the three vibrational modes of adenine, square (NH_2 (AS)), circle (N9H), triangle (NH_2 (SS)). Horizontal colored lines indicate the experimental VTMAs and frequencies for the corresponding vibrational modes.

Table 6.3: VTMA comparisons of the A9 tautomer structures obtained from MP2 and B3LYP level of theory with 6-311G++(d,p) and 6-311G(d,p) basis sets

			VTMA		
			NH$_2$ (AS) (°)	N9H (°)	NH$_2$ (SS) (°)
Exp.^{a}			24	63	77
	Theory	Basis set			
Full	B3LYP	6-311G++(d,p)	3	69	82
Optimization		6-311G(d,p)	7	71	85
	MP2	6-311G++(d,p)	21	59	76
		6-311G(d,p)	21	60	78
Non-planar	B3LYP^b	6-311G++(d,p)	20	62	79
Constraint		6-311G(d,p)	20	64	81
Planar	MP2^c	6-311G(d,p)	3	69	83
Constraint		6-31G(d,p)	2	69	84

^{a} Experimental VTMAs from this work.
^{b} Fixed the dihedral angle N^{1}C^{6}N^{10}H^{14} of adenine to 20°
^{c} Fixed the dihedral angle N^{1}C^{6}N^{10}H^{14} of adenine to 0°

function of the dihedral angle of the $N^1C^6N^{10}H^{14}$ from $0\,°$ to $30\,°$. It is worth pointing out that the adenine tautomer, A9, is constrained to be purely planar when the dihedral angle of the $N^1C^6N^{10}H^{14}$ is fixed to $0\,°$ with an MP2 level of theory, which is very similar to the result with a B3LYP method. At this geometry of the molecule (planar), the VTMAs of the all three vibrational bands, namely NH_2 (AS), N9H and NH_2 (SS) (with an MP2 method) result in the VTMAs that are very similar to those when calculated with the B3LYP method (see Table 6.3 and figure 6.10(b)). The calculations were conducted by freezing the dihedral angle, $N^1C^6N^{10}H^{14}$, while all the others were fully relaxed. As shown in Figure 6.10(a), the dihedral angles of the $N^1C^6N^{10}H^{15}$ and $C^2N^1C^6N^{10}$ indicate that the NH_2 group is out of the planar purine ring. Interestingly, the VTMAs of the three vibrational modes with a full optimization with MP2 level can also be reproduced by constraining the dihedral angle $N^1C^6N^{10}H^{14}$ of the planar adenine to $20\,°$ with a B3LYP method, shown in Table 6.3. Therefore, taking all of the experimental and theoretical data presented above together, we have incontrovertible experimental evidence of the nonplanarity of adenine.

6.4   Summary

In this study we have presented the infrared laser spectroscopic investigation of isolated adenine in helium nanodroplets. We have observed only the global minimum structure of adenine, A9, determined by using *ab initio* frequency calculations and the measurement of vibrational transition moment angles (VTMAs) for each vibrational stretching mode. Most interestingly, the experimental VTMAs of NH_2 (AS) only matches with the *ab initio* value that is obtained from a non-planar structure geometry, which shows the first direct experimental evidence for the nonplanarity of the nucleic acid base (NAB) [79]. The nonplanarity of adenine has been further confirmed by studying the evolution of the VTMAs of the NH_2 (AS) mode as the dihedral angle, $N^1C^6N^{10}H^{14}$ is
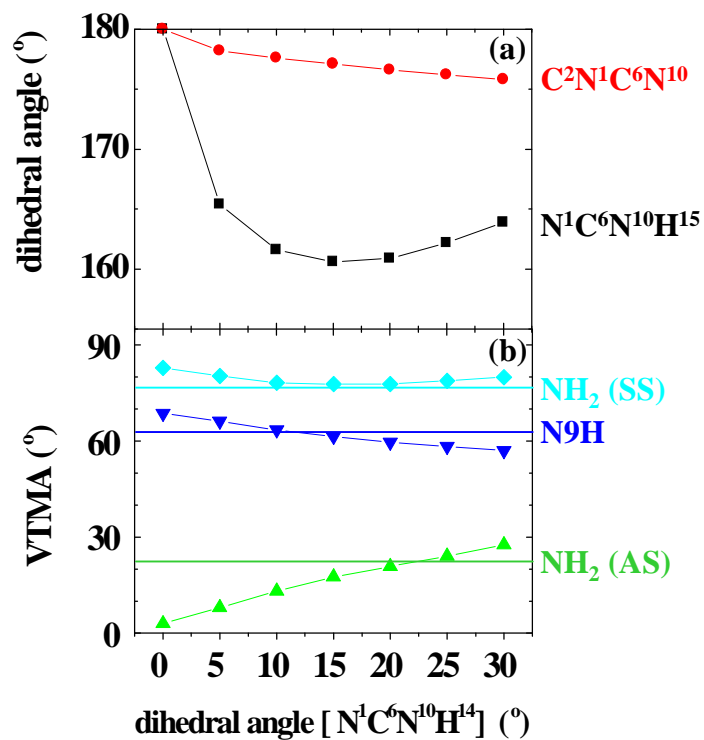
Figure 6.10: The evolution of the dihedral angles (a) and VTMAs (b) with nonplanarity of NH_2 group in adenine. The experimental VTMAs are also shown as the horizontal colored lines in the figure.

changed.

Chapter 7

Multiple Isomers of Uracil–Water Complexes: Infrared Spectroscopy in Helium Nanodroplets

Infrared laser spectroscopy is used to show that four structural isomers of the uracil–water binary complex are formed in helium nanodroplets. The assignment of the infrared spectra is aided by measurements of vibrational transition moment angles (VT-MAs) for various vibrational modes of these complexes. The experimental results are in excellent agreement with *ab initio* calculations, which had previously predicated the existence of the same four isomers. The results suggest that the relative abundances of the various isomers formed in helium droplets has more to do with the widths of the valleys in the potential surface that funnel into a particular local minimum than on the associated energetics.

7.1   Introduction

Although the importance of hydration in the structure and dynamics of DNA is well established, its specific role in various processes is still only qualitatively understood

[232–241]. Although some of these effects can be explained by treating water as a continuum dielectric, others are sensitive to the location and orientation of individual water molecules [232, 240, 242–244], illustrating the importance of treating such systems on the molecular level. For example, water assisted proton transfer in guanine [245–247] and cytosine [248–250] is thought to involve a single water molecule that forms a double hydrogen bond that bridges the proton donor and proton acceptor sites on the molecules. In such cases, where an individual water molecule plays such a pivotal role in such processes, there is considerable motivation for studying the isolated binary complexes. The present study represents our first attempt at applying this approach to the study a nucleic acid base (NAB) / water binary complex.

Considerable theoretical [242, 243, 251–257] and experimental [258–261] effort has already been devoted to the study of NAB–water complexes. In general, the theoretical studies vastly outnumber the experiments, owing to the fact that these systems are rather spectroscopically complex, particularly given that they often have multiple isomers. Nevertheless, considerable progress is being made in the development of experimental methods for studying such systems [79–82], particularly for those where theory and experiment can be applied together to gain deeper insights. In particular, infrared spectroscopy (sometimes used in double resonance with UV spectroscopy [193]) is playing an important role in these studies, given that the vibrational spectra of these complexes are highly sensitive to structure.

Although considerable progress is being made by comparing the experimental results with harmonic vibrational frequencies (scaled to approximately account for anharmonicity), such comparisons are qualitative at best. Unfortunately, more quantitative comparisons between experimental and *ab initio* vibrational frequencies are hampered by the fact that the vibrational motion of molecules occurs on a multidimensional surface (3N–6 for a non-linear molecule), making the exact solution of the nuclear dy-

146

namics formidable for even moderate size systems [243], and intractable for larger ones. At present, NAB–water complexes fall in the "large" category from this point of view. Take cytosine–water for example, where the vibrational dynamics is occurring on a 42 dimensional potential energy surface. The problem becomes critical when closely spaced vibrational bands are encountered in an experimental spectrum, making the assignment unclear. Even when spectra can be assigned, the problem remains that it is difficult to use the experimental spectra to make systematic and quantitative refinements to the molecular structure. Thus challenges remain for both experiment and theory in making these approaches more useful in refining structure.

In a recent paper we showed that the problem of assigning closely spaced vibrational bands in an experimental spectrum could be largely overcome by experimentally measuring the angles between the vibrational transition moments and the permanent dipole moment of the molecule for the associated vibrational modes [86]. These vibrational transition moment angles (VTMAs) also provide detailed structural information on the species of interest. The determination of these quantities is accomplished by orienting the molecule in a large DC electric field [37, 108, 167, 262] and measuring the integrated intensities of the vibrational bands as a function of the laser polarization direction. For the case of well isolated, high frequency X–H stretches, we find that these angles could be reliably calculated using conventional *ab initio* methods, based upon harmonic frequency calculations. Indeed, these angles are much less sensitive to the detailed multidimensional potential surface, but rather depend primarily on the structure of the molecule, particularly for these high frequency modes of the molecule. The sensitivity of the method to the molecular structure was first demonstrated for adenine, where the experimental VTMAs for the N–H and NH_2 stretches were highly dependent upon the out-of-plane NH_2 tilt angle [79]. In the present study we apply these methods to the study of the isomers of the uracil–water binary complex.

Complexes between water and uracil have become benchmark systems for the study of solvent interactions involving NABs, owing to the relative simplicity of uracil. Even here, however, *ab initio* calculations have repeatedly shown that there are at least four low energy isomers [239, 242, 243, 252, 253, 255–257, 263]. As expected for a hydrogen bonded complex, and recently revealed by Monte Carlo calculations [242, 243, 257], these complexes are not particularly rigid. Nevertheless, they are separated by rather high barriers, suggesting that they should be experimentally observable under the right conditions.

Infrared spectroscopy has been used to study the uracil–water complex in argon matrices [261] and in aqueous media having a range of dielectric constants [260]. Unfortunately, these studies did not provide conclusive structures for the associated carriers of the infrared bands. The dipole-bound anion of uracil–water has also been experimentally observed [232, 258], and mass spectra have been reported for $(uracil)_m$-$(H_2O)_n$ (m=1–3 and n=1–16) [264]. Most recently, Casaes *et al.* [265] used infrared cavity ring-down spectroscopy in a jet to observe bands associated with gas-phase uracil-$(water)_n$ complexes, which they assigned up to n=5. Once again, however, the assignment of these bands to specific isomers of these complexes was not possible. Thus, despite the obvious theoretical interest in these systems, the existing experiments have not provided the type of detailed structural information needed for making comparisons.

Figure 7.1 shows the four isomers of uracil–water, determined from *ab initio* calculations. In all cases, the water molecule forms a double hydrogen bond, bridging a proton donor and proton acceptor site on the uracil. The goal here is to use infrared laser spectroscopy of uracil–water complexes formed in helium nanodroplets [4, 18, 36, 154, 155] to identify and characterize these species. It has been amply demonstrated in previous studies [18, 36, 156–158] that the vibrational spectra of helium solvated molecules are only weakly perturbed from that in vacuum. In particular, the matrix shift is

much smaller than that typically encountered in conventional matrix isolation spectroscopy [149–153]. The low temperature of these nanodroplets (0.37 K [18, 22]) also helps to simplify the infrared spectrum. Although the complexes of interest here do not show rotationally resolved spectra, the low temperature of the helium nanodroplets facilitates the orientation of the complexes by a modest DC electric field. The latter is used to great advantage in the present study to determine VTMAs for the vibrational modes associated with the different isomers of the uracil–water binary complex.
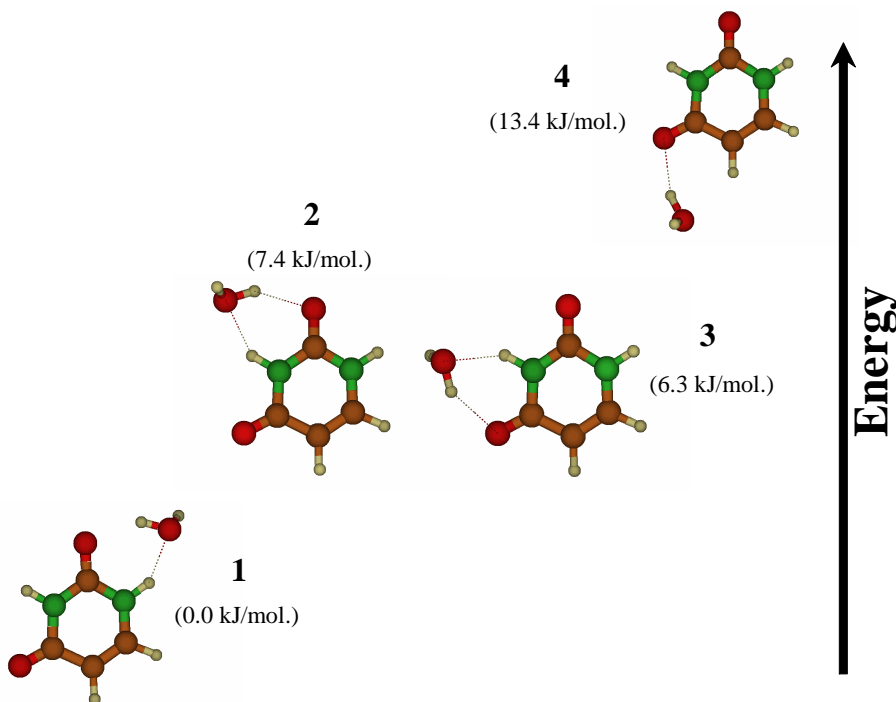
Figure 7.1: The four most stable uracil–water binary complexes, calculated at the MP2/6-311++G(d,p) level of theory. The values in the brackets give the energies relative to isomer 1, including a harmonic zero point energy correction.

7.2 Experimental Methods

The helium nanodroplet apparatus used in the present study has been discussed previously in some detail [102]. The nanodroplets are formed by expanding ultra-high purity helium gas (99.9999%) from a 5 μm diameter nozzle that is cooled by a closed cycle helium refrigerator (CTI cryogenics). The mean size of the nanodroplets is determined by the source pressure and temperature and is estimated using a published empirical formula [93]. Once formed, the nanodroplets pass through an oven containing a low vapor pressure (between 10^{-6} and 10^{-5} Torr) of uracil (Aldrich, 98% purity). Poisson statistics apply to the pick-up process, so that the number of uracil molecules captured by the nanodroplets can be controlled by varying the oven temperature (uracil pressure) [42]. For the purposes of the present study, the conditions were optimized for the pick-up of a single uracil molecule. In practice, the uracil sample was baked at 110 °C overnight in the vacuum to remove water from the sample and then heated to 180 °C to optimize for the pick-up of a single molecule. A second pick-up cell was positioned downstream of the oven and used to add water to the droplets. The doped nanodroplets then pass through a multi-pass/Stark cell [102] that is used to produce multiple crossings of the infrared laser with the helium nanodroplet beam and to apply a large DC electric field to the interaction region, respectively. Preliminary experiments were carried out using an F–center laser [266], the output power of which is approximately 5 mW in the region of interest. However, a recently acquired periodically poled lithium niobate (PPLN) cw–OPO [159,160] from Linos Photonics was used for most of the measurements, given that it has considerably higher power (70 mW). A series of external etalons and a wavemeter were used to calibrate the resulting infrared spectra.

Laser induced vibrational excitation of a helium solvated molecule or complex is followed by vibrational relaxation to the liquid helium, resulting in the evaporation of several hundred helium atoms. This causes a depletion of the helium flux to a bolometer

detector located on the droplet beam axis [165]. The spectra are made background free by amplitude modulating the laser and using phase sensitive detection methods.

The vibrational bands observed here are not rotationally resolved, presumably due to rapid vibrational relaxation. Indeed, the observed band profiles are all well represented by a Lorentzian function. This is in contrast to smaller systems, where the relaxation is slower and the molecules often rotate rather freely in the liquid helium. In these cases the spectra are often rotationally resolved and well represented by the corresponding gas-phase energy level expression, with modified rotational constants that account for the effects of the helium. As noted below, the VTMAs associated with a given vibrational band are obtained by measuring the integrated areas of the corresponding band, as a function of electric field polarization, so that this broadening is not really a problem in the present study.

7.2.1 Measurement of VTMAs

Brute force orientation has been used extensively in both gas-phase molecular beam [104, 120, 190, 191, 231] and helium nanodroplet [37, 108, 120, 155, 167] experiments. The method is based upon the application of a large DC electric field (E) to a polar molecule, such that μE is large in comparison to the rotational temperature. Under these conditions the molecule undergoes pendular-like motion and the dipole becomes strongly oriented along the field direction. In the present experiments the (linearly polarized) laser electric field is then aligned either parallel or perpendicular to the DC electric field. Hereafter, these are referred to as parallel and perpendicular polarization alignments, respectively.

Consider a vibrational mode that has its transition moment approximately parallel to the permanent dipole moment. In parallel polarization, the orientation of the permanent dipole with the DC field will also align the transition moment with the laser

electric field. As a result, the application of the electric field will result in an increase in the associated band intensity, owing to the improved alignment between the laser electric field and the transition moment of the molecules. Rotation of the laser polarization by $90°$ (perpendicular polarization) will result in a decrease in the band intensity upon application of the DC electric field. For a $0°$ VTMA and complete orientation of the molecules in the field, the band intensity will go to zero in perpendicular polarization. Alternatively, if the transition moment is perpendicular (VTMA $= 90°$) to the permanent dipole moment, the band intensity will be enhanced when the laser is polarized perpendicular to the DC field. At finite electric fields, the permanent dipole orientation distribution can be calculated using the methods discussed most comprehensively by Kong *et al.* [128–131]. This distribution is dependent upon the detailed rotational structure in the band, which is in turn dependent upon the rotational temperature. However, since the present experimental spectra are broadened beyond the rotational contour, the sensitivity of the orientation distribution to the rotational constants is rather muted. As a result, we find that the *ab initio* rotational constants, divided by a factor of three to approximately account for the effects of the helium [99], can be used to determine accurate VTMAs. This is largely the result of the fact that the rotational temperature is well determined in these experiments (namely, the droplet temperature of 0.37K [18, 22]). The normalized orientation distribution is then given by $P(cos\theta)$, Equation 2.23.

The absorption intensity for a linearly polarized laser depends upon the angle α (VTMA) between the permanent dipole and the transition dipole direction, as well as the laser polarization direction, namely; equation 2.25 and 2.26. As a result, the polarization ratio as a function of α is obtained from Equation 2.27.

Experimental VTMAs can then be determined by measuring this ratio, from the integrated band intensities for parallel and perpendicular polarization, and then using

Table 7.1: A summary of the ab initio rotational constants and dipole moments obtained for isomers 1 – 4, at the MP2/6-311++G(d,p) level. The orientation distributions needed for the VTMA measurements were determined using the droplet temperature and the ab initio rotational constants, divided by a factor of three to account for the effects of the helium.

	A GHz	B GHz	C GHz	μ Debye
UW1	1.216	0.325	0.257	3.94
UW2	0.727	0.452	0.279	4.59
UW3	0.738	0.447	0.279	3.86
UW4	0.727	0.452	0.279	2.84

equation 2.27 to determine α.

The *ab initio* VTMAs are obtained directly from a Gaussian03 calculation, which gives both the direction of the permanent dipole and all of the transition dipole moments for the various normal modes [169]. Figure 7.2 shows the four isomers of uracil–water, onto which are superimposed the various transition moment directions (dotted vectors) and the permanent dipole moment direction (solid vectors). Unless specified otherwise, the *ab initio* calculations reported here were carried out using Møller-Plesset perturbation theory at the 2nd order level (MP2) with a 6-311++G(d,p) basis set. Once again, the calculated dipole moment and rotational constants (see Table 7.1) (reduced by a factor of 3 to account for the effects of helium [99]) were used in the calculation of the orientation distribution.

7.3 Results

We begin the discussion of the uracil–water results by considering the spectrum in the free O–H stretching region, where uracil itself has no vibrational bands. Figure 7.3 shows a number of spectra corresponding to (a) pure water clusters and (b), (c), and (d) to conditions optimized for the pick up of a single molecule of uracil and water,
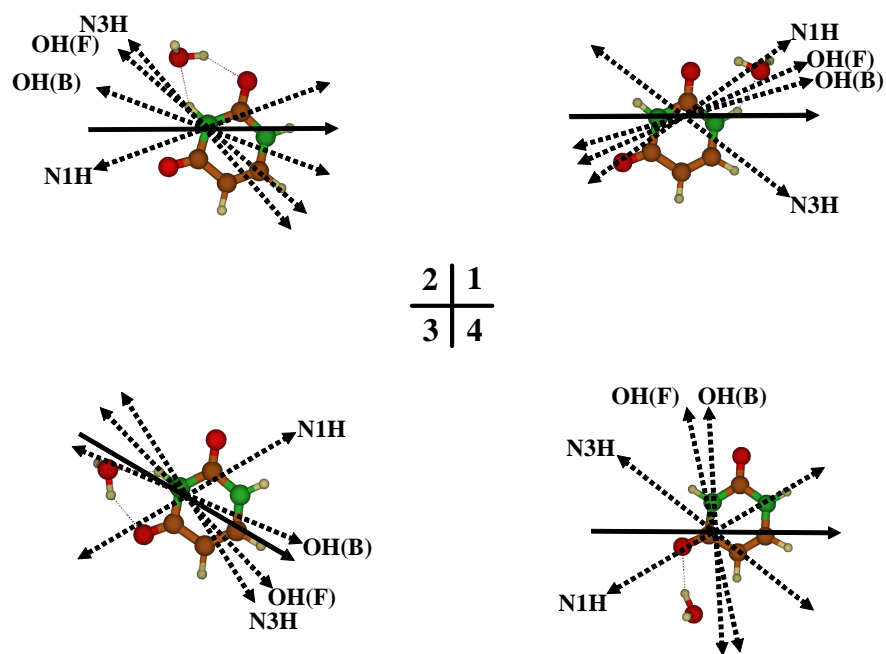
Figure 7.2: Vector diagrams showing the directions of the permanent electric dipole moments (solid single headed arrows) and the vibrational transition dipole moments (dashed double headed arrows) for the relative vibrational modes of the four uracil–water binary complexes considered here.

with perpendicular polarization, zero-field, and parallel polarization, respectively. The peaks observed in spectrum (a) are all assigned to water monomer and dimer in helium. Upon addition of uracil to the droplets, four new peaks appear in this spectral region, indicative of the formation of uracil–water complexes. The vertical arrows appearing at the bottom of Figure 7.3 indicate the harmonic *ab initio* frequencies for the free O–H vibrational modes (scaled by a factor of 0.94) for the four isomers of uracil–water. Although the overall spread of the vibrational bands in the experimental and calculated spectra are comparable, the bands are too closely spaced to make a definitive assignment based purely on the vibrational frequencies. Indeed, the four bands span a frequency range of less than 10 cm^{-1}, which is much smaller than the extent to which we can trust the *ab initio* calculations.

We begin the discussion of the assignment of these four peaks by noting that the corresponding intensities have precisely the same dependence on the uracil oven temperature, which is also the same as that for the uracil monomer bands. In addition, the water pick-up cell pressure dependence for all of these bands is the same as that of the water monomer. From this we can conclude that all four of these bands are associated with the uracil–water binary complex. Since all four of the *ab initio* isomers of uracil–water have only a single free O–H stretch each, the most obvious assignment of these bands is to four isomers.

Although the scaled *ab initio* vibrational frequencies are insufficient for a conclusive assignment of these bands, we can now turn to the corresponding VTMAs, determined from the polarization dependence of the spectral band intensities, recorded in the presence of a large electric field. It is evident from Figure 7.3(b) that only one of the four bands survives in perpendicular polarization. Thus only one isomer of the uracil–water binary complex has a free O–H vibrational mode with a VTMA larger than the magic angle (54.7°). This is in excellent agreement with the *ab initio* VTMAs, as indicated

155
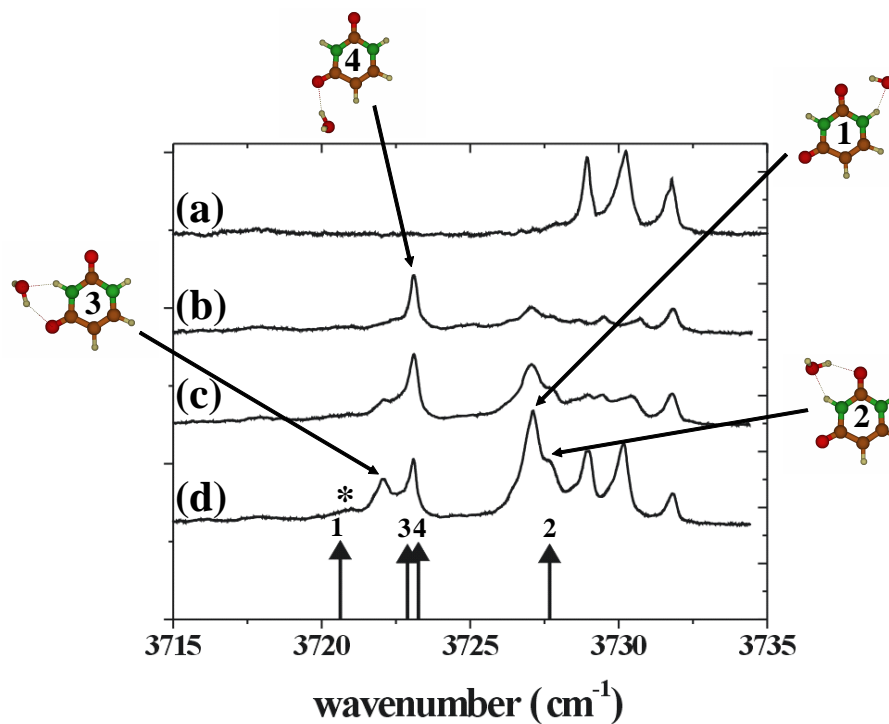
Figure 7.3: Infrared spectra of (a) pure water clusters and (b), (c), and (d) uracil–water complexes, recorded either (c) without an applied field or with a DC electric field oriented (b) perpendicular or (d) parallel to the laser polarization direction. The vertical arrows show the *ab initio* results for the free O–H vibrational modes of the different isomers. The height of each arrow reflects the calculated intensities of the different bands. The band marked with an * is due to uracil complexes containing more than one water molecule.

in Figure 7.2. Indeed, only isomer 4 has its OH(F) transition moment approximately perpendicular to the permanent dipole moment vector, while for the other three isomers the VTMAs all less than the magic angle. The quantitative experimental and *ab initio* VTMAs for the free O–H stretches of the four isomers are summarized in Table 7.2. Although the agreement between theory and experiment for isomer 4 is not as quantitative as we have seen for some other systems [86], the assignment of the band to isomer 4 is clear. The discrepancy between the experimental and *ab initio* values for this isomer has several interesting possible sources and the understanding of these could provide further insights into this system. For example, since isomer 4 is the most weakly bound of the isomers, it might have particularly wide amplitude vibrational motions that average to give an experimental VTMA that is rather different from that of the equilibrium geometry. We will come back to this point in the discussion.

The agreement between the experimental and *ab initio* VTMAs for the other three (more stable) isomers is clearly much better, the typical differences being only a few degrees. The problem here, however, is that the experimental and *ab initio* VTMAs for the isomers 1 and 3 are rather similar for this free O–H mode, making the assignment still somewhat unclear. The assignment listed in Table 7.2 was chosen because it gives the best overall agreement with the data. Fortunately, there are other vibrational modes that can be used to obtain more definitive assignments, as discussed below. The assignment give in Table 1 is also the one that gives the best relative intensity agreement with the other vibrational bands, which are more definitively assigned. For example, the intensities of the two bands assigned to isomers 1 and 3 are quite different, allowing us to transfer assignments made in one spectral region to another. It is certainly reasonable that the band associated with isomer 1, the global minimum on the potential energy surface, is the most intense in the spectrum. Fortunately, the VTMA for isomer 2 is quite different from the other three, making the associated assignment rather definitive.

Table 7.2: A summary of the experimental and calculated vibrational frequencies and VTMAs for isomers 1 – 4.

	Harm. Freq. (cm^{-1})	Scaled[a] Freq. (cm^{-1})	Exp. Freq. (cm^{-1})	IR Intensity (km/mol)	Assignment	ab initio VTMA ($^\circ$)	Exp VTMA ($^\circ$)
UW1							
	3959.7	3773.6	3727.1	119	OH (F)	23	31
	3741.5	3565.7	3467.5	232	OH (B)	19	14
	3617.7	3447.6	$[3442.7]^b$	72	N3H (F)	38	–
	3489.1	3325.1	3317.3	504	N1H (B)	35	35
UW2							
	3967.2	3780.7	3727.8	113	OH (F)	43	44
	3773.1	3595.8	3500.7	155	OH (B)	21	36
	3666.4	3494.1	$[3491.6]^b$	116	N1H (F)	26	–
	3460.3	3297.7	3265	346	N3H (B)	48	55
UW3							
	3962.1	3775.9	3722.3	112	OH (F)	29	29
	3744.2	3568.2	3467.5	216	OH (B)	11	14
	3664.2	3492.0	$[3491.6]^b$	119	N1H (F)	63	–
	3451.3	3289.1	3271	347	N3H (B)	19	18
UW4							
	3962.5	3776.3	3723.1	116	OH (F)	80	61
	3743.2	3567.2	3508.4	338	OH (B)	87	90
	3662.4	3490.3	3491.6	124	N1H (F)	38	33
	3615.9	3445.9	3442.7	75	N3H (B)	30	29

[a] The *ab initio* calculations were performed at the MP2/6-311++G(d,p) level and the scaled frequencies were obtained by multiplying the harmonic frequencies by a factor of 0.953.

[b] The experimental frequencies in square brackets (for some of the free N–H stretching bands) are only estimates, assuming that these bands overlap with the monomer, given that they were not observed in the spectrum. The corresponding VTMAs were clearly not determined

These bands provide important information concerning the relative populations of the four isomers, given that the corresponding free O–H stretches all have approximately the same infrared intensity (see Table 7.2). We will return to this issue in the discussion.

Having assigned the four bands in the free O–H stretching region to the four isomers obtained from *ab initio* theory, it is interesting to compare the *ab initio* frequencies with those from experiment. In both cases, the highest frequency band is due to isomer 2 and isomers 3 and 4 are grouped together at lower frequency. However, in the *ab initio* calculations the free O–H stretch of isomer 1 is shifted even further to the red (compared to the others), in contrast with the experimental results. As a result, an assignment based purely on the vibrational frequency ordering would be incorrect.

The results presented here already show that all four of the theoretically predicted isomers are formed by cluster growth in liquid helium. Apparently the water molecule simply falls into the potential well that is closest to the point where it encounters the uracil molecule. In light of this, we presume that the relative intensities of these bands have more to do with the relative widths of the potential energy basins that funnel into a given minimum than they do on the relative energies.

We now turn our attention to some of the other vibrational modes of the uracil–water system, which can help in making the case for the formation of all four isomers stronger still. Figure 7.4 shows an extended scan of the region of the spectrum corresponding to the OH (F), OH (B), NH (F), and NH (B) vibrations. Uracil has both an N3H and N1H vibration, providing even further experimental information. The *ab initio* calculations for the four isomers are also summarized in Figure 7.4, based on a single scaling factor (0.953) for all of the vibrational modes (namely that needed to give good agreement between theory and experiment for the free N–H stretches). Note that this scaling factor gives rather poor agreement for the case of the free and bonded O–H stretches.
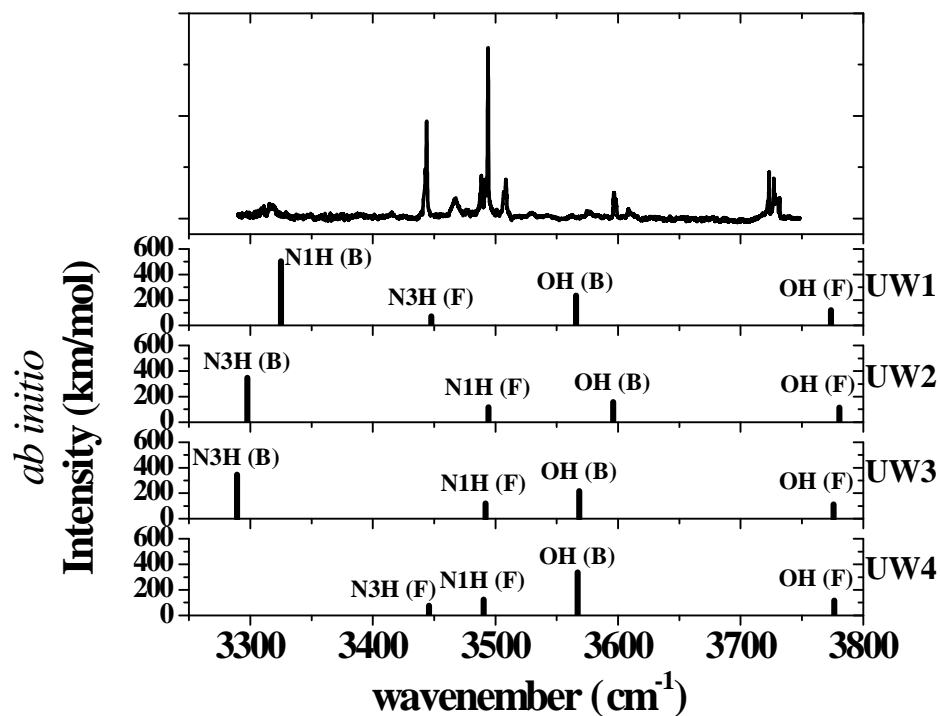
Figure 7.4: An overview spectrum of uracil–water formed in helium nanodroplets. The vertical arrows in the bottom panels summarize the *ab initio* frequencies and intensities for the OH (F), OH (B), NH (F), and NH (B) modes of isomers 1 – 4. The harmonic ab initio calculations were all scaled by a factor of 0.953 to obtain the best overall agreement between theory and experiment, particularly for the free N–H stretches.

According to the *ab initio* calculations shown in Figure 7.4, the OH(B) vibrational modes are quite well separated from the free N–H stretches, the former being approximately 100 cm^{-1} to the blue of the latter. However, in the expanded spectra shown in Figure 7.5, we can see that the bonded O–H stretches are actually in the same region of the spectrum as the N–H stretches of the monomer, the latter being the intense peaks labeled with an *. To help sort out which of the bands in this region are due to the bonded O–H stretching vibrations we also recorded a spectrum of the uracil-D_2O complex. As discussed below, the rather sharp bands, assigned below as free N–H stretches of the complex, are still present in the uracil-D_2O spectrum, while the broader bands (marked with vertical arrows in the upper spectrum) are completely absent. This is expected since the vibrational frequencies of the free N–H stretches are not affected by deuterium substitution, since by definition the water binds at sites remote from the free N–H stretch. In contrast, the bonded O–H stretches are clearly strongly shifted by deuterium substitution, making the assignment of the bands indicated by the arrows clear. It is important to point out that we see no evidence for isotopic scrambling in these experiments. Indeed, since the D_2O and uracil are brought together under the low temperatures conditions characteristic of the helium droplets, the energies are simply too low to facilitate isotopic exchange. Thus the deuterium atoms stay where they are initially labeled, a clear advantage given that otherwise many different isotopomers would be formed, further complicating the spectra. In fact, this is often a problem is free jet experiments, where the two molecules are brought together in the high temperature region [267–269].

Figure 7.6 shows an expanded view of spectra now tentatively assigned to the bonded O–H stretches, along with their dependence on the electric field and polarization direction. The dependence of the intensities of these bands on water pick-up cell pressure and the uracil oven temperature indicate that the peak marked with an asterisk is due
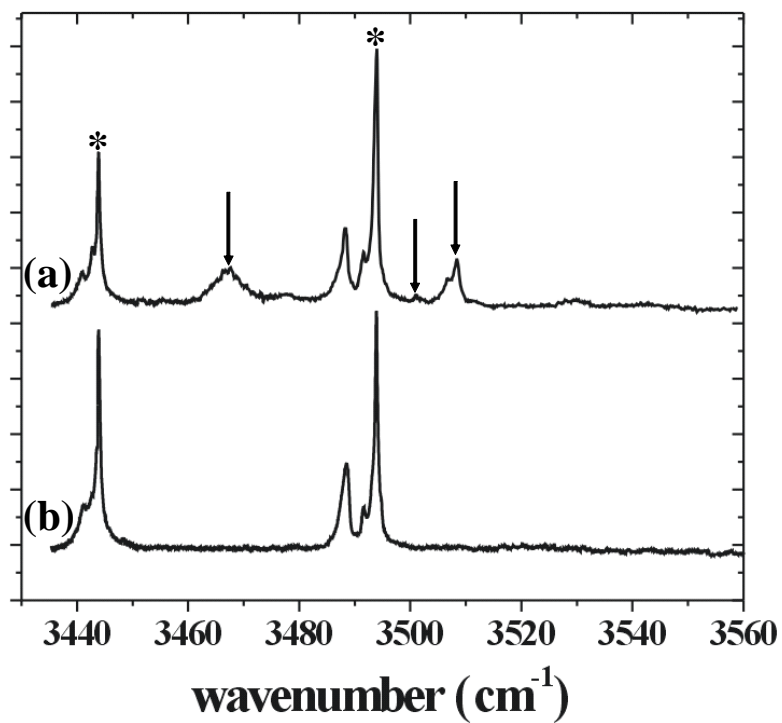
Figure 7.5: Spectra of the bonded O–H stretching region, which is overlapped with the N–H stretches. The bands marked with an * are assigned to the free N–H stretches of uracil monomer, while the bands labeled with vertical arrows in the uracil–H_2O spectrum (a) (which are missing in the uracil–D_2O spectrum b) are assigned to bonded O–H stretches of isomers 1 – 4.

162

to a complex consisting of a uracil molecule bound to two water molecules, while the other three bands in the spectra are associated with binary uracil–water complexes. Here again, as is evident from Figure 7.6, only one of the bands has an experimental VTMA (90°) that is larger than the magic angle, namely the one appearing at the highest frequency. Only isomer 4 has a perpendicular *ab initio* VTMA (87°). The vertical arrows in Figure 4 show the *ab initio* vibrational frequencies for the four isomers, now having been rescaled (0.927) so that the group of bands falls underneath the broad band in the experimental spectrum. This scaling clearly does not account for the position of the band for isomer 4, but as we will see below, it does give the best overall agreement for the four bands. In the end we conclude that the *ab initio* calculations are particularly bad in predicting the vibrational frequencies for these bonded O–H stretches. Fortunately, the VTMAs give a definitive assignment for the band associated with isomer 4.

In considering the assignment of the other peaks in the spectrum, we note that the weakest peak in the spectrum has a VTMA that best matches the *ab initio* value for isomer 2. The weakness of this band once again suggests that isomer 2 has the lowest population in helium droplets. In fact, the quantitative integrated intensities for the various bands in the bonded and free O–H regions of the spectrum (see Table 7.3) make sense when compared to the corresponding data for the free O–H stretch.

We are now left with the broad band, at 3467 cm^{-1} in the experimental spectra, which clearly has parallel character. We assume here that the breadth of this peak is due to the overlap of the two bands associated with isomers 1 and 3. Indeed, as shown in Table 7.2, the *ab initio* VTMAs for these isomers are both parallel (19° and 11°, respectively). For comparison, the experimental VTMA determined for the broad band in Figure 7.6 is 14°, consistent with the average of the two values. Once again, the relative integrated intensity of this band (see Table 7.3) is consistent with those

Figure 7.6: Expanded spectra of the bonded O–H stretching region. Spectra (a), (b), and (c) were recorded with parallel polarization, zero-field, and perpendicular polarization conditions, respectively. The band marked with an * is assigned to uracil complexes containing more than one water molecule. The vertical arrows summarize the scaled *ab initio* results for the bonded O–H stretches of isomers 1 – 4.

Table 7.3: A summary of the integrated experimental and ab initio intensities for the various vibrational bands, normalized to isomer 1.

	Free OH		Bonded OH		Bonded NH	
	Exp. area	*ab initio* intensity	Exp. area	*ab initio* intensity	Exp. area	*ab initio* intensity
UW1	1	1	1.00 *	0.69	1	1
UW2	0.09	0.95	0.07	0.46	0.18	0.69
UW3	0.27	0.94	1.00 *	0.64	0.59	0.69
UW4	0.51	0.97	0.78	0.64	–	–

* Since the bonded O–H stretching bands for isomers 1 and 3 are
  overlapped, the intensities quoted in the table (marked with an *)
  correspond to an equal sharing of the observed intensity between
  the two.

obtained from the free O–H stretching region, assuming that it corresponds to the sum of the two bands associated with isomers 1 and 3.

We now turn out attention to the region of the free N–H stretches of the uracil–water complexes. This region is complicated by the fact that the uracil monomer also absorbs here. In addition, we have observed several bands that are assigned to the uracil dimer. A full discussion of the monomer and dimer spectra will be published in a future article. In Figure 7.7 the uracil and uracil dimer bands are indicated by an "*" and "#", respectively, and are not directly relevant to the present discussion. As expected, the monomer vibrational band intensities (N1H stretch at 3494.9 cm^{-1} and N3H stretch at 3443.7 cm^{-1}) decreased monotonically with increasing water pick-up cell pressures. The peaks appearing between the monomer (*) and dimer (#), indicated by the vertical arrows in Figure 7.7, optimized at a water pick-up cell pressure of approximately 2.5 $\times$ 10^{-6} Torr. At even higher pressures (5 $\times$ 10^{-6} Torr) other peaks appeared in the spectrum that are tentatively assigned to uracil-(water)$_2$, although the discussion of these is beyond the scope of the present study.

The small frequency shifts for the new (water related) bands in the N–H stretch

Figure 7.7: Expanded spectra of the free N–H stretch region. Spectra (a), (b), and (c) were recorded with parallel polarization, zero-field, and perpendicular polarization conditions, respectively. The bands marked with an * and # sign correspond to the free N–H stretches of the uracil monomer and dimer, respectively. The bands marked with the downward point arrows are assigned to the free N1H and N3H modes of isomer 4. The *ab initio* results for the free N–H stretches of isomers 1 – 4 are indicated by the upward pointing arrows.

spectrum shown in Figure 7.7 are consistent with uracil–water isomers that have the water bound at a site remote from the corresponding N3H or N1H stretches. This is confirmed by the *ab initio* calculations for these two vibrational modes, shown in Figure 7.7 as the vertical arrows. Examination of Figure 7.1 reveals that only isomers 1 and 4 have free N3H vibrations, while isomers 2, 3, and 4 all have free N1H stretches. Unfortunately, of the 5 bands we would expect to see in this spectral region, only two are clearly resolved from the monomer. Since isomer 2 is a minor species in the helium droplets, we can assume that the associated band is weak and perhaps overlapped with the monomer bands. We therefore focus on trying to differentiate between isomers 1 and 4 in the N3H region of the spectrum and isomers 3 and 4 near the N1H band.

For the N3H vibrational mode, the experimental VTMA (33°) for the water related band agrees best with the *ab initio* value for isomer 4 (38°). For the free N1H the experimental VTMA is 29°, compared with the *ab initio* values for isomers 3 or 4 of 63° and 38°, respectively. The former is well outside our the typical experimental uncertainty, suggesting that the peak at 3491.6 cm^{-1} is the N1H of isomer 4, which coincidently is the isomer that has the larger *ab initio* frequency shift (relative to the uracil monomer) and thus is expected to be better resolved. The assignment is also consistent with the fact that the intensity of the free O–H band associated with isomer 3 is weaker than that for isomer 4. In future it should be possible to use IR–IR double resonance schemes to separate out the bands that are overlapped by the monomer and dimer vibrations, however this is beyond the scope of the present study. Without this type of data, the free N–H stretch region thus only gives information on isomer 4.

The final region of the spectrum that needs to be discussed is that of the bonded N–H stretching vibrations. The structures in Figure 7.1 show that isomers 1, 2 and 3 all have either an N1H or N3H vibration involved in hydrogen-bonding to water. As a result, we expect to observe a total of three bands in the region of the bonded N–H

stretches. An expanded view of this region of the spectrum is shown in Figure 7.8. The bands in this region are obviously weak, mainly due to the fact that they are also extremely broad. This is typical of hydrogen bonded vibrations, as is well documented in the literature [270]. The *ab initio* calculations for these three vibrational modes are more useful in this case, owing to the fact that the frequency shifts from the monomer vibrations are much larger and the bands span approximately 40 cm^{-1}. In the upper panel, corresponding to parallel polarization, there are two very obvious bands, both of which are enhanced by the electric field and therefore must be associated with complexes with nearly parallel VTMAs. The *ab initio* vibrational frequencies for isomers 1 and 3 (based upon the shifts from the monomer) are in good agreement with experiment in this case. The experimental (theoretical) VTMAs for isomers 1 and 3 are 35° (35°) and 18° (19°), respectively. The agreement is excellent for both bands, providing a convincing confirmation of the assignment based upon the vibrational frequencies.

The band associated with isomer 2 is less obvious in the spectrum, which is not surprising given that isomer 2 is a minor species in the droplets. Nevertheless, many scans were taken in order to convince ourselves that there is actually a weak band in this region of the spectrum, sufficient to estimate a corresponding experimental VTMA of 55°. This is to be compared with the *ab initio* value given in Table 7.2, namely 48°. Taking all of the data presented above together, there is no doubt that all four of the theoretically predicted isomer of uracil–water are formed in helium nanodroplets.

In the above discussion, we made use of the relative intensities of the various bands in the different spectral regions to aid in the assignment. Table 7.3 gives a summary of the (integrated) experimental and *ab initio* intensities for the various bands, normalized to the most stable isomer, namely isomer 1. For overlapped bands, indicated by an asterisk, the intensity was simply shared equally between the two.
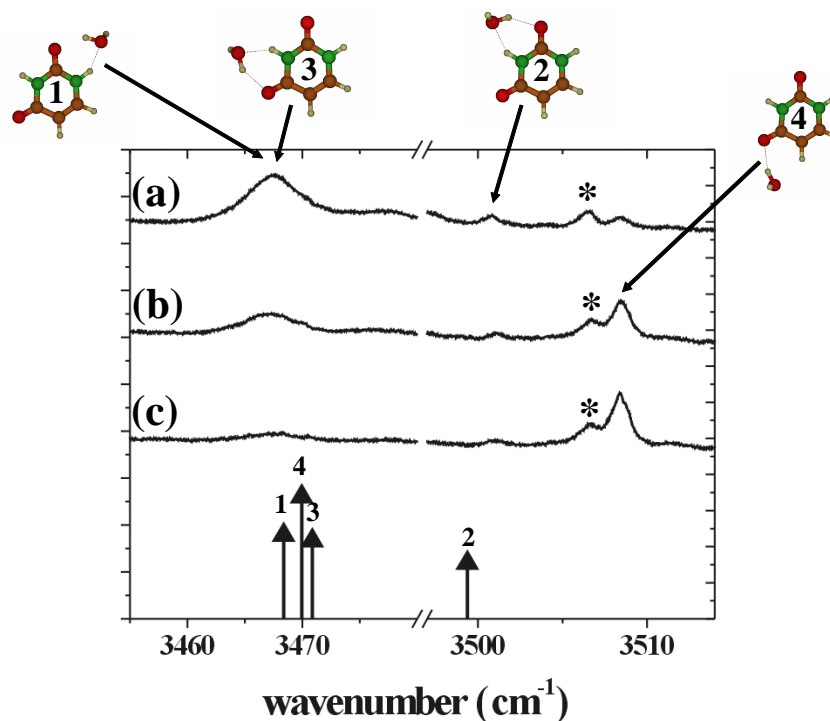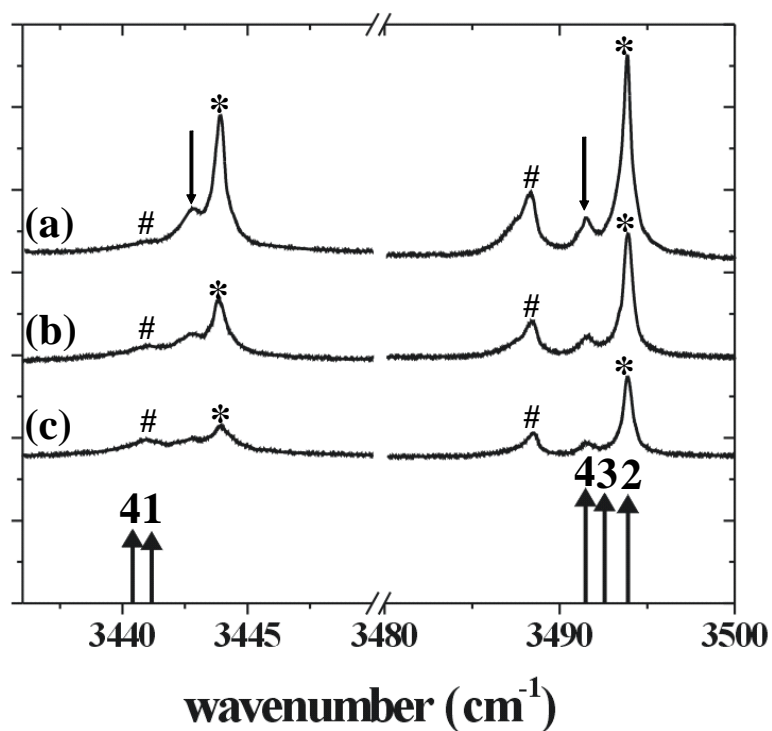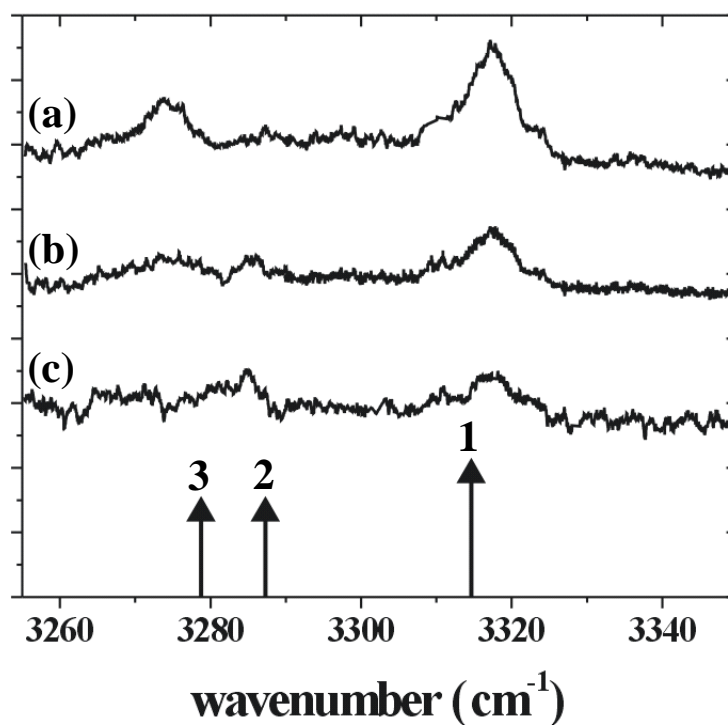
Figure 7.8: Expanded spectra of the bonded N–H stretches. Spectra (a), (b), and (c) were recorded with parallel polarization, zero-field, and perpendicular polarization conditions, respectively. The *ab initio* frequencies and intensities for the bonded N–H stretches of isomers 1 – 3 are indicated by the vertical arrows.

7.4 Discussion

The data presented above gives convincing evidence that, upon sequential pick-up of one uracil molecule and one water molecule by helium nanodroplets, four different isomers of the uracil–water binary complex are formed. This broad conclusion may at first seem puzzling, given our previous work on $(HCN)_n$ clusters [155] , which showed that the associated dipole-dipole forces dominate in complex formation, such that only the linear structures are observed, namely those for which the dipoles of all of the HCN molecules are oriented parallel to one another. Since both water and uracil are highly polar, one might have expected to see the same behavior, given rise to only that isomer which has this head-to-tail dipole configuration. In fact, the *ab initio* results in Table 7.1 show that isomer 2 is the most polar, and yet it is the least populated isomer. In fact, based upon the *ab initio* infrared intensities and the experimental integrated intensities for all of the vibrational modes, we estimate that the relative abundances of the four isomers are 11 : 1 : 3 : 6 for isomers 1, 2, 3, and 4, respectively. So why is it that the dipole oriented structure is not exclusively formed, as was the case of $(HCN)_n$?

The explanation for this apparent discrepancy comes from considering the relative magnitudes of the rotational constants of HCN and water. In fact, the rotational constants associated with the water monomer are roughly 20 times larger than that of HCN, making the former much more difficult to orient when encountering another polar molecule. While an HCN molecule is strongly oriented at long range by its interaction with an $(HCN)_n$ cluster, and is therefore guided into the linear form of the n + 1 complex, water continues to rotate at relatively small intermolecular separations. As a result, it appears more like an approaching atom than a polar molecule. Indeed, rotational averaging of the water dipole weakens the associated dipole-dipole interactions, making this steering mechanism much less important. Thus by the time the anisotropic forces become large enough to begin to orient the water molecule, it has

already entered a valley (funnel) in the potential energy surface from which it cannot escape, given the low temperature of the helium nanodroplet environment. Based on this picture for cluster growth in helium, we postulate that the populations for the various isomers are likely determined primarily by the widths of the entrance valleys leading to the different isomers, rather than by energetic considerations.

Quantitative theoretical determinations of relative "widths" of these entrance valleys should be possible (from the full *ab initio* intermolecular potential surface), although this is beyond the scope of the present study. Nevertheless, it is interesting to speculate concerning why the population of isomer 2 is particularly low. One possibility comes from considering the fact that the local minimum corresponding to isomer 2 lies between those of isomers 1 and 3, both of which are lower in energy. This is likely to make the entrance valley for isomer 2 rather narrow, given the tendency of the system to enter the deeper valleys associated with isomers 1 and 3. In contrast, even though isomer 4 is the least stable isomer, according to *ab initio* theory, it is likely to have a comparatively broader valley, given that the binding sites on the C–H side of uracil are extremely weak. Thus water molecules landing in this region of the potential will likely end up in the minima corresponding to isomers 1 and 4. There is clearly much that can still be learned about the nature of these entrance valleys by comparing detailed potential energy surfaces with the present experimental populations. Further experiments on other systems will also be needed to test these ideas and look for general trends.

As evident in Figure 7.1, the structures of all four isomers of the uracil–water system are non-planar, with the free O–H bond pointing somewhat out of the plane of the uracil. Actually, the *ab initio* calculations indicate that uracil is itself slightly non-planar in these complexes. Although the effects of this non-planarity is far too weak to be observed here, the *ab initio* calculations suggest that the minima corresponding to the free O–H pointing "up" or "down" are slightly different. To a very good approx-

imation, however, these systems can be thought of as having a double well potential, corresponding to tunneling through the planar geometry. In recent diffusion Monte Carlo calculations, van Mourik *et al.* [257] showed that the free hydrogen is actually delocalized above and below the plane of the molecule. Indeed, the ground state wavefunction for isomer 1 shows the free hydrogen completely delocalized above and below the plane. This issue is relevant to the present study, given that all of our comparisons between the experimental and *ab initio* VTMAs have not included the effects of vibrational averaging in the latter. Such wide amplitude motion clearly has the potential to modify the VTMAs from their equilibrium values. To a first approximation, however, the complex can be thought of as spending equal time in the "up" and "down" configurations. The *ab initio* calculations show that the VTMAs are essentially identical for these two geometries, so that to a very good approximation the effects of this motion should be small.

Although the VTMAs for the various vibrational bands of the uracil–water binary complexes have been critical in the assignment process, there were a few for which the agreement between theory and experiment is outside the experimental uncertainty. Vibrational averaging could still be important in these cases, given that there may be other wide amplitude motions for which the averaging has a larger effect on the VTMAs. Another possibility that needs to be kept in mind is that, for isolated cases, the observed vibrational bands could be anharmonically coupled to other "dark" vibrational states of the complex, giving rise to bands that have mixed character. In such cases, the VTMAs would reflect a weighted average for the two states.

There is another important possibility to consider, namely that the *ab initio* structures for one or more of these isomers are not quantitative, such that the differences between the experimental and *ab initio* VTMAs is indicative of structural issues. Indeed, we found previously that the VTMAs for adenine [79] could be used to differentiate

between a planar and non-planar geometry. Fortunately, it may be possible in time to use a set of VTMAs to carry out a structural optimization, given that the values for the high frequency modes of molecules are mainly determined by structure, rather than depending in a complex way on the potential energy surface of the system in all 3N-6 degrees of freedom. However, we are still in the early days of using VTMAs for structure determination so more work will be needed before a general strategy can be established.

7.5 Conclusions

In this combined experimental/theoretical study of the uracil–water binary complex, we have shown that all four of the theoretically predicted isomers are formed by growth in helium nanodroplets. The relative abundances of the isomers, referred to here as 1, 2, 3, and 4, are found to be 11 : 1 : 3 : 6. We argue that these populations are related to the dynamics associated with the formation of the clusters in the helium. In particular, the low temperatures associated with helium nanodroplets ensures that once a water molecule enters a given valley (funnel) in the long range potential surface, it will be unable to cross over into the next. As a result, the populations given above provide detailed information about the relative "widths" of the entrance valleys in the uracil–water potential. Future theoretical work on this system could provide direct comparisons with these values. Further insights into the nature of these energy landscapes might be forthcoming from experiments designed to use infrared laser pumping of the molecules from one local minimum to another, as reported elsewhere for other systems [125, 271].

Vibrational transition moment angles were used throughout this study, to confirm the assignments of the various vibrational modes of these uracil–water complexes. Here again, more theoretical work is needed to include the effects of anharmonicity and

wide amplitude motion in the calculation of these angles. Nevertheless, the present study clearly shows the power of using VTMAs in assigning vibrational spectra and determining molecular structure, particularly when more than one isomer is present in the sample. It still remains to be seen if a more complete set of VTMAs could be used to systematically refine molecular structures obtained from *ab initio* calculations.

Chapter 8

Infrared Laser Spectroscopy of Imidazole Complexes in Helium Nanodroplets: Monomer, Dimer, and Binary Water Complexes

Infrared laser spectroscopy has been used to characterize imidazole (IM), imidazole dimer (IMD), and imidazole–water (IMW) binary systems formed in helium nanodroplets. The experimental results are compared with *ab initio* calculations reported here. Vibrational transition moment angles provide conclusive assignments for the various complexes studied here, including IM, one isomer of IMD, and two isomers of the IMW binary complexes.

8.1   Introduction

Recently, the first structure of a neutral ammonia channel from a bacterial membrane was determined, providing considerable insight into the process of neutral gas transport in membranes [272, 273]. The structure shows that the hydrogen-bonding network be-

tween the imidazole (IM) moiety of the histidine and ammonia molecules in the channel plays an important role in neutral ammonia gas transport through the membrane. Not only is the intermolecular interaction between IM and ammonia important, but the self-associating interaction of IM, i.e., the IM dimer (IMD), also plays an important role in the hydrogen-bonding networks of the ammonia channel. Due to the unique IM structure, which contains a proton donor N–H and a proton acceptor N atom, IMD has been extensively studied as a model system both theoretically [274–278] and experimentally [279–282].

Understanding the intermolecular interaction of IM–water complexes is also relevant owing to their importance in hydrated biological systems such as histidine residue [283] and hydrated nucleic acid base (NAB) complexes [87, 258–261]. Indeed, the location and orientation of individual water molecules in the binary complexes play a pivotal role in some other biological processes. For example, water-assisted proton transfer in guanine [245–247] and cytosine [248–250] involve a single water molecule that forms a double hydrogen bond which bridges the proton donor and proton acceptor sites in the molecule.

Many theoretical [284–287] and experimental [282, 288, 289] investigations have been devoted to the structures and relative energies of IM–water (IMW) complexes, due to the occurrence of the IM five-membered ring in adenine and guanine. *ab initio* calculations have consistently shown that the two isomers, $>$NH $\cdots$ OH$_2$ (IMW1) and $>$N: $\cdots$ H–O–H (IMW2) (see Figure 8.1), have almost the same energy. Infrared spectroscopy was used to study the hydrogen bond interaction of the two isomers of the IM–water complex by matrix-isolation FTIR spectroscopy [288]. However, to our knowledge, no gas-phase vibrational study of IM–water complexes has been previously reported. Recently, the IM derivatives, 4/5-phenyl IM, complexes with a single water were studied by the IR ion dip spectroscopy [283, 290] which suggested the presence of

only one isomer, $>$N: $\cdots$ H–O–H, out of the three predicted ones.
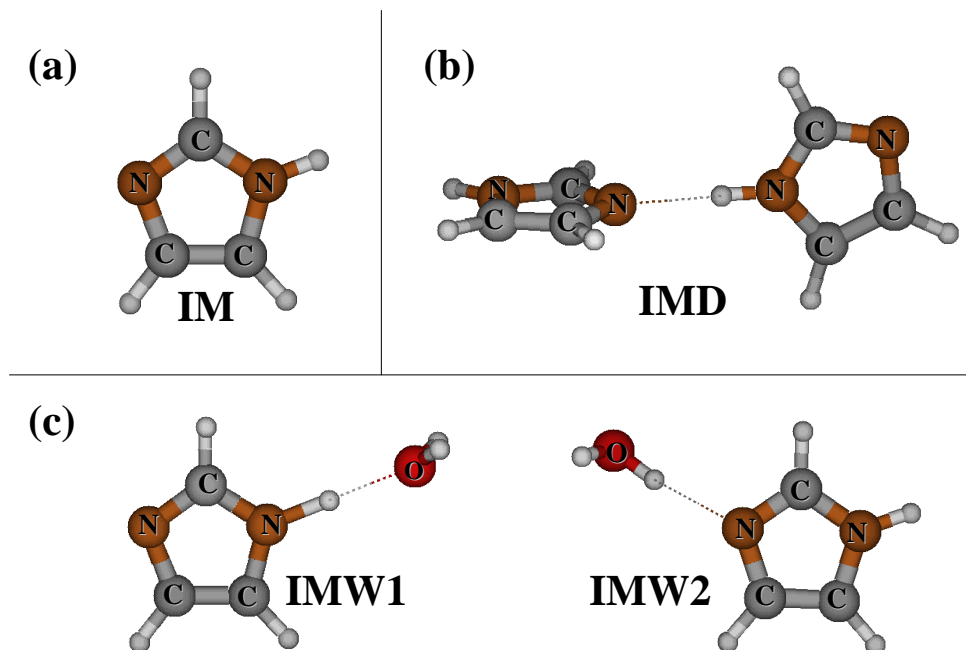
Figure 8.1: (a) Imidazole monomer (IM), (b) the global minimum of imidazole dimer (IMD), and (c) two isomers of imidazole water binary complexes (IMW1 and IMW2).

Our approach in this study involves the use of helium nanodroplets which has been shown to be an ideal matrix for infrared spectroscopy [4, 18, 36, 154, 155]. The weak interactions between the helium and the molecules of interest give rise to small vibrational frequency shifts (within a few wavenumbers) and high spectral resolution due to ultra cold helium nanodroplets (0.37K) [18, 22]. In a recent paper [87], we reported on a combined experimental/theoretical study of all four of the theoretically predicted isomers of uracil–water, using infrared laser spectroscopy in helium nanodroplets, which revealed the conformational energy landscapes of those hydrated complexes. We assigned closely spaced vibrational bands by experimentally measuring the angles between the vibrational transition moments and the permanent dipole moment of the molecule for the associated vibrational modes [86, 87, 89]. These vibrational transition moment angles

(VTMAs) also provide detailed structural information on the species of interest. Determination of these quantities is accomplished by orienting the molecule in a large DC electric field [37,108,167,262] and measuring the integrated intensities of the vibrational bands as a function of the laser polarization direction. For the case of well-isolated, high-frequency X–H stretches, we find that these angles can be reliably calculated using conventional *ab initio* methods, based upon harmonic frequency calculations [79]. Indeed, these angles are much less sensitive to the detailed multidimensional potential surface, but rather depend primarily on the structure of the molecule, particularly for its high frequency modes. The sensitivity of the method to the molecular structure was first demonstrated for adenine, where the experimental VTMAs for the N–H and NH_2 stretches were highly dependent upon the out-of-plane NH_2 tilt angle [79]. In the present study we apply this method to report on the isomers of the IM–water binary complexes (IMW) and the IM dimer (IMD) (see Figure 8.1), in helium nanodroplets.

8.2   Experimental Section

The helium droplet apparatus has been previously described [102] and is illustrated in Figure 8.2. In the present study the nanodroplets pass within 2 mm of the exit of the oven producing a low vapor pressure (between 10^{-6} and 10^{-5} Torr) of IM (Aldrich, 99 % purity). Collisions between the gas phase molecules and the droplets result in solvation of the former by the latter. The vapor pressure at the exit of the oven can be varied to pick up the desired number of IM molecules, according to the associated Poisson statistics [93]. In practice, useful operating temperatures for IM were from 25 to 35 °C with our effusive pick-up cell oven. To maximize the pick up of molecules into the helium nanodroplets at a minimum heating temperature, we developed a pick-up oven through which the helium droplets entered and exited via 2 mm holes [101, 291, 292]. However, because of the high IM vapor pressure, this oven resulted in the pick up of

too many molecules. We thus constructed a new effusive oven, shown in Figure 8.2, which was less efficient, and thus solved this problem. In detail, the tip of the effusive oven, a 1 mm diameter hole, faces along the droplet beam axis. The end of the oven is positioned just below the helium nanodroplet beams, and the droplets pass by and pick up the target molecules at the exit of the effusive oven. A second pick-up cell was positioned downstream of the oven in order to add water to the droplets. Because of the high mobility of molecules in the helium droplets, all molecules added to the droplets end up in a complex, located close to the middle of the droplet. This is based on the fact that most molecules are solvated by liquid helium rather than by "vacuum". Notable exceptions are the alkali atoms which reside on the surface of the droplets due to their weaker interactions with helium atoms than the He–He interactions [293–296].
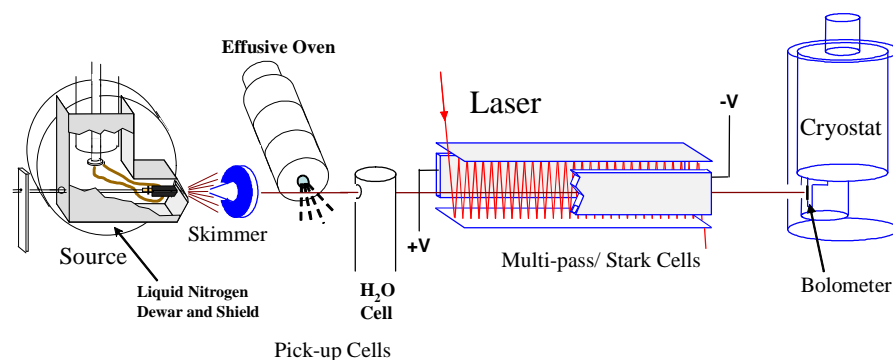
Figure 8.2: A schematic diagram of the experimental apparatus used in the present study. An effusive oven was used. A bolometer was used to monitor laser induced depletion helium droplet beam intensity.

Once the species of interest are formed, the doped nanodroplets pass between the plates of a multipass/Stark cell [102], which is used to generate many crossings between the infrared laser and the helium nanodroplet beam. The result is efficient vibrational excitation of the solvated molecules. A large DC electric field can also be applied to the interaction region, for the purposes of orienting the molecules in the laboratory frame of reference. This was done in order to measure the vibrational transition moment angles of the various species, as discussed below. All of the spectra reported here were obtained using a periodically poled lithium niobate (PPLN) cw–OPO [159, 160] from Linos Photonics (70 mW output power in the region of interest). Several external etalons and a wavemeter were used to calibrate the spectra reported here.

The pendular state method used to orient the molecules of interest has been applied previously to both gas-phase [104,120,190,191,231] and helium nanodroplet [37,108,120, 155, 167] studies. A large DC electric field results in the orientation of the permanent dipole moment of the target molecules (e.g., IM, IMD, and IMW complexes) parallel to the electric field, in the limit where μE is large compared to the rotational temperature (in this case 0.37 K [18, 22]). For a linearly polarized laser the result will be a change in the excitation efficiency, given that the molecular transition moments will also be oriented in the laboratory frame of reference. If the laser electric field is aligned parallel (perpendicular) to the DC electric field (referred to here as parallel and perpendicular polarization alignments) the corresponding change in the vibrational band intensity will depend on the angle between the permanent dipole axis and the corresponding transition moment direction. This angle is referred to here as the vibrational transition moment angle or VTMA. For a vibrational mode with its transition moment parallel to the permanent dipole moment, parallel (perpendicular) polarization will result in a significant increase (decrease) in the band intensity, compared to the zero-field case.

A quantitative description of this effect requires that the orientation distribution for

the permanent dipole moment be known. This distribution depends on the magnitude of the dipole moment, the applied electric field, the rotational constants and temperature of the molecule in question. The methods for calculating these distribution have been discussed in detail previously [128–131]. For the IM monomer the partially resolved rotational structure is observed in the zero-field. For the other systems discussed herein, the experimental spectra are broadened to a Lorentzian line shape. Although this means that the rotational constants cannot be directly determined from the experimental spectra, it also means that the overall orientation distribution is less sensitive to the rotational constants. In this case we used the *ab initio* rotational constants, divided by a factor of three to account for the effects of the helium [99], to determine the orientation distribution needed to calculate the VTMAs. This approach works rather well given that the rotational temperature of the droplets, and hence the rotational temperature of the molecules, is well known, namely, 0.37 K. A detailed discussion of how the experimental VTMAs are extracted from the integrated areas of the zero-field and parallel and perpendicular polarization spectra is given elsewhere [79,86,87,89,216]. The experimental VTMAs can be compared directly with those obtained from *ab initio* calculations, carried out using Gaussian 03 [169]. The calculations reported here were all carried out at the MP2 level, with a 6-311++G(d,p) basis set except for IMD where a 6-311+G(d) basis set is used.

8.3 Results and Discussion

8.3.1 Imidazole Monomer and Dimer

We begin this discussion by considering the case where the water vapor pick-up cell is left empty, so that only the IM monomer or the associated complexes are formed in the droplets. The upper panel in Figure 8.3 shows an experimental spectrum of IM and

an isomer of IMD in helium nanodroplets that spans the regions corresponding to the free N–H and bonded N–H stretching vibrations. The survey spectrum was recorded at rather low oven temperatures, so that the monomer and the self-associated dimer are the only species formed. The middle panel shows the *ab initio* spectra (frequencies scaled by a factor of 0.9556 with a 6-311++G(d,p) basis set) for the IM monomer and the bottom panel shows those of the global minimum structure of IMD scaled by a factor of 0.957 with a 6-311+G(d) basis set. (The energetics and *ab initio* calculations for the isomers of IMD will be discussed as below.) The largest peak in the spectrum is easily assigned to the N–H stretching vibration of the IM monomer, at 3517.8 cm^{-1}. Two additional bands observed in the spectrum and indicated in the figure are assigned to the IMD. Figure 8.4 shows an expanded view of the region corresponding to the free N–H stretches of the monomer and dimer, also showing the effect of applying a DC electric field with different polarization directions: (a) parallel polarization, (b) zero electric field, and (c) perpendicular polarization (the corresponding electric field being 80 kV/cm). The zero-field spectrum of the IM monomer shows partially resolved rotational fine structure, in the form of a PQR contour. The observed vibrational origin and the corresponding *ab initio* values are listed in Table 8.1.

It is immediately obvious from the polarization dependence of the N–H stretch of the IM monomer in Figure 8.4 that this band is approximately parallel (VTMA close to 0°). This is consistent with the *ab initio* calculation of the VTMA for this mode, namely, 18°, (see Table 8.1) The experimental determination of this quantity requires the inclusion of all of the rotational states, given that the band is partially rotationally resolved. The origin of the peak marked with an asterisk in parallel polarization is not known at this moment.

The weaker band near 3515.8 cm^{-1} is tentatively assigned to the IMD, based upon the pick-up oven temperature dependence of the associated signals. Here again, we find
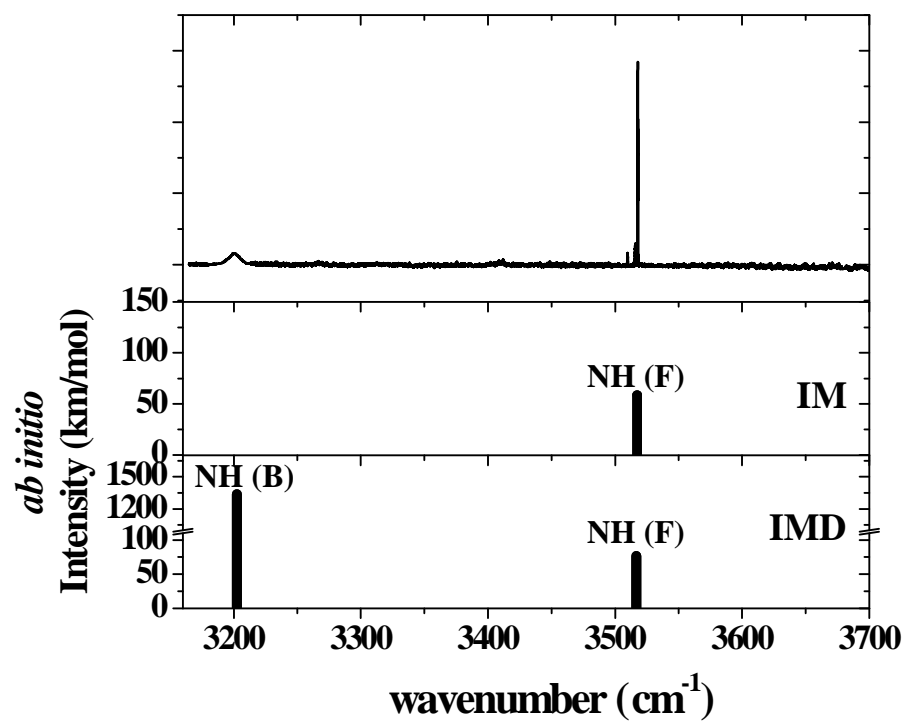
Figure 8.3: A survey spectrum of imidazole monomer (IM) and dimer (IMD) isolated in helium droplets. The corresponding *ab initio* vibrational spectra for IM (scaled by a factor of 0.9556 with 6-311++G(d,p) basis set) and the IMD (scaled by a factor of 0.957 with 6-311+G(d) basis set) are shown below the experimental spectrum.
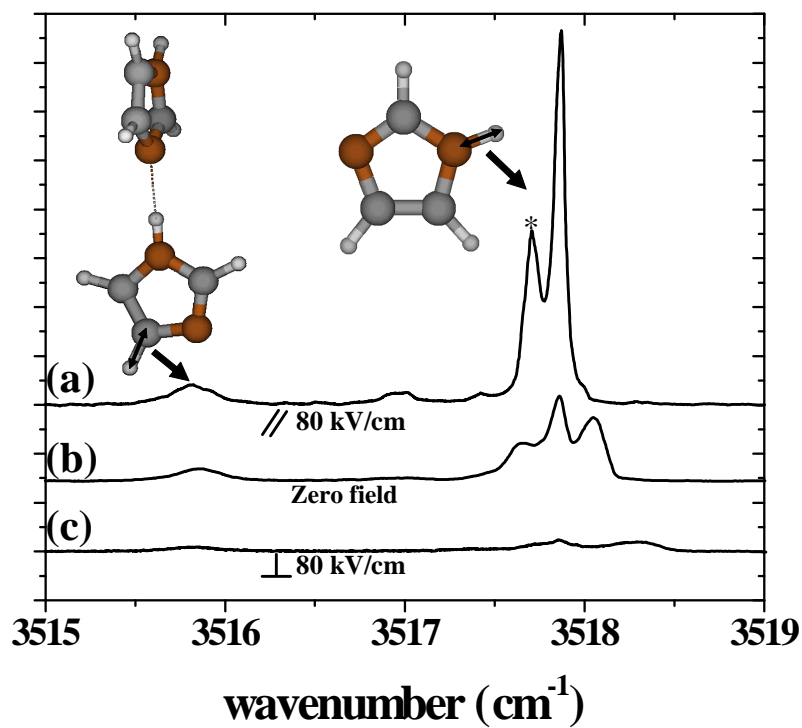
Figure 8.4: An expanded view of the N–H stretch of the imidazole monomer and dimer. Spectra (a), (b), and (c) correspond to parallel polarization, zero-field, and perpendicular polarization (the corresponding electric field being 80 kV/cm), respectively. The assignments shown in the figure are based upon comparisons in VTMAs and frequencies between the experimental and *ab initio* values. The origin of the band marked with an asterisk is not clearly known at this time.

Table 8.1: A summary of the experimental and ab initio data for the imidazole monomer (IM), the imidazole dimer (IMD) and the two lowest energy isomers of imidazole-water binary complex (IMW1 and IMW2).

	Harm.[a] freq. (cm^{-1})	Scaled[b] freq. (cm^{-1})	Exp. freq. (cm^{-1})	IR Intensity (km/mol)	Assignment	ab initio VTMA $(°)$	Exp. VTMA $(°)$	μ (D)
IM	3681.3	3517.9	3517.9	77.7	NH (F)	18	para.	3.97
IMD								9.62
	3673.8	3515.8	3515.8	81.6	NH (F)	30	33	
	3388.0	3242.3	3200.1	1225.3	NH (B)	10	20	
IMW1								6.67
	3988.5	3811.4	3747.7	99.6	OH (AS)	90	90	
	3870.5	3698.7	–	22.6	OH (SS)	26	–	
	3560.2	3402.1	3411.8	568.1	NH (B)	6	22 (10)[d]	
IMW2[e]								5.72
	3959.6	3783.8	3719.7	84.0	OH (F)	33	33	
	3678.8	3515.5	3517.8	46.9	NH (F)	76	perp.	
	3668.5	3505.6	3447.9	763.3	OH (B)	12	27 (–)	

[a] The *ab initio* calculations were performed at the MP2/6-311++G(d,p) level (for IMD a 6-311+G(d) basis set was used).

[b] The scaled frequencies were obtained by multiplying the harmonic frequencies by a factor of 0.9556 to account for the effects of anharmonicity (for IMD a factor of 0.957 was used).

[c] The energy was obtained with zero point energy correction.

[d] The experimental VTMA for the bonded NH band for IMW1 in a parenthesis was obtained from deuterium substitution.

[e] Relative energies of IMW2 to IMW1 is 0.5 kJ/mol with a zero point energy correction.

that the band is enhanced by application of a DC electric field in parallel polarization. A detailed analysis of the associated integrated intensities yields a VTMA for this band of 33°. The *ab initio* VTMA for the free N–H mode of the IMD is 30°, in good agreement with the experimental result. The small frequency shift associated with this band (from the IM monomer) indicates that this is a "free" N–H vibrational mode in the dimer. We have carried out extensive *ab initio* calculations on the four lowest energy dimers shown in Figure 8.5 using the MP2 level with a 6-311+G(d) basis set. The corresponding *ab initio* values are listed in Table 8.2. The relative energies are 17, 22, and 27 kJ/mol (with zero-point energy corrections) higher than the global minimum. The global minimum is the "twisted" hydrogen-bonded complex, shown in Figure 8.1, which has strong intermolecular N $\cdots$ H–N hydrogen bonds while the three higher energy isomers have weaker N $\cdots$ H–C hydrogen bonds. It is worth mentioning here that the structure of this twisted hydrogen-bonded complex (IMD) is very similar to the structure of the hydrogen-bond IM complex (at the histidine residue) in the ammonia channel [272, 273] mentioned above.

A summary of the *ab initio* results for all four isomers is given in Table 8.2. Although all of these isomers have "free" N–H vibrational bonds, it is interesting to note that only the global minimum structure gives a VTMA for the "free" N–H stretch that is in agreement with experiment. As shown in Table 8.2, the VTMAs of the "free" N–H stretches for the three higher energy dimers vary from 50° to 90° which is very different from that of the global minimum dimer (IMD), 33°. It is also interesting to note that this is the most polar structure, which is also consistent with the fact that the observed spectrum is strongly dependent upon the application of a DC electric field.

The "twisted" hydrogen-bonded dimer complex is the only one that shows a strongly shifted N–H vibrational mode. As a result, further evidence for the formation of this isomer can be obtained through probing the corresponding spectrum. Figure 8.6 shows

IMD
(0.0)

IMD1
(17.1)

IMD2
(22.1)

IMD3
(26.8)
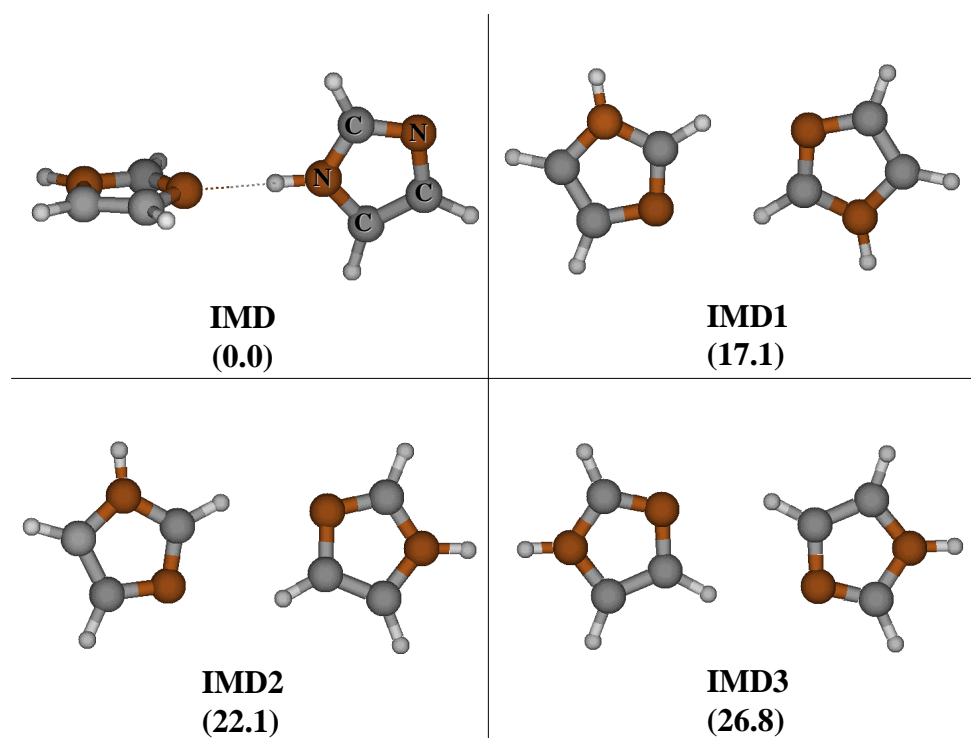
Figure 8.5: The relative energies (kJ/mol) were calculated at MP2 level with a 6-311+G(d) basis set.

Table 8.2: A summary of the experimental and ab initio data for the four lowest energy imidazole dimers.

	Harm.[a] freq. (cm^{-1})	Scaled[b] freq. (cm^{-1})	IR. Intensity (km/mol)	Assignment	ab initio VTMA ($^\circ$)	Exp. VTMA ($^\circ$)	μ (D)	Relative[c] Energy (kJ/mol)
IMD							9.62	0
	3673.8	3515.8	81.6	NH (F)	30	33		
	3388	3242.3	1225.3	NH (B)	10	20		
IMD1							0.02	17.1
	3677.8	3519.6	6.9	NH (F)	90	-		
	3677.7	3519.6	126.4	NH (F)	90	-		
IMD2							3.15	22.1
	3678.5	3520.3	60	NH (F)	50	-		
	3677.9	3519.7	72.9	NH (F)	52	-		
IMD3							0.01	26.8
	3677.6	3519.5	1.6	NH (F)	85	-		
	3677.5	3519.3	132	NH (F)	88	-		

[a] The *ab initio* calculations were performed at the MP2/6-311+G(d) level.

[b] The scaled frequencies were obtained by multiplying the harmonic frequencies by a factor of 0.957 to account for the effects of anharmonicity.

[c] The relative energies were obtained with zero point energy corrections.

a scan of a spectrum which has the same oven temperature dependence as the dimer band observed in the "free" N–H stretching region. We assign this band to the bonded NH stretching mode. Detailed analysis of the polarization dependence of this band reveals an experimental VTMA of $20°$, which is less parallel than the *ab initio* value of $10°$. The difference, which is a bit larger than what we have seen for other bands, probably results from the increased error in determining experimental VTMAs when the angle is small, e.g., below $15°$ [88]. Assignment of this band to the bonded N–H stretch of IMD is further supported below. Note that the line width of this band is in excess of 10 cm^{-1} and the experimental frequency shift from the free N–H stretch is almost 316 cm^{-1}, which is slightly larger than the *ab initio* calculation value of 274 cm^{-1}. It is evident that the band is associated with a strong hydrogen bond, based on the magnitude of the frequency red-shift and the peak broadening. Such a broad band associated with a hydrogen bond was previously observed in the indole–water system by Zwier and co-workers [297] and could come from the dipole-induced dipole interactions [298, 299]. A recent paper by Sibert *et al.* [300] provides a theoretical model for the band broadening. It is interesting to note that the total integrated area under the zero-field spectrum is about 16 times larger than that of the corresponding "free" N–H stretch. This is also in good agreement with the ratio of the corresponding *ab initio* intensities, namely 15 times (see Table 8.1). In conclusion, it is quite clear that the only isomer of the IMD that is formed in helium nanodroplets is the one corresponding to the global minimum on the potential energy surface. This is also the structure that corresponds to the dipole-oriented structure that we have come to expect to form from highly polar, moderately heavy molecules in helium nanodroplets [101].

Formation of linear chains of polar molecules in helium is well established from previous studies carried out in our laboratory [121, 155]. The reason for this is the sequential addition of monomer units to existing chains, beginning with the dimer, whose
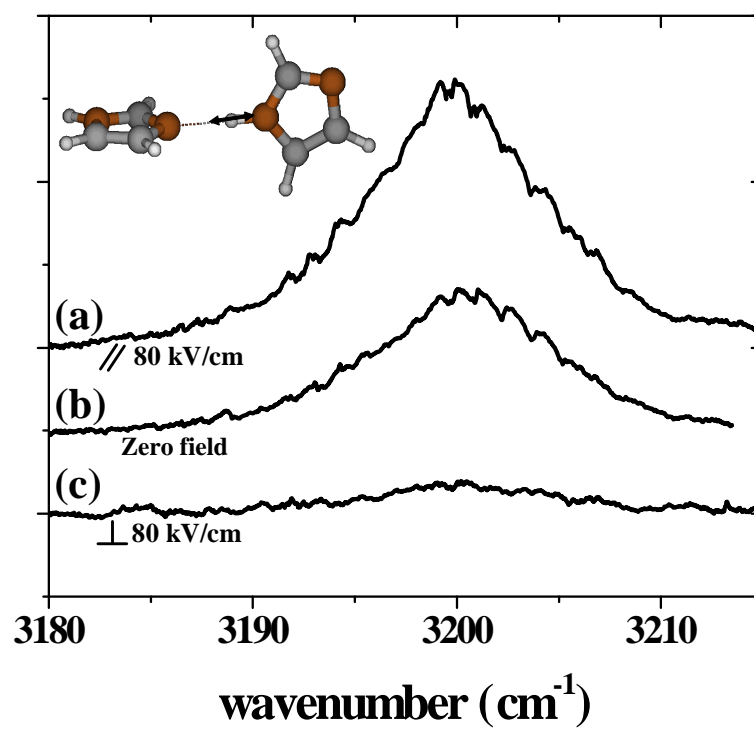
Figure 8.6: An expanded view of the bonded N–H stretch of the imidazole dimer. Spectra (a), (b), and (c) were recorded with parallel polarization, zero-field, and perpendicular polarization conditions, respectively.

structure is trapped in its potential well in the low-temperature helium environment. It is therefore interesting to consider the series of spectra shown in Figure 8.7, obtained as a function of the nozzle temperature and hence the mean droplet size. Large droplets have large cross sections and sufficiently high heat capacities to capture and cool many IM molecules. The rather smooth evolution of the spectra corresponding to the "free" N–H stretches suggest the formation of chains. We have, however, not analyzed these peaks in any detail. Nevertheless, the formation of such linear chains is interesting in its own right given that the IMD molecule has an inherent $30°$ bend in the monomer unit.
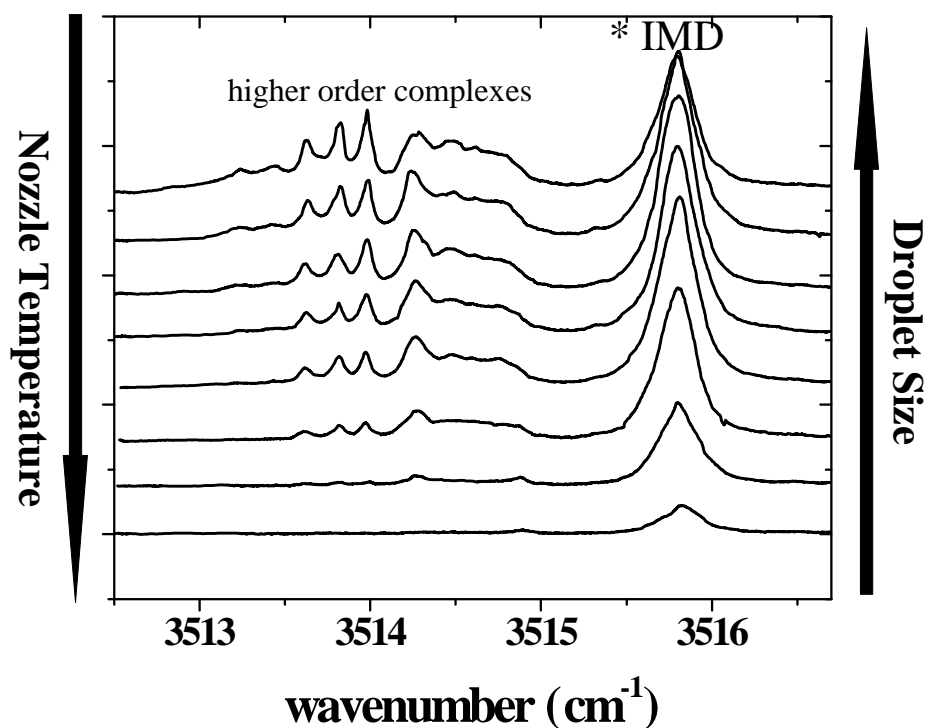
Figure 8.7: An evolution of the spectra for different nozzle temperatures (top to bottom: 15 K, 17.5 K, 18.5 K, 19.5 K, 20.5 K, 21.5 K, 23 K, 25 K). The band marked with an asterisk is the free N–H stretch of imidazole dimer.

8.3.2 Imidazole–Water Complexes

We now turn our attention to the binary complexes of IM with water (IMW). Two hydrogen-bonded isomers of the IMW binary complex ($>$NH $\cdots$ OH$_2$ and $>$N: $\cdots$ H–O–H, see Figure 8.1) are presented here. The two isomers were formed by sequential pick-up of one IM and one water molecule by helium droplets. Figure 8.8 shows the two lowest energy *ab initio* structures for the IMW binary system, onto which are superimposed vectors representing the directions of the permanent electric dipole moments (solid arrows) and the vibrational transition moments (dashed arrows). The magnitudes of the various moments are given in Table 8.1. It is clear from the figure that the pattern of VTMAs for the two isomers is quite different, making them a useful tool for distinguishing these two isomers and assigning the associated vibrational spectra.

The lowest energy form (IMW1) corresponds to the water acting as a proton acceptor, while the slightly higher energy form (IMW2) has the water donating a proton to the nitrogen atom in the IM ring. The spectrum (a) upper panel, shown in Figure 8.9, in which the water source was closed, shows that only IM monomer and dimer are present in the helium droplets. The rich spectrum (b) is obtained by optimizing the pick-up conditions for the capture of a single IM molecule and one water molecule; therefore, the additional peaks in (b) must involve H$_2$O. The dotted lines are meant as guides to associate the bands with their calculated frequencies. The *ab initio* frequency calculations for the two isomers are summarized in the bottom panels of Figure 8.9, in which we used a single scaling factor of 0.9556 for all of the vibrational modes. This gives good agreement between theory and experiment for the free N–H stretches. Although this single scaling factor gives rather poor agreement for the case of the free and bonded O–H stretches, [86, 87, 89] the experimental frequency difference (278.3 cm^{-1}) between the free and bonded O–H stretches is in good agreement with the *ab initio* calculations (271.8 cm^{-1}). Once again, the relative integrated intensities (corrected

with *ab initio* intensities) of bonded N–H and O–H bands (see Table 8.1) are almost 1 : 1, thereby suggesting that the relative abundance of the two isomers is similar.

The other bands in Figure 8.9 may be associated with higher order clusters. Although the water pressure is optimized for binary complexes, the pick-up of more than one water molecule by the droplets is still significant under these conditions, and some of the peaks in the spectrum are due to complexes containing three molecules (IMD plus water or IM plus two waters). However, the discussion of the latter species is beyond the scope of the present study.
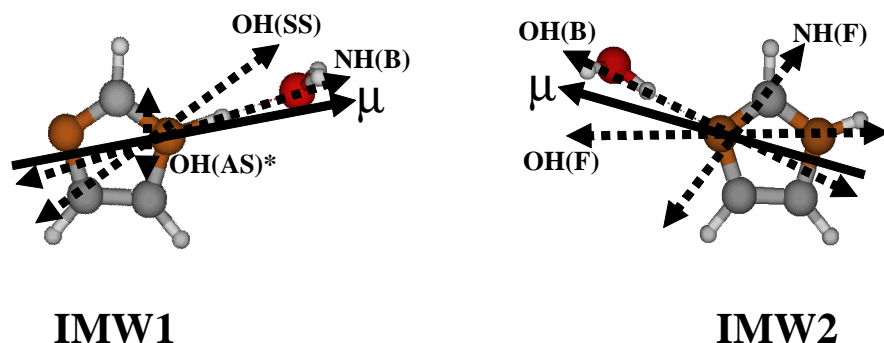
Figure 8.8: The two lowest energy isomers of imidazole–water binary complexes (IMW1 and IMW2), showing the corresponding directions of the permanent electric dipole moments (solid arrows) and the vibrational transition moments (dashed arrows) for the various vibrational modes. Note that the vibrational transition dipole moment of OH (AS) marked with an asterisk is out-of-plane, so that the VTMA of this being 90 °. The magnitudes of these moments are given in Table 8.1

We now proceed to consider the assignment of the high frequency portion of the spec-
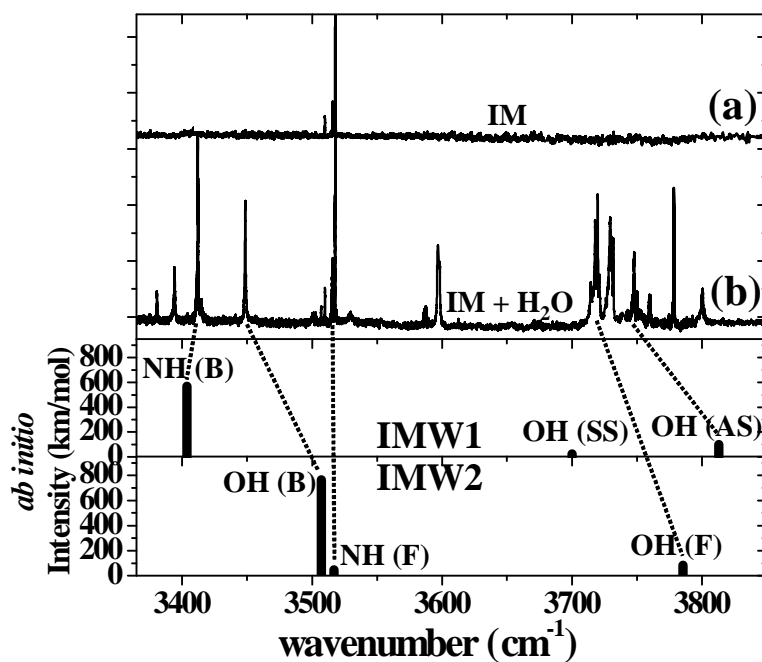
Figure 8.9: A survey spectrum of imidazole (a) without and (b) with water isolated in helium droplets. The *ab initio* frequency calculations for the corresponding isomers, IMW1 and IMW2, (scaled by a factor of 0.9556 with 6-311++G(d,p) basis set) are shown below the experimental spectra.

trum appearing in the region near 3730 cm^{-1}, corresponding to the free O–H stretches of the water molecule. Figure 8.10 shows this region measured with (a) parallel polarization, (b) zero electric field, and (c) perpendicular polarization (the corresponding electric field being 80 kV/cm). The peaks labeled as "w" are due to water monomer and high-order water clusters ($(H_2O)_{1-2}$). Examination of the oven temperature dependence and water pick-up pressure dependence of the various peaks in this region of the spectrum reveals that only bands (i) and (ii) are due to the IM–water binary system, namely asymmetric stretch mode (OH (AS)) of IMW1 and free O–H stretch mode (OH (F)) of IMW2. The symmetric O–H stretch of IMW1 was not observed in the region below 3700 – 3600 cm^{-1}, which is not surprising given that the expected band intensity is much weaker (see Table 8.1). Nevertheless, a number of scans were taken in order to convince us that there is no band in this region of the spectrum. It is also not observed in the study of H_2O in helium droplets [301]. The remaining peaks in the spectrum are all uniquely assigned to other species and will be discussed in detail elsewhere [302].

It is evident from the polarization dependence of the two IM–water bands that the one appearing at lower frequency is nearly parallel, while the higher frequency mode completely disappears with the parallel polarization. Analysis of these bands, based upon fitting to Lorentzian line shapes, yielded VTMAs for these two bands of 33° (ii) and 90° (i). For comparison the *ab initio* VTMAs for the two isomers are 33° and 90° for the "free" O–H stretch (ii) of IMW2 and the asymmetric stretch (i) of IMW1, respectively. The agreement between experiment and theory is clearly excellent. It is interesting to note that the frequency difference (28.0 cm^{-1}) is in excellent agreement with the *ab initio* calculations (27.6 cm^{-1}), even though the absolute scaled frequencies are not as well reproduced especially for free O–H stretches [86, 87, 89]. The relative integrated intensity ratio of (i) and (ii) bands (see Table 8.1) is 1 : 1 ratio, which is
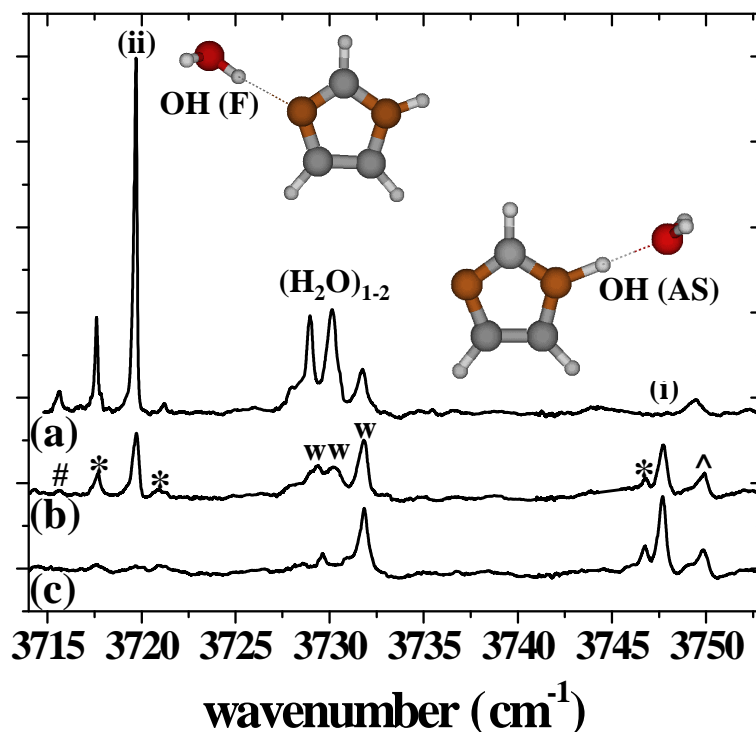
Figure 8.10: An expanded view of the high frequency section (OH (AS) and OH (F)) of the imidazole-water complex spectrum. Infrared spectra (a), (b), and (c) correspond to parallel polarization, zero-field, and perpendicular polarization, respectively. The higher frequency band (i) corresponds to the OH (AS) stretch mode of IMW1, while the lower frequency band (ii) is associated with the OH (F) stretch mode of IMW2. The bands marked with an asterisk are due to imidazole monomer with two water molecules determined by water pressure dependence experiments. The band marked with a "#" and "^" is due to IMD with one water molecule determined by IM temperature dependence experiments and water-nitrogen complexes, respectively. The bands marked with a "w" are related to pure water and water–nitrogen complexes.

consistent with the expected ratio populations of these two nearly equal energy isomers.

We now turn our attention to the bonded vibrations of the IM–water binary system, which appear in the region from $3400 - 3500$ cm^{-1}. Given the structures shown in Figure 8.8, we expect to see a bonded N–H vibrational mode for IMW1 and a bonded O–H stretch for IMW2. Figure 8.11 shows a comparison of spectra obtained using both H_2O and D_2O. The disappearance of the peak at 3450 cm^{-1} upon deuteration identifies it as a bonded O–H stretch. Its complete disappearance also confirms a previous result [87] that there is no isotopic scrambling in these helium nanodroplet experiments. We conclude that the vibrational band (i) is associated with the bonded O–H stretch of IMW2. From the oven temperature and water pressure dependence of the peaks in this spectrum we can also conclude that the only peaks that correspond to the binary complex are the bands (i) and (ii). As a result, we assign the bands (i) and (ii) to the bonded O–H stretch of IMW2 and the bonded N–H stretch of IMW1, respectively. The remainder of the peaks in the spectrum are due either to the IM monomer and dimer (discussed above) or higher order complexes that will be discussed in detail elsewhere [302].

Figure 8.12 shows the electric field dependence of the two bands discussed above, from which the VTMAs are determined for the bonded N–H stretch of IMW1 ($22°$) and the bonded O–H stretch of IMW2 ($27°$). In these cases, the agreement with the *ab initio* VTMAs of $6°$ and $12°$ is poor. These two bands are very close to being pure parallel bands (below 15^0) [88] for which the experimental VTMAs give larger errors as mentioned above. Nevertheless, this error is well outside the experimental uncertainty that we have come to expect, leading us to consider other explanations for the differences. Since we are confident in the assignment of these two bands, we are forced to consider other mechanisms that might affect this comparison. One possibility is that there are other bands that overlap with these bands, which would affect the
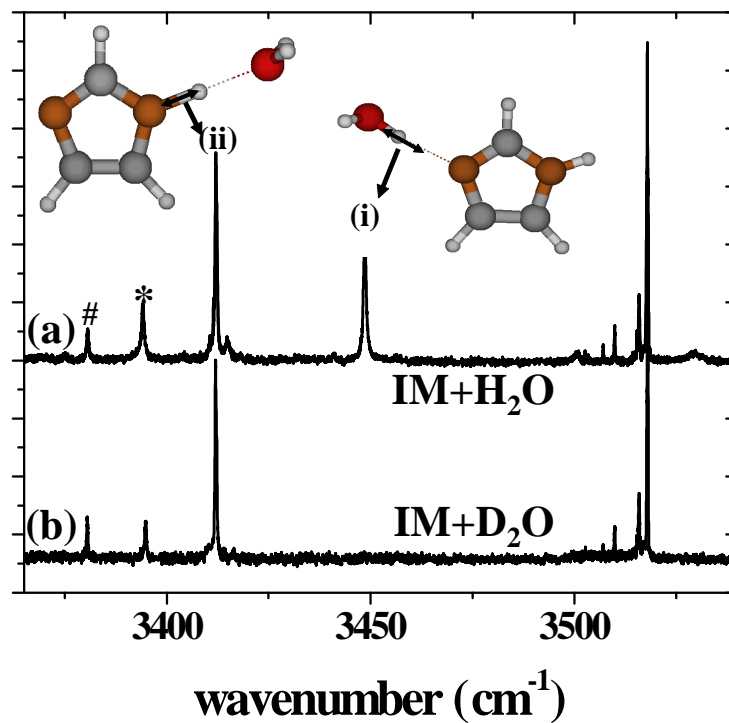
Figure 8.11: A comparison of spectra of the bonded O–H and N–H stretching region obtained using both (a) H_2O and (b) D_2O. The higher frequency band (i) corresponds to the bonded O–H stretch mode of IMW2, while the lower frequency band (ii) is associated with the bonded N–H stretch mode of IMW1. The bands marked with an "*" are due to imidazole monomer with two water molecules determined by water pressure dependence experiments. The bands marked with a "#" are due to imidazole dimer with one water molecules determined by imidazole temperature dependence experiments.

corresponding experimental results. Another is that these complexes are rather floppy, so that the *ab initio* results for the equilibrium geometry are not sufficient.

To test these ideas we also obtained VTMAs for the bonded NH vibrational bands in the IM–D_2O complex. The data for this band are shown in Figure 8.13. In this case, the experimental VTMA is determined to be $10°$, in much better agreement with the *ab initio* value of $6°$. Unfortunately, we are not able to conclusively decide which of the above effects is responsible for the large difference between the water and deuterium results. Indeed, there could be an O–H band from some other species present in the droplet that overlaps with the bonded N–H vibration when water is used, which disappears when using D_2O, or alternatively the heavier mass of the deuterium could reduce the wide amplitude motion and thus given better agreement with the *ab initio* results. The fact that the agreement in the free O–H region is so good, leads us to believe that the problem is the former, rather than the latter. This is somewhat supported by the fact that the spectrum is much smoother in the IM–D_2O spectrum, in comparison to that of IM–H_2O, which might indicate that there are overlapping bands in the H_2O case. Theoretical studies of the wide amplitude motions in these binary complexes will be needed to clarify this issue.

Finally, we consider the free N–H stretch of IMW2, which should also be visible in the spectral region of interest here. Unfortunately, this vibrational band is expected to be only slightly shifted from the very intense vibration band of the IM monomer and weaker as well, making it difficult to observe. However, as indicated in Table 8.1, the free N–H band of IMW2 is predicted by theory to be a nearly perpendicular band (VTMA = $76°$), while the monomer band is nearly parallel. To confirm that this band exists in the spectrum, we took advantage of this difference and used a perpendicular polarization geometry to eliminate the monomer from the spectrum, while at the same time enhancing the contribution from the IM–water complex. Figure 8.14 shows the
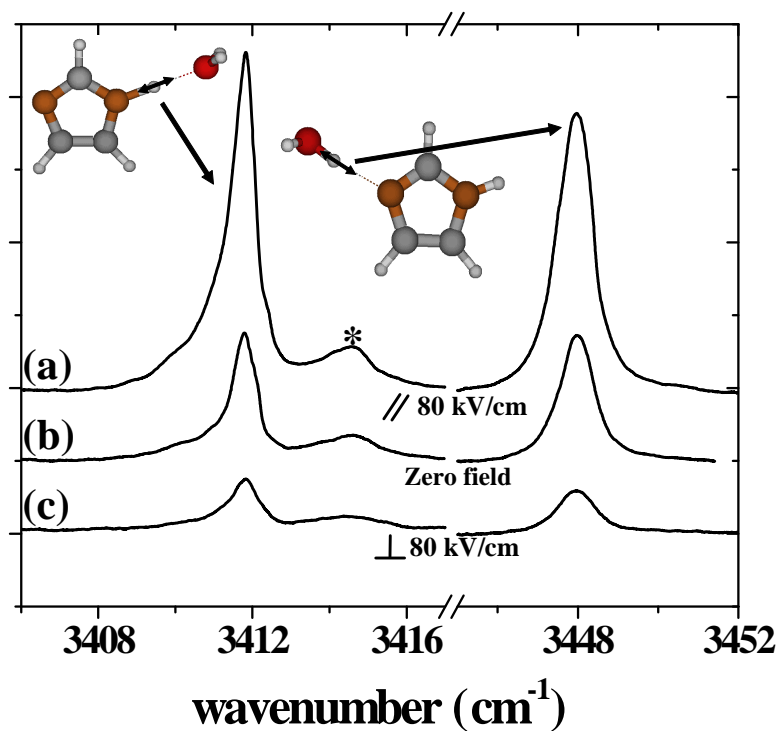
Figure 8.12: Expanded spectra of the bonded O–H and N–H stretching region. Spectra (a), (b), and (c) were recorded parallel polarization, zero-field, and perpendicular polarization conditions, respectively. The band marked with an asterisk is assigned to imidazole complexes containing more than one water molecule.
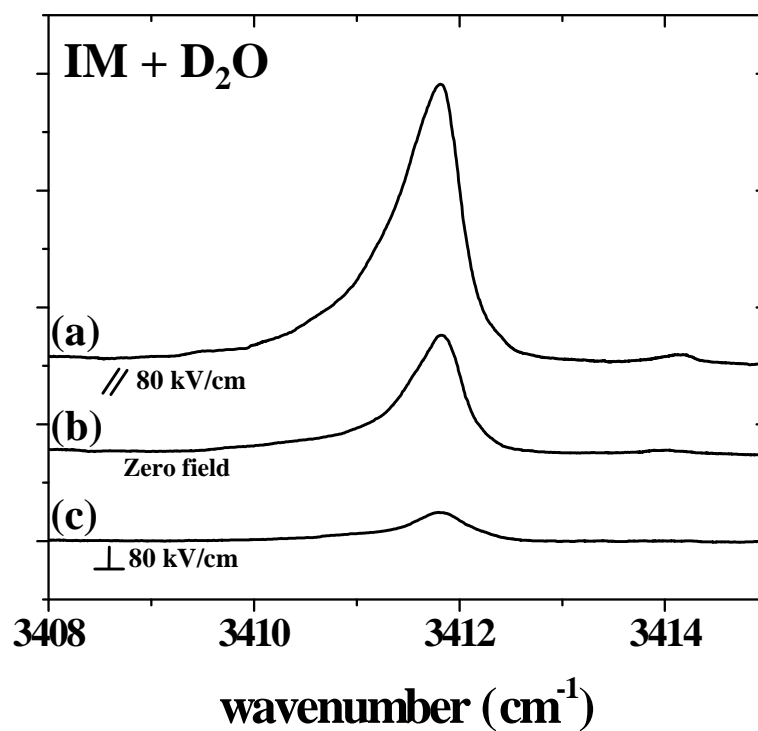
Figure 8.13: Expanded spectra of the bonded N–H stretch mode of the imidazole–D_2O complex. Spectra (a), (b), and (c) were recorded parallel polarization, zero-field and perpendicular polarization conditions, respectively.
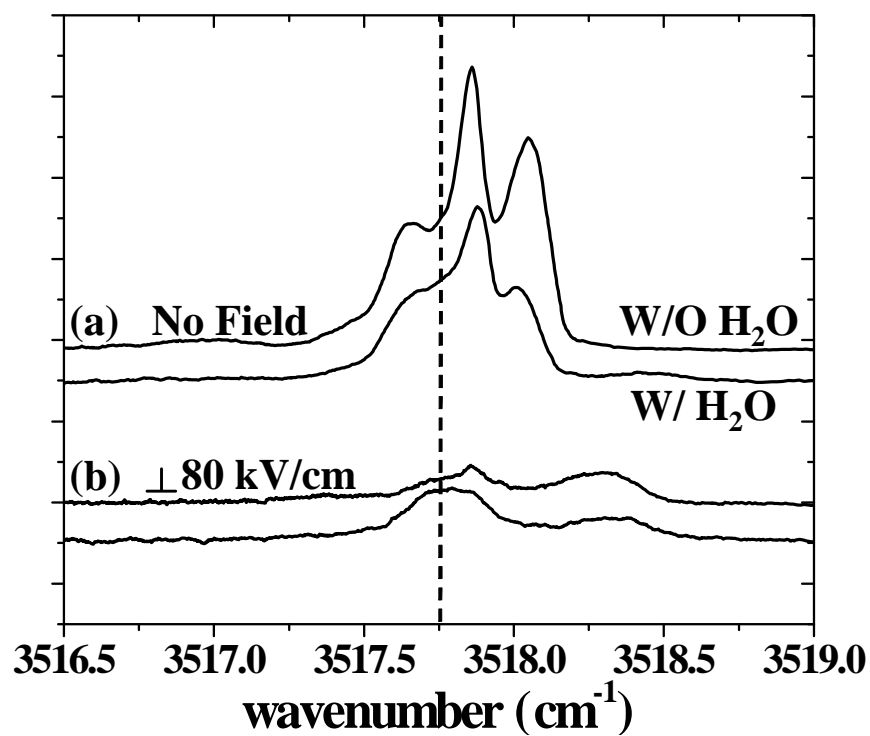
Figure 8.14: A comparison between the free N–H stretch region without (upper) and with (below) water added to the droplets. Spectra (a) and (b) were recorded zero-field and perpendicular polarization conditions, respectively. The vapor pressure of water was 9×10^{-7} Torr at the pick-up cell.

spectra in the free N–H stretch region, recorded with (a) no applied field and (b) an applied DC electric field directed perpendicular to the laser polarization direction and a comparison between the experimental results, with and without water added to the droplets. The water pressure at the pick-up cell was up to 9×10^{-7} Torr, which is very low compared to that of the optimum condition for one water (2.4×10^{-6} Torr), to make sure that the band comes from only the IM with one water complex. The vertical dashed line shows that there is a perpendicular band underneath the monomer band at about 3517.8 cm^{-1} that is evident only when the water is present. Although this enables us to identify this band, we are unable to report a VTMA for this band because the corresponding zero-field and parallel polarization spectra could not be obtained. The data are nevertheless sufficient to confirm that this band is nearly perpendicular, as reported in Table 8.1.

It is clear from the above results that both IMW1 and IMW2 are formed in helium nanodroplets, consistent with the idea that the water approaches from a random direction and then gets trapped in the nearest minimum on the potential energy surface that is separated from the other by a sufficiently high barrier to prevent rearrangement.

8.4 Conclusions and Future Work

In this combined experimental/theoretical study we report high-resolution infrared laser spectra of imidazole (IM), imidazole dimer (IMD) and two isomers of imidazole water complexes (IMWs) isolated in helium nanodroplets. For IM monomer and dimer, the calculated frequencies are very well matched with the observed frequencies. By orienting the molecules with a strong DC electric field, we achieved a definitive assignment for the IMD using the vibrational transition moment angles (VTMAs). For the case of the IM–water binary complexes, as shown in Figure 8.9, the calculated frequencies of the bonded O–H and asymmetric stretches are in poor agreement with the observed

frequencies. However, an unambiguous assignment of the above bands is achieved with the aid of the VTMAs and deuterium substitution for the binary complexes.

The relative abundances of the two isomers, IMW1 and IMW2, are found to be almost $1:1$, which could be the result of both energetic and dynamical effects associated with the formation of the clusters in the helium. In particular, the formation of the two IMW complexes in almost equal population could be ascribed to their almost identical relative energies and to the equal widths of the entrance valley (funnel) where a water molecule can be trapped by the long-range potential energy surface.

The studies of IMW complexes are of help in the characterization of the experimental spectra of adenine– and guanine–water complexes, which we plan to study. We are currently carrying out studies of higher order IM–water complexes, such as IM + two waters (IM2W) and IMD + one water (IMDW) complexes [302] which would provide further fundamental understanding of hydrogen-bonding effects associated with IMD in the ammonia channel. Nevertheless, in future studies we also plan to investigate the IM–ammonia complex, which is directly related to the mechanism of the ammonia gas transport in physiological conditions.

Chapter 9

Summary and Outlook

9.1 Summary

We have shown that the application of helium nanodroplet spectroscopy on isolated biomolecules has great potential in characterizing and determining structures of various biomolecule systems, such as nucleic acid bases (NABs) and their water complexes. The unique properties of helium, superfluidity at ultra low temperature and weak solute–solvent interactions, provide a gas-phase environment, which permits spectra to be analyzed. The cold helium environment significantly reduces the spectral complexity which is partially important in large systems. The vapor pressure needed for pick up by the helium droplets is partially advantageous for biomolecules that are often thermally unstable. The use of a multipass cell and a high power laser also contributes significantly to the success of this project because it increases the signal-to-noise, which is an important issue in larger systems.

Binary and higher order complexes in the helium droplets are formed by sequential pick up of the molecules in the beam path. The cluster growth in the liquid helium is fundamentally different from that in the gas-phase expansions. In the latter, the most stable complexes are often formed by overcoming small barriers via collisions. On the other hand in the helium droplets the freezing rate is so fast that higher free energy

complexes, once formed, are trapped in the free energy potential surface minimum, which is not necessarily the global minimum. We have mostly focused on the NAB binary complexes with a water molecule in this thesis, because water plays an important role in biological processes.

In this thesis, we have applied the measurement of vibrational transition moment angles (VTMAs) and dipole moment curves to the isolated NAB systems by using the pendular-state spectroscopic technique. One of the advantages is that the results can be directly compared with high confidence to moderate-level *ab initio* calculations. The important results from this thesis are summarized below.

The fact that nature seeks out the lowest energy configuration is used to great advantage in science. In particular, theoretical methods rely on the variational principle to find minimum energy structures and paths that correspond to those observed experimentally. Indeed, the entire field of molecular modeling depends upon the fact that the true molecular structure is the one that minimizes the energy on the corresponding potential energy surface. It is therefore somewhat surprising the experimental determination of these molecular energies, for example, for the different tautomers of a nucleic acid base or a polypeptide, is still problematic. In many cases, we have good methods for determining their structure, but the small energy differences between these tautomeric forms for biomolecules (in the few kcal/mol range) is often difficult to determine experimentally. Similarly, despite their overwhelming importance in biology, hydrogen-bonding energies are generally poorly determined from experiment. Indeed, much of our understanding of molecular biology comes from structure, rather than the study of subtle energetic differences between the various molecular structures.

The question why nature has chosen certain building blocks for the structure of life still remains mystery. However, significant progress in research made in small steps will eventually provide answers for this puzzle.

9.1.1 Tautomerism of NABs

The relative stability of tautomers of NABs is of great importance to the functioning of base pairs. The occurrence of rare tautomers in biosynthesis has been postulated as the mechanism for spontaneous mutation because of their altered base-pairing properties [83]. The structural details and the relative stability of the various tautomers of NABs are more difficult to study if these systems are not isolated both experimentally and theoretically [145]. In this thesis, we have studied the structural information and the relative energetics of various tautomers of NABs, such as cytosine, guanine, adenine, uracil and thymine. All of their lowest energy forms were detected and characterized. Furthermore, several higher energy tautomers of cytosine and guanine were also observed and studied in this thesis. Studying even higher energy tautomers at moderate temperature would be possible and give more information about the tautomerism of NABs.

9.1.2 Structural Assignments: Correcting Previous Assignments

Cytosine

Our study of the cytosine tautomers has ended a dispute that had lasted almost two decades. The dispute began from the first experimental observation and assignment of the three lowest energy cytosine tautomers present in the gas-phase (C1, C21 and C31, see Figure 3.1) with low level *ab initio* calculations. There have been numerous theoretical studies since then on the relative energies of the cytosine tautomers showing that indeed, C31, C32 and C1 are the three lowest energy tautomers, which is different from the previous experimental result. Because the microwave spectroscopy on the cytosine tautomers was the only available experimental data, the theoretical studies

reached different explanations based on the experimental result [74, 137, 146, 162, 303–310]. However, our study has fully confirmed the microwave result in that the three tautomers (C1, C21 and C31) have turned out to be the same tautomers observed in this work, C32, C31 and C1, respectively.

Guanine

Studying isolated guanine with a thermal evaporation technique has been a challenging task for a long time due to its thermal decomposition at the necessary temperature for the vapor pressure needed in the gas-phase study. Even microwave spectroscopy on guanine has not yet been conducted for the same reason and it is the only NAB that has no microwave spectroscopic data. As a result, infrared spectroscopy has been the sole tool for the guanine system, having been investigated by two groups. However these studies disagreed in several respects, in part because *ab initio* vibrational frequencies could not be reconciled with the experimental spectra, and also perhaps because of thermal decomposition. Because helium droplet spectroscopy requires a much lower vapor pressure and because of the high reliability of the VTMAs in assigning structures, helium droplet spectroscopy is an ideal tool for the study of the guanine tautomers. The results presented in Chapter 4 shows an unambiguous assignment of the four lowest energy tautomers with measurements of VTMAs and dipole moment curves for the bands of the various tautomers. However, this result turned out to be conflicted with the previous IR–UV double resonance spectroscopic studies [70, 182, 183]. It is worth noting that there has been good agreement between the gas-phase and helium droplet studies for NABs (cytosine, adenine, uracil and thymine) (within a few wavenumber), except for the guanine system. Therefore, we presented a third point of view in the guanine system which would help clarify the puzzles associated with the previous studies on the guanine system using laser desorption techniques in IR–UV experiments.

9.1.3 Nonplanarity

Isolated NABs were believed to be perfectly planar for decades. Recently, isolated NABs have been proposed to be nonplanar due to the pyramidalization of the amino groups. To demonstrate the nonplanarity of NABs, adenine was used to show the first experimental evidence of the nonplanarity. Adenine was chosen for this study because its structure has only a single global minimum, and because it gives higher signal-to-noise compared to other systems used in this thesis. This work has been made possible by the fact that the VTMAs associated with the high frequency X–H vibrations are dependent mainly on the structure or the orientation of the corresponding groups within the molecule. We have shown that adenine is indeed nonplanar, with the NH_2 group tilted approximately $20°$ out of plane, as the *ab initio* calculations predicted. This approach will be applied to the other NABs (cytosine and guanine) whose structures show nonplanarity at least from *ab initio* calculations.

9.1.4 Hydrated Biomolecules

We have conducted vibrational spectroscopic studies of the mono-hydrated uracil conformational landscapes. Hydrated uracil is one of the most studied NAB-H_2O systems due to its simplicity and the fact that the energy gap between the global minimum of uracil and the next lowest energy tautomer is relatively higher than other NABs such that the possibilities of forming complexes of higher energy hydrated uracil tautomer complexes are reduced. We observed four weakly bound uracil–water conformers in the helium nanodroplets, structures that were predicted as the four lowest energy complexes by diffusion Monte Carlo simulations of uracil-(water)$_n$ (n=1-3) by van Mourik and co-workers [242, 243, 257]. The vibrational band assignments of the uracil–water binary complexes were conducted with the aid of VTMAs and comparison of the uracil monomer spectrum. The existence of four uracil–water conformers (UW1 – 4) can be

seen by scanning the free O–H stretching region of the uracil–water system as shown in Figure 7.3. In this study each uracil–water binary complex is formed in helium droplets by sequential pick-up of the two molecules. The formation of complexes in the helium droplets is governed by long range intermolecular interactions. However, the water molecule, which has large rotational constants, rotates at the time it enters the attractive potential valley of the uracil molecule, so it can not escape and thus forms complexes at the local minimum. We postulated that the population distribution of the uracil–water binary complexes is strongly determined by the widths of the entrance valley for each complex. This is supported by the relative abundances from the experimental results which is more relevant to the hypothesis of the entrance valley widths than the energetic consideration of the binary complexes.

Imidazole–water binary complexes were also studied as a stepping stone for the study of imidazole-ammonia complexes, which would be a very interesting system in the gas-phase studies because of the recent structural analysis of a channel in a bacterial membrane, the neutral condition of the channel. The hydrogen-bonding network between the imidazole moiety of the histidine and ammonia molecules in the channel has a very close relevance to the study of the imidazole water binary complexes. Not only because of this, but also because of its importance in the biological systems, the studies of the imidazole–water complexes have been conducted and shown that there were two binary complexes formed in the helium droplets which have not been studied in the gas-phase. Although the experimental frequencies are in poor agreement with *ab initio* frequency calculations, the VTMA analysis and deuterium substitution study show a conclusive assignments in this system.

9.2 Outlook

The application of helium droplet spectroscopy with VTMA analysis to biologically important systems is wide open. The results presented here, which deal with only small group of molecules, suggest intriguing research directions in the future. The studies of more complicated isolated NAB systems, self-associated complexes, base pair and their hydrated complexes should be possible. For example, as shown throughout this thesis, several bands observed in the monomer or binary complex spectral region are due to the higher energy tautomers or higher order complexes, self associated complexes. Because we use single resonance, linear spectroscopic technique, the observation of these bands is readily possible especially when using with high power IR lasers and higher oven temperatures to increase the monomer's signal-to-noise ratio. This actually will give a possibility to study the hydrogen-bonding of the pairs of NABs which is a fundamental to the structure and dynamics of DNA and RNA and the subject of intensive study. Although the Watson-Crick base pairs are justifiably often the center of such attention, NAB dimers can also provide important information concerning such hydrogen-bonding. For example, N–H $\cdots$ O–C hydrogen bonds are of fundamental importance and are amenable to study in the simplest of these systems, namely the uracil dimer. Nevertheless, the studies of NAB dimers easily lead us to the study of the base pairs, which can be done experimentally using sequential double ovens. This study will provide insight into the understanding the mechanisms of how the structural rearrangements are expressed, such as in the process of DNA replications, DNA – drug interaction and protein foldings and so on.

9.2.1 Thermochemistry of Biomolecules: Experimental Measurement

The relative energies of the various tautomers of nucleic acid bases have not been experimentally determined, despite the fact that rare tautomers of NABs were first implicated in DNA mutation by Watson and Crick in their landmark paper [144]. Indeed, the thermochemistry is largely missing for systems that exist as an equilibrium mixture of several different tautomers, isomers or conformers, which lie within a few kcal/mol of one another. A detailed characterization of the associated thermochemistry would clearly provide us with a better understanding of a wide range of biologically important processes, including mutation, protein folding (secondary structure) and the influence of solvent interactions, including hydrogen-bonding.

In the work described in this thesis, we have shown that high resolution infrared laser spectroscopy in helium droplets can determine NAB structures [79, 86, 87, 89]. Although the associated conditions are far from physiological, they allow for direct comparisons with theory, both at the *ab initio* and molecular modeling levels. Indeed, the tremendous growth in the study of gas-phase biomolecules is the result of the potential of this approach for improving our fundamental understanding of the associated interactions.

The experimental method proposed here is based upon the fact that the molecules are cooled extremely quickly upon capture by a helium nanodroplet, as a result the high temperature tautomer populations can be trapped with little change in their high temperature equilibrium concentration. The high resolution of the current spectroscopic methods then should enable us to determine the relative populations of the various tautomers as a function of the pick-up cell temperatures, providing direct information on the associated ΔH's.

In future studies we plan to carry out studies at even higher oven temperatures with

the goal of observing more tautomers of NABs at even higher energies, as mentioned above. Adenine, uracil and thymine which have relatively large energy gaps between the major and minor tautomers are the challenge for next experiment. Guanine, which has several energetically acceptable tautomers, will be challenging because it is rather thermally unstable [89], so that the range of temperatures over which we can perform these experiments will be more limited. Furthermore, it will be a test of *ab initio* calculations of guanine which shows that the energy of the global minimum is very dependent on zero point energy corrections and basis sets. Since cytosine is a good system to study first because it is more thermally stable than guanine, and we have observed six low energy tautomers with tentative assignments of three higher energy tautomers, C21, C22 and C4 (see Figure 3.1) at higher oven temperatures.

Now that we have a method for unambiguously identifying the various tautomers of a given system, the challenge for the future is the development of experimental methods that are compatible with the helium nanodroplet experiment and will enable us to measure their relative energies.

Once cooled to 0.4 K, the molecules can be characterized by high resolution laser spectroscopy by varying the temperature of the pick-up cell and measuring the corresponding changes in the isomer population upon super rapid cooling in helium nanodroplets. Therefore, the sudden cooling that a molecule experiences when it is captured by a helium droplet prevents the system from accommodating to the new temperature, so far as its isomer population distribution is concerned. There are a number of factors that support this hypothesis. First, a wide range of experiments suggest that the cooling rate for a captured molecule is very large. For example, Scheidemann *et al.* [15] estimated the cooling rate associated with charge transfer in helium to be approximately 10^{16} K/s, much faster than those typical of free jet expansions, namely 10^8 K/s [311]. Our estimate is that vibrational cooling for most small molecules oc-

curs on the sub-nanosecond time scale. Nevertheless, we know that for many systems the relaxation rate is not much faster than this, given the high resolution of the corresponding spectra. On the other hand, for larger molecules we often observe even broader linewidths [79, 86, 87, 89], which is thought to result from faster vibrational relaxation, due to high state densities.

Further evidence suggesting that helium droplets will freeze the high temperature conformer distributions comes from extensive matrix isolation work [312, 313], which shows that, in systems that are co-deposited onto a cold substrate with rare gases to form the matrix, the heavy rare gases tend to disrupt the tautomer population distributions, relative to those in the gas-phase, while the lighter ones do not. Liquid helium has not been studied, but extrapolation of the results from solid matrices of the heavier rare gases suggests that it should be the best in this regard. As noted above, Potts and Baer [311, 314] found that even the cooling in an argon free jet expansion can be fast enough to quench the isomer populations distributions for some systems. The fact that we see multiple tautomers in the previous experiments [86, 89] confirms that the helium is indeed a good quencher, not allowing the various energy tautomers to re-equilibrate at the helium temperature.

Oven Design

In the ovens we have been using for the biomolecule studies in this thesis, the solid samples are placed directly in the section of the oven that is exposed to the helium beam (shown in Figure 2.3). As a result, the operating temperature of the oven is restricted to the sample vapor pressure that corresponds to the optimum pick-up of a single molecule. Since the goal of the present work is to measure the temperature dependence of the signals associated with different isomers, we will have to construct an oven with two separately heated sections, one that controls the vapor pressure and

the other through which the helium droplet beam passes, so that the temperature of the latter can be controlled independently (see Figure 9.1). Long channels will be used for entry and exit of the helium droplet beam (to reduce temperature gradients) and a thin wall stainless steel tube or a vacuum (ideally) will separate the two sections of the oven, so that they can be maintained at different temperatures. Note that since the experimental measurements to be performed here constitute the ratio of the band intensities for the various tautomers, the density changes associated with the temperature of the second stage will not affect the results. In any case, an essentially quantitative correction for these density effects will be straightforward. To ensure that changes in the second stage temperature do not significantly change the temperature of the first stage, which would cause significant changes in the vapor pressure, both stages will need to be actively temperature controlled.

Experimental Measurements

As noted above, the primary measurements in this experiment will be the pick-up cell temperature dependence of the intensities of various vibrational bands in the infrared spectra. As the temperature of the oven is increased, higher energy isomers will become more favorably populated, changing the ratios of the peak intensities. Consider for the moment the simple case of a system with only two isomers. As shown previously by Potts and Baer [311, 314, 315] the spectroscopic band intensities, as a function of the temperature, can be related to ΔH through the van't Hoff equation:

$$\frac{d\ln(K)}{d(1/T)} = \frac{-\Delta H^\circ}{R} \tag{9.1}$$

where K is the temperature dependent equilibrium constant. This can be done by noting that K is the ratio of the tautomer populations, which are in turn related to the spectral band intensity (integrated area $= A$) by:
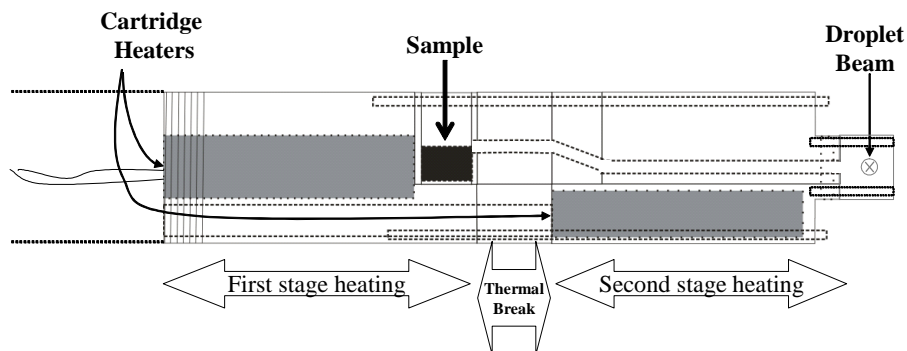
Figure 9.1: A schematic diagram of two-stage oven that can be load-locked into the helium droplet appartus shown in Figure 2.2. The first stage is for controlling the vapor pressures of the sample and the second stage controls the temperature at which the pick-up occurs. The temperatures between the first and second stage must be independent by using a thermal break (e.g., stainless steel or vacuum).

$$A_i = P_i \times t_i \tag{9.2}$$

where i is 1 or 2, representing the two isomers, t_i are the corresponding transition moments and P_i are the populations. We can now write:

$$\frac{d}{d(1/T)} (\ln K) = \frac{d}{d(1/T)} \left(\ln \frac{t_1 A_1}{t_2 A_2} \right) \tag{9.3}$$

$$= \frac{d}{d(1/T)} \left(\ln F + \ln \frac{A_1}{A_2} \right) \tag{9.4}$$

where F is the ratio of the transition moments. Since F does not depend upon temperature, we can write:

$$\frac{d \ln(A_1/A_2)}{d(1/T)} = \frac{-\Delta H^\circ}{R} \tag{9.5}$$

Thus, even in the absence of accurate transition moment magnitudes, we are able to obtain ΔH directly from a measurement of the temperature dependence of the band intensities (areas). In many of the systems of interest, there are more than two isomers, and the generalized version of the above theory will be used, providing ΔH's for all the isomers. For example, in the case of cytosine and guanine, we have identified at least 3 (possibly 6) and 5 tautomers in helium nanodroplets, respectively, and plane to measure their relative enthalpies using the above methods.

All of the above analysis assumes that we have a firm assignment of the vibrational spectrum, meaning that the various vibrational bands are properly assigned to the appropriate vibrational modes of the correct tautomers. As noted above, the vibrational transition moment angles are ideally suited for this and will be used to determine assignments.

In the above analysis the ratio of the tautomer populations is used in order to remove the vibrational transition moment magnitude from the equation. However, these values are actually calculated quite accurately by *ab initio* calculations, so to a first approximate we can turn the above ratios into absolute population ratios, which means that the van't Hoff plot can be extrapolated to infinite temperature ($1/T \rightarrow 0$) in order to obtain an estimate of ΔS. The latter results could be extremely useful in providing qualitative information on the relative "stiffness" of the different isomers. Finally, if a wide enough temperature range can be explored to reveal some curvature in the data displayed in the van't Hoff plot, it might be possible to extract some information on the temperature dependence of these thermodynamics quantities.

The fact that we typically have multiple vibrational modes (C–H, N–H and O–H stretches) from which to obtain independent estimates of the populations ratios, it should be possible to obtain quite good estimates of the absolute population ratios. The first phase of this study will be to accumulate a large data base for many different molecules and vibrational states to assess the accuracy of the approach. In the studies of Potts and Baer [311, 314, 315] the ΔH's were determined to an accuracy of approximately $\pm$ 0.1 kcal/mol. Given that the vibrational spectroscopy used in the proposed studies is a linear spectroscopy, while REMPI was used in the Potts and Baer [311, 314, 315] studies, we expect that our error bars will be somewhat better than this. It is interesting to compare these errors with the expected energy differences (from *ab initio* calculations) for a typical system. In the case of the three cytosine and four guanine lowest energy tautomers, the relative energies of the tautomers span a range of approximately 1.9 and 1.2 kcal/mol, respectively.

Ab initio Calculations

There are numerous number of *ab initio* data already available in the literature, which will provide us with many opportunities to make comparisons. Nevertheless, we plan to carry out our own theoretical investigations, in part because very few people quote vibrational transition moments in their papers. We will need these both for aiding in the assignment of the experimental spectra (the theoretical vibrational transition moment angles are needed for comparison with experiment) and for comparison with the measured ΔH's.

Molecules to be Studied

As noted above, the thermochemistry of isolated biomolecule tautomers is poorly characterized experimentally. This includes the nucleic acid bases, for which we have already obtained infrared spectra in helium nanodroplets. The previous work [79, 86, 87, 89] clearly demonstrates that the methods presented here will be straightforward to apply to these systems. As a result, a systematic study of all of these systems will be necessary. It is clear that we must perform full studies on purines alkylated in the N9 position and we must do the same with the pyrimidines alkylated in the N1 position which is more physiologically relevant. Likewise, it will be essential to include 5-bromouracil which is known to lead to mutations via the mechanism involving an enhanced tautomeric form [316, 317]. Guanine will be the most challenging, given that it is rather thermally unstable, so that the range of temperatures over which we can perform these experiments will be more limited than for some of the other systems. Then it will be essential to systematically add water molecules to the tautomers to assess the role of solvation. Amino acids and peptides are also of great interest and can be studied. The application of these methods to other systems, including sugars and steroids, can also be explored.

BIBLIOGRAPHY

[1] Tilley, D. R.; Tilley, J. *Superfluidity and Superconductivity;* IOP Publishing: Bristol, 3rd ed.; 1990.

[2] Wilks, J.; Betts, D. S. *An Introduction to Liquid Helium;* Clarendon Press: Oxford, 2nd ed.; 1987.

[3] Tabbert, B.; Gunther, H.; zu Putlitz, G. *J.Low Temp.Phys.* **1997,** *109,* 653–707.

[4] Lehmann, K. K.; Scoles, G. *Science* **1998,** *279,* 2065–2066.

[5] Toennies, J. P.; Vilesov, A. F. *Annu.Rev.Phys.Chem.* **1998,** *49,* 1–41.

[6] Ceperley, D. M. *Rev.Mod.Phys.* **1999,** *67,* 279–355.

[7] Becker, E. W. *Z.Phys.D* **1986,** *3,* 101–107.

[8] Gough, T. E.; Knight, D. G.; Scoles, G. *Chem.Phys.Lett.* **1983,** *97,* 155–160.

[9] Onnes, H. K. *Commun.Phys.Lab.Univ.Leiden* **1908,** *105,* 1–6.

[10] Onnes, H. K. *Commun.Phys.Lab.Univ.Leiden* **1908,** *108,* 1–23.

[11] Kapitza, P. *Nature* **1938,** *141,* 74.

[12] Allen, J. F.; Misener, A. D. *Nature* **1938,** *141,* 75.

[13] Gspann, J.; Vollmar, H. *J.Chem.Phys.* **1980,** *73,* 1657–1664.

[14] Scheidemann, A.; Schilling, B.; Toennies, J. P.; Northby, J. A. *Physica.B* **1990,** *165,* 135–136.

[15] Scheidemann, A.; Schilling, B.; Toennies, J. P. *J.Phys.Chem.* **1993,** *97,* 2128–2138.

[16] Goyal, S.; Schutt, D. L.; Scoles, G. *Phys.Rev.Lett.* **1992,** *69,* 933–936.

[17] Frochtenicht, R.; Toennies, J. P.; Vilesov, A. F. *Chem.Phys.Lett.* **1994,** *229,* 1–7.

[18] Hartmann, M.; Miller, R. E.; Toennies, J. P.; Vilesov, A. F. *Phys.Rev.Lett.* **1995,** *75,* 1566–1569.

[19] Harms, J.; Hartmann, M.; Toennies, J. P.; Vilesov, A. F.; Sartakov, B. *J.Mol.Spectrosc.* **1997,** *185,* 204–206.

[20] Barnett, R. N.; Whaley, K. B. *J.Chem.Phys.* **1993,** *99,* 9730–9744.

[21] Krotscheck, E.; Chin, S. A. *Chem.Phys.Lett.* **1994,** *227,* 143–148.

[22] Brink, D. M.; Stringari, S. *Z.Phys.D* **1990,** *15,* 257–263.

[23] Hartmann, M.; Mielke, F.; Toennies, J. P.; Vilesov, A. F.; Benedek, G. *Phys.Rev.Lett.* **1996,** *76,* 4560–4563.

[24] Grebenev, S.; Toennies, J. P.; Vilesov, A. F. *Science* **1998,** *279,* 2083–2086.

[25] Grebenev, S.; Hartmann, M.; Havenith, M.; Sartakov, B.; Toennies, J. P.; Vilesov, A. F. *J.Chem.Phys.* **2000,** *112,* 4485–4495.

[26] Even, U.; Jortner, J.; Noy, D.; Lavie, N. *J.Chem.Phys.* **2000,** *112,* 8068–8071.

[27] Even, U.; Al-Hroub, I.; Jortner, J. *J.Chem.Phys.* **2001,** *115,* 2069–2073.

[28] Callegari, C.; Higgins, J.; Stienkemeier, F.; Scoles, G. *J.Phys.Chem.A* **1998,** *102,* 95–101.

[29] Stienkemeier, F.; Meier, F.; Lutz, H. O. *J.Chem.Phys.* **1997,** *107,* 10816–10818.

[30] Stienkemeier, F.; Higgins, J.; Callegari, C.; Kanorsky, S. I.; Ernst, W. E.; Scoles, G. *Z.Phys.D* **1996,** *38,* 253–263.

[31] Stienkemeier, F.; Higgins, J.; Ernst, W. E.; Scoles, G. *Phys.Rev.Lett.* **1995,** *74,* 3592–3595.

[32] Stienkemeier, F.; Vilesov, A. F. *J.Chem.Phys.* **2001,** *115,* 10119–10137.

[33] Higgins, J.; Ernst, W. E.; Callegari, C.; Reho, J.; Lehmann, K. K.; Scoles, G.; Gutowski, M. *Phys.Rev.Lett.* **1996,** *77,* 4532–4535.

[34] Stienkemeier, F.; Ernst, W. E.; Higgins, J.; Scoles, G. *J.Chem.Phys.* **1995,** *102,* 615–617.

[35] Higgins, J.; Callegari, C.; Reho, J.; Stienkemeier, F.; Ernst, W. E.; Gutowski, M.; Scoles, G. *J.Phys.Chem.A* **1998,** *102,* 4952–4965.

[36] Hartmann, M.; Miller, R. E.; Toennies, J. P.; Vilesov, A. F. *Science* **1996,** *272,* 1631–1634.

[37] Nauta, K.; Miller, R. E. *Phys.Rev.Lett.* **1999,** *82,* 4480–4483.

[38] Lindinger, A.; Toennies, J. P.; Vilesov, A. F. *J.Chem.Phys.* **1999,** *110,* 1429–1436.

[39] Hartmann, M.; Toennies, J. P.; Vilesov, A. F.; Benedek, G. *Czech.J.Phys.* **1996,** *46,* 2951–2956.

[40] Behrens, M.; Buck, U.; Frochtenicht, R.; Hartmann, M.; Huisken, F.; Rohmund, F. *J.Chem.Phys.* **1998,** *109,* 5914–5920.

[41] Frochtenicht, R.; Kaloudis, M.; Koch, M.; Huisken, F. *J.Chem.Phys.* **1996,** *105,* 6128–6140.

[42] Lewerenz, M.; Schilling, B.; Toennies, J. P. *J.Chem.Phys.* **1995,** *102,* 8191–8207.

[43] Lewerenz, M.; Schilling, B.; Toennies, J. P. *Chem.Phys.Lett.* **1993,** *206,* 381–387.

[44] Callicoatt, B. E.; Forde, K.; Ruchti, T.; Jung, L. L.; Janda, K. C.; Halberstadt, N. *J.Chem.Phys.* **1998,** *108,* 9371–9382.

[45] Halberstadt, N.; Janda, K. C. *Chem.Phys.Lett.* **1998,** *282,* 409–412.

[46] Seong, J.; Janda, K. C.; Halberstadt, N.; Spiegelmann, F. *J.Chem.Phys.* **1998,** *109,* 10873–10884.

[47] Ruchti, T.; Forde, K.; Callicoatt, B. E.; Ludwigs, H.; Janda, K. C. *J.Chem.Phys.* **1998,** *109,* 10679–10687.

[48] Callicoatt, B. E.; Mar, D. D.; Apkarian, V. A.; Janda, K. C. *J.Chem.Phys.* **1996,** *105,* 7872–7875.

[49] Farnik, M.; Henne, U.; Samelin, B.; Toennies, J. P. *Z.Phys.D* **1997,** *40,* 93–98.

[50] Farnik, M.; Henne, U.; Samelin, B.; Toennies, J. P. *Phys.Rev.Lett.* **1998,** *81,* 3892–3895.

[51] Henne, U.; Toennies, J. P. *J.Chem.Phys.* **1998,** *108,* 9327–9338.

[52] Carney, J. R.; Zwier, T. S. *J.Phys.Chem.A* **2000,** *104,* 8677–8688.

[53] Viant, M. R.; Fellers, R. S.; McLaughlin, R. P.; Saykally, R. J. *J.Chem.Phys.* **1995,** *103,* 9502–9505.

[54] Colarusso, P.; Zhang, K. Q.; Guo, B.; Bernath, P. F. *Chem.Phys.Lett.* **1997,** *269,* 39–48.

[55] Evard, D. D.; Bieler, C. R.; Cline, J. I.; Sivakumar, N.; Janda, K. C. *J.Chem.Phys.* **1988,** *89,* 2829–2838.

[56] Hair, S. R.; Cline, J. I.; Bieler, C. R.; Janda, K. C. *J.Chem.Phys.* **1989,** *90,* 2935–2943.

[57] Hockridge, M. R.; Robertson, E. G.; Simons, J. P.; Borst, D. R.; Korter, T. M.; Pratt, D. W. *Chem.Phys.Lett.* **2001,** *334,* 31–38.

[58] Nir, E.; Kleinermanns, K.; de Vries, M. S. *Nature* **2000,** *408,* 949–951.

[59] Brown, R. D.; Godfrey, P. D.; McNaughton, D.; Pierlot, A. P. *J.Am.Chem.Soc.* **1989,** *111,* 2308–2310.

[60] Pratt, D. W. *Science* **2002,** *296,* 2347–2348.

[61] Nir, E.; Muller, M.; Grace, L. I.; de Vries, M. S. *Chem.Phys.Lett.* **2002,** *355,* 59–64.

[62] Lindinger, A.; Toennies, J. P.; Vilesov, A. F. *Phys.Chem.Chem.Phys.* **2001,** *3,* 2581–2587.

[63] Lindinger, A.; Lugovoj, E.; Toennies, J. P.; Vilesov, A. F. *Z.Phys.Chem.* **2001,** *215,* 401–416.

[64] Hartmann, M.; Lindinger, A.; Toennies, J. P.; Vilesov, A. F. *Chem.Phys.* **1999,** *239,* 139–149.

[65] Hartmann, M.; Lindinger, A.; Toennies, J. P.; Vilesov, A. F. *J.Phys.Chem.A* **2001,** *105,* 6369–6377.

[66] Hartmann, M.; Lindinger, A.; Toennies, J. P.; Vilesov, A. F. *Phys.Chem.Chem.Phys.* **2002,** *4,* 4839–4844.

[67] Slenczka, A.; Dick, B.; Hartmann, M.; Toennies, J. P. *J.Chem.Phys.* **2001,** *115,* 10199–10205.

[68] Lehnig, R.; Slenczka, A. *J.Chem.Phys.* **2003,** *118,* 8256–8260.

[69] Robertson, E. G.; Simons, J. P. *Phys.Chem.Chem.Phys.* **2001,** *3,* 1–18.

[70] Mons, M.; Dimicoli, I.; Piuzzi, F.; Tardivel, B.; Elhanine, M. *J.Phys.Chem.A* **2002,** *106,* 5088–5094.

[71] Nir, E.; Grace, L.; Brauer, B.; de Vries, M. S. *J.Am.Chem.Soc.* **1999,** *121,* 4896–4897.

[72] F.Piuzzi,; M.Mons,; I.Dimicoli,; B.Tardivel,; Q.Zhao, *Chem.Phys.* **2001,** *270,* 205–214.

[73] Snoek, L. C.; Kroemer, R. T.; Hockridge, M. R.; Simons, J. P. *Phys.Chem.Chem.Phys.* **2001,** *3,* 1819–1826.

[74] Podolyan, Y.; Gorb, L.; Leszczynski, J. *Int.J.Mol.Sci.* **2003,** *4,* 410–421.

[75] Jarrold, M. F. *Acc.Chem.Res.* **1999,** *32,* 360–367.

[76] Bakker, J. M.; Compagnon, I.; Meijer, G.; von Helden, G.; Kabelac, M.; Hobza, P.; de Vries, M. S. *Phys.Chem.Chem.Phys.* **2004,** *6,* 2810–2815.

[77] McClure, R. J.; Craven, B. M. *Acta.Crystallogr.Sect B* **1973,** *29,* 1234–1238.

[78] Dreyfus, M.; Bensaude, O.; Dodin, G.; Dubois, J. E. *J.Am.Chem.Soc* **1976,** *98,* 6338–6349.

[79] Dong, F.; Miller, R. E. *Science* **2002,** *298,* 1227–1230.

[80] Nir, E.; Janzen, C.; Imhof, P.; Kleinermanns, K.; de Vries, M. S. *J.Chem.Phys.* **2001,** *115,* 4604–4611.

[81] Park, Y. D.; Rizzo, T. R.; Peteanu, L. A.; Levy, D. H. *J.Chem.Phys.* **1986,** *84,* 6539–6549.

[82] Dian, B. C.; Longarte, A.; Zwier, T. S. *Science* **2002,** *296,* 2369–2373.

[83] Drake, J. W. *The Molecular Basis of Mutation;* Holden-Day: San Francisco, 1970.

[84] Basiuk, V. A.; Navarro-Gonzalez, R. *Icarus* **1998,** *134,* 269–278.

[85] Knochenmuss, R.; Leutwyler, S. *J.Chem.Phys.* **1992,** *96,* 5233–5244.

[86] Choi, M. Y.; Dong, F.; Miller, R. E. *Philos.Trans.R.Soc.A* **2005,** *363,* 393–413.

[87] Choi, M. Y.; Miller, R. E. *Phys.Chem.Chem.Phys.* **2005,** *7,* 3565–3573.

[88] Choi, M. Y.; Douberly, G. E.; Falconer, T. M.; Lewis, W. K.; Lindsay, C. M.; Merritt, J. M.; Stiles, P. L.; Miller, R. E. *Int. Rev. Phys. Chem.* **2006,** *25,* 15–75.

[89] Choi, M. Y.; Miller, R. E. *J.Am.Chem.Soc.* **2006,** *128,* 7320–7328.

[90] Knuth, E. L.; Li, W.; Toennies, J. P. *Prog.Astronaut.Aeronaut.* **1989,** *117,* 329–334.

[91] Toennies, J. P.; Harms, J.; Knuth, E. L. *J.Chem.Phys.* **1997,** *106,* 3348–3357.

[92] Nauta, K.; Miller, R. E. The Spectroscopy of Molecules and Unique Clusters in Superfluid Liquid Helium Droplets. In ; Campargue, R., Ed.; Springer Verlag: Berlin, 2001.

[93] Knuth, E. L.; Schilling, B.; Toennies, J. P. On Scaling Parameters for Predicting Cluster Sizes in Free Jets. In , Vol. 19; Oxford Univ. Press: Oxford, UK, 1995.

[94] Guirao, A.; Pi, M.; Barranco, M. *Z.Phys.D* **1991,** *21,* 185–188.

[95] McCarthy, R. D. *J.Phys.Chem.Ref.Data* **1973,** *2,* 923.

[96] Harms, J.; Toennies, J. P.; Dalfovo, F. *Phys.Rev.B* **1998,** *58,* 3341–3350.

[97] Stringari, S.; Treiner, J. *J.Chem.Phys.* **1987,** *87,* 5021–5027.

[98] Buchenau, H.; Knuth, E. L.; Northby, J. A.; Toennies, J. P.; Winkler, C. *J.Chem.Phys.* **1990,** *92,* 6875–6889.

[99] Callegari, C.; Lehmann, K. K.; Schmied, R.; Scoles, G. *J.Chem.Phys.* **2001,** *115,* 10090–10110.

[100] Northby, J. A. *J.Chem.Phys.* **2001,** *115,* 10065–10077.

[101] Toennies, J. P.; Vilesov, A. F. *Angew.Chem.Int.Edit.* **2004,** *43,* 2622–2648.

[102] Nauta, K.; Miller, R. E. *J.Chem.Phys.* **1999,** *111,* 3426–3433.

[103] Rost, J. M.; Griffin, J. C.; Friedrich, B.; Herschbach, D. R. *Phys.Rev.Lett.* **1992,** *68,* 1299–1301.

[104] Block, P. A.; Bohac, E. J.; Miller, R. E. *Phys.Rev.Lett.* **1992,** *68,* 1303–1306.

[105] Friedrich, B.; Herschbach, D. R. *Int.Rev.Phys.Chem.* **1996,** *15,* 325–344.

[106] Friedrich, B.; Herschbach, D. R. *Nature* **1991,** *353,* 412–414.

[107] Miller, R. E. *J.Phys.Chem.* **1986,** *90,* 3301–3313.

[108] Miller, R. E. *SPIE Proceedings* **1998,** *3271,* 151–163.

[109] Nahler, N.; Baumfalk, R.; Buck, U.; Bihary, Z.; Gerber, R.; Friedrich, B. *J.Chem.Phys.* **2003,** *119,* 224–231.

[110] Beuhler, R. J.; Bernstein, R. B.; Kramer, K. H. *J.Am.Chem.Soc.* **1966,** *88:22,* 5331–5332.

[111] Brooks, P. R.; Jones, E. M. *J.Chem.Phys.* **1966,** *45,* 3449–2450.

[112] Brooks, P. R. *Science* **1976,** *193,* 11–16.

[113] Parker, D. H.; Jalink, H.; Stolte, S. *J.Phys.Chem.* **1987,** *91,* 5427–5437.

[114] Jalink, H.; Parker, D. H.; Stolte, S. *J.Chem.Phys.* **1986,** *85,* 5372–5373.

[115] den Ende, D. V.; Stolte, S. *Chem.Phys.Lett.* **1980,** *76,* 13–15.

[116] Oudejans, L.; Miller, R. E. *J.Chem.Phys.* **2000,** *113,* 971–978.

[117] Castle, K. J.; Abbott, J. E.; Peng, X.; Kong, W. *J.Phys.Chem.A* **2000,** *104,* 10419–10425.

[118] Ortigoso, J.; Fraser, G. T.; Pate, B. H. *Phys.Rev.Lett.* **1999,** *82,* 2856–2859.

[119] Hongzhi, L.; Franks, K. J.; Hanson, R. J.; Kong, W. *J.Phys.Chem.* **1998,** *102,* 8084–8090.

[120] Moore, D. T.; Oudejans, L.; Miller, R. E. *J.Chem.Phys.* **1999,** *110,* 197–208.

[121] Nauta, K.; Moore, D. T.; Miller, R. E. *Faraday Disc.* **1999,** *113,* 261–278.

[122] Nauta, B. K.; Miller, R. E. *J.Chem.Phys.* **2002,** *117,* 4846–4852.

[123] Stiles, P. L.; Nauta, K.; Miller, R. E. *Phys.Rev.Lett.* **2003,** *90,* 135301.

[124] Stiles, P. L.; Moore, D. T.; Miller, R. E. *J.Chem.Phys.* **2004,** *121,* 3130–3142.

[125] Douberly, G. E.; Miller, R. E. *J.Chem.Phys.* **2005,** *122,* 024306.

[126] Douberly, G. E.; Merritt, J. M.; Miller, R. E. *Phys.Chem.Chem.Phys.* **2005,** *7,* 463–468.

[127] Dong, F.; Miller, R. E. *J.Phys.Chem.A* **2004,** *108,* 2181–2191.

[128] Franks, K. J.; Li, H. Z.; Kong, W. *J.Chem.Phys.* **1999,** *110,* 11779–11788.

[129] Kong, W.; Bulthuis, J. *J.Phys.Chem.A* **2000,** *104,* 1055–1063.

[130] Kong, W. *Int.J.Mod.Phys.B* **2001,** *15,* 3471–3502.

[131] Castle, K. J.; Abbott, J.; Peng, X.; Kong, W. *J.Chem.Phys.* **2000,** *113,* 1415–1419.

[132] Portner, N.; Vilesov, A. F.; Havenith, M. *Chem.Phys.Lett.* **2003,** *368,* 458–464.

[133] Lehmann, K. K.; Dokter, A. M. *Phys.Rev.Lett.* **2004,** *92,* 173401.

[134] Szczesniak, M.; Szczepaniak, K.; Kwiatkowski, J. S.; KuBulat, K.; Person, W. B. *J.Am.Chem.Soc.* **1988,** *110,* 8319–8330.

[135] Aamouche, A.; Ghomi, M.; Grajcar, L.; Baron, M. H.; Romain, F.; Baumruk, V.; Stepanek, J.; Coulombeau, C.; Jobic, H.; Berthier, G. *J.Phys.Chem.A* **1997,** *101,* 10063–10074.

[136] Dreyfus, M.; Bensaude, O.; Dodin, G.; Dubois, J. E. *J.Am.Chem.Soc.* **1976,** *98,* 6338–6349.

[137] Hobza, P.; Sponer, J. *Chem.Rev.* **1999,** *99,* 3247–3276.

[138] Shishkin, O. V.; Gorb, L.; Hobza, P.; Leszczynski, J. *Int.J.Quantum Chem.* **2000,** *80,* 1116–1124.

[139] Estrin, D. A.; Paglieri, L.; Corongiu, G. *J.Phys.Chem.* **1994,** *98,* 5653–5660.

[140] Civcir, P. *J.Mol.Struct.-THEOCHEM* **2000,** *532,* 157–169.

[141] Kwiatkowski, J. S.; Leszczynski, J. *J.Phys.Chem.* **1996,** *100,* 941–953.

[142] Santamaria, R.; Charro, E.; Zacarias, A.; Castro, M. *J.Compu.Chem.* **1999,** *20,* 511–530.

[143] Spirko, V.; Sponer, J.; Hobza, P. *J.Chem.Phys.* **1996,** *106,* 1472–1479.

[144] Watson, J. D.; Crick, F. H. C. *Nature* **2004,** *171,* 737–738.

[145] Trygubenko, S. A.; Bogdan, T. V.; Rueda, M.; Orozco, M.; Luque, F. J.; Sponer, J.; Slavicek, P.; Hobza, P. *Phys.Chem.Chem.Phys.* **2002,** *4,* 4192–4203.

[146] Kobayashi, R. *J.Phys.Chem.A* **1998,** *102,* 10813–10817.

[147] Plützer, C.; Nir, E.; de Vries, M. S.; Kleinermanns, K. *Phys.Chem.Chem.Phys.* **2001,** *3,* 5466–5469.

[148] Nir, E.; Imholf, P.; Kleinermanns, K.; de Vries, M. S. *J.Am.Chem.Soc.* **2000,** *122,* 8091–8092.

[149] Destexhe, A.; Smets, J.; Adamowicz, L.; Maes, G. *J.Phys.Chem.* **1999,** *98,* 1506–1514.

[150] Dkhissi, A.; Houben, L.; Smets, J.; Adamowicz, L.; Maes, G. *J.Phys.Chem.A* **2000,** *104,* 9785–9792.

[151] Smets, J.; Adamowicz, L.; Maes, G. *J.Phys.Chem.* **1996,** *100,* 6434–6444.

[152] Sponer, J.; Florian, J.; Hobza, P.; Leszczynski, J. *J. Biomol. Struct. Dynam.* **1996,** *13,* 827–833.

[153] Sponer, J.; Sponer, J. E.; Gorb, L.; Leszczynski, J.; Lippert, B. *J.Phys.Chem.A* **1999,** *103,* 11406–11413.

[154] Nauta, K.; Miller, R. E. *Science* **2000,** *287,* 293–295.

[155] Nauta, K.; Miller, R. E. *Science* **1999,** *283,* 1895–1897.

[156] Nauta, K.; Miller, R. E. *J.Chem.Phys.* **2001,** *115,* 10254–10260.

[157] Nauta, K.; Miller, R. E. *Chem.Phys.Lett.* **2001,** *350,* 225–232.

[158] Nauta, K.; Miller, R. E. *J.Chem.Phys.* **2001,** *115,* 8384–8392.

[159] Schneider, K.; Kramper, P.; Schiller, S.; Mlynek, J. *Optics.Letters.* **1997,** *22,* 1293–1295.

[160] Schneider, K.; Kramper, P.; Mor, O.; Schiller, S.; Mlynek, J. *Advanced Solid State Lasers; Trends in Optics and Photonics* **1998,** *19,* 256–258.

[161] Yevgeniy, P.; Yury, V. R.; Jerzy, L. *Int.J.Quantum Chem.* **2001,** *83,* 203–212.

[162] Nowak, M. J.; Lapinski, L.; Fulara, J. *Spectrochim. Acta Part A* **1989,** *45,* 229–242.

[163] Gould, I. R.; Vincent, M. A.; Hillier, I. H.; Lapinski, L.; Nowak, M. J. *Spectrochim. Acta* **2002,** *A48,* 811–818.

[164] Gough, T. E.; Mengel, M.; Rowntree, P. A.; Scoles, G. *J.Chem.Phys.* **1985,** *83,* 4958–4961.

[165] Gough, T. E.; Miller, R. E.; Scoles, G. *Appl.Phys.Lett.* **1977,** *30,* 338–340.

[166] Callegari, C.; Conjusteau, A.; Reinhard, I.; Lehmann, K. K.; Scoles, G. *J.Chem.Phys.* **2000,** *113,* 10535–10550.

[167] Nauta, K.; Moore, D. T.; Stiles, P. L.; Miller, R. E. *Science* **2001,** *292,* 481–484.

[168] Michl, J.; Thulstrup, E. W. *Spectroscopy with polarized light: solute alignment by photoselection, in liquid crystals, polymers, and membranes;* VCH Publisher. Inc: Weinheim, 1995.

[169] Frisch, M. J. *et al. Gaussian 03* **2004,** *Revision C.02,* Wallingford CT.

[170] Gerber, R. B.; Brauer, B.; Gregurick, S. K.; Chaban, G. M. *Phys.Chem.Comm.* **2002,** *5,* 142–150.

[171] Huisken, F.; Werhahn, O.; Ivanov, A. Y.; Krasnokutski, S. A. *J.Chem.Phys.* **1999,** *111,* 2978–2984.

[172] Abrams, M. L.; Sherrill, C. D. *J.Chem.Phys.* **2003,** *118,* 1604–1609.

[173] Sponer, J.; Hobza, P. *J.Phys.Chem.* **1994,** *98,* 3161–3164.

[174] Weinkauf, R.; Schermann, J. P.; Vries, M. S. D.; Kleinermanns, K. *Eur.Phys.J.D.* **2002,** *20,* 309–316.

[175] Brown, R. D.; Godfrey, P. D.; Mcnaughton, D.; Pierlot, A. P. *J.Am.Chem.Soc.* **1988,** *110,* 2329–2330.

[176] Brown, R. D.; Godfrey, P. D.; Mcnaughton, D.; Pierlot, A. P. *J.Chem.Soc.Chem.Commun.* **1989,** 37–38.

[177] Brown, R. D.; Godfrey, P. D.; McNaughton, D.; Pierlot, A. P. *Chem.Phys.Lett.* **1989,** *156,* 61–63.

[178] Godfrey, P. D.; Brown, R. D. *J.Am.Chem.Soc.* **1995,** *117,* 2019–2023.

[179] Nir, E.; Janzen, C.; Imholf, P.; Kleinermanns, K.; de Vries, M. S. *Phys.Chem.Chem.Phys.* **2002,** *4,* 740–750.

[180] Bienko, D. C.; Michalska, D.; Roszak, S.; Wojciechowski, W.; Nowak, M. J.; Lapinski, L. *J.Phys.Chem.A* **1997,** *101,* 7834–7841.

[181] McCarthy, W.; Smets, J.; Adamowicz, L.; Plokhotnichenko, A. M.; Radchenko, E. D.; Sheina, G. G.; Stepanian, S. G. *Mol.Phys.* **1997,** *91,* 513–525.

[182] Nir, E.; Plutzer, C.; Kleinermanns, K.; de Vries, M. *Eur.Phys.J.D.* **2002,** *20,* 317–329.

[183] Brauer, B.; Gerber, R. B.; Kabelac, M.; Hobza, P.; Bakker, J. M.; Riziq, A. G. A.; de Vries, M. S. *J.Phys.Chem.A* **2005,** *109,* 6974–6984.

[184] Junk, G.; Svec, H. *J.Am.Chem.Soc.* **1963,** *85,* 839–845.

[185] Gaffney, J. S.; Pierce, R. C.; Friedman, L. *J.Am.Chem.Soc.* **1977,** *99,* 4293–4298.

[186] Szczepaniak, K.; Szczesniak, M. *J.Mol.Struct.* **1987,** *156,* 29–42.

[187] Sheina, G. G.; Stepanian, S. G.; Radchenko, E. D.; Blagoi, Y. P. *J.Mol.Struct.* **1987,** *158,* 275–292.

[188] Crews, B.; Abo-Riziq, A.; Grace, L.; Callahan, M.; Kabela'c, M.; Hobza, P.; de Vries, M. S. *Phys.Chem.Chem.Phys.* **2005,** *7,* 3015–3020.

[189] Fraser, G. T.; Pine, A. S.; Lafferty, W. J.; Miller, R. E. *J.Chem.Phys.* **1987,** *87,* 1502–1508.

[190] Wu, M.; Bemish, R. J.; Miller, R. E. *J.Chem.Phys.* **1994,** *101,* 9447–9456.

[191] Bemish, R. J.; Chan, M. C.; Miller, R. E. *Chem.Phys.Lett.* **1996,** *251,* 182–188.

[192] Holmen, A. *J.Phys.Chem.A* **1997,** *101,* 4361–4374.

[193] Zwier, T. S. *J.Phys.Chem.A* **2001,** *105,* 8827–8839.

[194] Hanus, M.; Ryjacek, F.; Kabela'c, M.; Kubar, T.; Bogdan, T. V.; Trygubenko, S. A.; Hobza, P. *J.Am.Chem.Soc.* **2003,** *125,* 7678–7688.

[195] Feynman, R. P. *Statistical Mechanics;* Perseus Books: Reading, Massachusetts, 1998.

[196] Glaesemann, K. R.; Fried, L. E. *J.Chem.Phys.* **2003,** *118,* 1596–1603.

[197] Dolgounitcheva, O.; Zakrzewski, V. G.; Ortiz, J. V. *J.Am.Chem.Soc.* **2000,** *122,* 12304–12309.

[198] Colominas, C.; Luque, F. J.; Orozco, M. *J.Am.Chem.Soc.* **1996,** *118,* 6811–6821.

[199] Leszczynski, J. *J.Phys.Chem.A* **1998,** *102,* 2357–2362.

[200] Haranczyk, M.; Gutowski, M. *J.Am.Chem.Soc.* **2005,** *127,* 699–706.

[201] Nir, E.; Hunig, I.; Kleinermanns, K.; de Vries, M. S. *Phys.Chem.Chem.Phys.* **2003,** *5,* 4780–4785.

[202] Choi, M. Y.; Miller, R. E. **2006,** In Preparation.

[203] Les, A.; Adamowicz, L. *J.Phys.Chem.* **1989,** *93,* 7078–7081.

[204] Leszczynski, J. *J.Phys.Chem.* **1992,** *96,* 1649–1653.

[205] Gould, I. R.; Hillier, I. H. *J. Chem. Soc., Perkin Trans.* **1990,** 329–330.

[206] Gould, I. R.; Burton, N. A.; Hall, R. J.; Hillier, I. H. *J.Mol.Struct.-THEOCHEM* **1995,** *331,* 147–154.

[207] Estrin, D. A.; Paglieri, L.; Corongiu, G. *J.Phys.Chem.* **1994,** *98,* 5653–5660.

[208] Brown, R. D.; Crofts, J. G.; Godfrey, P. D.; McNaughton, D.; Pierlot, A. P. *J.Mol.Struct.* **1988,** *190,* 185–193.

[209] Viant, M. R.; Fellers, R. S.; McLaughlin, R. P.; Saykally, R. J. *J.Chem.Phys.* **1995,** *103,* 9502–9505.

[210] Peon, J.; Zewail, A. H. *Chem.Phys.Lett.* **2001,** *348,* 255–262.

[211] Gustavsson, T.; Sharonov, A.; Onidas, D.; Markovitsi, D. *Chem.Phys.Lett.* **2002,** *356,* 49–54.

[212] Gustavsson, T.; Sharonov, A.; Markovitsi, D. *Chem.Phys.Lett.* **2002,** *351,* 195–200.

[213] Sharonov, A.; Gustavsson, T.; Carre, V.; Renault, E.; Markovitsi, D. *Chem.Phys.Lett.* **2003,** *380,* 173–180.

[214] Onidas, D.; Markovitsi, D.; Marguet, S.; Sharonov, A.; Gustavsson, T. *J.Phys.Chem.B* **2002,** *106,* 11367–11374.

[215] Gustavsson, T.; Banyasz, A.; Lazzarotto, E.; Markovitsi, D.; Scalmani, G.; Frisch, M. J.; Barone, V.; Improta, R. *J.Am.Chem.Soc.* **2006,** *128,* 607–619.

[216] Douberly, G. E.; Miller, R. E. *J.Phys.Chem.B* **2003,** *107,* 4500–4507.

[217] Sponer, J.; Hobza, P. *J.Am.Chem.Soc.* **1994,** *116,* 709–714.

[218] Komarov, V. M.; Polozov, R. V.; Konoplev, G. G. *J.Theor.Biol.* **1992,** *155,* 281–294.

[219] Sponer, J.; Leszczynski, J.; Hobza, P. *J.Mol.Struc.-THEOCHEM* **2001,** *573,* 43–53.

[220] Szczepaniak, K.; Szczesniak, M. M.; Person, W. B. *J.Phys.Chem.A* **2000,** *104,* 3852–3863.

[221] Aamouche, A.; Ghomi, M.; Coulombeau, C.; Grajcar, L.; Baron, M. H.; Jobic, H.; Berthier, G. *J.Phys.Chem.A* **1997,** *101,* 1808–1817.

[222] Aamouche, A.; Ghomi, M.; Coulombeau, C.; Jobic, H.; Grajcar, L.; Baron, M. H.; Baumruk, V.; Turpin, P. Y.; Henriet, C.; Berthier, G. *J.Phys.Chem.* **1996,** *100,* 5224–5234.

[223] Luisi, B.; Orozco, M.; Sponer, J.; Luque, F. J.; Shakked, Z. *J.Mol.Biol.* **1998,** *279,* 1123–1136.

[224] Kung, H. C.; Wang, K. Y.; Goljer, I.; Bolton, P. H. *J.Magn.Resonance Ser. B* **1995,** *109,* 323–325.

[225] Bludsky, O.; Sponer, J.; Leszczynski, J.; Spirko, V.; Hobza, P. *J.Chem.Phys.* **1996,** *105,* 11042–11050.

[226] McCarthy, W. J.; Lapinski, L.; Nowak, M. J.; Adamowicz, L. *J.Chem.Phys.* **1995,** *103,* 656–662.

[227] Sabio, M.; Topiol, S.; Lumma, W. C. *J.Phys.Chem* **1990,** *94,* 1366–1372.

[228] Gu, J. D.; Leszczynski, J. *J.Phys.Chem.A* **1999,** *103,* 2744–2750.

[229] Huang, Y.; Kenttamaa, H. *J.Phys.Chem. A* **2004,** *108,* 4485 –4490.

[230] Hanus, M.; Kabelac, M.; Rejnek, J.; Ryjacek, F.; Hobza, P. *J.Phys.Chem.B* **2004,** *108,* 2087–2097.

[231] Jucks, K. W.; Miller, R. E. *J.Chem.Phys.* **1987,** *87,* 5629–5633.

[232] Smets, J.; McCarthy, W. J.; Adamowicz, L. *J.Phys.Chem.* **1996,** *100,* 14655–14660.

[233] Smets, J.; Smith, D. M. A.; Elkadi, Y.; Adamowicz, L. *J.Phys.Chem.A* **1997,** *101,* 9152–9156.

[234] Gorb, L.; Leszczynski, J. *Int. J. Quantum Chem.* **1997,** *65,* 759–765.

[235] Broo, A.; Holmen, A. *J.Phys.Chem.A* **1997,** *101,* 3589–3600.

[236] Smets, J.; Destexhe, A.; Adamowicz, L.; Maes, G. *J. Phys. Chem. B* **1997,** *101,* 6583–6599.

[237] Aleman, C. *Chem.Phys.* **1999,** *244,* 151–162.

[238] Aleman, C. *Chem.Phys.Lett.* **1999,** *302,* 461–470.

[239] Dolgounitcheva, O.; Zakrzewski, V. G.; Ortiz, J. V. *J.Phys.Chem.A* **1999,** *103,* 7912–7917.

[240] Nguyen, M. T.; Chandra, A. K.; Zeegers-Huyskens, T. *J. Chem. Soc., Faraday Trans.* **1998,** *94,* 1277–1280.

[241] Gaigeot, M. P.; Kadri, C.; Ghomi, M. *J.Mol.Struct.* **2001,** *565-566,* 469–473.

[242] van Mourik, T.; Price, S. L.; Clary, D. C. *J.Phys.Chem.A* **1999,** *103,* 1611–1618.

[243] van Mourik, T.; Benoit, D. M.; Price, S. L.; Clary, D. C. *Phys.Chem.Chem.Phys.* **2000,** *2,* 1281–1290.

[244] Hu, X.; Li, H.; Liang, W.; Han, S. *J.Phys.Chem.B* **2004,** *108,* 12999–13007.

[245] Smedarchina, Z.; Siebrand, W.; Fernandez-Ramos, A.; Gorb, L.; Leszczynski, J. *J.Chem.Phys.* **2000,** *112,* 566–573.

[246] Gee, M.; Bourdaa, M. H.; Tao, F. M., Eds.; *Tautomerization of guanine and the effect of water,* ; 217th ACS National Meeting, 1999.

[247] Gorb, L.; Leszczynski, J. *J.Am.Chem.Soc.* **1998,** *120,* 5024–5032.

[248] Gorb, L.; Leszczynski, J. *Int.J.Quantum Chem.* **1998,** *70,* 855–862.

[249] Sobolewski, A. L.; Adamowicz, L. *J. Chem. Phys* **1995,** *102,* 5708.

[250] Gorb, L.; Leszczynski, J. *Int.J.Quantum Chem.* **1998,** *70,* 855–862.

[251] Jalbout, A. F.; Adamowicz, L. *J.Phys.Chem.A* **2001,** *105,* 1033–1038.

[252] Aamouche, A.; Berthier, G.; Cadioli, B.; Gallinella, E.; Ghomi, M. *J.Mol.Struct.-THEOCHEM* **1998,** *426,* 307–312.

[253] Bencivenni, L.; Ramondo, F.; Pieretti, A.; Sanna, N. *J. Chem. Soc., Perkin Trans.* **2000,** 1685–1693.

[254] Maltese, M.; Passerini, S.; Nunziante-Cesaro, S.; Dobos, S.; Harsanyi, L. *J.Mol.Struct.* **1984,** *116,* 49–65.

[255] Smets, J.; McCarthy, W. J.; Adamowicz, L. *J.Phys.Chem.* **1996,** *100,* 14655–14660.

[256] Smets, J.; Smith, D. M. A.; Elkadi, Y.; Adamowicz, L. *J.Phys.Chem.A* **1997,** *101,* 9152–9156.

[257] van Mourik, T.; Price, S. L.; Clary, D. C. *Faraday Disc.* **2001,** *118,* 95–108.

[258] Schiedt, J.; Weinkauf, R.; Neumark, D. M.; Schlag, E. W. *Chem.Phys.* **1998,** *239,* 511–524.

[259] Terpstra, P. A.; Otto, C.; Greve, J. *J.Chem.Phys.* **1996,** *106,* 846–848.

[260] Ilich, P.; Hemann, C. F.; Hille, R. *J.Phys.Chem.B* **1997,** *101,* 10923–10938.

[261] Graindourze, M.; Grootaers, T.; Smets, J.; Zeegers-Huyskens, T.; Maes, G. *J.Mol.Struct.* **1991,** *243,* 37–60.

[262] Heath, J. R.; Zhang, Q.; O'Brien, S. C.; Curl, R. F.; Kroto, H. W.; Smalley, R. E. *J.Am.Chem.Soc.* **1987,** *109,* 359–363.

[263] Gaigeot, M. P.; Kadri, C.; Ghomi, M. *J.Mol.Struct.* **2000,** *565-566,* 469–473.

[264] Kim, S. K.; Lee, W.; Herschbach, D. R. *J.Phys.Chem.* **1996,** *100,* 7933–7937.

[265] Casaes, R. N.; Paul, J. B.; McLaughlin, R. P.; Saykally, R. J. *J.Phys.Chem.A* **2004,** *108,* 10989–10996.

[266] Miller, R. E. *Science* **1988,** *240,* 447–453.

[267] Kay, B. D.; Castleman, A. W. *J.Chem.Phys.* **1983,** *78,* 4297–4302.

[268] Ryali, S. B.; Fenn, J. B. *Berich.Bunsen.Gesell.* **1984,** *88,* 245–253.

[269] Anex, D. S.; Davidson, E. R.; Douketis, C.; Ewing, G. E. *J.Phys.Chem.* **1988,** *92,* 2913–2925.

[270] Jeffrey, G. A.; Saenger, W. *Hydrogen Bonding in Biological Structures;* Sprinter-Verlag: New York, 1991.

[271] Merritt, J. M.; Douberly, G. E.; Miller, R. E. *J.Chem.Phys.* **2004,** *121,* 1309–1316.

[272] Khademi, S.; O'Connell III, J.; Remis, J.; Robles-Colmenares, Y.; Larry, J. W. M.; Stroud, R. M. *Science* **2004,** *305,* 1587–1594.

[273] Zheng, L.; Kostrewa, D.; Berneche, S.; Winkler, F. K.; Li, X. *Proc.Natl.Acad.Sci.U.S.A.* **2004,** *101,* 17090–17095.

[274] Basch, H.; Krauss, M.; Stevens, W. J. *J.Am.Chem.Soc.* **1985,** *107,* 7267–7271.

[275] O'Malley, P. J. *J.Am.Chem.Soc.* **1998,** *120,* 11732–11737.

[276] Machado, F. B. C.; Davidson, E. R. *J.Chem.Phys.* **1992,** *97,* 1881–1891.

[277] Scheiner, S.; Yi, M. *J.Phys.Chem.* **1996,** *100,* 9235–9241.

[278] Tatara, W.; Wojcik, M. J.; Lindgren, J.; Probst, M. *J.Phys.Chem.A* **2003,** *107,* 7827–7831.

[279] Perchard, C.; Novak, A. *J.Chem.Phys.* **1968,** *48,* 3079–3084.

[280] Colombo, L.; Bleckmann, P.; Schrader, B.; Schneider, R.; Plesser, T. *J.Chem.Phys.* **1974,** *61,* 3270–3278.

[281] Loeffen, P. W.; Pettifer, R. F.; Fillaux, F.; Kearley, G. J. *J.Chem.Phys.* **1995,** *103,* 8444–8455.

[282] Su, C. C.; Chang, H. C.; Jiang, J. C.; Wei, P. Y.; Lu, L. C.; Lin, S. H. *J.Chem.Phys.* **2003,** *119,* 10753–10758.

[283] Hockridge, M. R.; Robertson, E. G.; Simons, J. P. *Chem.Phys.Lett.* **1999,** *302,* 538–548.

[284] Nagy, P. I.; Durant, G. J.; Smith, D. A. *J.Am.Chem.Soc.* **1993,** *115,* 2912–2922.

[285] Fritscher, J. *Phys.Chem.Chem.Phys.* **2004,** *6,* 4950–4956.

[286] Hummer, G.; Pratt, L. R.; Garcia, A. E. *J.Phys.Chem.A* **1998,** *102,* 7885–7895.

[287] Torrent, M.; Musaev, D. G.; Morokuma, K.; Ke, S. C.; Warncke, K. *J.Phys.Chem.B* **1999,** *103,* 8618–8627.

[288] Bael, M. K. V.; Smets, J.; Schoone, K.; Houben, L.; McCarthy, W.; Adamowicz, L.; Nowak, M. J.; Maes, G. *J.Phys.Chem.A* **1997,** *101,* 2397–2413.

[289] Carles, S.; Lecomte, F.; Schermann, J. P.; Desfrancois, C. *J.Phys.Chem.A* **2000,** *104,* 10662–10668.

[290] Talbot, F. O.; Simons, J. P. *Eur. Phys. J. D* **2002,** *20,* 389–398.

[291] Nauta, K. *Infrared Spectroscopy and Dynamics of Molecules and Molecular Complexes in Liquid Helium Droplets,* Thesis, University of North Carolina at Chapel Hill, 2000.

[292] Miller, R. E. *Faraday Disc.* **2001,** *118,* 1–17.

[293] Chakravorty, K. K.; Parker, D. H.; Bernstein, R. B. *Chem.Phys.* **1982,** *68,* 1–12.

[294] Stienkemeier, F.; Bunermann, O.; Mayol, R.; Ancilotto, F.; Barranco, M.; Pi, M. **2004,** *70,* 214508.

[295] Scoles, G. *Int.J.Quantum Chem.* **1990,** *24,* 475–479.

[296] Dalfovo, F. *Z.Phys.D* **1994,** *29,* 61–66.

[297] Carney, J. R.; Hagemeister, F. C.; Zwier, T. S. *J. Chem. Phys* **1988,** *108,* 3379–3382.

[298] Eichenauer, D.; Roy, R. J. L. *J.Chem.Phys.* **1988,** *88,* 2898–2912.

[299] Kang, C.; Korter, T. M.; Pratt, D. W. *J. Chem. Phys.* **2005,** *122,* 174301/1–174301/8.

[300] Florio, G. M.; Zwier, T. S.; Myshakin, E. M.; Jordan, K. D.; Sibert, E. L. *J. Che. Phys.* **2003,** *118,* 1735–1746.

[301] Lindsay, C. M.; Douberly, G. E.; Miller, R. E. *J.Mol.Struct.* **2006,** *786,* 96–104.

[302] Choi, M. Y.; Miller, R. E. **2006,** In Preparation.

[303] Yang, Z.; Rodgers, M. T. *Phys.Chem.Chem.Phys.* **2004,** *6,* 2749–2757.

[304] Fogarasi, G. *J.Phys.Chem.A* **2002,** *106,* 1381–1390.

[305] Fogarasi, G. *J.Mol.Struct.* **1997,** *413-414,* 271–278.

[306] Aleman, C. *Chem.Phys.* **2000,** *253,* 13–19.

[307] Estrin, D. A.; Paglieri, L.; Corongiu, G. *J.Phys.Chem.* **1994,** *98,* 5653–5660.

[308] Ha, T.-K.; Keller, H.-J.; Gunde, R.; Gunthard, H.-H. *J.Phys.Chem. A* **1999,** *103,* 6612–6623.

[309] Russo, N.; Toscano, M.; Grand, A. *J.Phys.Chem. B* **2001,** *105,* 4735–4741.

[310] Russo, N.; Toscano, M.; Grand, A. *J.Am.Chem.Soc.* **2001,** *123,* 10272–10279.

[311] Potts, A. R.; Baer, T. *J.Chem.Phys.* **1998,** *108,* 869–875.

[312] Reva, I. D.; Stepanian, S. G.; Adamowicz, L.; Fausto, R. *Chem.Phys.Lett.* **2003,** *374,* 631–638.

[313] Pettersson, M.; Macoas, E. M. S.; Khriachtchev, L.; Fausto, R.; Rasanen, M. *J.Am.Chem.Soc.* **2003,** *125,* 4058–4059.

[314] Potts, A. R.; Baer, T. *J.Chem.Phys.* **1996,** *105,* 7605–7612.

[315] Potts, A. R.; Baer, T. *J.Phys.Chem.A* **1997,** *101,* 8970–8978.

[316] Benzer, S.; Freese, E. *Proc. Natl. Acad. Sci. USA* **1958,** *44,* 112–119.

[317] Kaufman, E. R. *Mol.Cell.Biol.* **1984,** *4,* 2449–2454.